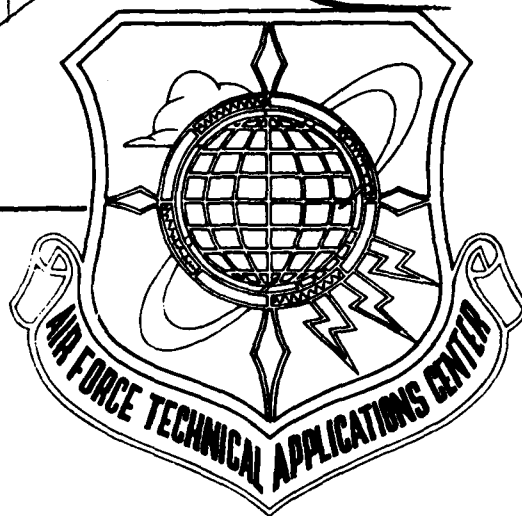


ADA 087242

15 ✓  
**LEVEL**

AFTAC-TR-80-23

TIME DELAY OF TERRESTRIAL LIGHT  
PULSES PROPAGATING THROUGH CLOUDS  
TO SATELLITE SYSTEMS



HSS Inc  
2 Alfred Circle  
Bedford, MA 01730

7 JULY 1980

DTIC  
ELECTE  
JUL 28 1980  
S D C

Final Report (1 April 1977 - 30 September 1979)

Approved for public release; Distribution unlimited.

AIR FORCE TECHNICAL APPLICATIONS CENTER  
HEADQUARTERS UNITED STATES AIR FORCE  
PATRICK AIR FORCE BASE, FLORIDA 32925

80 7 23 083

UNCLASSIFIED

SECURITY CLASSIFICATION OF THIS PAGE (When Data Entered)

REPORT DOCUMENTATION PAGE		READ INSTRUCTIONS BEFORE COMPLETING FORM	
1. REPORT NUMBER AFTAC-TR-80-23	2. GOVT ACCESSION NO. AD-A084242	3. RECIPIENT'S CATALOG NUMBER	
4. TITLE (and Subtitle) TIME DELAY OF TERRESTRIAL LIGHT PULSES PROPAGATING THROUGH CLOUDS TO SATELLITE SYSTEMS.		5. TYPE OF REPORT & PERIOD COVERED Final Report, Tasks 4.1- 4.7-1 Apr '77 - 30 Sep '79	
6. AUTHOR(s) H. S. Stewart L. B. Woolaver		7. PERFORMING ORG. REPORT NUMBER HSS-B-058	
9. PERFORMING ORGANIZATION NAME AND ADDRESS HSS Inc 2 Alfred Circle, Bedford, Mass 01730		8. CONTRACT OR GRANT NUMBER(s) F08606-77-C-0024	
11. CONTROLLING OFFICE NAME AND ADDRESS 1035 TCHO (TFE) Patrick AFB Florida 32925 Maj John Van Workum		10. PROGRAM ELEMENT, PROJECT, TASK AREA & WORK UNIT NUMBERS 11	
14. MONITORING AGENCY NAME & ADDRESS (if different from Controlling Office) Same		12. REPORT DATE 7 Jul 80	
13. NUMBER OF PAGES 202		15. SECURITY CLASS. (of this report) UNCLASSIFIED	
16. DISTRIBUTION STATEMENT (of this Report) Approved for public release; Distribution unlimited 9 Final rept. 1 Apr 77-30 Sep 77 only Task 4.1-4.7		15a. DECLASSIFICATION/DOWNGRADING SCHEDULE N/A	
17. DISTRIBUTION STATEMENT (of the abstract entered in Block 20, if different from Report)			
18. SUPPLEMENTARY NOTES			
19. KEY WORDS (Continue on reverse side if necessary and identify by block number) propagation      time delay pulse              scattering optical            light clouds             delay			
20. ABSTRACT (Continue on reverse side if necessary and identify by block number) A method is described and applied for interpreting optically filtered all sky photographs so as to generate curves of the time dependent proba- bility that a photon emitted by an isotropic source near the earth's surface will reach a satellite at any elevation and azimuth in the sky. Two basic concepts are involved: first, that the probability at $\lambda = 0.76\mu$ for absorp- tion of light by atmospheric oxygen is proportional to the square root of the dwell time of the light in the atmosphere and second, that a time			

DD FORM 1 JAN 73 1473

EDITION OF 1 NOV 65 IS OBSOLETE

UNCLASSIFIED

SECURITY CLASSIFICATION OF THIS PAGE (When Data Entered)

390794

UNCLASSIFIED

SECURITY CLASSIFICATION OF THIS PAGE(When Data Entered)

20. (Continued) dependent reciprocity theorem exists allowing observations of the skylight incident on a ground based detector to be interpreted in terms of the probability that a photon starting at the detector can reach a satellite in the direction of the sun. Detailed theory and operating equations were developed and appropriate equipment was built and operated. Computerized reduction of microdensitometer scans of the all sky photographs led to values of mean time delay and transmission for 125000 equal elements of solid angle in the sky. These were summed to generate the time dependent probability. Photographs made at Kennedy Space Center were used to generate delay curves for seven satellite directions on nine separate occasions.

Accession For	
NTIS GRA&I	<input checked="checked" type="checkbox"/>
DDC TAB	<input type="checkbox"/>
Unannounced	<input type="checkbox"/>
Justification	
By _____	
Distribution/	
Availability/	
Dist	Available for special
A	

SECURITY CLASSIFICATION OF THIS PAGE(When Data Entered)

## TABLE OF CONTENTS

<u>Section</u>	<u>Title</u>	<u>Page</u>
	TABLE OF CONTENTS	1
	LIST OF ILLUSTRATIONS	3
	LIST OF TABLES	5
1.	INTRODUCTION	6
2.	EXPERIMENTAL CONCEPT	7
2.1	Elements of the Problem	7
2.2	Experimental Approach	10
2.3	The Reciprocity Theorem	12
2.4	Geometric Delay	15
2.5	Scattering Delay	16
2.6	Pulse Shape Synthesis	17
3.	CERTAIN THEORIES AND APPROXIMATIONS	21
3.1	Transport Mean-Free-Path	21
3.2	Two-Stream Theory	22
3.3	The Reduced Atmosphere	25
3.4	Diffusion Theory and Monte Carlo Calculations	26
3.5	Low Resolution O <sub>2</sub> - Band Absorption	36
4.	RELATIONSHIP USED IN DATA REDUCTION	41
4.1	Height of Cloud Base	41
4.2	Calibration of All Sky Radiometer and of All Sky Cameras	47
4.2.1	Geometric Relationships	47
4.2.2	Camera System Radiometric Relationship	56
4.2.3	All-Sky Radiometer Calibration	57
4.2.4	Red Channel Camera System Calibration	59
4.2.5	Red Channel Camera Calibration Results	61
4.2.6	Calibration of the On/Off Band Camera System	63
5.	WORKING EQUATIONS FOR DATA ANALYSIS	71
5.1	General Comments	71

## TABLE OF CONTENTS (Cont)

<u>Section</u>	<u>Title</u>	<u>Page</u>
5.2	Transmission of an Overcast	73
5.3	Ratio of Transport Mean Free Path to Cloud Thickness	73
5.4	Overcast Thickness	73
5.5	Mean Time Delay in Overcasts	77
5.6	Geometric Delay from Cloud Top to Satellite	78
5.7	Radiance Centroid	80
5.8	Effects of Ground Reflectivity	84
6.	COMPUTER PROCESSING	85
6.1	Introduction	85
6.2	Digitization	88
6.3	Photographic Sensitometry	89
6.4	Image Registration	89
6.5	Field-of-View Limitation	92
6.6	Blue Sky Flagging	93
7.	EXPERIMENTAL RESULTS	97
7.1	General Comments	97
7.2	Predicted Light Pulse Shapes	97
7.3	Time Delays	98
7.4	Centroid of Radiance	102
7.5	Effect of Earth Albedo	104
8.	CONCLUSIONS	177
	REFERENCES	181
	APPENDIX A- EXPERIMENTAL EQUIPMENT	183

## LIST OF ILLUSTRATIONS

<u>Figure</u>	<u>Legend</u>	<u>Page</u>
2.1	Schematic illustration of possible photon paths with, (A) geometric delay, (B) scattering delay, and (C) combined geometric and scattering delay.	9
3.1	Time dependent probability of delayed transit for a hypothetical overcast of diffuse transmission 0.25.	29
3.2	Time dependent probability of delayed transit for a hypothetical overcast of diffuse transmission 0.10.	30
3.3	Comparison of the Mie phase function to the isotropic phase function used in diffusion theory.	31
3.4	Time dependent probability of delayed transit for a hypothetical optically thin overcast.	32
3.5	Comparison of the probability of delayed transit with and without $O_2$ absorption.	34
4.1	Relationship between the off-axis angle, $z$ , and the image height, $d$ , for the Fairchild $f/1.5$ lens.	42
4.2	Automax camera with Fairchild $f/1.5$ lens attached.	44
4.3	All sky photograph from the stereo camera at Station A showing features selected for cloud height determinations.	45
4.4	All sky photograph from stereo camera at Station B showing features selected for cloud height determination.	46
4.5	Geometric relationship of feature $f$ as seen from Stations A and B for cloud height determination.	48
4.6	All sky detectors using reflections from a spheric surface.	49
4.7	Relationship of external angle of camera $\beta$ , and external angle of camera-sphere system, $z$ .	50
4.8	Ratio of image height at zenith angle, $z$ , to image height at $z = 90$ plotted against external angle, $z$ .	52
4.9	Relationship between an element of area, $da$ , in the image plane (upper drawing) to an element of solid angle, $d\Omega$ , in object space (lower drawing).	55

# LIST OF ILLUSTRATIONS (Cont)

<u>Figure</u>	<u>Legend</u>	<u>Page</u>
4.10	Data recorded on August 2, 1977 by the sun photometer giving values of transmission, T, to the sun versus wavelength $\lambda$ .	62
4.11	Transmission of the atmosphere in low resolution (From Ref. 16).	64
4.12	Atmospheric transmission showing the oxygen absorption band of interest (From Ref. 17).	65
4.13	Schematic diagram of calibration equipment for on-band/off-band camera filters.	67
4.14	Photograph of calibration equipment for on-band/off-band filters.	68
4.15	Data obtained with calibration equipment showing the logarithm of the on-band/off-band ratio plotted against the square root of the oxygen path length.	69
5.1	Cloud in real (left) and reduced atmosphere (right).	75
6.1	Schematic presentation of the major steps in the data reduction system used to derive predicted pulse shapes.	86
6.2	Contact photographic print from 3 data runs showing typical original data.	87
6.3	D-log E curve for the 2476 film scanned at Optronics.	90
6.4	D-log E curve for high speed infrared film (HIE) scanned at Optronics.	91
6.5	All sky image reconstructed from digital data.	94
6.6	Two density level mask showing locations of blue sky as identified by blue/red ratio.	96
7.1	Time Delays .	101
7.	Uncaptioned figures - experimental results.	105
A1	General view of equipment installation at A site.	185
A2	General view of equipment installation at B site.	186
A3	Detailed view of spheric mirror and support structure.	187
A4	View of All Sky Radiometer and Support.	189
A5	View of Teleradiometer and Support.	191

## LIST OF TABLES

<u>Table</u>	<u>Title</u>	<u>Page</u>
3.1	Comparison of values of $A_0(z)$ reported by Danielson and calculated by two-stream theory.	36
4.1	Cloud base heights for 8/1/77 at 1715 hours calculated for the numbered features in the stereo pair of Figures 4.4 and 4.5.	48
4.2	Magnitude of errors introduced by treating finite camera-mirror separation as infinite.	53
7.1	Probable correct zero times.	99
7.2	Coordinates of radiance centroid.	103
8.1	Comparison of the coupling coefficient with characteristics of relative amplitude vs delay curves.	179



## SECTION 1

### INTRODUCTION

The work discussed here is an experimental means to estimate cloud and overcast induced probable errors in a geodetic technique of interest to AFTAC. The errors of interest relate to the difference in the assigned times for the initiation of a surface light pulse clocked from three wide field-of-view observing stations located in space. The errors are related to the degree of time smearing a fast light pulse suffers due to the multitude of path lengths taken by the photons which contribute to the received pulse. This report presents experimentally derived estimates of the pulse shape one would expect from a delta function light source at or near the earth's surface at a wide field-of-view optical receiver in earth orbit after transit through a sampling of natural clouds. The experimental technique employed does not attempt a direct measurement of the shape of the received light pulse (a more valid but more costly method) but rather infers the pulse shape from cloud geometric and radiance measurements and radiation transport theory.

The work covered by this report was supported by the Air Force Technical Applications Center (TFE), Patrick AFB, FL. The experimental phase of the work was conducted at Kennedy Space Center during the summer of 1977 in conjunction with the Thunderstorm Research International Program, Trip 77. The data reduction and analysis phase has been carried out at HSS Inc, Bedford, MA using the computer located at the Air Force Geophysics Laboratory, Hanscom AFB. This is the final report for this project and includes revised versions of material presented earlier by interim report and by papers read at the Satellite Working Group Meetings held at Patrick AFB.

## SECTION 2

### EXPERIMENTAL CONCEPT

#### 2.1 ELEMENTS OF THE PROBLEM

The presence of an overcast or clouds in the line-of-sight degrades the capability of the geodetic technique based on the time-of-arrival of a sharply rising light pulse at three or more stations with wide field-of-view receivers. The loss in capability arises directly from the reduction in the rate-of-rise of the leading edge of the light pulse with a consequent loss in resolution for the time assigned to the arrival of the pulse. The degree to which such a system would be degraded can be estimated from the pulse shape one would expect from a delta function light pulse after transit through various cloud types. The experimental concept presented here was developed to provide a means of extracting such pulse shapes from experimental measurements on natural clouds and to provide data useful in estimating the geodetic errors which would prevail for the cloud types measured.

Any photon originating in the delta function light pulse which transits from source to receiver along the direct path arrives at the receiver in the minimum elapsed time after the occurrence of the pulse. A photon traveling by any other path suffers a delay compared to the minimum time, the magnitude of the delay depending on the extra path length. In clear weather essentially all of the energy arriving at the receiver travels by the direct route. In the case of an overcast or intervening clouds only a tiny fraction of the energy arrives by the direct route and most arrives by a multitude of paths dictated by the scattering conditions in the intervening cloud.

Figure 2.1 presents three possible photon paths between an isotropic source near the ground and a receiver located in space (the direct path from source to receiver is not included). Paths of the type shown by A result from a single photon scatter by an air molecule or aerosol particle, the scattering particle may or may not be located in an identifiable cloud. If the location of the scattering particle can be established, the total path length can be computed and the excess over the direct path determined. This is a purely geometric problem and leads to geometric delay. Paths of the type shown by B result from multiple scattering of photons along the direct path where the emergent photon continues to travel along the direct path from source to receiver. The extra path length leads to scattering delay and results entirely from the multiple scatter with the geometry of the source and receiver playing no part. A more probable path is shown by C in which the extra path length results from both geometry and scattering and leads to a combined geometric and scattering delay. The received pulse shape is the sum over time of all photons arriving with their respective geometric and scattering delays.

The most direct solution to the problem of acquiring cloud modified pulse shapes is one of direct measurement with a suitable source and receiver deployed as shown in Figure 2.1. In practice this approach is both difficult and costly. An indirect solution to the problem is presented here which employs pulse shape synthesis from three quantities. For every line-of-sight contributing to the final pulse shape these quantities are:

1. The probability that a photon will arrive along that path
2. The geometric delay for that path
3. The mean scattering delay for that path

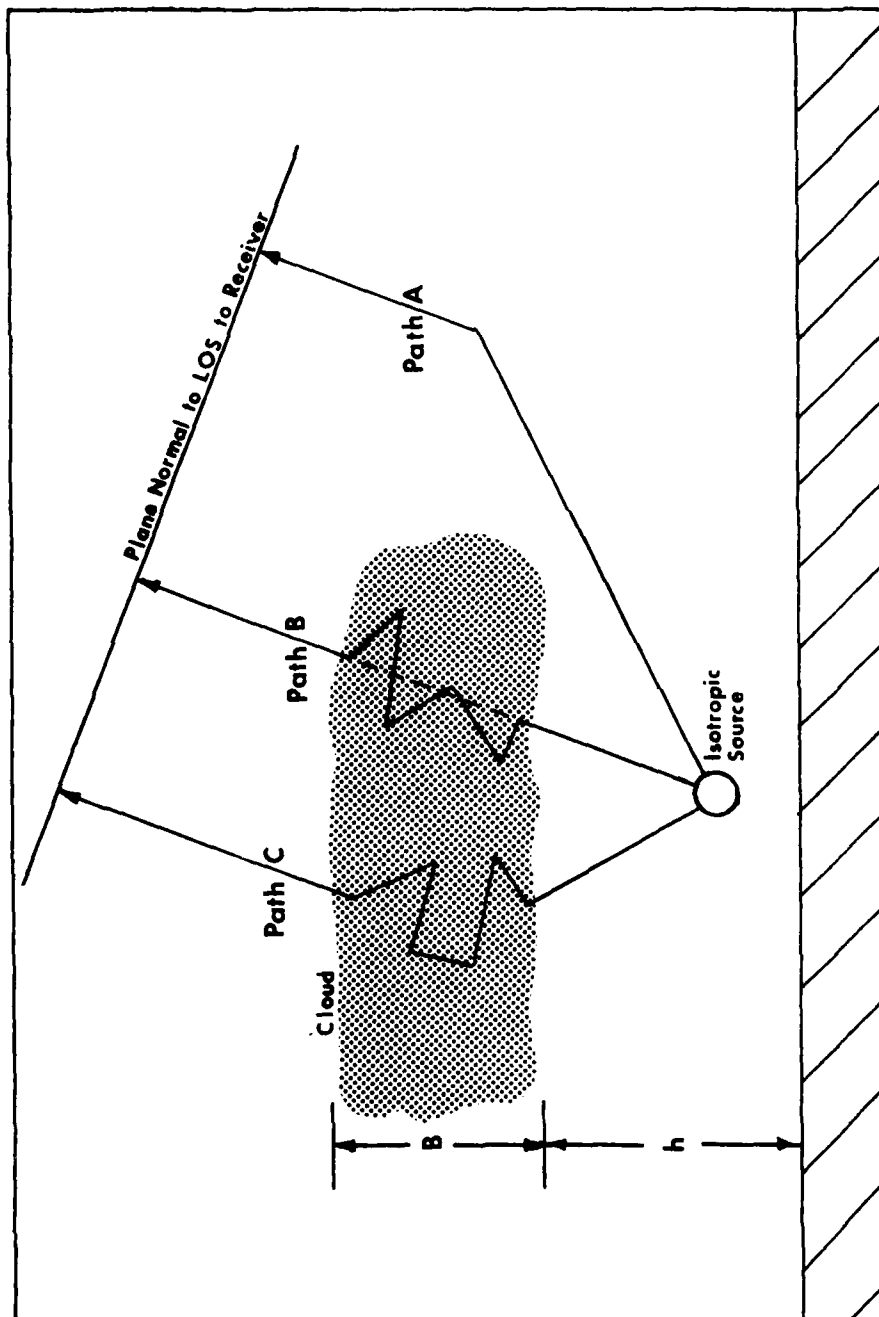


Figure 2.1. Schematic illustration of possible photon paths with, (A) geometric delay, (B) scattering delay, and (C) combined geometric and scattering delay.

The experimental concept now becomes one of devising a means of recording cloud data from which these quantities can be derived. The remainder of this section is devoted to a review of experimental concept and a non-mathematical presentation of how the expected pulse shape is synthesized. A full development of the system is given in subsequent sections.

## 2.2 EXPERIMENTAL APPROACH

The geodetic measurement application of primary importance concerns pulsed isotropic sources at or near the surface with the receivers in space. The approach presented here make two fundamental transformations in the problem for experimental reasons: (1) the receiver is placed on the ground, and (2) a steady, as opposed to a pulsed, light source is employed, the sun. These transformations permit a valid and experimentally simple approach to the problem. The first transformation is based on the reciprocity theorem (discussed fully below) which states that, when only linear processes are involved, the source and receiver can be interchanged with no change in result. The second transformation is based on the ability to extract from the steady state experimental data the geometric and scattering delays required to synthesize the pulse shape.

The primary experimental procedure consisted of photographically recording with all-sky cameras the radiance of the bottom of sun illuminated clouds simultaneously in four wavelength bands; red, blue, narrow band at  $7606 \text{ \AA}$ , and narrow band at  $7530 \text{ \AA}$ . The narrow band at  $7606 \text{ \AA}$  is located in one of the  $\text{O}_2$  absorption bands of the atmosphere (ON-BAND) and the narrow band at  $7530 \text{ \AA}$  is adjacent but not in the absorption band (OFF-BAND). Each of these photographs provide data for all azimuth angles around the recording station and for all zenith angles down to the horizon. The exposed photographic film was processed under sensitometric control to permit the extraction of cloud bottom radiance in absolute radiometric terms. In

addition to the primary cameras stereo photographs of the clouds were recorded from two separated stations by cameras with wide angle lenses. Various calibration and support equipment completed the experimental plan. The applicability of these choices and the manner by which this plan supplies the data required to synthesize an expected pulse shape can be summarized by the following statements.

1. The sun has a spectral power distribution similar to that of the sources of interest and is therefore an acceptable substitute for these sources.
2. Digitization of the four primary photographs provides data for all lines-of-sight of interest where each data element corresponds to one line-of-sight.
3. Registration of the four primary photographs brings all data elements of the photograph from each wavelength band into coincidence which allows any one data element from all four photographs to be assigned to a single line-of-sight.
4. The stereo pair photographs provide the height of the cloud bottoms.
5. The absolute radiance along any line-of-sight is a measure of the transmission from sun to camera and can be related to the probability that a photon will arrive along that line-of-sight.

6. Any line-of-sight which is associated with an area of blue sky and does not terminate on the bottom of an identifiable cloud can be located from the ratio of the blue radiance to the red radiance. Such lines-of-sight contribute a negligible fraction of the total energy received and will be ignored during data processing.
7. A portion of the total geometric delay can be determined from the direction of any line-of-sight and the cloud bottom height. This will be discussed more fully below.
8. The scattering delay along a line-of-sight due to photon diffusion within the cloud can be evaluated by comparing the radiance in the narrow band at 7606 Å (ON-BAND) to radiance in the narrow band at 7530 Å (OFF-BAND). Any ON-BAND radiance value is related to the total path through the atmosphere that is, (1) from the top of the atmosphere to the cloud top, (2) through the cloud, and (3) from cloud bottom to the camera. This will be discussed more fully below.

The equipment to implement this experimental plan was designed, constructed, and operated at Kennedy Space Center during the summer of 1977. A more complete description of the equipment is given in Appendix A.

### 2.3 THE RECIPROCITY THEOREM

The reciprocity theorem concerns the reversibility of photon propagation. The theorem was first stated by Helmholtz (Ref. 1) and, from an

experimentalists point of view, the theorem is used in a most articulate elaboration by Minnaert . (Ref 2). Helmholtz's original statement is translated here as:

"From point A a unit quantity of light of a given color, polarized in a given direction  $\alpha$ , goes in such a direction that after a series of reflections and refractions the quantity  $x$  finally arrives at B and is polarized in the direction  $\beta$ . If we now allow a unit quantity of  $\beta$  polarized light to start out backwards in the reverse direction from this final ray, then after the light undergoes all of the former reciprocal and reversible processes the same quantity  $x$  and the same fraction of the  $\alpha$  polarized light arrives at the initial point."

Minnaerts' comments are significant. "This principle is widely applicable: it applies to reflecting, refracting, absorbing and scattering media, for each separate wavelength and for each plane of polarization. It fails only in the cases of fluorescence and of magnetic rotation." If Minnaert were writing now he might have described the principle as one including all linear processes and excluding only non-linear processes.

The reciprocity theorem was written to describe source and receiver exchanges in steady state situations. To apply it to the problem addressed here requires that the theorem be expanded to cover transient light signals. The authors of this report are unaware of any publications which discuss a time dependent reciprocity theorem although some techniques of Monte Carlo calculations imply time dependent reciprocity. Two statements can be developed from the reciprocity theorem (1 and 2 below) and a "reasonable" additional statement is added (3 below) which implies a time



dependent reciprocity theorem. The validity of time dependent reciprocity can be demonstrated for specific cases but no general theorem has been found or developed as part of the work reported here. The three statements are:

1. In the presence of any condition of weather or of ground reflectivity the power received from the sun by an isotropic detector is in fixed proportion to the power which would be received at the same time by a satellite in the direction of the sun from an isotropic source at the same location as the isotropic detector. This assumes that the spectral power distribution of the isotropic source corresponds to that of the sun.

2. The isotropic detector of statement 1 above can be replaced in the argument by a receiver having a specific solid angle of response if only the isotropic source is replaced by a source radiating into the same solid angle and direction.

3. Relative to  $t_0$ , the direct passage transit time of a photon from sun to the location of the receiver of statements 1 or 2 above, the probability that a photon will arrive at some later time  $t$ ,  $\beta(t-t_0)$  is the same as the probability of a photon's delayed arrival at the satellite  $\beta(t-t_1)$  when the appropriate source is substituted for the receiver. Here  $t_1$  is the transit time for direct passage from the location of the ground based source to the satellite.

A significant conclusion is reached from statement 1 above. That is: for any weather conditions during the day, the radiant power from the sun measured by an isotropic detector in any location can be used to calculate the transmission of power from an isotropic source at that location to a satellite in the direction of the sun.

Statement 3 above indicates in part that if the probability of time delay of photons traveling from the sun to an isotropic detector is known then the probability of delay from an isotropic source to a detector in the direction of the sun is also known. It follows that a pulse shape derived from a ground based detector can be used to infer the pulse shape which would have been measured at a satellite.

#### 2.4 GEOMETRIC DELAY

Referring again to Figure 2.1 photon paths of the type illustrated by A are not a matter of concern in the study reported here. Such paths occur in areas outside an identifiable cloud; that is, in blue sky areas, and are considered negligible contributors to the total received energy. Paths of the type illustrated by B are special cases leaving paths of the type illustrated by C for consideration.

The photon path illustrated by C in Figure 2.1 is one of a family of possible paths from the bottom to the top of the cloud (assuming the source on the ground and the receiver in space). The one shown leaves the top of the cloud at a point directly above and a distance B from the point of entry at the bottom of the cloud. This path is representative of the average geometric delay. The extra path length which leads to delay is the difference between the direct path from source to receiver and the path consisting of (1) source to cloud bottom, (2) the distance, B, and (3) top of the cloud to receiver. The data reduction procedures used this definition of geometric delay.

In the absence of absorption the transmission of a cloud or overcast is a function of the ratio of the cloud thickness, B, to the scattering mean free path,  $\ell$ . That is the absorption free transmission is a function of  $B/\ell$ . This ratio can be calculated for each line of sight by proper data reduction using the absolute radiance of the bottom of the

cloud from the red photograph taken in the wavelength region  $\lambda = 6700 \text{ \AA}$  (see subsequent sections).

This method of deriving the cloud thickness,  $B$ , from the recorded data makes the experimental plan given above complete with no independent measurement of cloud thickness (or cloud top heights) required. Once data reduction was underway, this method proved inadequate for a significant fraction of the lines-of-sight leading to spurious results for these data elements. The computer programming automatically ignored such results and excluded the data point from contributing to the final pulse shape. In some severe cases a third of the total data was being rejected by this criterion. At this point, a modification was made in the data procedures to permit the quantity  $B$  to be assigned on the basis of typical published values for the cloud types being considered. With this change only a few per cent of the lines-of-sight were automatically rejected.

## 2.5 SCATTERING DELAY

The photon path marked  $C$  in Figure 2.1 includes scattering delay in addition to geometric delay due to the random path followed by the photon in its transit from the bottom to the top of the cloud. The random path increases the total path and the increase over the distance  $B$ , the cloud thickness, leads to the scattering delay. The extra path length, and therefore the scattering delays which occur due to light diffusion through a cloud may be evaluated by correlating the strength of an observable optical absorption structure of the atmosphere to the path length required to produce such absorption strength. Part of this path length is due to light paths external to the cloud which can be calculated as in the case of the geometric delay. The remainder of the absorption related path length is then due to the average total random walk path length of the photons traversing the cloud. The average excess path length is related to the average scattering delay through the velocity of light. For this study the

atmospheric absorption feature measured was that of molecular oxygen at  $7606 \text{ \AA}$ , the ON-BAND camera.

As stated in the previous section in the absence of absorption the transmission of a cloud or overcast is a function of the ratio of cloud thickness,  $B$ , to scattering mean free path  $\ell$ ; that is, to  $B/\ell$ . When absorption is present the ratio of cloud transmission with absorption to transmission without absorption is a function of  $B^2/\ell$ . This latter ratio can be calculated for each line-of-sight to the cloud by the proper radiometric reduction of the pair of photographs taken at wavelengths  $\lambda = 7606 \text{ \AA}$  and  $\lambda = 7530 \text{ \AA}$ , the ON-BAND and OFF-BAND pair of photographs.

## 2.6 PULSE SHAPE SYNTHESIS

The procedures and quantities outlined above were used to derive the pulse shape of power versus time one would expect at a detector in space from an isotropic delta function light source near the earth's surface through the cloud conditions which prevailed at the time the experimental measurements were made. These predicted pulse shapes are the final output from this study. The synthesis was accomplished by computer processing the experimental data in the following manner.

Assuming all calibration and other preliminary data processing steps completed, each pulse shape synthesis starts with the following quantities.

1. Solar irradiance on the top of the cloud or overcast.
2. Azimuth and zenith angle to the sun.
3. Height of the cloud bottom.
4. Height of the cloud top (except when this quantity is to be derived from the data).
5. The azimuth and zenith angle for every line-of-sight which contributes to the received pulse (this excludes all lines-of-sight that terminate in blue sky).

6. The absolute radiance of the cloud bottom in the red band along every contributing line-of-sight.
7. The ratio of the radiance of the cloud bottom for every contributing line-of-sight in the oxygen absorption band (ON-BAND) and just outside the oxygen absorption band (OFF-BAND).

By the methods outlined above and explained in detail in subsequent sections the following quantities are derived for each line-of-sight that contributes to the final pulse shape.

1. The rectangular coordinates of the tops of the clouds corresponding to each line-of-sight to the bottom of the cloud.
2. The mean transit time from the top of the cloud to the point of detection along each line-of-sight. (This statement refers to the measurement configuration with sun and ground based detector.)
3. The transmission of the cloud along each line of sight.

The reciprocity theorem is applied to the interpretation of the values of transmission and mean time of transit. In the process outlined so far values of transmission and transit time have been calculated in terms of downward flowing light from the sun (the source) to the isotropic receiver (the camera systems). The reciprocity theorem allows these values to be used in treating a delta function isotropic source located at the position of the measuring equipment and a receiver in the direction of the sun. Corresponding to each of the equal elements of solid angle of the camera system there are equal solid angle elements of the source. When pulsed, equal amounts of energy are invested in each element of solid angle.

Reciprocity theorem allows assignment for each of these elements of solid angle a mean transit time and a transmission value to the corresponding element of area at the top of the cloud.

Let the number of data elements of the all sky camera picture be  $N$  with each element having an unique assigned number  $n$ . ( $1 \leq n \leq N$ ). If the transmission associated with element  $n$  is  $T_n$  then for those elements exposed to blue sky,  $T_n = 0$ . Let the rectangular coordinates of the location of the cameras be  $x = y = z = 0$  then for each of the elements exposed to clouds there is an element of area at the top of a cloud with coordinates  $x_n, y_n, z_n$ , with associated transmission  $T_n$  and associated mean transit time from  $(0,0,0)$  of  $\bar{t}_n$ . If a satellite is located in the direction of the sun at coordinates  $x_s, y_s, z_s$  then the time of flight of light from the source directly to the satellite is  $t_o$  where

$$t_o = \frac{\sqrt{x_s^2 + y_s^2 + z_s^2}}{c}$$

and  $c$  is the velocity of light.

The mean time delay  $\bar{\Delta t}_n$  of the portion of the light pulse radiated into the  $n$ -th element of solid angle is given by

$$\bar{\Delta t}_n = \frac{\sqrt{(x_s - x_n)^2 + (y_s - y_n)^2 + (z_s - z_n)^2}}{c} + \bar{t}_n - t_o$$

The energy arriving at the satellite from the element of cloud top area at  $z_n, y_n, x_n$ , is proportional to  $T_n$  and is treated here as arriving as a pulse at  $\bar{\Delta t}_n$ . Normalization is done in terms of the direct energy the satellite would receive in the absence of clouds.

When all  $N$  points have been treated in this way the accumulated normalized energies in the time boxes are plotted sequentially from 0 to 299  $\mu\text{sec}$ . Such plots are interpreted as representing the power as a function

of time that would arrive at the satellite if a delta function light source were fired at the location and the time of the cloud photographs.

Using the same values of  $x_n$ ,  $y_n$ ,  $z_n$ ,  $\Delta t_n$ , and  $T_n$  similar power vs time curves can be calculated for satellites in other directions than that of the sun. (These directions involve new values of  $x_s$ ,  $y_s$ ,  $z_s$ .) Some additional assumptions are involved when this is done but they are probably not as great as those already made.

## SECTION 3

### CERTAIN THEORIES AND APPROXIMATIONS

#### 3.1 TRANSPORT MEAN-FREE PATH

Reasonable analytic statements about overcast transmission and associated time delays can be made using the concept of the transport mean-free path. This was first introduced into optical computations by Sigmund Fritz (Ref. 3) who adapted the idea from work on neutron diffusion done by Victor Weisskopf (Ref. 4). This powerful computational tool is seldom used in optical calculations. It is applied here to the discussions of two-stream theory and diffusion theory outlined below. Edward Bucher uses the concept of transport mean-free path and discusses some of its limitations in his paper on Monte Carlo simulations of pulse propagation through clouds (Ref. 5).

A simple overcast may be represented as a layer of great lateral extent and of thickness  $B$  wherein there are uniformly distributed scattering centers resulting in an average scattering coefficient,  $\sigma$ , and phase function for scattering  $\Phi(\phi)$ . Corresponding to this realistic representation there is a pseudo-overcast having the same thickness but made up of isotropic scattering centers of size and number density such that in this pseudo-medium the scattering coefficient  $\Sigma$  is given by

$$\Sigma = \sigma(1 - \overline{\cos \phi}) \quad 3.1$$

where

$$\overline{\cos \phi} = \frac{\int_0^\pi \Phi(\phi) \cos \phi \sin \phi \, d\phi}{\int_0^\pi \Phi(\phi) \sin \phi \, d\phi} \quad 3.2$$



that is  $\overline{\cos \phi}$  is the average cosine of the scattering angle relative to the direction of the incident radiation. In the "real" medium the mean-free path,  $\ell$  is given by

$$\ell = 1/\sigma \quad 3.3$$

In the pseudo-medium, the value  $L$  is called the transport mean-free path and is given by

$$L = \frac{1}{\Sigma} = \ell (1 - \overline{\cos \phi})^{-1} \quad 3.4$$

In some diffusion theory calculations the mean-free path and its associated phase function may be replaced by the transport mean-free path and its associated, single valued phase function which is equal to  $1/4 \pi$ . This can result in a major reduction in the complexity of calculations. Bucher (Ref. 5) shows that when the ratio of overcast thickness  $B$  to transport mean-free path  $L$ ,  $B/L$ , is larger than 2 or 3 then the isotropic scattering approximation may be used in diffusion calculations without serious compromise of accuracy.

In the work reported here measurements are made and interpreted in terms of  $B/L$  or  $B^2/L$ . For instance, measured overcast transmission is used to calculate  $B/L$ . Measured values of oxygen absorption within overcasts are used to calculate values of  $B^2/L$ . The work done here does not deal with  $\ell$ , the true mean-free path in the overcast or with  $\overline{\cos \phi}$ , the average cosine of the scattering angle.

### 3.2 TWO-STREAM THEORY

Two-stream theory may be used to develop expressions for the transmission and the reflection of a uniform overcast of great extent. When

it is assumed that there is no absorption within the overcast and no reflection from the ground below the overcast, equations such as those given by Schuster (Ref. 6) and Dietzius (Ref. 7) reduce to those given by Mecke (Ref. 8). Mecke's methods of calculations have been applied to the case of isotropic scattering and, for this simplification, equations have been developed for the radiance as a function of angle of view of the bottom and of the top of an overcast for any angle of incidence of sunlight (Ref. 9 & 10). These results are summarized here.

For a uniform overcast of great extent made up of isotropic scattering centers with no absorption within the overcast and no ground reflection, the transmission of the overcast,  $T$ , when illuminated by diffuse radiant power is

$$T = \frac{1}{1 + B/L} \quad 3.5$$

where  $B$  is the overcast thickness and  $L$  is its transport mean-free path. For diffuse illumination the reflection,  $R$ , is

$$R = \frac{B/L}{1 + B/L} \quad 3.6$$

When parallel radiant power is incident on the overcast at an angle  $z$  from the normal to the overcast the diffuse reflection is given by

$$R_z = \frac{2 \frac{B}{L} - (2 \cos z - 1) \left\{ 1 - \exp \left( -\frac{B}{L} \sec z \right) \right\}}{2 (1 + B/L)} \quad 3.7$$

and the diffuse transmission is

$$T_z = \frac{2 + (2 \cos z - 1) \left\{ 1 - \exp \left( -\frac{B}{L} \sec z \right) \right\}}{2 \left( 1 + \frac{B}{L} \right)} \quad 3.8$$

When parallel radiant power,  $H_o$ , is incident on the overcast at angle  $z$  from the normal, the radiance of the top of the overcast,  $N_{tz}$ , is independent of angle of view and equal to

$$N_{tz} = \frac{H_o \cos z}{\pi} \left( \frac{2 \frac{B}{L} - (2 \cos z - 1) \left\{ 1 - \exp \left( -\frac{B}{L} \sec z \right) \right\}}{2 (1 + B/L)} \right) \quad 3.9$$

The radiance of the base of the overcast,  $N_{bz\theta}$ , is dependent on the angle of view,  $\theta$ , measured from the downward normal to the base. It is given by

$$N_{bz\theta} = \frac{3H_o \cos z (2 \cos \theta + 1) \left\{ 2 + (2 \cos z - 1)(1 - \exp \left[ -\frac{B}{L} \sec z \right]) \right\}}{14 \pi (1 + B/L)} \quad 3.10$$

When  $(B/L) \sec z \rightarrow \infty$ , that is, for overcasts through which one cannot see the sun

$$R_z = \frac{\frac{B}{L} - (\cos z - 1/2)}{1 + B/L} \quad 3.11$$

$$T_z = \frac{\cos z + 1/2}{1 + B/L} \quad 3.12$$

$$N_{tz} = \frac{H_o \cos z}{\pi} \left( \frac{B/L - (\cos z - 1/2)}{1 + B/L} \right) \quad 3.13$$

$$N_{bz\theta} = \frac{3 H_o \cos z (2 \cos \theta + 1) (2 \cos z + 1)}{14 \pi (1 + B/L)} \quad 3.14$$

### 3.3 THE REDUCED ATMOSPHERE

Considerable simplification in the working equations and calculations used in describing scattering and absorption in clouds result from transferring the problem from the real to the reduced atmosphere. The reduced atmosphere is one of constant density equal to that at sea level and extending from the sea level to an altitude H called the scale height. Above this height the atmospheric density is zero. The same atmospheric mass above unit area at sea level is involved in the real as is the reduced atmosphere. Within the reduced atmosphere the molecular scattering coefficient and the oxygen absorption coefficient are constant.

It is assumed here that in the true atmosphere the air density,  $\rho(h)$ , is an exponential function of height, h, obeying the law

$$\rho(h) = \rho(0) e^{-h/H} \quad 3.15$$

where  $\rho(0)$  is the atmospheric density at sea level ( $h = 0$ ) and H is the scale height. Unless stated otherwise H is taken here as equal to 8 km and  $\rho(0)$  is taken to be  $1.29 \times 10^{-3} \text{ g cm}^{-3}$ . With this model for the real atmosphere the reduced atmosphere, having vertical coordinate Z, has constant density equal to  $\rho(0)$  from  $Z = 0$  to  $Z = H$  and zero density for  $Z > H$ . That is

$$\rho(Z) = \rho(0) \quad \text{for } 0 \leq Z \leq H$$

$$\text{and} \quad \rho(Z) = 0 \quad \text{for } Z > H \quad 3.16$$

Values of  $Z$  and  $h$  are related as follows

$$Z = H (1 - e^{-h/H})$$

$$\frac{dZ}{dh} = e^{-h/H}$$

and

$$h = H \ln \left( \frac{H}{H - Z} \right) \quad 3.17$$

If a cloud in the real atmosphere has its base at altitude  $h$  and its top at altitude  $h + B$  then in the reduced atmosphere the thickness of the cloud  $\beta$  is given by

$$\beta = H e^{-h/H} (1 - e^{-B/H}) \quad 3.18$$

If a cloud in the reduced atmosphere has its base at altitude  $Z$  and its top at altitude  $Z + \beta$  then the thickness in the real atmosphere,  $B$ , is given by

$$B = H \ln \left( \frac{H - Z}{H - Z - \beta} \right) \quad 3.19$$

#### 3.4 DIFFUSION THEORY AND MONTE CARLO CALCULATIONS

The probability as a function of time,  $p(t)$ , that a photon incident on the top of an overcast of great extent at time  $t = 0$  will leave its bottom at time  $t$  may be stated analytically by use of stochastic methods (Ref. 11) or diffusion theory (Ref. 12), or may be calculated by Monte Carlo simulation (Ref. 5). If the scattering processes in the overcast are modeled as isotropic and of uniform distribution a single value of transport mean-free path may be assigned. When this is done, the analytic statements

reduce to forms which can be solved easily and the Monte Carlo simulation can be carried out with greatly reduced effort. The diffusion theory equations derived by J. S. DeGroot, R. M. Frank and H. S. Stewart (Ref. 12) are given here with a few illustrative calculations of  $p(t_d)$ . Here the time base is changed so that  $t_d = 0$  at the earliest time that a photon could exit from the bottom of the cloud. Then  $t_d = t - B/c \{ 1 - m (1 - \cos z) \}$ . Monte Carlo results obtained by E. A. Bucher (Ref. 4) are compared to the analytic results and certain useful relationships developed by Bucher are simplified by use of two-stream theory and presented here.

The equation for  $p(t_d) \Delta t$  developed in Reference 12 is given here with some changes of symbols.

$$p(t_d) \Delta t = \frac{1}{4} \sqrt{\frac{3B}{\pi mc}} [1 - e^{-\frac{1}{m \cos z}}] e^{-g(t)} \frac{\Delta t}{(t_d + t_1)^{3/2}} \cdot$$

$$\sum_{n=-\infty}^{n=\infty} \left[ \begin{aligned} & - \frac{3}{4} \frac{B}{mc (t_d + t_1)} (f_n - x_1)^2 e^{-\frac{3}{4} \frac{B}{mc (t_d + t_1)} (f_n + x_1)^2} \\ & (f_n - x_1) e^{-\frac{3}{4} \frac{B}{mc (t_d + t_1)} (f_n + x_1)^2} - (f_n + x_1) e^{-\frac{3}{4} \frac{B}{mc (t_d + t_1)} (f_n + x_1)^2} \end{aligned} \right]$$

3.20

where

$$t_1 = \frac{+B}{c} \{ 1 - m(1 - \cos z) \}$$

$$x_1 = m(\cos z + 0.71)$$

$$f_n = (1 - 2n) - .71 m$$

$$B = \text{cloud thickness, km}$$

$$c = \text{velocity of light}$$

$$m = L/B$$

$$L = \text{transport mean-free path, km}$$

- $f_m = (1-2n)(1+1.42m) - 0.71m$   
 $g(t) =$  time based absorption function  
 $g(t) = 0$  for absorption free medium  
 $g(t) = b \sqrt{\beta / B (nc \Delta t) + Y}$   
 $b =$  coefficient from calibration  $T_{O_2} = e^{-b \sqrt{P}}$   
 $P =$  path length through  $O_2$  in atmosphere at sea level  
 $T_{O_2} =$  oxygen transmission in sea level path of length  $P$   
 $\beta =$  Cloud thickness in reduced atmosphere  
 $Y =$  equivalent sea level path length through oxygen for paths external to cloud  
 $t_d =$  time measured from time of first possible exit of a photon from bottom of cloud

Figure 3.1 presents plots of  $p(t_d)$  vs  $t$  for a hypothetical overcast when the value of  $B$  used was 1.56 km and the value of  $m$  was  $1.92 \times 10^{-2}$ . The dotted curve is calculated using diffusion theory and the solid curve is from Figure 6 of Bucher (Ref. 5). Figure 3.2 is similar to Figure 3.1 except here  $B = 4.14$  km and  $m = 0.0725$ . Bucher used a phase function for scattering calculated by Mie theory for  $\lambda = 0.7\mu$  and for a distribution of water droplet radii between  $3.8\mu$  and  $4.8\mu$ . The minor differences between the Monte Carlo curves and the diffusion theory curves appearing in Figures 3.1 and 3.2 arise from the difference in scattering models. In Figure 3.3 the scattering phase function used by Bucher (Mie) is compared to that used in the diffusion solution (isotropic). In this figure the more conventional phase function for scattering  $\Phi(\phi)$  has been multiplied by  $\sin \phi$ . The effect of the strong forward scattering in the Mie theory compared to the isotropic scattering of the diffusion theory model seems very minor for the

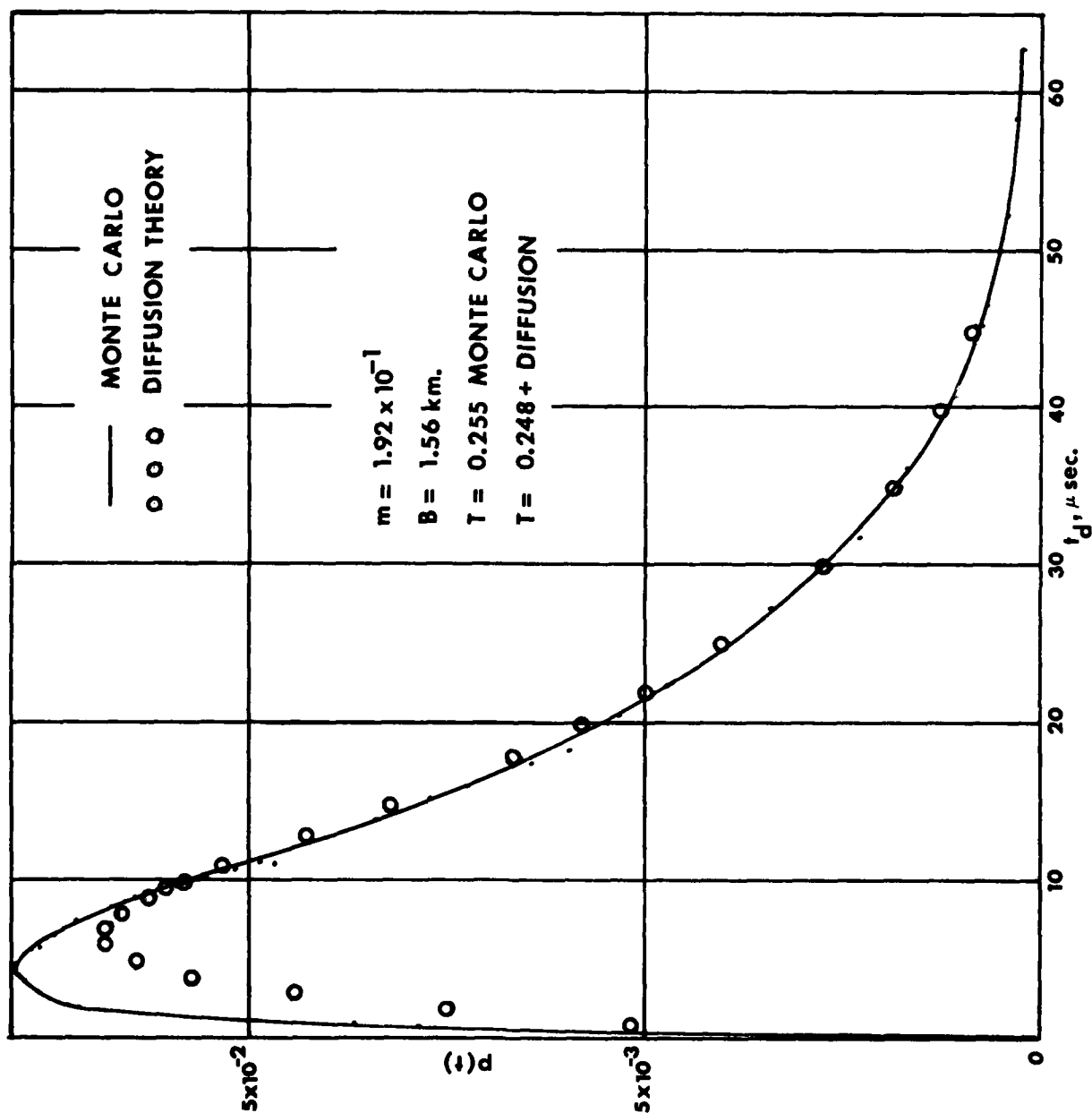


Figure 3.1. Time dependent probability of delayed transit for a hypothetical overcast of diffuse transmission 0.25.



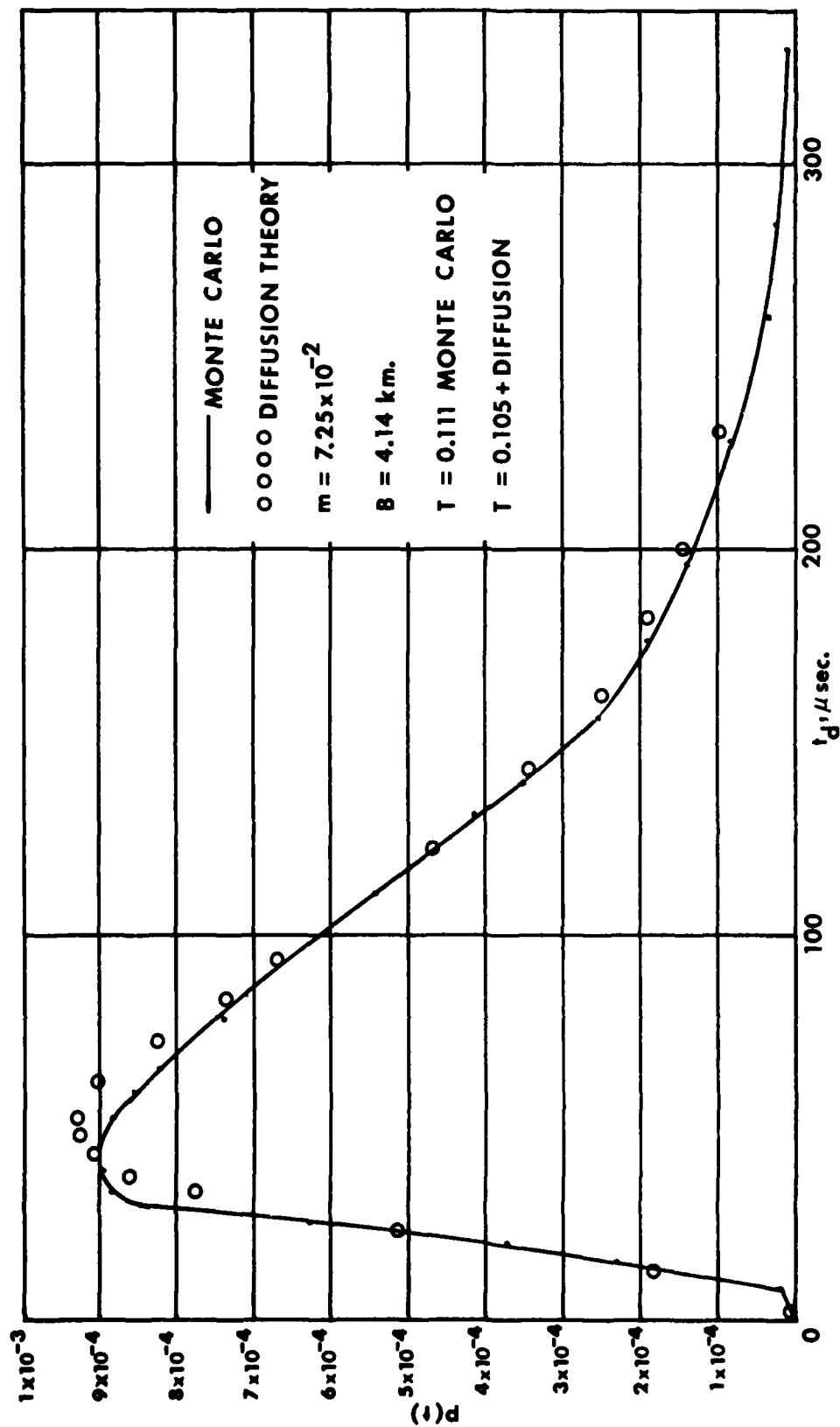


Figure 3.2. Time dependent probability of delayed transit for a hypothetical overcast of diffuse transmission 0.10.

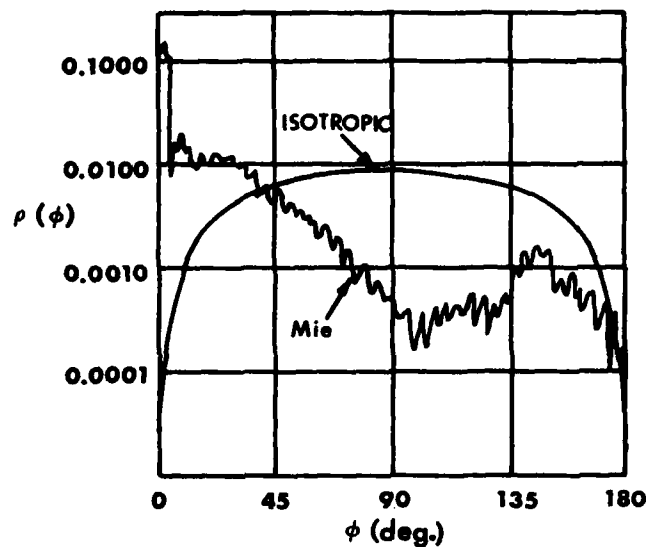


Figure 3.3. Comparison of the Mie phase function to the isotropic phase function used in diffusion theory.

relatively thick clouds of Figures 3.1 and 3.2 (diffuse transmissions 0.25 and 0.11). However, the effect is quite pronounced in an optically thin cloud such as that of Figure 3.4 where the diffuse transmission is 42 percent. Although the Monte Carlo results are more nearly representative of real overcasts, diffusion calculations are used here because of their low cost in time and money.

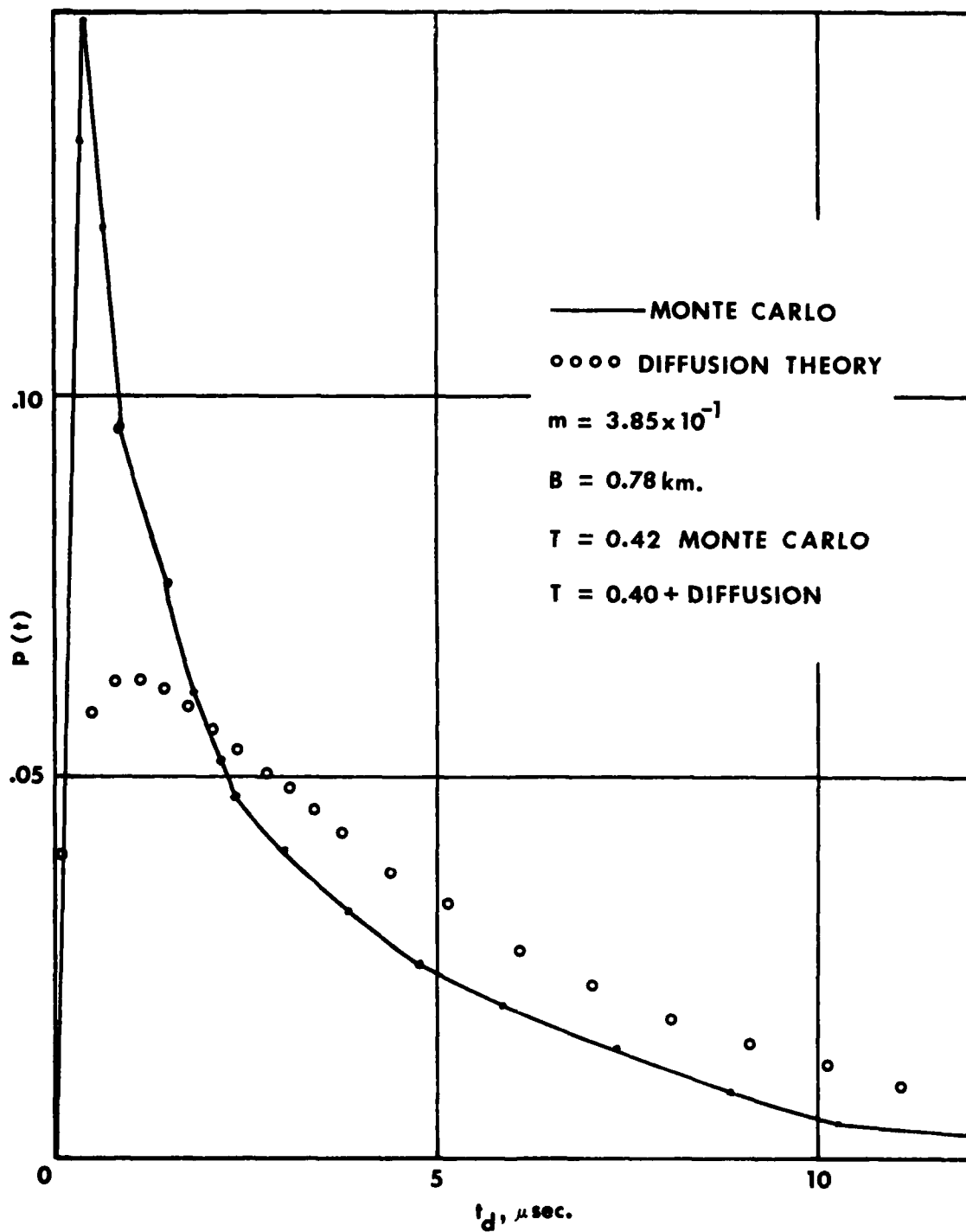


Figure 3.4. Time dependent probability of delayed transit for a hypothetical optically thin overcast.

In equation 3.20, which describes the time dependent probability of delayed transit of a photon incident on an overcast, there is a term,  $e^{-g(t)}$ , which accounts for absorption processes which may occur within the cloud. The curves of Figures 3.1, 3.2 and 3.4 were calculated with  $g(t) = 0$ , that is, with no absorption. In the case of the oxygen absorption treated here  $g(t) = b \{ \beta/B (c t) + Y \}^{1/2}$  since  $t = n\Delta t$ . For the data reported here  $b = 0.51 \text{ km}^{-1/2}$ . For the cloud of Figure 3.1  $B = 1.56 \text{ km}$  ( $\beta = 1.33 \text{ km}$  in the reduced atmosphere) and if the zenith angle of the sun is  $0^\circ$  and that of the line of sight  $60^\circ$  then the total path through oxygen above and below the cloud,  $Y$  is  $7.15 \text{ km}$ . The term  $g(t)$  includes  $Y$ , the external path through oxygen because the fraction of the total absorption which occurs within the cloud is dependent on the fraction absorbed external to the cloud. Figure 3.5 presents a plot of  $p(t_d)$  versus  $t$  for a hypothetical cloud including absorption. Note that absorption reduces the mean time of delay from  $14.4 \mu\text{sec}$  (without absorption) to  $12.7 \mu\text{sec}$ .

Equation 12 from Bucher's paper (Ref. 5) is rewritten here as

$$c \overline{t_d} = 0.62 B \left( \frac{1}{m} \right)^{0.94}$$

or

$$\overline{t_d} = \frac{2.1 B}{m^{0.94}} \quad c = 0.3 \text{ km}/\mu\text{sec} \quad 3.21$$

Equation 17 of the same reference is rewritten

$$T = \frac{A_o}{C + 1/m} \quad 3.22$$

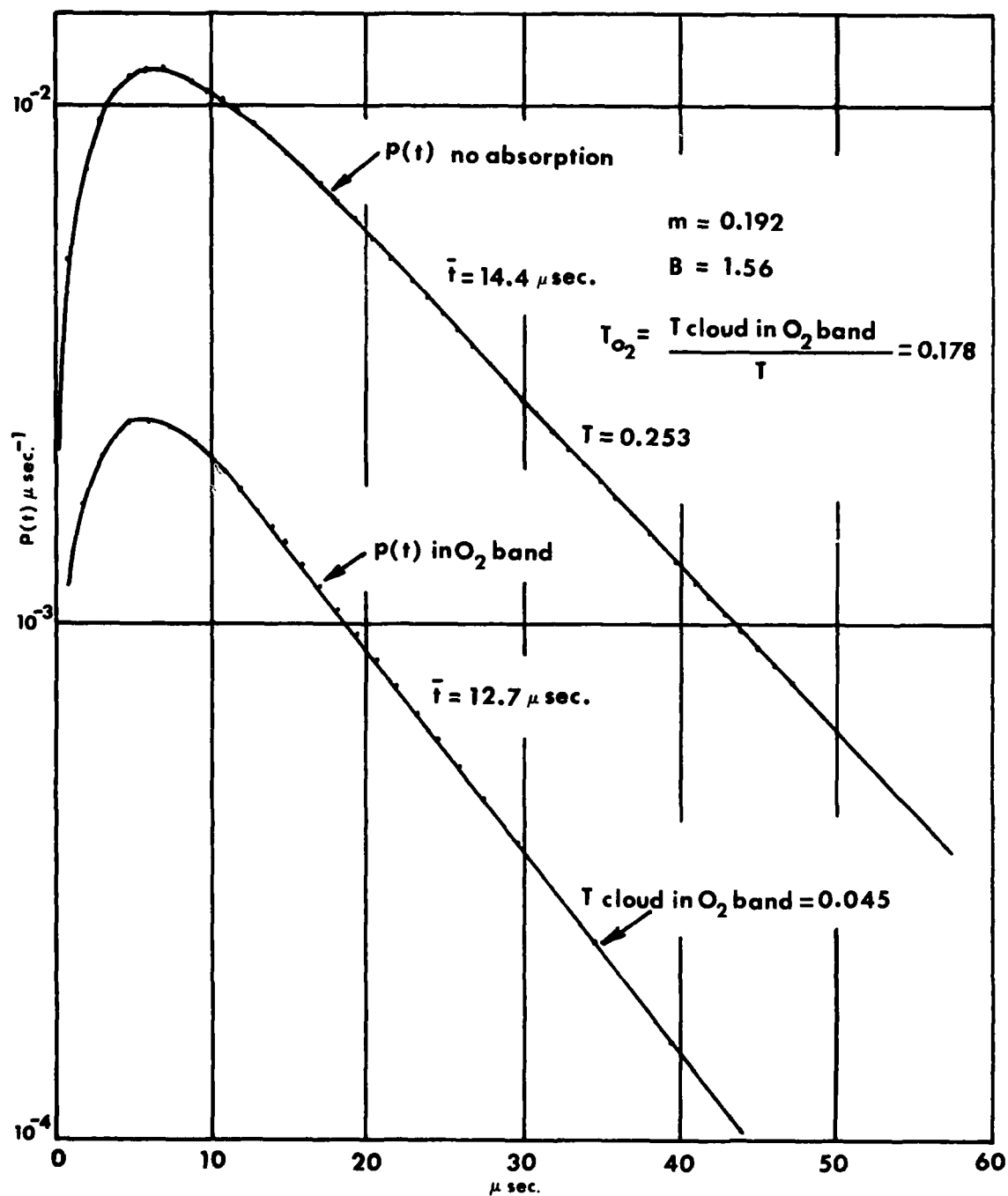


Figure 3.5. Comparison of the probability of delayed transit with and without  $O_2$  absorption.

Bucher notes quite a pedigree for this expression which he attributes to Van de Hulst (Ref. 13) and Danielson, Moore and Van de Hulst (Ref. 14). The value of C is given as 1.42. Values of  $A_0$  as a function of  $z$ ,  $A_0(z)$ , are given in Table 3.1 from Danielson et al (Ref. 14). Included in Table 3.1 are values of  $A_0(z)$  calculated from two-stream results, see equation 3.12, and normalized to Danielson et al at  $\cos z = 1$ . Using this approximation and equations 3.21 and 3.22 one may write the following sequence of equations.

$$T = \frac{1.13 (\cos z + 1/2)}{1.42 + \frac{1}{m}}$$

$$\frac{1}{m} = \frac{1.13 (\cos z + 1/2)}{T} - 1.42$$

$$\bar{t}_d = 2.1 B \left( \frac{1.13 (\cos z + 1/2)}{T} - 1.42 \right)^{0.94}$$

$$\frac{\bar{t}_d}{B} = 2.36 \left( \frac{\cos z + 1/2}{T} - 1.26 \right)^{0.94}$$

or, in terms of  $\tau$ , time measured so that incidence on top of cloud occurs at  $\tau = 0$

$$\frac{\tau}{B} = 2.36 \left( \frac{\cos z + 1/2}{T} - 1.26 \right)^{0.94} + \frac{1}{c} \quad 3.23$$

This hybrid equation plays an important part in data reduction.

Table 3.1. Comparison of values of  $A_o(z)$  reported by Danielson et al and calculated by two-stream theory.

Cos z	$A_o(z)$	
	From Reference 14	$\frac{1.69}{1.5} (\cos z + 1/2)$
1	1.69	1.69
0.9	1.59	1.58
0.7	1.38	1.35
0.5	1.16	1.13
0.3	0.92	0.90
0.1	0.62	0.68
0.05	0.52 - 0.62	0.62

### 3.5 LOW RESOLUTION $O_2$ - BAND ABSORPTION

In the work reported here the  $O_2$  absorption in a  $10 \text{ \AA}$  band centered on  $.7606\mu$  is measured for the path sun through overcast to point observed on its base and on to detector. The results so obtained are expressed in terms of multiples of the scale height of the atmosphere. This choice of units comes from the method of calibration wherein the absorption to the sun is measured on a clear day from sunrise to noon or from noon to sunset. This is a variation on the Langley method. The results of the

calibration fit an expression for oxygen transmission,  $T_{O_2}$ , of the form

$$T_{O_2} = e^{-b \sqrt{H \sec z}} \quad 3.24$$

where  $H$  = scale height of atmosphere = 8 km

$z$  = zenith angle of sun

The square-root relationship between  $\ln T_{O_2}$  and the sea level equivalent path length through  $O_2$ ,  $H \sec z$ , is not surprising. It is discussed briefly in an excellent outline of molecular band absorption theory which is given in McClatchey et al (Ref. 15) along with references which treat the subject in depth.

In the reduced atmosphere the oxygen density is constant and path length through atmospheric oxygen is equal to path length per se. Elapsed time and path length through atmospheric oxygen are related through  $c$  the velocity of light. Equation 3.24 may be written

$$T_{O_2} = e^{-b \sqrt{26.67 c \sec z}}$$

There is a mean transit time for the diffusion of light through an over-cast given by

$$\bar{t} = \frac{\int_0^\infty p(t) t \, dt}{\int_0^\infty p(t) \, dt} \quad 3.25$$



where  $p(t)$  is the probability that a photon will penetrate the overcast in time  $t$ . In the reduced atmosphere the mean time of transit,  $\bar{\tau}$ , is

$$\bar{\tau} = \bar{t} \beta / B$$

where  $B$  is the true cloud thickness and  $\beta$  is that thickness in the reduced atmosphere. The probability function in the reduced atmosphere,  $p(\tau)$ , is related to that of the real atmosphere as follows

$$p(\tau) = p(t) \beta / B$$

$$\bar{\tau} = \frac{\int_0^{\infty} p(\tau) \tau d\tau}{\int_0^{\infty} p(\tau) d\tau} \quad 3.26$$

The transmission of sunlight through the overcast,  $T$ , is

$$T = \int_0^{\infty} p(\tau) d\tau \quad 3.27$$

The transmission of oxygen in the total path sun through overcast to detector,  $T_{O_2}$ , is written as

$$T_{O_2} = \frac{\int_0^{\infty} p(\tau) e^{-b \sqrt{Y + c\tau}} d\tau}{\int_0^{\infty} p(\tau) d\tau} \quad 3.28$$

where, in the reduced atmosphere,  $Y$  is the path length of sunlight from the top of the atmosphere to the top of the cloud plus the path length from the observed point on the bottom of the cloud to the detector.

$$\begin{aligned}
 \text{Now } e^{-b\sqrt{Y+c\tau}} &= e^{-b\sqrt{Y+c\bar{\tau}+c(\tau-\bar{\tau})}} \\
 &= e^{-b\sqrt{Y+c\bar{\tau}}} \left[ 1 + c(\tau-\bar{\tau})/(Y+c\bar{\tau}) \right]^{1/2}
 \end{aligned}
 \tag{3.29}$$

$$\text{For } \frac{c(\tau-\bar{\tau})}{Y+c\bar{\tau}} \ll 1
 \tag{3.30}$$

$$\left( 1 + \frac{c(\tau-\bar{\tau})}{Y+c\bar{\tau}} \right)^{1/2} \approx 1 + \frac{1}{2} \frac{c(\tau-\bar{\tau})}{Y+c\bar{\tau}}
 \tag{3.31}$$

$$\text{and } e^{-b\sqrt{Y+c\tau}} \approx e^{-b\sqrt{Y+c\bar{\tau}}} \cdot e^{-\frac{b}{2} \frac{c(\tau-\bar{\tau})}{\sqrt{Y+c\bar{\tau}}}}
 \tag{3.32}$$

$$\text{For the case } \frac{b}{2} \frac{c(\tau-\bar{\tau})}{\sqrt{Y+c\bar{\tau}}} \ll 1
 \tag{3.33}$$

$$e^{-\frac{b}{2} \frac{c(\tau-\bar{\tau})}{\sqrt{Y+c\bar{\tau}}}} \approx 1 - \frac{b}{2} \frac{c(\tau-\bar{\tau})}{\sqrt{Y+c\bar{\tau}}}
 \tag{3.34}$$

With these approximations equation 3.28 may be written

$$T_{O_2} \approx e^{-b\sqrt{Y+c\bar{\tau}}} + \frac{cb}{2\sqrt{Y+c\bar{\tau}}} \left( \bar{\tau} - \frac{\int_0^\infty p(\tau) d\tau}{\int_0^\infty p(\tau) d\tau} \right)
 \tag{3.35}$$

By the definition of  $\bar{\tau}$ , equation 3.26, the term in parentheses goes to zero and

$$T_{O_2} \approx e^{-b\sqrt{Y + c\bar{\tau}}} \quad 3.36$$

Equation 3.36 is the heart of the work reported here because it relates measured oxygen transmission to mean transit time through the overcast. It is an approximation based on the conditions of equations 3.30 and 3.34. It is a good approximation if for all times for which  $p(\tau)$  is significant the following conditions hold

$$\text{and} \quad \frac{c(\tau - \bar{\tau})}{Y + c\bar{\tau}} \ll 1 \quad 3.37$$

The photographs taken in the work reported here were reduced with equivalent resolution of 0.43 degrees in space. It is probable that most of the data taken meets the above conditions. This is due in part to the small solid angle represented by each pixel. The conditions may not be met at the edges of clouds or in the presence of complex overcasts. The risk of violating the assumptions increases with field of view of the resolution element.

## SECTION 4

### RELATIONSHIP USED IN DATA REDUCTION

#### 4.1 HEIGHT OF CLOUD BASE

The heights of the bases of the clouds were determined by analysis of stereo pictures. The stereo cameras were located at the primary data station, A, and the secondary station, B. Station A was at location UCS2 at Kennedy Space Center. The coordinates of A were:

Latitude  $28^{\circ} 31' 31.27''$

Longitude  $80^{\circ} 37' 20.61''$

The separation of B from A was 3215.5 feet or 980 meters. The line from A to B was rotated clockwise  $34^{\circ} 01'$  from true north. The stereo cameras were positioned at station A and B such that a line from the top to the bottom of the image format was parallel to the line from station A to B with both formats oriented the same.

Two stereo camera pairs were used. The first involved Flight Research cameras with 18.5mm Angenieux Lenses. These operated satisfactorily but their limited field-of-view made them almost useless on the many occasions when cloud bases were low. The second stereo pair used Automax cameras with Fairchild 160° f/1.5 lenses for 35mm format. These gave satisfactory coverage for almost all cloud base heights encountered. Relationships used in reduction of data from these cameras are discussed in the following paragraphs.

Figure 4.1 presents the manufacturers' relationship between the off-axis distance in inches,  $d$ , in the image plane (called the image height by the manufacturer) versus the external off-axis angle,  $z$ , in degrees for the Fairchild f/1.5 lens. An empirical relationship matching

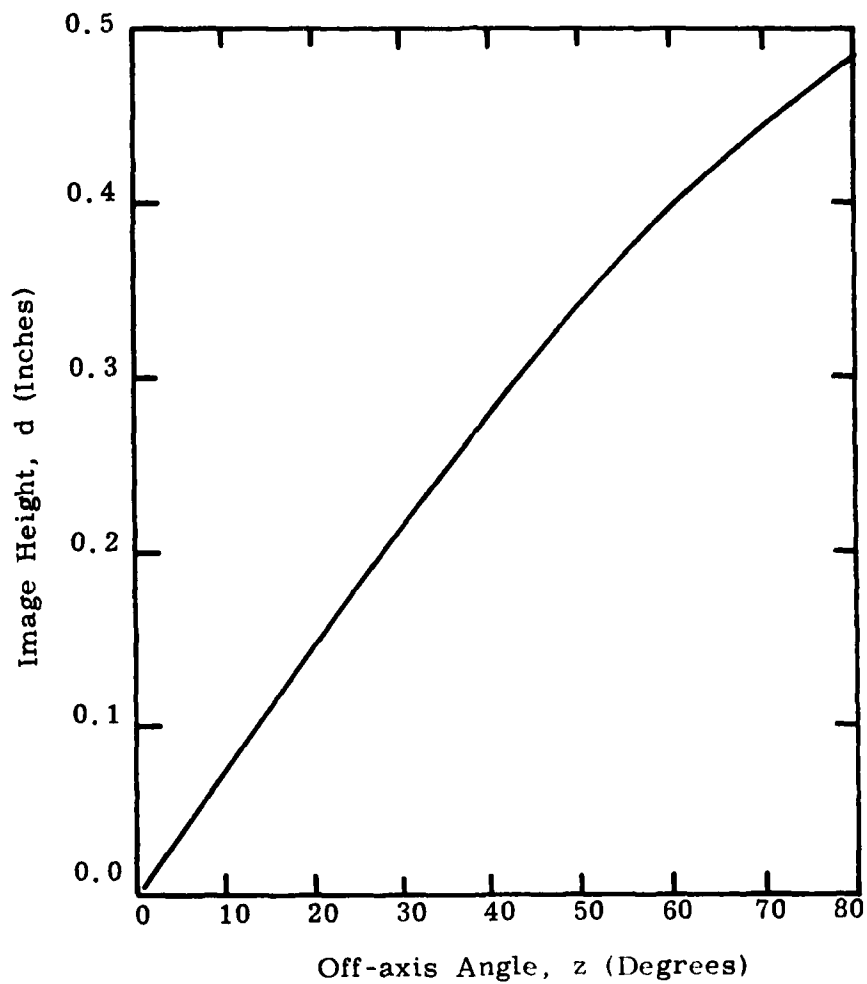


Figure 4.1. Relationship between the off-axis angle,  $z$ , and the image height,  $d$ , for the Fairchild  $f/1.5$  lens.

the curve of Figure 4.1 is:

$$z = 1.373 \times 10^2 d + 0.12(10^{4.25d} - 1) \quad 4.1$$

In use the cameras were mounted with optical axis pointed to the zenith and, under these conditions, the value of  $z$  assigned to a particular point was the zenith angle of that point. A photograph of an Automax camera with Fairchild lens attached is shown in Figure 4.2. A picture of the camera system mounted in a weatherproof enclosure is given in Appendix A. The camera and enclosure are supported by a pedestal which provided adjustments at its base to orient the optical axis of the camera system vertical. Such alignment was achieved using a special lens cap to which a sensitive level dome was attached.

During data runs an operator at station B was in telephonic contact with station A and took synchronous pictures with those taken at station A. Proper film labeling allowed synchronized stereo pictures to be matched after processing. Figures 4.3 and 4.4 are black and white positives made from a matched pair of 35mm color positive transparencies from station A and station B respectively. Particular features were identified on both prints and numbered. The original 35mm transparencies were viewed with a Richardson film reader and the magnified film coordinates of the numbered features were read and recorded. The images were rotated in the reader using the film edge as control to bring each image of the stereo pair in line with the camera axis defined by the line from station A to station B. Displacements on the film were read with the center of the sky image as the origin of an  $x, y$  coordinate system. With knowledge of the magnification of the Richardson, image height values,  $h$ , could be calculated and used in

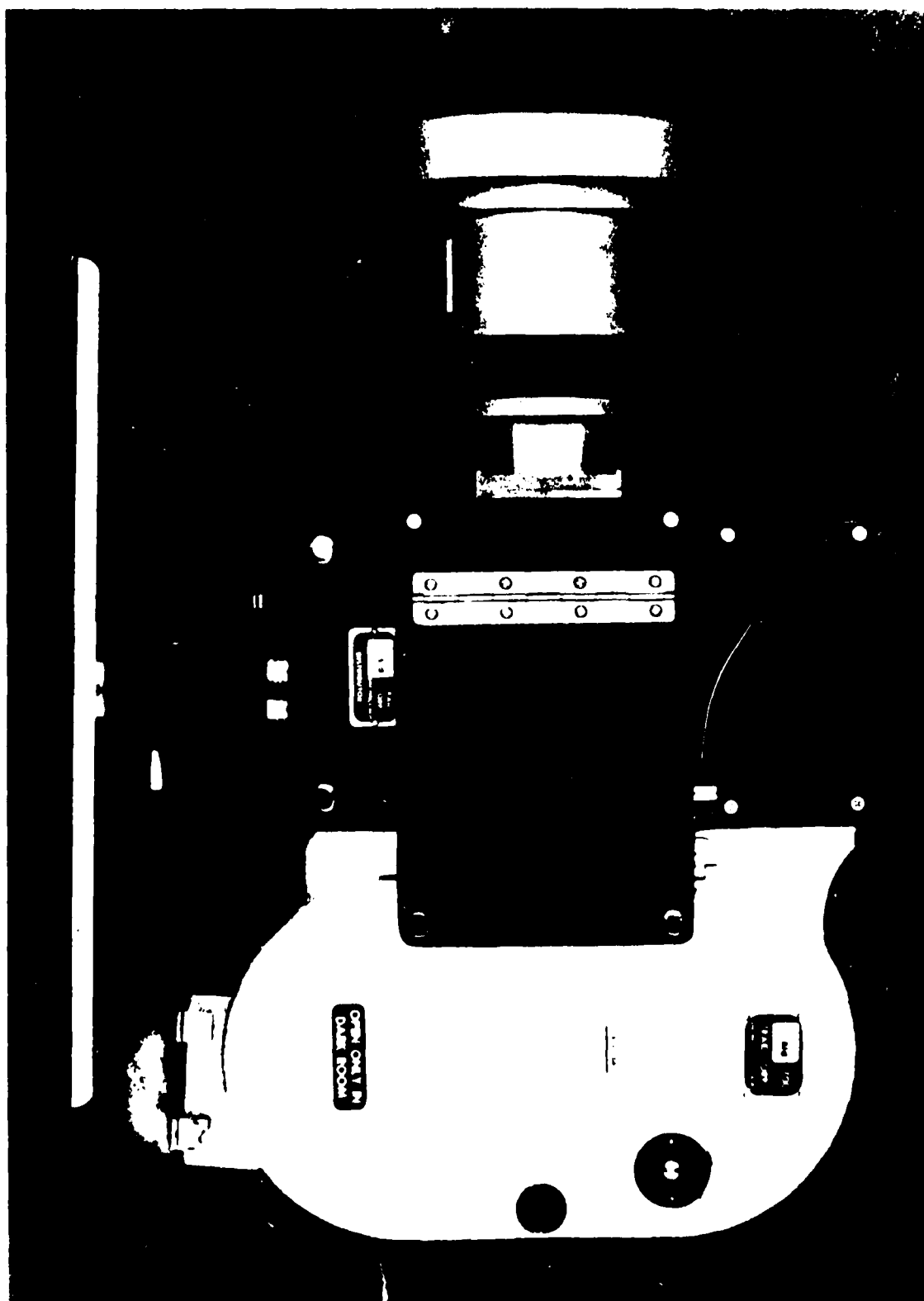


Figure 4.2. A camera camera with a lens and a shutter.



Figure 4.3. All sky photograph from the stereo camera at Station A showing features selected for cloud height determination.



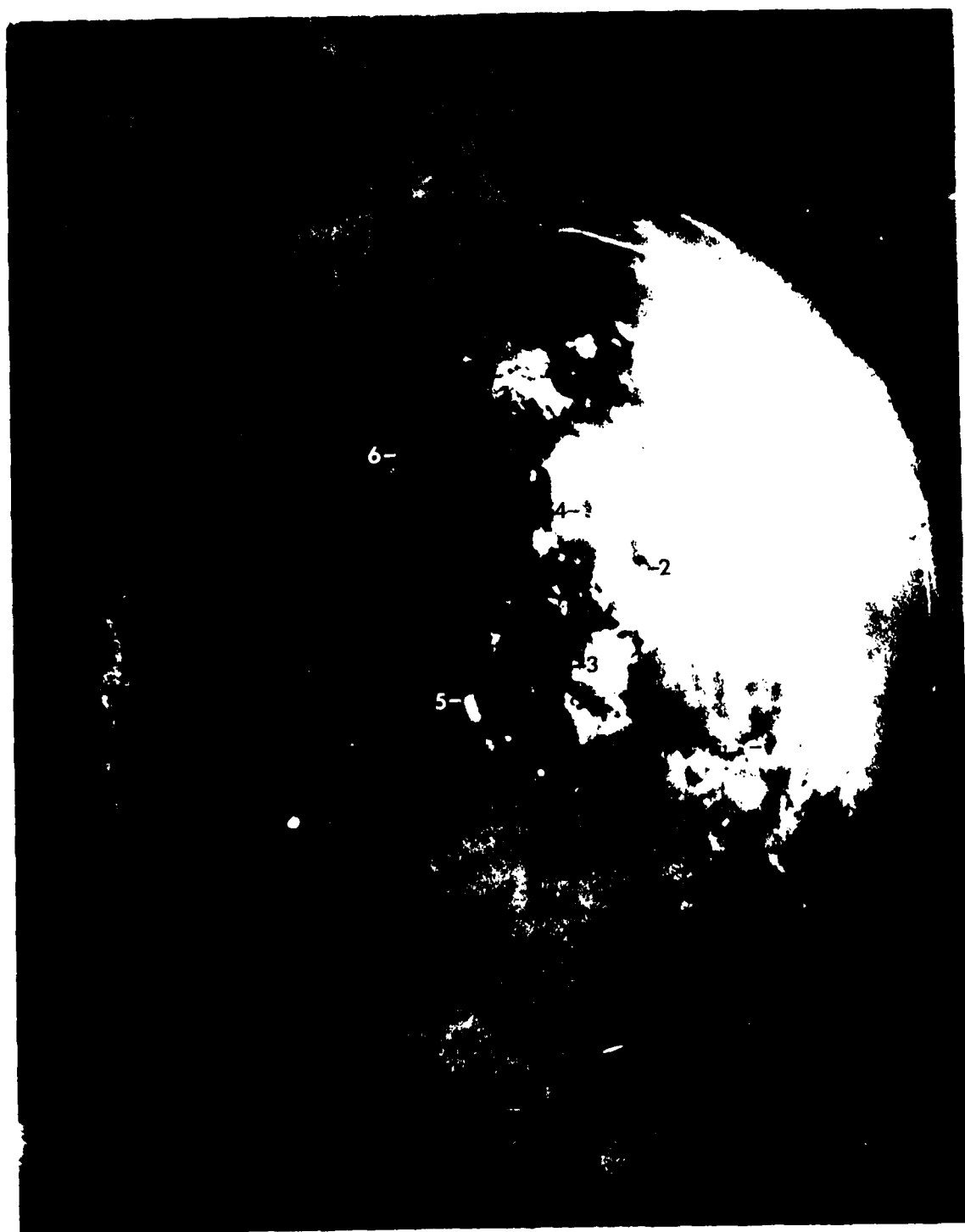


Figure 4-1. The object is a bright, irregularly shaped object with a rough, textured surface. The object is labeled with numbers 2, 3, 4, 5, and 6.

Equation 4.1 to obtain the zenith angle,  $z$ , or a particular feature as observed by the camera. The azimuth angle,  $\alpha$ , of the feature was easily calculated referenced to the station A-station B axis from the feature coordinates. Figure 4.5 shows the relationships between  $\alpha_A$ ,  $\alpha_B$ ,  $z_A$  and  $z_B$  for a particular feature location, F. If R is the separation of A and B then h the height of feature, F, is given by

$$h = \frac{R \cos z_B}{\cos \alpha_B - \sin \alpha_B \cot \alpha_A} \quad 4.2$$

and

$$h = \frac{R}{\tan z_B \cos \alpha_B - \tan z_A \cos \alpha_A} \quad 4.3$$

where equation 4.2 is the more accurate of the two in the two quadrants defined by  $\alpha$  between  $45^\circ$  and  $135^\circ$  and  $\alpha$  between  $225^\circ$  and  $315^\circ$ . Equation 4.3 is better in the other two quadrants. Values of the readings from the Richardson appropriate to Figures 4.3 and 4.4 are presented in Table 4.1 with the calculated values of h using both equation 4.2 and 4.3.

## 4.2 CALIBRATION OF ALL SKY RADIOMETER AND OF ALL SKY CAMERAS

### 4.2.1 Geometric Relationships

The basic tools of this experiment record data reflected from a spheric mirror surface. The all sky radiometer and the two camera systems, the on-band/off-band and the red-blue cameras, are included in this statement. Figure 4.6 shows such systems. The camera shown in Figure 4.6a photographs the virtual image of the hemisphere of the sky which is formed somewhat below the surface of the reflecting sphere. In Figure 4.6b a similar virtual image is re-imaged by an objective lens onto a relay lens assembly which, in turn, images the objective lens onto a radiation detector.

Table 4.1. Cloud base heights for 8/1/77 at 1715 hours calculated for the numbered features in the stereo pair of Figures 4.4 and 4.5.

Feature No.	Richardson Readings*				Feature Height	
	Station A		Station B		by Eqn 1	by Eqn 2
	x	y	x	y	meters	meters
1	706	-431	729	-254	4800	4715
2	450	19	434	241	4705	4714
3	241	-273	234	-5	4285	4056
4	270	174	262	401	4539	4504
5	-53	-366	-60	-126	3908	4441
6	-254	+347	-238	+577	3955	3925

\* Arbitrary Units

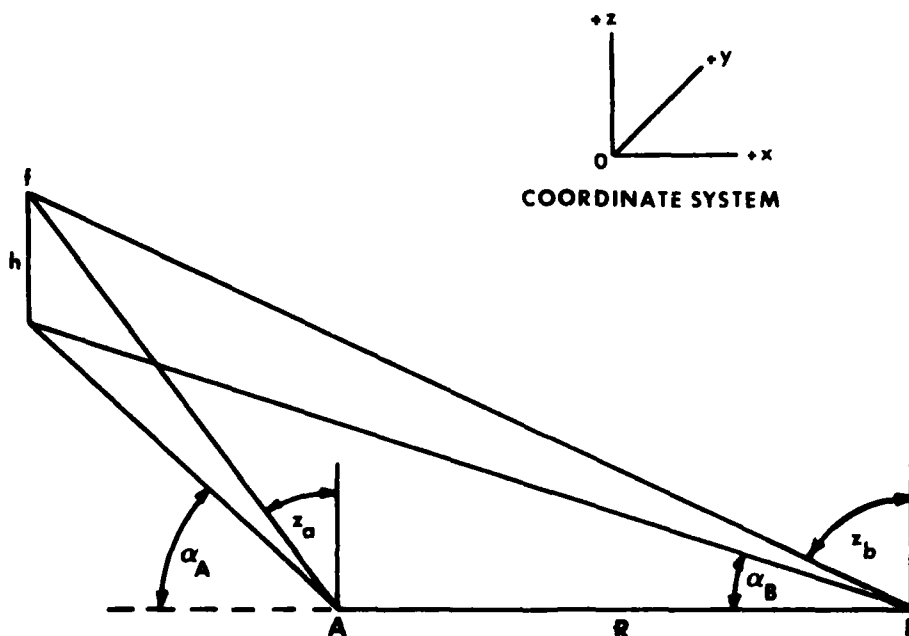


Figure 4.5. Geometric relationship of feature  $f$  as seen from Stations A and B for cloud height determination.

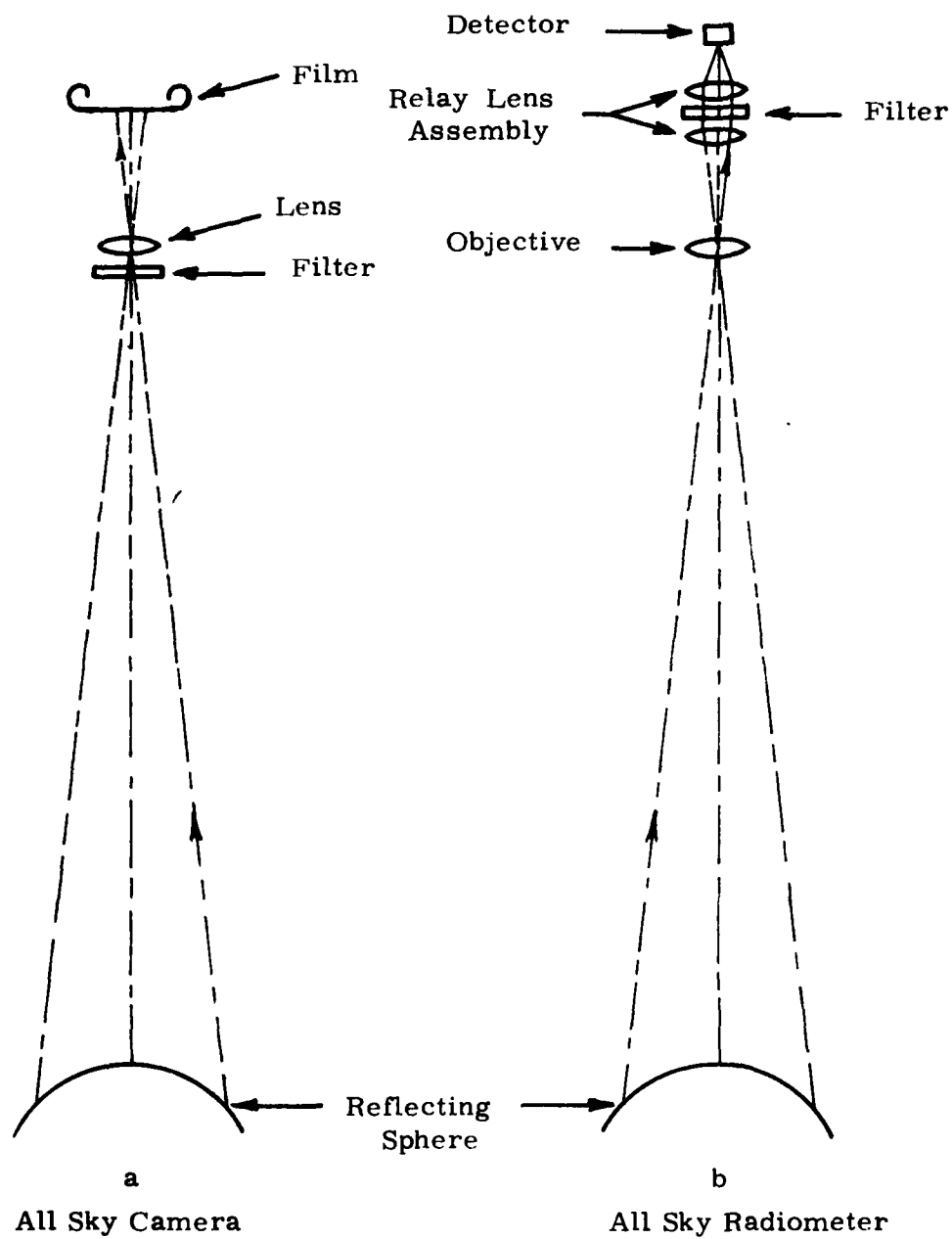


Figure 4.6. All sky detectors using reflections from a spheric surface.

With reference to the camera-sphere system of Figure 4. 6a the relationship between the external angle of the camera  $\beta$  and the external angle of the camera sphere system,  $z$ , is shown in Figure 4. 7. In that figure the optical axis of the camera is directed vertically downward toward the center of the sphere at C. The radius of the sphere is R and the distance from the sphere surface to camera lens is D. A line from the lens center with external angle  $\beta$  intercepts the spheric surface at point P and is reflected at angle  $z$  from the vertical. The line from P to the center of the sphere is at angle  $\alpha$  to the line from sphere center to center of the camera lens (the vertical). The horizontal distance,  $y$ , of the point P from the line between lens center and sphere center may be written as

$$y = R \sin \alpha$$

or

$$y = [D + R (1 - \cos \alpha)] \tan \beta$$

and so

$$\beta = \tan^{-1} \frac{R \sin \alpha}{D + R (1 - \cos \alpha)} \quad 4.4$$

By inspection of Figure 4. 7 one may write

$$z = 2\alpha + \beta = 2\alpha + \tan^{-1} \frac{R \sin \alpha}{D + R (1 - \cos \alpha)} \quad 4.5$$

As the ratio of  $R/D$  goes to 0 the angle  $\beta$  goes to 0 and  $\alpha = z/2$ . That is, when  $z = 90^\circ$  and the line from the lens to P is reflected to the horizon,  $\alpha_h = 45^\circ$ . In practice  $R/D$  is finite. If it is equal to 0.1 then the value of  $\alpha_h$  such that the line from the lens is reflected to the horizon is  $\alpha_h = 43.1^\circ$  and if  $R/D = 0.2$ ,  $\alpha_h = 41.4^\circ$ . Figure 4. 8 shows the relationship between

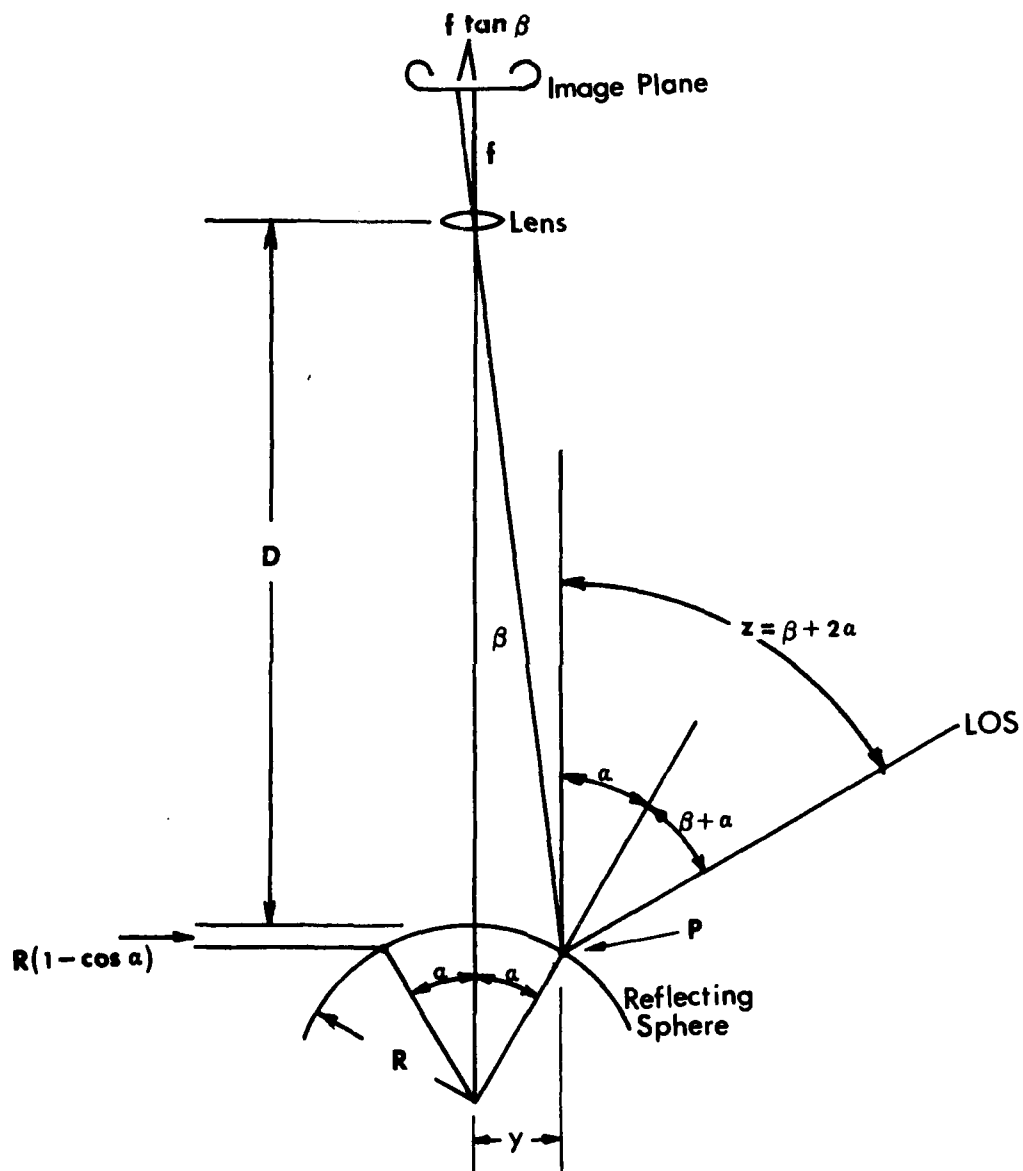


Figure 4.7. Relationship of external angle of camera,  $\beta$ , and external angle of camera-sphere system,  $z$ .

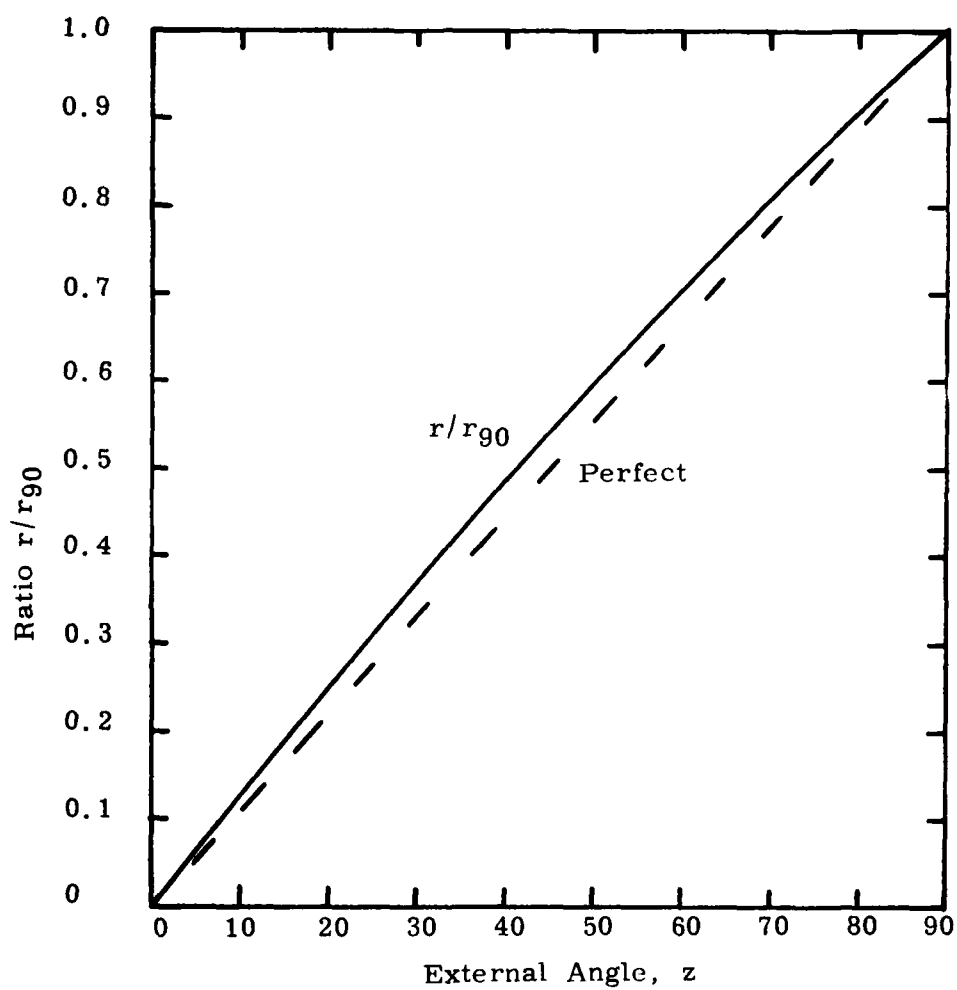


Figure 4.8. Ratio of image height at zenith angle,  $z$ , to image height at  $z = 90$  plotted against external angle,  $z$ .

the external angle,  $z$ , to the image height for the ideal camera-sphere system where  $R/D \rightarrow 0$ . What is plotted in Figure 4.8 is the ratio of the image height at external angle  $z$  to the image height at  $z = 90^\circ$ . For comparison Table 4.2 presents the deviation of this ratio from the ideal case when  $R/D = 0.1$  and  $R/D = 0.2$ . It is apparent that minor errors are introduced by treating the system with  $R/D \leq 0.2$  as ideal (i.e.  $R/D = 0$ ).

Table 4.2. Magnitude of errors introduced by treating finite camera-mirror separation as infinite.

External Angle Degrees	Fractional Deviation	
	$R/D = 0.1$	$R/D = 0.2$
5	1.011	1.020
15	1.012	1.020
30	1.011	1.017
55	1.008	1.013
75	1.004	1.006

In the following we discuss the relationship between area in the focal plane of a camera-sphere system and external solid angle. The approximation  $z = 2\alpha$ , which was discussed above, is used. With reference to Figure 4.7, a point in the focal plane of the camera can be



located in the polar coordinate system  $\rho, \theta$ . In this case

$$\rho = M R \sin \alpha \quad 4.6$$

where  $M$  is the magnification of the camera as used and  $M \approx F/D$ . The angle  $\theta$  is about the optical axis and is measured from any convenient fiducial (usually north). As shown in Figure 4.9 an element of area in the focal plane,  $da$ , is

$$\begin{aligned} da &= \rho \, d\rho \, d\theta \\ da &= M^2 R^2 \sin \alpha \cos \alpha \, d\alpha \, d\theta \end{aligned} \quad 4.7$$

Referring again to Figure 4.9, the solid angle

$$d\Omega = \frac{1}{2} \sin z \, dz \, d\theta \quad 4.8$$

$$\text{but } z = 2\alpha$$

$$\text{or } d\Omega = \sin 2\alpha \, d\alpha \, d\theta \quad 4.9$$

$$\text{Since } \sin 2\alpha = 2 \sin \alpha \cos \alpha$$

$$d\Omega = 2 \sin \alpha \cos \alpha \, d\alpha \, d\theta \quad 4.10$$

$$\text{or } d\Omega = \frac{2}{M^2 R^2} da, \text{ steradians} \quad 4.11$$

This exercise has demonstrated that for a particular camera-sphere system there is a single valued coefficient relating area in the camera focal plane to the associated external solid angle. This is an important concept. For example, if the hemisphere of the sky is photographed by such a camera-

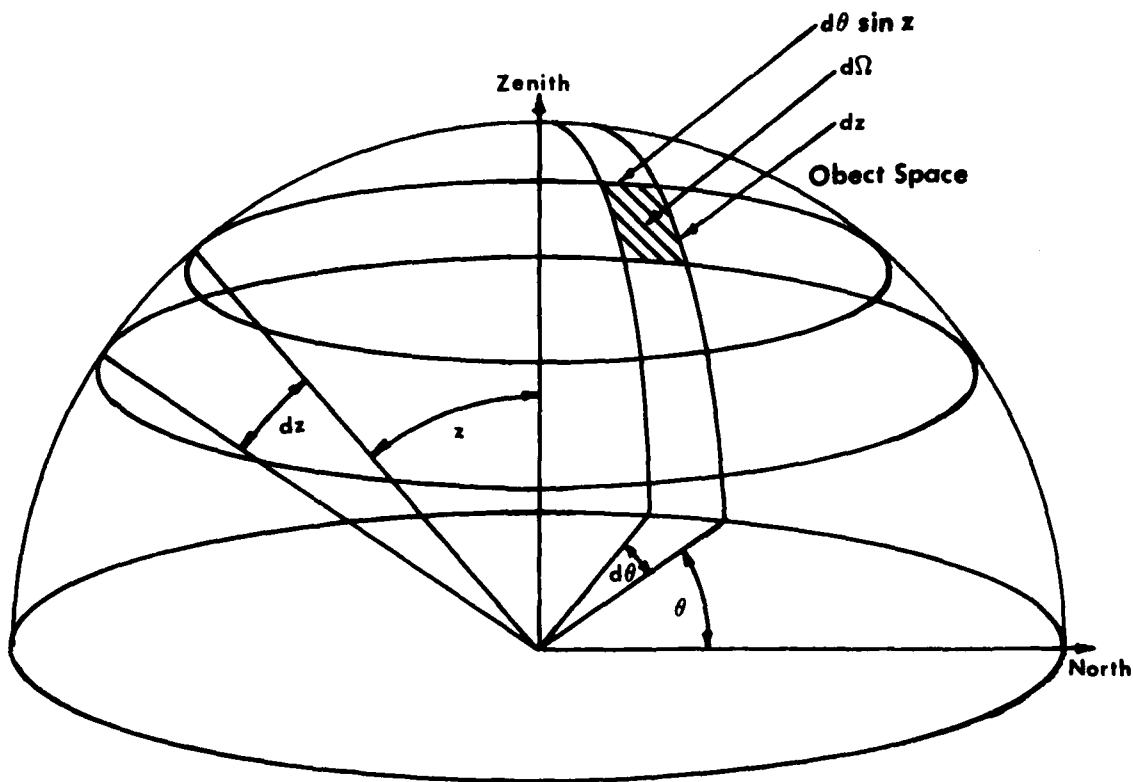
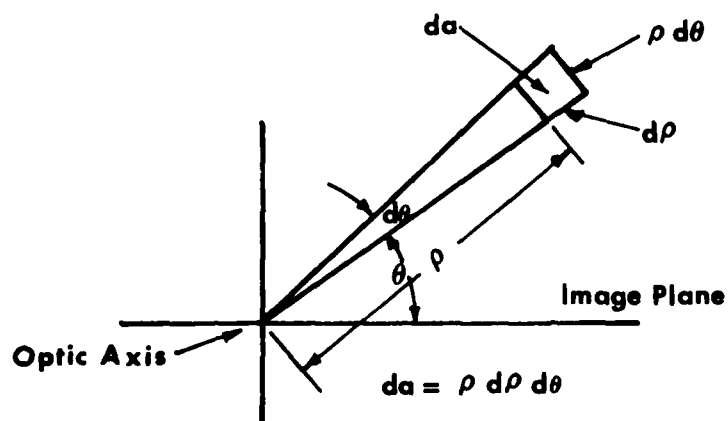


Figure 4.9. Relationship between an element of area,  $da$ , in the image plane (upper drawing) to an element of solid angle,  $d\Omega$ , in object space (lower drawing).

sphere system and if 30 percent of the exposed circular area represents clear sky (as opposed to cloudy) then there is 30 percent of the hemisphere of the sky for which there is cloud free line-of-sight.

#### 4.2.2 Camera System Radiometric Relationship

If the exposed circular area in the focal plane of the camera recording system as shown in Figure 4.8 is divided into  $P$  elements of solid angle  $\Delta a$ , these will correspond to  $P$  elements of solid angle  $\Delta \Omega$  in the hemisphere of the sky. The exposure  $E_p$  of the  $p^{\text{th}}$  element  $\Delta a_p$  is given by

$$E_p = \frac{\pi N_p \Delta t T}{4 (f/n)^2} \quad 4.12$$

where  $N_p$  is the radiance of the  $p^{\text{th}}$  solid angle element of the hemisphere of the sky,  $\Delta t$  is the exposure time,  $T$  is the transmission of the camera-sphere system and  $(f/n)$  is the camera f-number (ratio of focal length to aperture diameter). The product of the exposure and the area of an element  $E_p \Delta a_p$  is the energy incident on the area during the exposure. The total energy involved in an exposure is

$$\sum_p E_p \Delta a_p = \frac{\pi}{4} \frac{\Delta t T}{(f/n)^2} \frac{M^2 R^2}{2} \sum_p N_p \Delta \Omega_p \quad 4.13$$

If, as in Figure 4.6b, the focal plane of the camera is replaced by a relay lens of transmission  $T_r$  forming an image of the objective lens onto a detector, then the energy incident on the detector in a time  $\Delta t$  is  $T_r \sum_p E_p \Delta a_p$ . The power incident on the detector,  $P_d$ , is the energy per unit time or

$$P_d = \frac{\pi}{8} \frac{T T_r R^2 M^2}{(f/n)^2} \sum_p N_p \Delta \Omega_p \quad 4.14$$

If the only source of power were the sun then  $\sum_p N_p \Delta \Omega_p$  would equal  $H_{\odot} T_{\odot}$ , the local solar irradiance. Here  $T_{\odot}$  is the atmospheric transmission in the path to the sun and  $H_{\odot}$  is the solar irradiance outside the earth's atmosphere. These equations are the basis of the camera systems calibration through the all-sky radiometer.

#### 4.2.3 All-Sky Radiometer Calibration

Calibration of the all-sky radiometer is carried out in the following way. The filter condition is selected, this implies that either no filter is used and the spectral response is characterized by the bare silicon detector, or the red filter is used. The red filter, which matches the red filter used in the red-blue all sky camera, has a 100 Å band pass centered on 0.672μ. Calibration with that filter is described here. The transmission to the sun,  $T_{\odot}$ , at the wavelengths 0.44μ, 0.5μ, 0.64μ, 0.88μ and 1.68μ is measured using a Sun Photometer made by Fred Volz of AFGL. From a plot of these transmission readings, a value for  $T_{\odot\lambda}$  the transmission to the sun at 0.672μ is obtained. A reading,  $s_{\odot} + s_s$ , of the output of the all sky radiometer is made as it is exposed to the full sky,  $s_s$ , plus direct sun,  $s_{\odot}$ . Then the direct sun is shaded so that only the sky irradiates the radiometer and the reading of sky signal,  $s_s$ , is made. The reading  $S_{\odot}$  which would be obtained by the radiometer if it were outside the earth's atmosphere and illuminated by the sun above is given by

$$S_{\odot} = \frac{(s_{\odot} + s_s) - s_s}{T_{\odot\lambda}} = K_{\odot} H_{\odot\lambda} \Delta\lambda T_f \quad 4.15$$

where  $K_{\odot}$  is the calibration coefficient of the all sky radiometer and filter,  $H_{\odot\lambda}$  is the spectral irradiance of the sun outside the earth's atmosphere at the central wavelength of the filter,  $\Delta\lambda$  is the band pass of the filter and  $T_f$  is the mean transmission of the filter.

The signal from the sun plus the sky ( $s_{\odot} + s_s$ ) is related to the radiance of the sky and the apparent radiance of the sun's disk as follows:

$$\frac{s}{K_o} = \frac{s_{\odot} + s_s}{K_o} = T_f \sum_p N_p \Delta \Omega_p \Delta \lambda \quad 4.16$$

Relations 4.15 and 4.16 do not depend on the details of the all sky radio-meter design, however the value of K does. In any situation, overcast, broken clouds or clear the observed signal,  $s$ , is related to the detailed radiance of the hemisphere of the sky by equation 4.16. In connection with these concepts the term "coupling coefficient" has been defined as follows

$$\text{Coupling Coefficient} = \frac{T_f \sum_p N_p \Delta \Omega_p \Delta \lambda}{S_o} = \frac{s}{S_o}$$

The same reasoning applies to the case of the all-sky radio-meter used without a filter. The results obtained are given in terms of coupling coefficients appropriate to bare silicon. The transmission to the sun is somewhat more complicated. It is defined as follows:

$$T_{\odot} = \frac{\int H_{\odot \lambda} G_{si \lambda} T_{\odot \lambda} d\lambda}{\int H_{\odot \lambda} G_{si \lambda} d\lambda} \quad 4.17$$

where  $H_{\odot \lambda}$  is the spectral solar irradiance outside the atmosphere,  
 $G_{si \lambda}$  is the relative spectral response function of silicon.  
 $T_{\odot \lambda}$  is the spectral atmospheric transmission to the sun.

The values of  $H_{\odot \lambda}$  and  $G_{si \lambda}$  are found in handbooks. The values of  $T_{\odot \lambda}$  are taken from the plot made from Sun Photometer readings.

#### 4.2.4 Red Channel Camera System Calibration

The objective of the calibration of the all-sky camera (camera-sphere system) is to relate through a calibration factor,  $K_1$ , the measured relative exposure  $E_p$  in an element of area  $\Delta a_p$  to the radiance of the sky  $N_p$  in corresponding element of solid angle,  $\Delta \Omega_p$ . The relationship is derived, however, from the total image area and total sky solid angle and their respective elements. The calibration is made by comparing results from the red all-sky camera records with readings from the calibrated all sky radiometer for the same time. Since both systems are linear in their responses and since an identical filter is used in the one as in the other the band pass and transmission of the filter can be omitted from the calculations of calibration. In addition the exposure time of the camera was unchanged between calibration and use so it too may be omitted from the calculations. The total energy involved in an exposure of the all sky camera is given by equation 4.13 and is rewritten here with the above comments in mind as

$$K_1 \sum_p E_p da_p = \sum_p N_p d\Omega_p \quad 4.18$$

and so

$$K_1 E_p = N_p \quad 4.19$$

The value of  $K_1$  is found by the following procedure. A daytime condition with overcast covering the sun is selected (the direct solar image "overexposes" the film). A picture is made using the red filter<sup>3</sup> all sky camera and at the same time a reading is made with the red filtered all sky radiometer. For this case  $\sum_p N_p \Delta \Omega_p$  is the same for the two instruments. The calibration signal  $s_c$  from the all sky radiometer is given by equation 4.16

which is rewritten here as

$$s_c = K_o \sum_p N_p \Delta \Omega_p \quad 4.20$$

and the calibration of the all sky radiometer gives

$$S_o = K_o H_o \quad 4.21$$

It follows that

$$\sum_p N_p \Delta \Omega_p = \frac{s_c}{S_o} H_o \quad 4.22$$

The film exposed in the red filtered all sky camera is processed and read in a controlled way so that the relative values  $E_p$  are determined. The sum  $\sum_p E_p da_p$  is calculated and is designated here as  $\overline{EA}$ . That is, for the calibration exposure

$$\overline{EA} = \sum_p E_p \Delta a_p \quad 4.23$$

and from equations 4.18 and 4.22

$$K_1 = \frac{s_c}{\overline{EA}} \frac{H_o}{S_o} \quad 4.24$$

#### 4.2.5 Red Channel Camera Calibration Results

This paragraph outlines a calibration of the filtered all-sky radiometer and the subsequent calibration of the filtered **all-sky** camera. The all-sky radiometer was calibrated at 1034 on August 2, 1977. Average readings were as follows

$$\begin{aligned} \text{sun plus sky } (s_{\odot} + s_s) &= 776.5 \text{ meter units} \\ \text{sky } s_s &= 129.0 \text{ meter units} \\ (s_{\odot} + s_s) - s_s = s_{\odot} &= 647.5 \text{ meter units} \end{aligned}$$

Transmission to the sun was measured at 1013 and at 1036 using the sun photometer. The resultant transmission curves are given in Figure 4.10. A value of transmission at  $0.672\mu$  was taken to be 0.76. The value of  $S_{\odot}$  the solar signal in the absence of the atmosphere is

$$S_{\odot} = \frac{s_{\odot}}{T_{\odot}} = 852 \text{ meter units}$$

Now  $H_{\odot\lambda}$  for  $\lambda = 672\mu$  is  $1.57 \times 10^3 \text{ w m}^{-2} \mu$

$$\text{or } K_{\odot} = 0.525 (\text{meter units}) \text{ m}^2 \text{ w}^{-1} \mu^{-1} \quad 4.25$$

If the reading,  $s$ , for an overcast were 220 then  $\sum_p N_p \Delta \Omega_p = 220/0.525 = 419 \text{ w m}^{-2} \mu$ . The average radiance of the overcast is  $67 \text{ w m}^{-2} \mu \text{ sr}^{-1}$  and the average transmission of the overcast is 13 percent. Note that  $\sum_p \Delta \Omega_p = 2\pi$  for the all sky radiometer.

Calibration of the all sky camera with the red filter is discussed in this paragraph. At 1702 on August 2, 1977, the sky was generally overcast. A red all sky picture was taken and the sum  $\sum_p E_p \Delta a_p = \overline{EA}$  was found to be equal to  $1.015 \times 10^2$ . At the time of the photograph the all sky radiometer read  $\overline{s} = 195$ . From the paragraph above,  $S_{\odot} = 852$  and  $H_{\odot} = 1.57 \times 10^3 \text{ w m}^{-2} \mu^{-1}$ . Equation 4.24 gives

$$K_1 = \frac{\overline{s} H_{\odot}}{\overline{EA} S_{\odot}} = 9.85 \times 10^{-3} \frac{\text{watts m}^{-2} \mu \text{ sr}^{-1}}{\text{relative exposure unit}}$$

This value of  $K_1$  is used in data reduction.



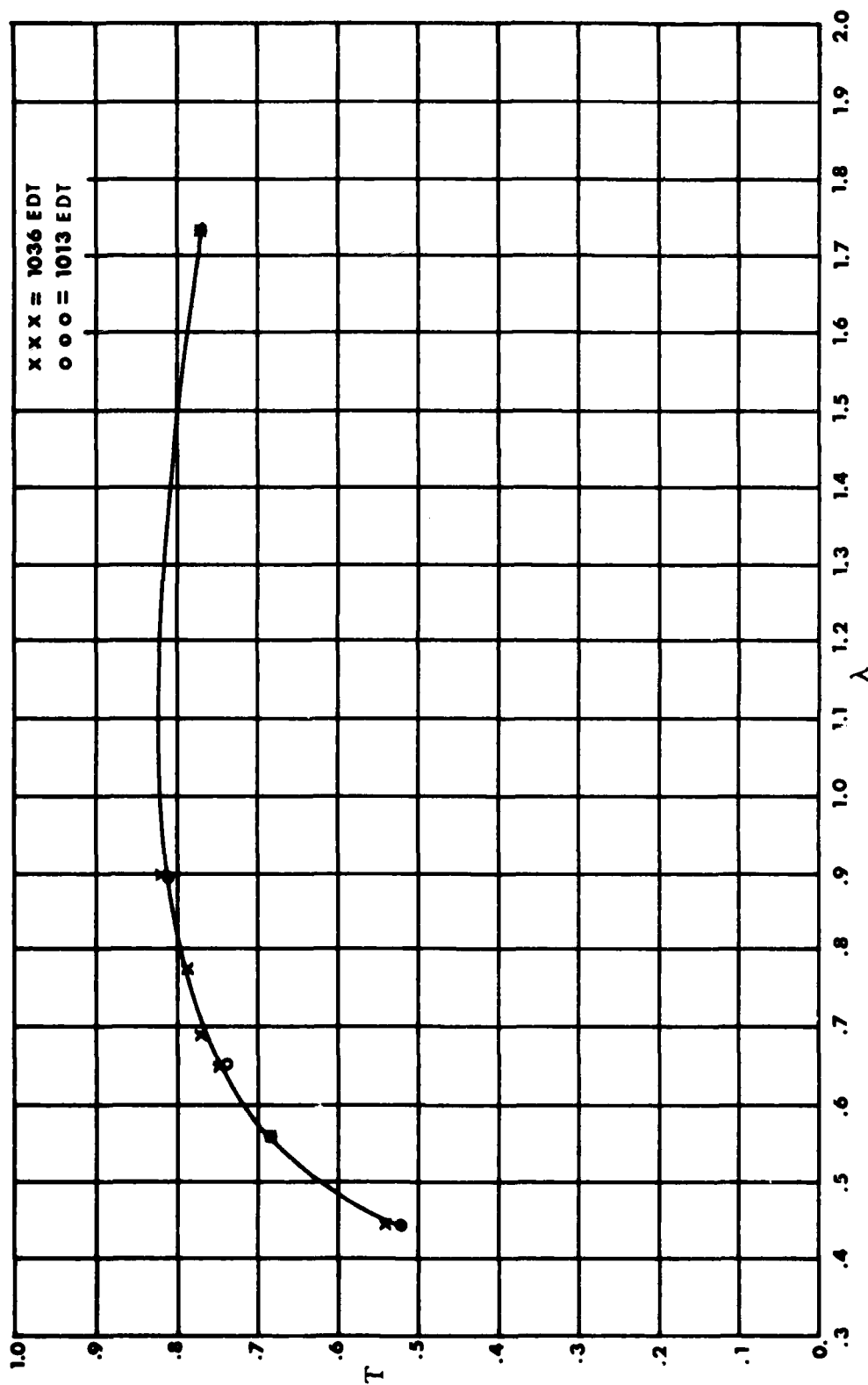


Figure 4.10. Data recorded on August 2, 1977 by the sun photometer giving values of transmission, T, to the sun versus wavelength  $\lambda$ .

#### 4.2.6 Calibration of the ON/OFF Band Camera System

The following paragraphs are concerned with the calibration of the filters used with an all-sky camera to measure the oxygen absorption associated with each element of solid angle  $d\Omega$ . This camera system need not be calibrated in absolute terms since only ratios of exposures are used in data reduction.

For each experiment two pictures were taken on High Speed Infrared Film with the all-sky camera assigned to oxygen absorption measurements. One picture was taken through a filter having  $13.8 \text{ \AA}$  bandwidth at half maximum centered on  $0.7608\mu$ . This wavelength interval is located within an atmospheric oxygen absorption band (the A band extending from its band head at  $0.7593\mu$  to  $0.778\mu$ ). In this report this picture is referred to "on-band". The second picture was taken through a filter having  $33 \text{ \AA}$  bandwidth at half maximum centered on  $0.7530\mu$ . This wavelength interval is free of any absorption by gasses normal to the atmosphere. This picture is referred to as "off-band". Figure 4.11 presents low resolution spectra of the transmission of the atmosphere for three lines of sight having zenith angles  $0^\circ$ ,  $60^\circ$ , and  $70.5^\circ$ . The shape of the envelope of any curve is determined by molecular and aerosol scattering. The structure of the curves is due to absorption by atmospheric gasses. The location of the peak wavelength of both the on-band filter and off-band filter are shown. Figure 4.12 is a higher resolution spectrum of the A band. It was made by Curcio and his associates at Naval Research Laboratory using a ten mile absorption path across Chesapeake Bay. The location of the center of the on-band transmission filter is shown. In this figure the abscissa represents wavelength and the ordinate is proportional to  $(1 - T_p)$  where  $T_p$  is the transmission of the processed spectrographic plates.

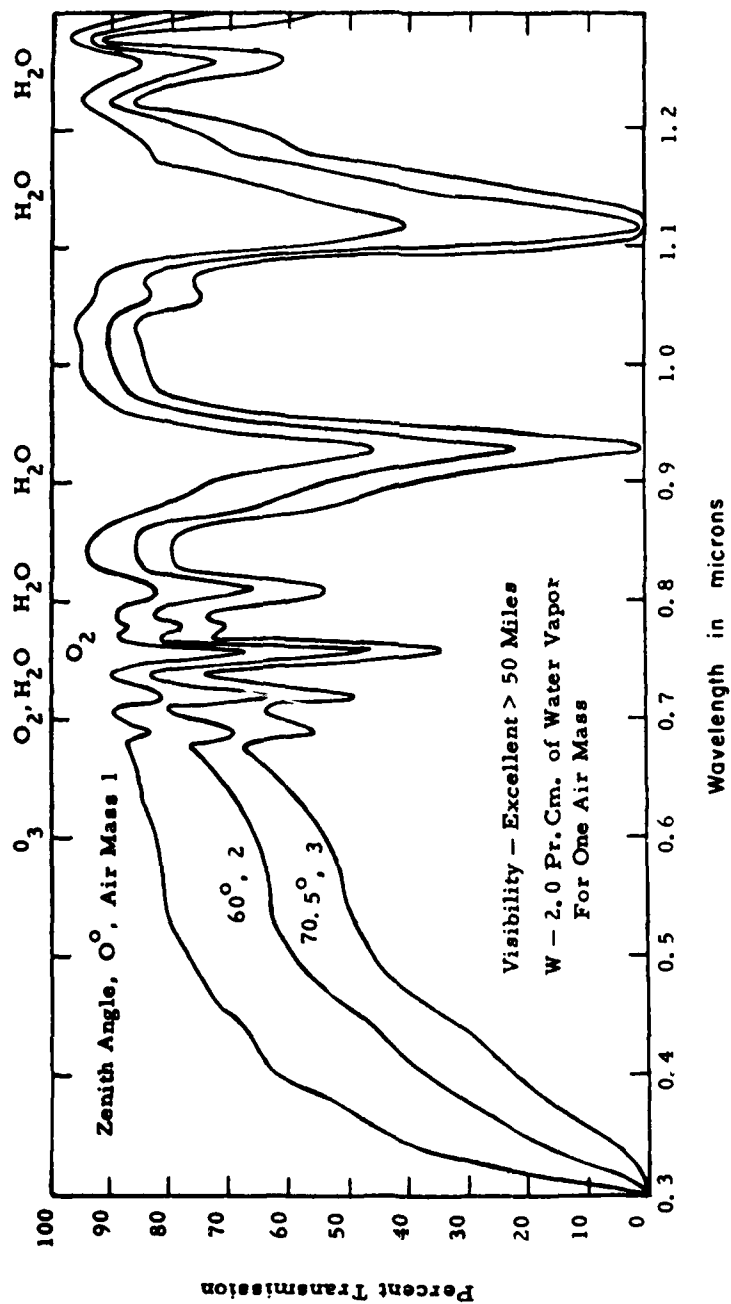


Figure 4.11. Transmission of the atmosphere in low resolution (From Ref. 16)



It was anticipated that for each element of area on the photographic films the ratio of the exposure through the on-band filter to that through the off-band filter would be a function of the mean quantity of oxygen in the path camera to sun. A modification of the Langley method was used to calibrate this ratio using known paths through atmospheric oxygen. The filters to be used with the on-band/off-band cameras were mounted so that they could be located alternately in front of the aperture of a Tektronix J-16 Teleradiometer. This, in turn, viewed a white plaque from an angle 45° off the plaque normal. During a calibration run this assembly was positioned so that the sun was on the normal to the plaque. Figure 4.13 is a lay-out sketch of the assembly and Figure 4.14 is a photograph of the instrument.

The equivalent sea level path length through atmospheric oxygen,  $L$ , was taken to be

$$L = H \sec z \quad 4.26$$

where  $H$  = Scale height of atmosphere

$z$  = Solar zenith angle

The scale height was taken to be equal to 8 km. Calibration ratios taken on 3 August 1977 are plotted against the square root of  $L$  in Figure 4.15. The equation accounting for the straight line through the points in this figure is

$$\frac{\text{on}}{\text{off}} = 6 e^{-0.51 \sqrt{L}} \quad 4.27$$

$$\text{or} \quad L = \left( \frac{\ln \frac{\text{on}}{\text{off}} - \ln 6}{0.51} \right)^2 \quad 4.28$$

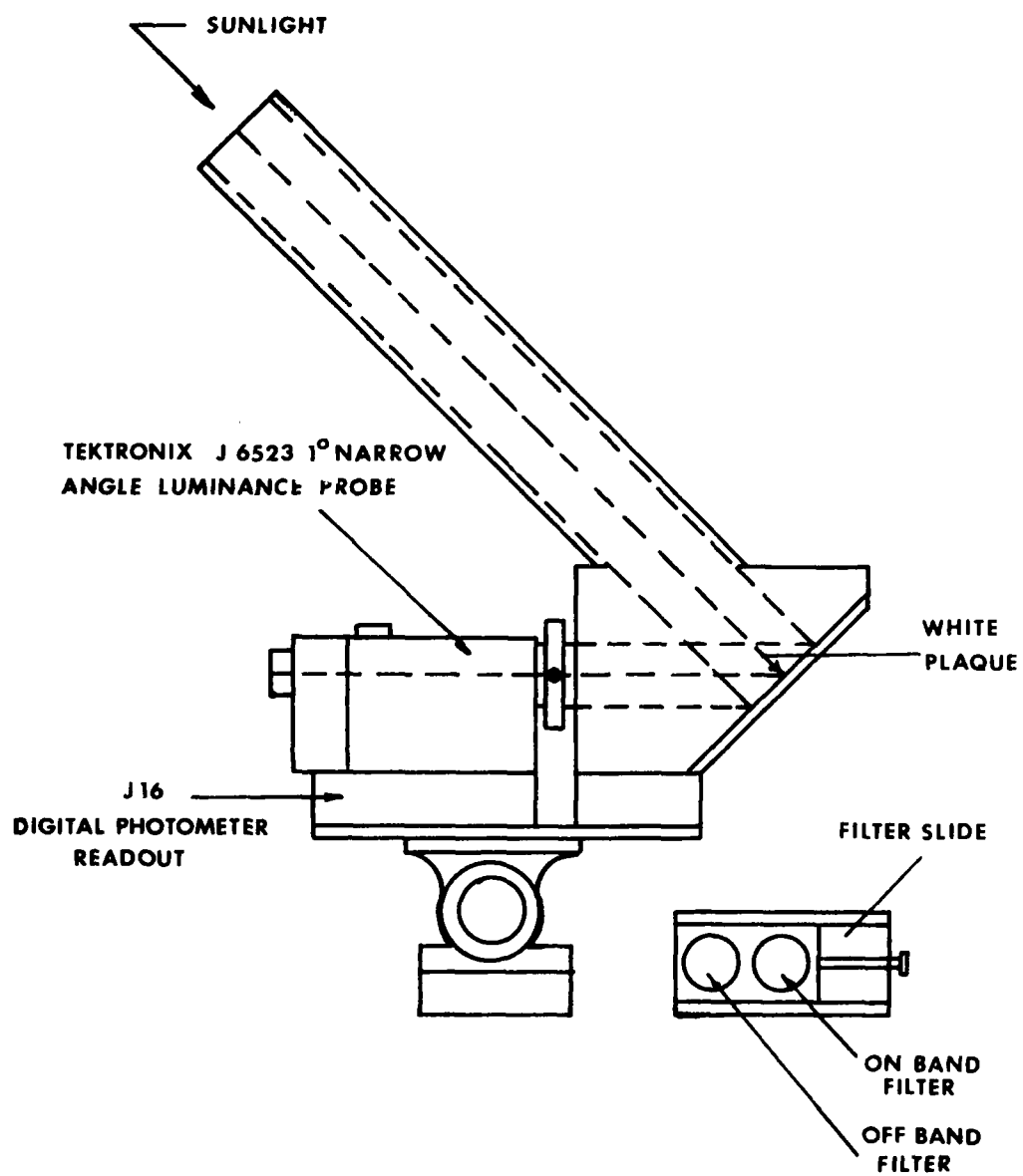


Figure 4.13. Schematic diagram of calibration equipment for on-band/off-band camera filters.

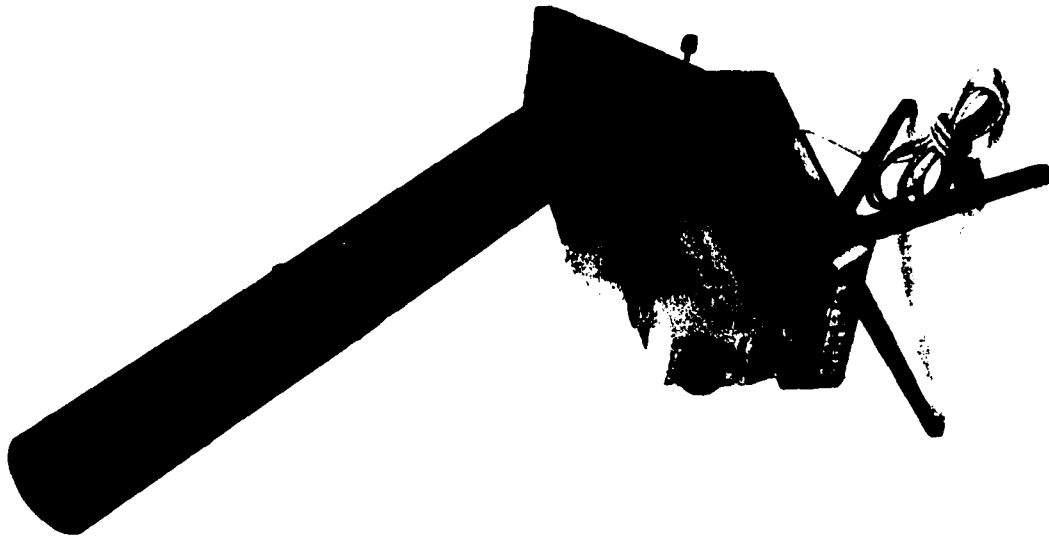


Figure 4.14. Photograph of calibration equipment for on-band/off-band filters.

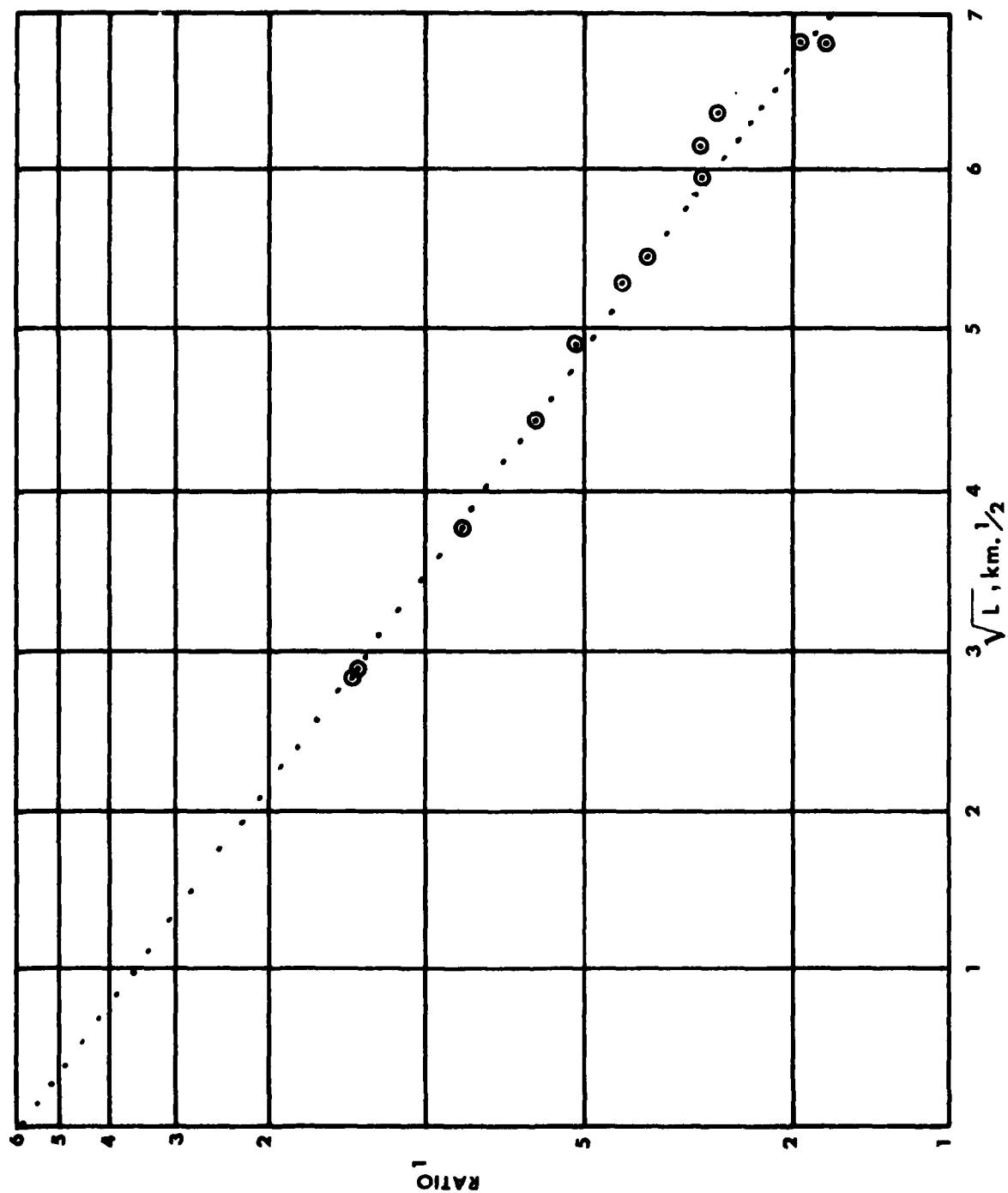


Figure 4.15. Data obtained with calibration equipment showing the logarithm of the on-band/off-band ratio plotted against the square root of the oxygen path length.



The ratio on/off is used to indicate the ratio of the teleradiometer reading through the on-band filter to that through the off-band filter. Equations 4.27 and 4.28 are used in data reduction to account for the ratios of calculated exposures per area element from the on-band and off-band filtered all-sky camera photographs.

## SECTION 5

### WORKING EQUATIONS FOR DATA ANALYSIS

#### 5.1 GENERAL COMMENTS

The experiments described here produce a limited amount of information for any area element on the data film and therefore its corresponding solid angle element in space. For each element the information is as follows:

- a. Whether the element views clear space or a cloud.
- b. If it is a cloud, a value for the height of its base.
- c. The radiance in a red wavelength band of the portion of the cloud viewed by the element.
- d. The transmission in a near infrared wavelength band of the atmospheric oxygen in the mean path from the sun to the all-sky camera via the cloud element.
- e. The azimuth and zenith angle to the sun and of the line of sight defined by the element.

There is such an assembly of information for each of the 127,000 elements of area on the film. Data reduction relating to the flow of power in the individual elements of solid angle does not involve interaction of information acquired at one element of solid angle with information acquired at another. This fact reduces the complexity of the bulk of the data reduction procedure to 127,000 repetitions of rather simple calculations.

It seems clear that the radiance of an area on a cloud is closely related to the efficiency of the path through that area in terms of getting light from the sun to the camera station. It is also sensible that photon flight times involve the geometric distances from the camera station to the area viewed and from the corresponding area directly above on the top of the cloud to the sun in addition to the flight time within the cloud.

Finally, absorption of light by oxygen is related in a somewhat complicated way to path lengths in the atmosphere within and free of clouds. These complications arise from the altitude dependence of oxygen pressure and the square root law of absorption by oxygen. There may be many sets of simplifying assumptions that allow reasonable calculations to be made. The set used here are:

- a. for every cloud represented by a data element, there is a corresponding pseudo cloud. The pseudo cloud "exists" in the reduced atmosphere, one in which the pressure of  $O_2$  is constant throughout. The observables of the pseudo cloud are identical to the real cloud. These observables include the on-band/off-band ratio and the radiance at the bottom of the cloud. The characteristic of the pseudo cloud is that all scattering within it is isotropic.
- b. the pseudo cloud has sufficient horizontal extent that edge effects can be neglected; that is, the cloud can be treated as though it were part of a uniform overcast whose properties are defined by the properties of the element.
- c. the density of scattering agents within the pseudo cloud in the reduced atmosphere is constant between the upper and the lower boundaries of the cloud.
- d. the size distribution of the scattering agents within the cloud does not vary from the bottom of the cloud to the top of the cloud.

These assumptions allow the two stream theory and the diffusion theory described in Section 3 to be used. In addition calculated path lengths

through oxygen equal the "real" path lengths in the reduced atmosphere. Obviously, conclusions reached in the reduced atmosphere must be unfolded back to the real atmosphere before the task is completed.

## 5.2 TRANSMISSION OF AN OVERCAST

Transmission of a cloud at a location associated with the area element at point  $p$  in the image plane,  $\Delta a_p$ , is calculated from the red filter picture. The relative exposure on this element of area of the film,  $E_p$ , is used in Equation 4.19 to calculate  $N_{p\alpha}$  the radiance of the cloud element as viewed at angle  $\alpha$  from the normal. Given the zenith angle of the sun and the radiance of the cloud base,  $N_{ap}$ , equations 3.12 and 3.14 are combined to express the value of cloud transmission.

$$T_{zp} = \frac{7\pi}{3} \frac{N_{\alpha p}}{H_{\odot}} \frac{1}{(1 + 2 \cos \alpha) \cos z} \quad 5.1$$

where  $H_{\odot}$  = the solar irradiance

$z$  = zenith angle of the sun

and  $\alpha$  = zenith angle of line of sight

## 5.3 RATIO OF TRANSPORT MEAN FREE PATH TO CLOUD THICKNESS

Equation 3.12 may be rewritten

$$m = \frac{L}{B} = \left\{ \frac{\cos z + 1/2}{T_z} - 1 \right\}^{-1} \quad 5.2$$

This provides a value of  $m$  for diffusion theory calculations

## 5.4 OVERCAST THICKNESS

In the following paragraphs the thickness of an overcast,  $B$ , is calculated from the base height of the overcast, its transmission and the

observed transmission of  $O_2$  in the path from sun, through overcast, to detector. Figure 5.1 will be a useful reference in the development of the working equation. The equations will be written in a manner appropriate to the reduced atmosphere (Section 3.3 above).

The equivalent sea level path length through atmospheric oxygen in the path from sun to cloud top to cloud bottom to observing point,  $Y$ , is easily written for the reduced atmosphere as  $Z \sec \alpha + (H-B-Z) \sec z$ . If  $\bar{\tau}_{O_2}$  is the mean increase in transit time (in the reduced atmosphere) for photons within the  $O_2$  absorption band traveling from the top of the cloud to the bottom then the mean path length through oxygen from the top of the atmosphere to the detector is

$$Y + c \bar{\tau}_{O_2} = c \bar{\tau}_{O_2} + Z \sec \alpha + (H-Z-B) \sec z \quad 5.3$$

For this path the ratio of an on-band to an off-band reading using the filters described in Section 4.2.6 is

$$\frac{\text{on}}{\text{off}} = 6 e^{-0.51 \sqrt{L}} \quad 4.27 \text{ (repeated)}$$

or

$$\left( \frac{\ln \frac{\text{on}}{\text{off}} - 6}{0.51} \right)^2 = c \bar{\tau}_{O_2} + Z \sec \alpha + (H-Z) \sec z - B \sec z \quad 5.4$$

When the approximation of Equation 3.36 holds then  $\bar{\tau}_{O_2} = \bar{\tau}$  where  $\bar{\tau}$  is the mean transit time of the cloud at a wavelength outside the oxygen absorption band. Now Equation 3.23 can be used to account for  $\bar{\tau}$ ; that is,

$$\bar{\tau}_{O_2} = \bar{\tau} = 2.36 B \left( \frac{\cos z + 0.5}{T} - 1.26 \right)^{0.94} + \frac{B}{c} \quad (5.5)$$

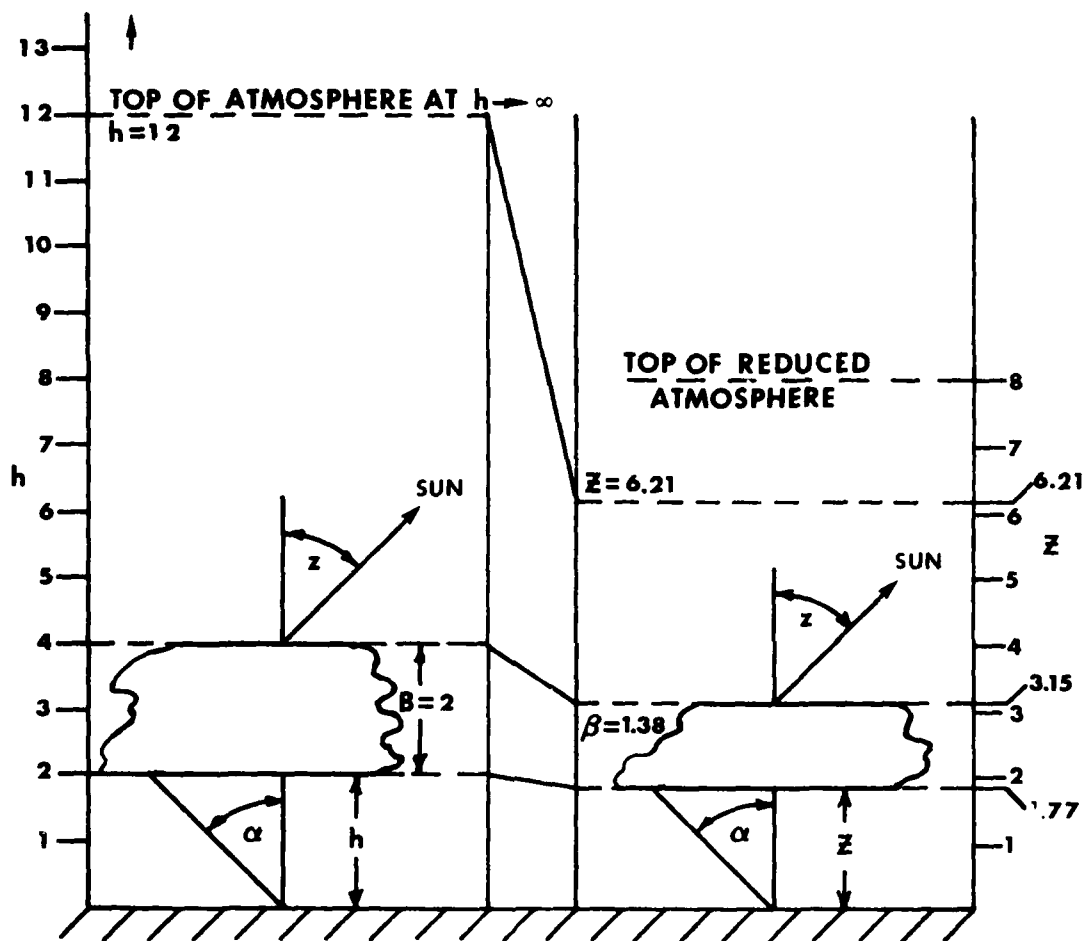


Figure 5.1. Cloud in real (left) and reduced atmosphere (right).

Making this substitution in Equation 5.4 and solving for B gives the following

$$B = \frac{\left( \frac{\ln \frac{\text{on}}{\text{off}} - 6}{0.51} \right)^2 - Z \sec \alpha - (H-Z) \sec z}{Q \left\{ 0.708 \left( \frac{\cos z - 0.5}{T} - 1.26 \right)^{0.94} + 1 \right\} - \sec z} \quad 5.6$$

The symbol Z has been introduced for reasons given below. In Equation 5.6,  $Q = 1$ .

An effort was made to improve on the approximation  $\bar{\tau}_{O_2} = \bar{\tau}$  of Equation 3.36. Many pairs of curves such as those shown in Figure 3.5 were generated using various possible values of Y and of T. From the calculations (which generated  $\bar{\tau}_{O_2}$  and  $\bar{\tau}$ ) the dependence of the ratio of  $\bar{\tau}_{O_2}$  to  $\bar{\tau}$  was studied as a function of Y and T. an empirical relationship was developed which is

$$Q = 0.99 \times 10^{0.097 \log T + 10^{-0.8 - 0.29 (\log T + 2) \log Y}} \quad 5.7$$

This value of Q was used in data reduction. In retrospect it seems its use was probably not justified by the accuracy of the total data reduction process.

With thin clouds and with significant ground reflection poor values of cloud thickness are obtained because use of the value of T in equation 5.6 assumes a cloud thick enough that diffusion theory holds and also assumes no ground reflection. Much of the data taken in this research effort involved thin clouds and surfaces which were the sides as opposed to the bottoms of clouds. To avoid the errors arising from these deviations from ideal conditions, most of the data has been reduced with cloud thickness assigned from best guesses of the conditions existant when the data pictures were taken.

## 5.5 MEAN TIME DELAY IN OVERCASTS

With a value of  $B$  calculated using Equations 5.6 and 5.7 and a value of  $T$  calculated using Equation 5.1 the value of  $\bar{\tau}$  can be determined using Equation 5.5. This yields the mean time delay in the reduced atmosphere. The mean time delay in the real atmosphere,  $\bar{\tau}$ , is

$$\bar{t} = \frac{B}{\beta} \quad \bar{\tau} = \frac{B^2}{CH (e^{-h/H} - e^{-(h+B)/H})} \cdot \left\{ 0.708 \left( \frac{\cos z + 0.5}{T} - 1.26 \right)^{0.94} + 1 \right\} \quad 5.8$$

When a value of  $B$  is measured or assumed then the following reasoning is used. The path length through oxygen outside the cloud is defined in the reduced atmosphere as  $z \sec \alpha + (H-Z-B) \sec z$ . The total mean path length through oxygen is measured as

$$\left[ \frac{\ln \frac{\text{on}}{\text{off}} - \ln 6}{0.51} \right]^2$$

and the difference must be the mean path length in the cloud. That is

$$c \bar{\tau} = \left[ \frac{\ln \frac{\text{on}}{\text{off}} - \ln 6}{0.51} \right]^2 - Z \sec \alpha - (H-Z-B) \sec z \quad 5.9$$

Converting to the real atmosphere gives

$$\bar{\tau} = \frac{B}{Hc} \frac{\left[ \frac{\ln \frac{\text{on}}{\text{off}} - \ln 6}{0.51} \right]^2 - H \left[ (e^{-(h+B)/H}) \sec Z + (1 - e^{-h/H}) \sec \alpha \right]}{[e^{-h/H} - e^{-(h+B)/H}]} \quad 5.10$$



## 5.6 GEOMETRIC DELAY FROM CLOUD TOP TO SATELLITE

In data reduction a coordinate system is assigned to points on the data film using the edges of the rectangular frame of the picture as the directions of the  $x$  and  $y$  axis. The relationships between coordinates of a point on the film of the camera-sphere system and the azimuth and zenith angles of the corresponding line-of-sight in space have been discussed in 4.2.1 above. A coordinate system  $X_s, Y_s$  and  $Z_s$  is set up in space with the camera at  $X_s = Y_s = Z_s = 0$ , with  $Z_s$  the positive vertical and with  $X_s$  parallel to  $x$ , the film coordinate, and  $Y$  parallel to  $y$ . If  $x_o$  and  $y_o$  are the film plane coordinates of the intersection of the camera optical axis, then  $\lambda$ , the clockwise azimuth of the point  $x, y$  from the positive  $x$  axis is:

$$\begin{aligned} \text{for } x \text{ positive and } y \text{ negative} \quad \lambda &= -\tan^{-1} \frac{y - y_o}{x - x_o} \\ \text{for } x \text{ negative and } y \text{ positive or negative} \quad \lambda &= 180^\circ - \tan^{-1} \frac{y - y_o}{x - x_o} \\ \text{for } x \text{ positive and } y \text{ positive} \quad \lambda &= 360^\circ - \tan^{-1} \frac{y - y_o}{x - x_o} \end{aligned}$$

The clockwise azimuth of the line-of-sight corresponding to point  $x, y$  is also  $\lambda$ . The zenith angle  $\alpha$  of such a line-of-sight as shown in 5.1 is

$$\alpha = \tan^{-1} \left\{ \frac{\sqrt{(x-x_o)^2 + (y-y_o)^2}}{f} \right\} + 2 \sin^{-1} \left\{ \frac{D \sqrt{(x-x_o)^2 + (y-y_o)^2}}{R f} \right\} \quad 5.11$$

where  $f$  is the focal length of the camera lens  $D$  is axial distance from camera lens to surface and  $R$  of sphere is radius of sphere.

Corresponding to  $x$  and  $y$  in the camera focal plane, the coordinates  $X_h, Y_h, Z_h$  of the intersection of the line-of-sight with the base of the

overcast at altitude are

$$X_h = (h \tan \alpha) \cos \lambda$$

$$Y_h = -h \tan \alpha \sin \lambda$$

$$Z_h = h$$

The coordinates of the top of the overcast,  $X_t$ ,  $Y_t$ ,  $Z_t$ , above this point are

$$X_t = X_h$$

$$Y_t = Y_h$$

$$Z_t = Z_h + B = h + B$$

Where  $B$  is the overcast thickness.

The difference between the distance from the point  $X_t$ ,  $Y_t$ ,  $Z_t$  to the satellite and the distance  $0, 0, 0$  to the satellite is  $\Delta \rho (X_t, Y_t, Z_t)$  given by

$$\Delta \rho (X_t, Y_t, Z_t) = -\sqrt{Z_t^2 + p^2} \cos [\sigma - \tan^{-1}(\frac{p}{Z_t})] \quad 5.12$$

where  $p = \sqrt{X_t^2 + Y_t^2} \cos (\lambda - \gamma + \beta)$   
 $\gamma$  = azimuth of satellite (clockwise from north)  
 $\beta$  = azimuth of positive  $X_s$  axis (clockwise from north)

The difference between the light transit time from  $X_t, Y_t, Z_t$  to the satellite and that from  $0, 0, 0$  is  $\Delta t(X_t, Y_t, Z_t)$ .

$$\Delta t(X_t, Y_t, Z_t) = \frac{\Delta \rho(X_t, Y_t, Z_t)}{c}$$

$$= -\frac{1}{c} \sqrt{Z_t^2 + p_t^2} \cos[\sigma - \tan^{-1}(\frac{p}{Z_t})] \quad 5.13$$

The mean time of flight of light from the source at  $0, 0, 0$  to the top of the cloud at  $X_t, Y_t, Z_t$   $\bar{t}(X_t, Y_t, Z_t)$  given by

$$\bar{t}(X_t, Y_t, Z_t) = h \sec \alpha + \bar{t} \quad 5.14$$

where  $\bar{t}$  is given by equation 5.10.

The mean time delay of light which starts from  $0, 0, 0$ , leaves the top of the overcast at  $X_t, Y_t, Z_t$  and is appraised at the satellite  $\Delta t(\sigma, \gamma)$  given by

$$\Delta t(\sigma, \gamma) = \Delta t(X_t, Y_t, Z_t) + h \sec \alpha + \bar{t} \quad 5.15$$

## 5.7 THE RADIANCE CENTROID

In the geodetic technique under study source location is determined by differences in times of arrival at several satellites of part of a light signature characteristic of the source. A different geodetic technique involves measurements of the angles to the source from reference platforms in several satellites. In this latter case the presence of clouds or overcast may cause a displacement of the apparent source direction and an associated error in the assigned source location. The data taken in the experiments described

here can be used to specify the centroid of radiance on the top of the cloud structure or the overcast. Most direction sensing equipment will point at the centroid.

For an overcast of thickness B and base altitude h the altitude of the centroid  $Z_c = Z_t = B + h$ . Equations for the other two coordinates,  $X_c$  and  $Y_c$  are developed in the following paragraphs.

The photographs are made up of a finite number of elements of equal area  $\Delta a$  (pixels) located at discrete positions  $x_j, y_k$ , where j runs from 1 to 401 and k runs from 1 to 401. The data is reduced so that an exposure,  $E_{jk}$ , is calculated for each position  $x_j, y_k$ . The centroid of exposure  $x_c, y_c$ , is defined as follows:

$$x_c = \frac{\sum_j \sum_k E_{jk} x_j}{\sum_j \sum_k E_{jk}}$$

and

5.16

$$y_c = \frac{\sum_j \sum_k E_{jk} y_k}{\sum_j \sum_k E_{jk}}$$

There is little physical significance to this centroid of exposure on the film. It has been described because it is expressed simply.

The important centroid is that which would exist at the top of the overcast or cloud structure if the only light source were an isotropic radiator at the location of the camera-sphere system. Let the source be a sphere with  $a_o$  the area of its cross section and  $N_o$  its radiance which is equal to the radiance of the sun. The radiance of the top of an overcast is written, using equation 3.14

$$N(X_{tj}, Y_{tk}) = \frac{N_o a_o \cos \alpha}{h^2 \sec^2 \alpha} \left( \frac{3(1 + 2 \cos \alpha)(1 + 2 \cos z)}{14\pi(1 + B/L)} \right)$$

5.17

where  $\alpha$  is given by equation 5.11

$z$  is zenith angle of sun

$h$  is base height of overcast

$$X_{tj} = h \tan \alpha \cos \lambda$$

$$Y_{tj} = -h \tan \alpha \sin \lambda$$

The power,  $\bullet p$ , radiated to the sun from unit area is

$$\bullet p = N(X_{tj}, Y_{tk}) \Omega_{\bullet} \cos z \quad 5.18$$

An identical expression results for  $\circ p$ , the power flowing to a spherical receiver at the camera location with cross section  $a_{\circ}$  when the overcast is irradiated by the sun. That is

$$\circ p = \bullet p = \frac{N_{\bullet} \Omega_{\bullet} a_{\circ} \cos z \cos \alpha}{h^2 \sec^2 \alpha} \left( \frac{3(1+2 \cos \alpha)(1+2 \cos z)}{14\pi(1+B/L)} \right) \quad 5.19$$

Note that at the point on the base of the overcast intercepted by the line of sight at zenith angle  $\alpha$  the solid angle subtended by the receiver (or source) located at the camera position is  $\Omega_{\circ}$ , where

$$\Omega_{\circ} = \frac{a_{\circ}}{h^2 \sec^2 \alpha}$$

For each pixel of area  $\Delta a$  there is a corresponding element of solid angle  $\Delta \omega$  given by equation 4.11 as

$$\Delta \omega = \frac{2}{M^2 R^2} \Delta a$$

The area of the base of the overcast intercepted by this element of solid angle is

$$\Delta A_h = h^2 \sec^3 \alpha \quad \Delta \omega = \frac{2 h^2 \sec^3}{M^2 R^2} \Delta a$$

If  $a_o$ , the receiver or source cross section, is taken to be the entrance aperture of the camera-sphere system then the exposure of the pixel at  $x_j y_k$  is

$$E_{jk} = {}_o P_{jk} \Delta T = {}_o p_b \Delta A_{hjk} T \Delta t \quad 5.20$$

where  $\Delta t$  is the exposure time

$T$  is the transmission of the camera sphere system

and the subscript  $j$  and  $k$  are used to specify values associated with the pixel at  $x_j y_k$ .

When an isotropic source of cross section  $a_o$  is used at the camera location the amount of power, radiated to the sun from an area  $\Delta A_{hjk}$  located at  $X_{tj}$ ,  $Y_{tp}$  is by Equation 5.19,

$$P_{tjk} \bullet {}_o p_{jk} \Delta A_{hjk} = {}_o p_{jk} \Delta A_{hjk} = \frac{E_{jk}}{T \Delta t} \quad 5.21$$

This important result relates the exposure of the film at a particular pixel to the amount of power that would reach the sun given a source radiating into the solid angle corresponding to the pixel. The source in this case has radiance equal to the sun and cross sectional area equal to the entrance pupil of the camera sphere system. The centroid of radiance on the top of the overcast is at  $X_{tc} Y_{tc}$

$$X_{tc} = \frac{\sum_j \sum_k E_{jk} X_{tj}}{\sum_j \sum_k E_{jk}}$$

$$Y_{tc} = \frac{\sum_j \sum_k E_{jk} Y_{tj}}{\sum_j \sum_k E_{jk}}$$

5.22

## 5.8 EFFECTS OF GROUND REFLECTIVITY

In all of the work described above it has been assumed that the isotropic source only radiates into the upper hemisphere. This would be the case if the isotropic source were located above a ground surface of zero reflectivity. In the case that the ground has a diffuse reflectivity equal to  $\rho$  then reflected light will contribute to the power radiated to space. If  $P_{\text{rad}+}$  is the power measured by all sky radiometer (which looks into the upper hemisphere alone)

$$P_{\text{rad}+} = g \sum_j \sum_k E_{jk}$$

where  $g$  is a calibration coefficient and  $E_{jk}$  is the exposure of the pixel at  $x_j, y_k$ . Then

$$P_{\text{total}} = P_{\text{rad}+} + 2g\rho \sum_j E_{jk} \cos \alpha_{jk}$$

or

$$P_{\text{total}} = g \sum_j \sum_k E_{jk} (1 + 2\rho \cos \alpha_{jk}) \quad 5.23$$

The term  $\cos \alpha_{jk}$  enters because it is assumed that the radiation is scattered from the ground has an intensity distribution about the normal which obeys Lambert's law.

## SECTION 6

### COMPUTER PROCESSING

#### 6.1 INTRODUCTION

This section presents the computer processing procedures used to derive expected pulse shapes from the photographic data and the mathematical relationships presented in previous sections. At the outset a "hands-off" set of computer programs was visualized. The term "hands-off" as used here means a system in which, once a computation is started using the measured input parameters and the photographic data, the derived pulse shape is a unique, inevitable outcome of the computations. Such a system does not allow for human judgement during the process. The data analyst serves only to keep the flow of data going and direct the outcome of one program to the next until the final pulse-shape plot is obtained.

For reasons which will be explained in more detail below, a completely "hands-off" system was not quite achieved. One parameter, cloud thickness, proved too difficult to derive satisfactorily exclusively from the experimental data and the decision was made to permit sufficient "hands-on" intervention to supply cloud thickness on the basis of typical clouds.

For either of these systems the computer processing starts with the primary photographic data plus support information and derives expected pulse shape. The final product of the system is a plot of the predicted, normalized power versus time at the receiver.

Figure 6.1 presents the major features of the complete data processing system most of which is accomplished in the computer. The functions named in several of the boxes of Figure 6.1 have been explained



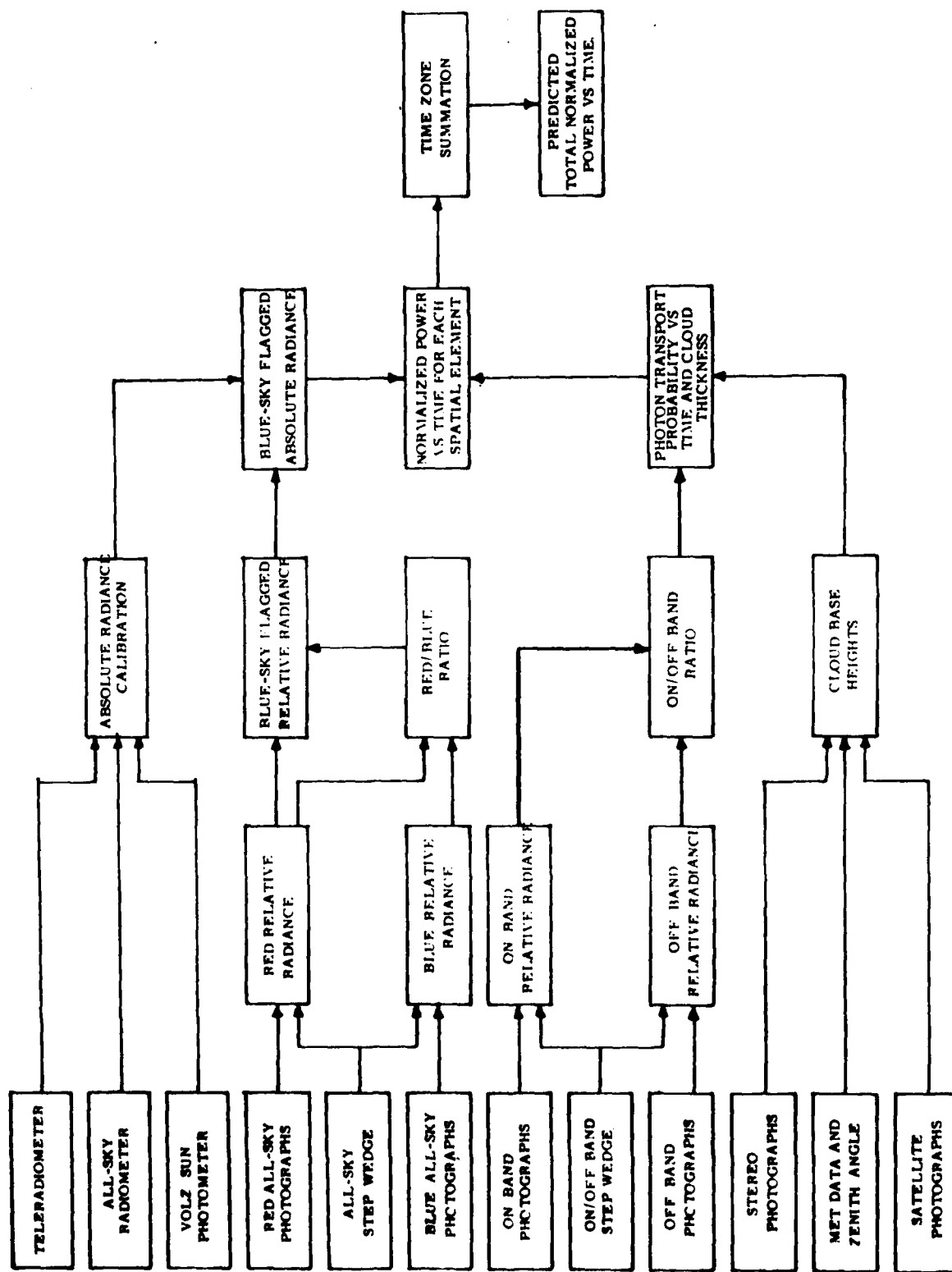


Figure 6.1 Schematic presentation of the major steps in the data reduction system used to derive predicted pulse shapes.

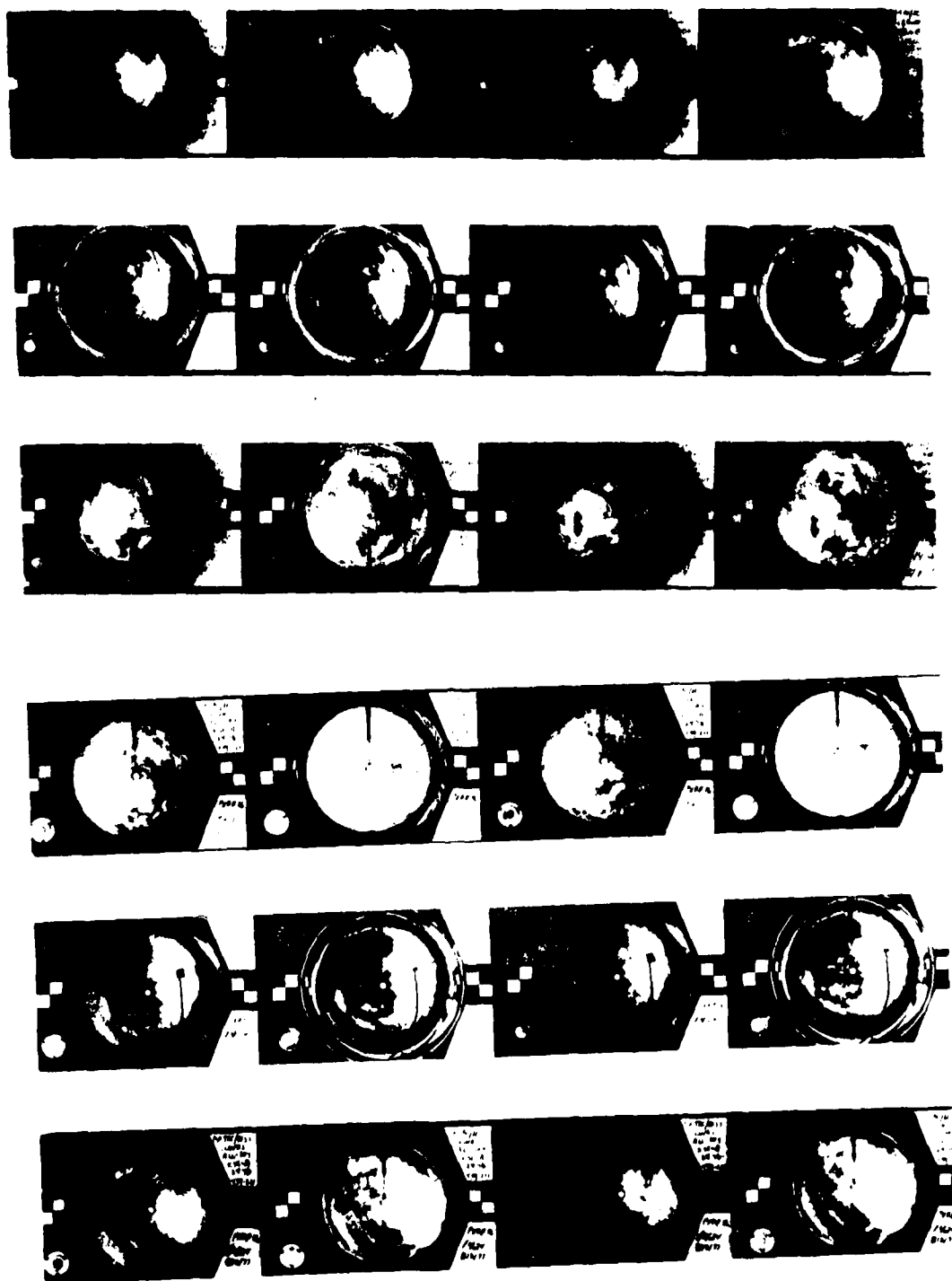


Figure 6.2. Contact photographic print from 3 data runs showing typical original data.

in other sections of this report and will not be discussed here. The computer processing system consisted of a series of six primary programs which were used sequentially, each providing one step in the chain from digitized data to final predicted pulse shape. Several additional programs were used in supporting roles. The digital data was organized into a square matrix of data points centered on the zenith and containing the data points of interest. The computer processing consisted of operating on each data point sequentially and independently of the others with the output stored on magnetic tape. All of the programming was standard FORTRAN and will not be discussed further. The following paragraphs present some of the problems unique to the data being processed and the manner in which these problems were handled.

## 6.2 DIGITIZATION

All film digitization was done at Optronics International Inc., Chelmsford, MA on a Model P-1700 Photomation Drum Scanner. This instrument has the necessary speed to make a two dimensional scan of the films in a reasonable time. It also has the capability to write the digitized data on unexposed film to verify, after photographic processing, that digitization has been properly accomplished. The digitized data is written on 9 track magnetic tapes ready for computer processing.

To prepare for scanning short strips of original data consisting of four related exposures were mounted on a transparent carrier sheet suitable for the digitizer drum. Figure 6.2 is a contact print of six such strips, the data from three data sets. The infrared film strips were all mounted at a slight angle to the red/blue film strips to compensate for a slight misalignment in azimuth between the two cameras. This angle, just under 2°, was determined by a careful examination of the film from the two cameras

in a projection type image plane digitizer which permitted the angle between the film edge and lard marks on the horizon to be measured. By mounting the films in this manner, all scans would follow the same azimuth track and thus avoid image rotation in the computer to obtain image registration..

The scanning parameters chosen were a 50 micron by 50 micron square data grid. This grid size is a compromise between the spatial resolution of the film and number of data points to be handled per image. This grid size leads to about 127000 data points in each circular image. More data points per image would have proved excessive and a courser grid can always be constructed in the computer if necessary.

### 6.3 PHOTOGRAPHIC SENSITOMETRY

One of the two primary cameras was loaded with Eastman Kodak Type 2476 film for the red and blue exposures and the other camera with Eastman Kodak High Speed Infrared film type HIE for the ON-BAND and OFF-BAND exposures. All films were machine processed with sensitometric exposure strips at the head and tail ends. Four of these sensitometric strips, a head and tail for each film, type, were digitized at the same time the primary data was digitized. A D-Log E curve was derived from the digitized data, one for each film type, which relates density on the film to relative exposure. Figures 6.3 and 6.4 are the final curves used in all subsequent computer processing.

### 6.4 IMAGE REGISTRATION

It is an implicit assumption with this data processing system that the line-of-sight associated with any given pixel from one photograph is the

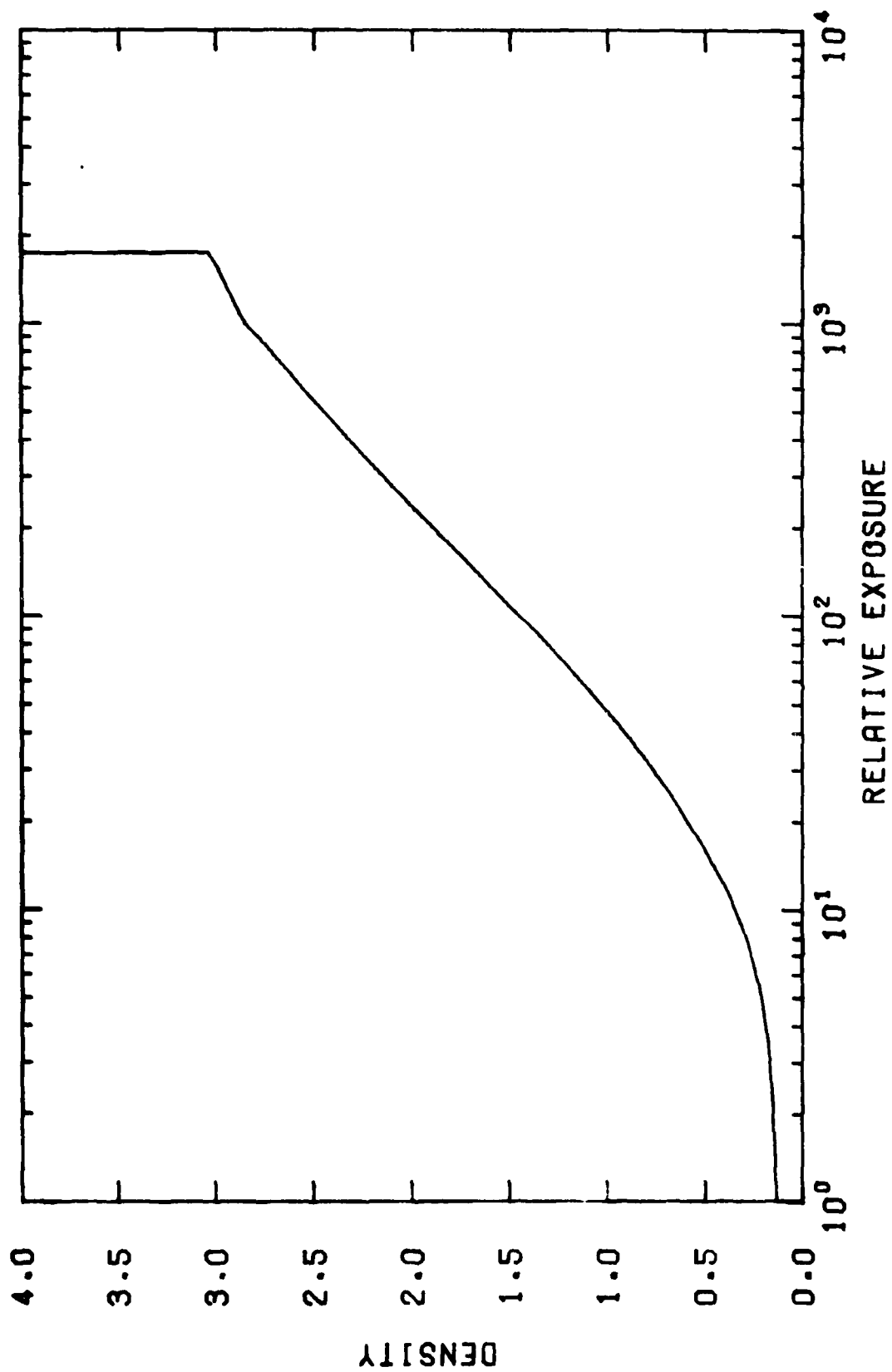


Figure 6.3. D-log E curve for the 2476 film scanned at Optronics.

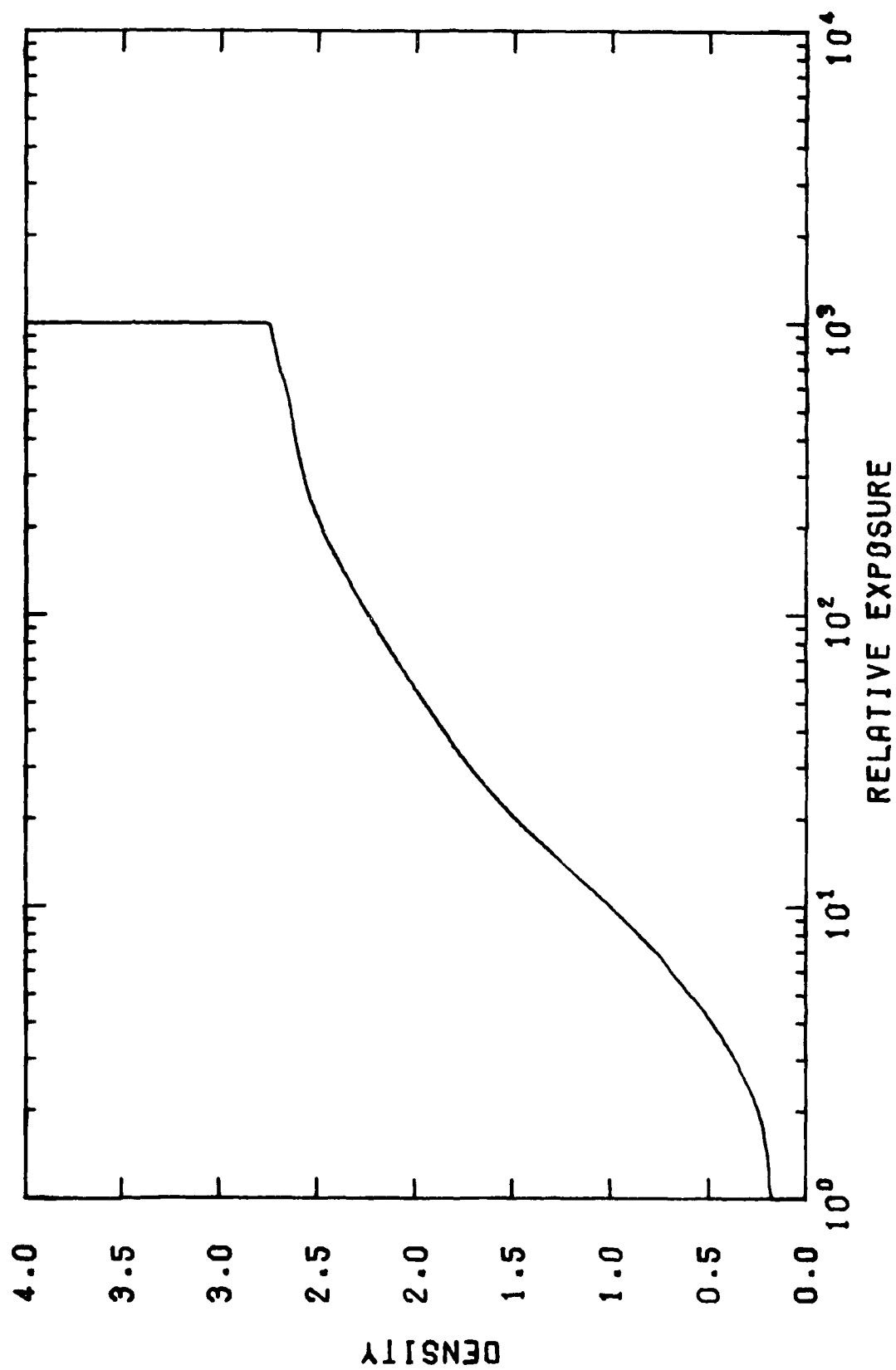


Figure 6.4. D-log E curve for high speed infrared film (HIE) scanned at Optronics.

same for all four photographs for that data set. Pictures can fail to register because of, (1) magnification, (2) translation in either or both of two directions, or (3) rotation. During set-up the magnification of the two cameras had been adjusted until they agreed within the dimensions of one pixel. Lack of register in rotation was handled by a counter-rotation of the pictures before digitization. Translation along and across the scan direction is caused by the axes of the two spherical mirrors being out of alignment. During set-up the axes were aligned by observing through the camera viewfinder a small white button (the zenith button) which had been accurately glued to the top of each spherical mirror such that a ruled cross on the button coincided with the axis of the sphere. The axes of both spherical mirrors were made vertical with a sensitive level on the mirror baseplates.

It was found using pictures reconstituted on the Optronics International P-1700 that, when the zenith buttons of a picture from the RED/BLUE/ pair was superimposed on one from the ON-BAND/OFF-BAND pair, the features of the photographs did not coincide exactly. A translation correction of a few pixels along both axes was required to bring the pictures into register. This correction was applied to all data sets.

## 6.5 FIELD-OF-VIEW LIMITATION

In Figure 6.2 it can be seen that each all-sky image occupies only the central portion of the frame. Outside of the image area appears data board information, a level, a watch, and fiducial markers. Prior to use as input data it is necessary to transfer to a secondary data tape only those pixels which pertain to the all-sky image and to refer each image to

a common point. This was accomplished by locating the scan number and data point number of the center of the zenith button and transferring those data points which fall within a square image area centered on the zenith button and extending to a zenith angle of  $85^\circ$ . This resulted in a final grid 401 scans wide and 401 data points long, a total of 160801 pixels. All data points falling within a circle of 201 pixels radius were transferred to the secondary tape unchanged while all pixels falling within the square but outside the circle were transferred as zero. Figure 6.5 is a typical image reconstructed from the data after such a transfer. There are just under 127000 pixels within the circular image. The pixels outside the circle were retained to provide scans with an equal number of digital data points, a procedure which simplifies the computer coding.

## 6.6 BLUE SKY FLAGGING

The digitized data from only one of the four primary data photographs is used to establish the radiance of the cloud base, the data from the red filtered photograph. Before this digital data can be used in a final pulse shape calculation, each pixel must be identified as one belonging with a clear line-of-sight into blue sky or one which relates to a cloud base. This was accomplished by entering the data from both the red and the blue pictures into the computer memory, taking the blue/red ratio for each pair of pixels, (one blue, one red) and deciding on the basis of the absolute value of the ratio whether the pixel related to blue sky or cloud base. Actually this was done a scan at a time to conserve computer memory space. In a preliminary computer run a histogram was constructed of the probability of occurrence for all values of blue/red ratio separated into 1000 bins. As



AD-A087 242

H S S INC BEDFORD MASS

F/8 B/5

TIME DELAY OF TERRESTRIAL LIGHT PULSES PROPAGATING THROUGH CLOUD--ETC(U)

JUL 80 H S STEWART, L B WOOLAVER

F08606-77-C-0024

UNCLASSIFIED

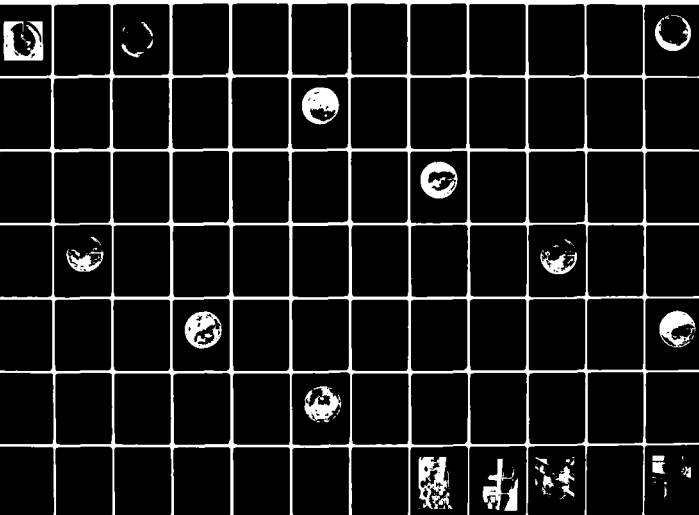
HSS-B-058

AFTAC-TR-80-23

NL

2 OF 3

AD-A087242



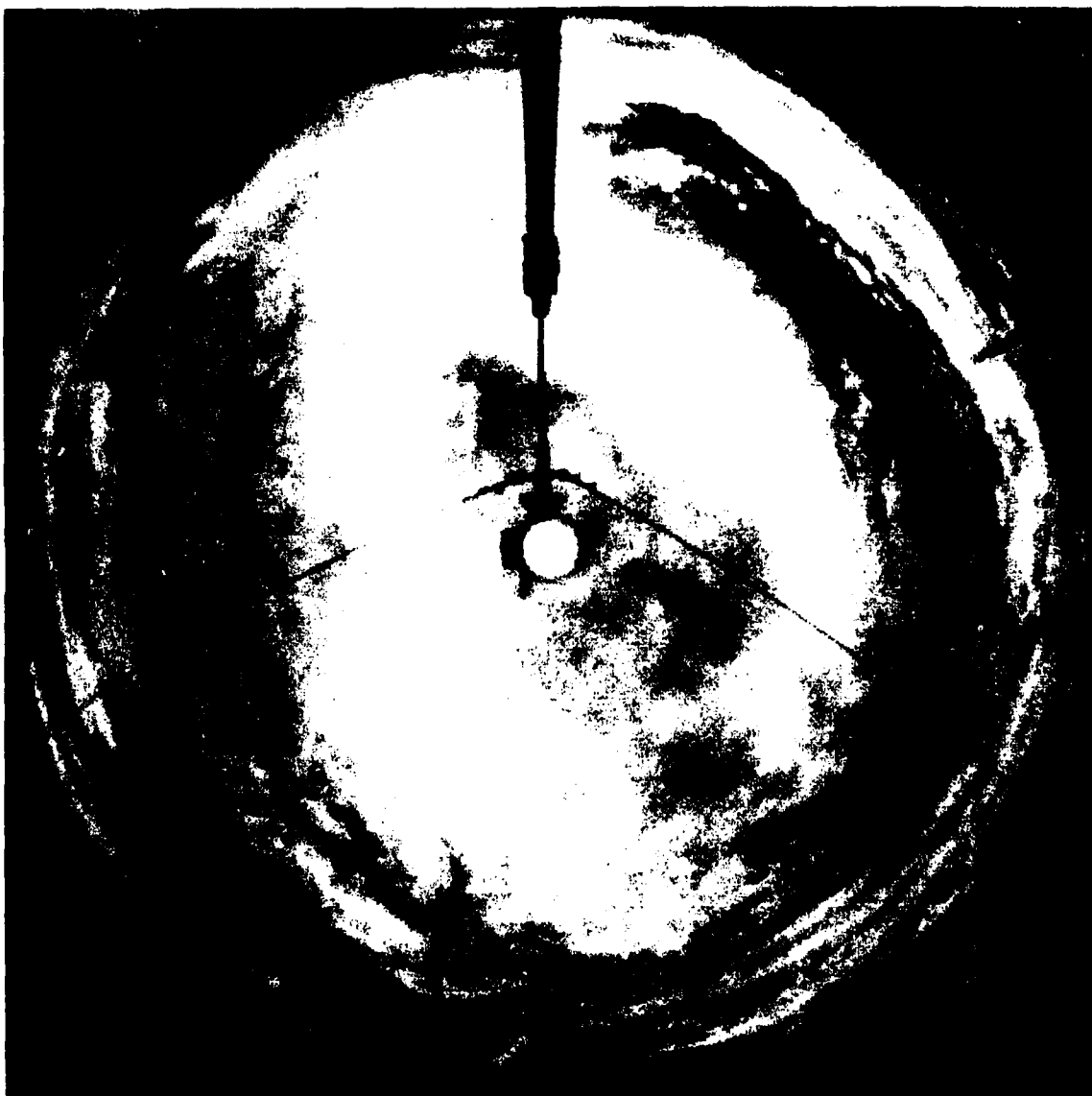


Figure 6.5. All sky image reconstructed from digital data.

expected this histogram exhibited a double peak with very few of the ratio values falling in the vicinity of ratio equal to one, values of ratio lower than one belonging to cloud and higher than one to blue sky. In the computer which produced the input to the final calculations the red radiance was transferred from input tape to output tape unchanged if the blue/red ratio indicated a cloud pixel and as a negative radiance if the ratio indicated blue sky. In all subsequent calculations the blue sky pixels are detected by a sign check on the radiance value.

As a check on this procedure for blue sky identification the flagged digital data was computer processed to generate a two density mask and put the results on magnetic tape. In this mask all blue sky pixels were given a uniform high density and all non-blue sky pixels a uniform low density. When the digital data was written on photographic film at Optronics and processed, the resulting film becomes an actual mask showing the blue sky regions. Figure 6.6 shows the mask produced by the blue sky flagging procedure described above. This mask applies to the data photographed shown in Figure 6.5.



Figure 6.6. Two density level mask showing locations of blue sky as identified by blue/red ratio.

## SECTION 7

### EXPERIMENTAL RESULTS

#### 7.1 GENERAL COMMENTS

This section presents results obtained from the experimental data by the procedures given above. The bulk of the material in this section concerns the predicted pulse shapes derived from the cloud photographs. Following these data are the two sections which present (1) estimates of the centroid of the cloud radiance and (2) the results obtained when an estimate of the earth's albedo is included in the calculations.

#### 7.2 PREDICTED LIGHT PULSE SHAPES

The predicted pulse shapes presented in this section are those obtained by applying the theory and procedures given above to the cloud data recorded at the Kennedy Space Center. All of the cloud conditions analyzed fall into the general category of "broken cloud". The weather which prevailed during the six week period of data recording provided no occurrence of a solid overcast without rain (the experimental equipment was not intended to operate in the rain). This is indeed unfortunate because broken cloud is more difficult to analyze and less amenable to comparison to computer models. The results presented were selected as the best representation of the occasions on which data from all cameras were available.

The predicted pulse shapes which follow are arranged by date and time as the data was recorded. For each date and time seven pulse shapes are given the first of which places the assumed satellite position along the line to the sun's position when the data was recorded. The remaining six pulse shapes were derived from the same recorded

data but where the line of sight to the assumed satellite position has one of three elevation angles and one of two azimuth angles. Each group of seven predicted pulse shapes is preceded by a photographic print of the red filtered sky data used to derive the pulse. The pulse heights have all been normalized to unity.

All of the data presented in this section with two exceptions were derived by the working equations which use an estimated cloud thickness as opposed to thicknesses derived from the data. The two exceptions are for 2 August 1977 at 1415 EDT and 2 August 1977 at 1416 EDT, the data from two data sets from the same data run. In these cases the cloud thickness was derived from the data.

Since all of the figures in this section are self-explanatory, they have not been numbered or captioned.

### 7.3 TIME DELAYS

The intent of the experiments reported here was to deduce the time dependent probability of delay in transit of photons originating from an isotropic source on the ground and received by satellites at various positions in space. Photons making direct (unscattered) passage from source to receiver would have zero time delay. Under these conditions the predicted light pulse shapes presented below would represent true delays. Unfortunately, the quality of the time base is in question; however, errors which exist in the absolute time of delay are constant for any set of seven curves relating to one time of data acquisition. This allows relative delays between lines-of-sight to be compared for the data reduced here because no direct lines-of-sight are involved. In addition, if the assumption is made that there is some range of "reasonable" shapes for the pulses, then "reasonable" zero times can be selected for the nine sets of curves and the data then compared to direct line-of-sight timing. This has been done. These concepts are elaborated in the following paragraphs.

When the on-band/off-band pictures were taken the exposure time was 1 second. There is evidence in the data that this exposure was sometimes erratic by amounts as great as  $\pm 30$  percent of the average. The effect of this erratic behavior can, at worst, multiply or divide the true on-band/off-band ratio by as much as 1.7. There seems to be no specific information in the data that can lead to a correction of this possible error.

One of the authors (HS) has inspected each set of seven light pulse shapes and decided on a most probable correct zero time. This was done without reference to any of the other eight sets and, once selected, these probable correct zero times have not been changed. These selected probable zero times are believed to be within  $\pm 5 \mu\text{sec}$  of the true zero times. The selected zero times are given in Table 7.1.

Table 7.1. Probable Correct Zero Times

DATE	TIME	TIME ON GRAPH OF CORRECT ZERO
July 28	1237	- 7 $\mu\text{sec}$
Aug 1	1622	- 5 $\mu\text{sec}$
Aug 2	1415	+ 27
Aug 2	1416	+ 7
Aug 3	0935	+ 12
Aug 3	0937	+ 5
Aug 4	1325	- 10
Aug 6	1300	- 15
Aug 7	1056	0

The effects of the clouds in the geodetic technique under study can be shown by convolving power pulse shape characteristic of the sources in question with the light pulse shapes presented here. The light pulse shapes shown here are those which would be observed with an isotropic delta function source. Some conclusions of the cloud effects can be reached by assuming the source to be a delta function and asking what the amount of cloud induced delay is at the time when the pulse reaches some fraction of its maximum value. This has been done for all 63 predicted pulse shapes. For the two sets of seven shapes appropriate to 3 Aug '77 a value of 60 percent of maximum was timed. This avoided decisions arising from the double pulses involved. All other curves were timed at 80 percent of maximum. The resulting times are presented graphically in Figure 7.1. In this figure the zero of time is that selected by the assumption of reasonable shapes described above. The crosses (x) represent the delayed time for the case of satellite in the direction of the sun. The altitude and azimuth of the sun is given beside the point. The circles (o) represent in descending order on the graph the delay times for 20°, 40°, and 60° elevation at azimuth 0° (north) and 60°, 40°, and 20° elevation at azimuth 180° (south). The repeatability of the whole process carried out here may be judged by inspection of the graphs for 2 August and for 3 August. For each day the results of two completely separate data runs are presented. The original pictures were taken one minute apart on 2 August and two minutes apart on 3 August. In the 2 August data reduction the cloud base height was measured and the cloud thicknesses were calculated using the radiance of the cloud base as an input. In the case of the 3 August data the cloud thickness was assigned. The close agreement each day between the plots of time delays for data taken a minute or two apart indicates that the overall system of data acquisition and reduction is repeatable with little error.



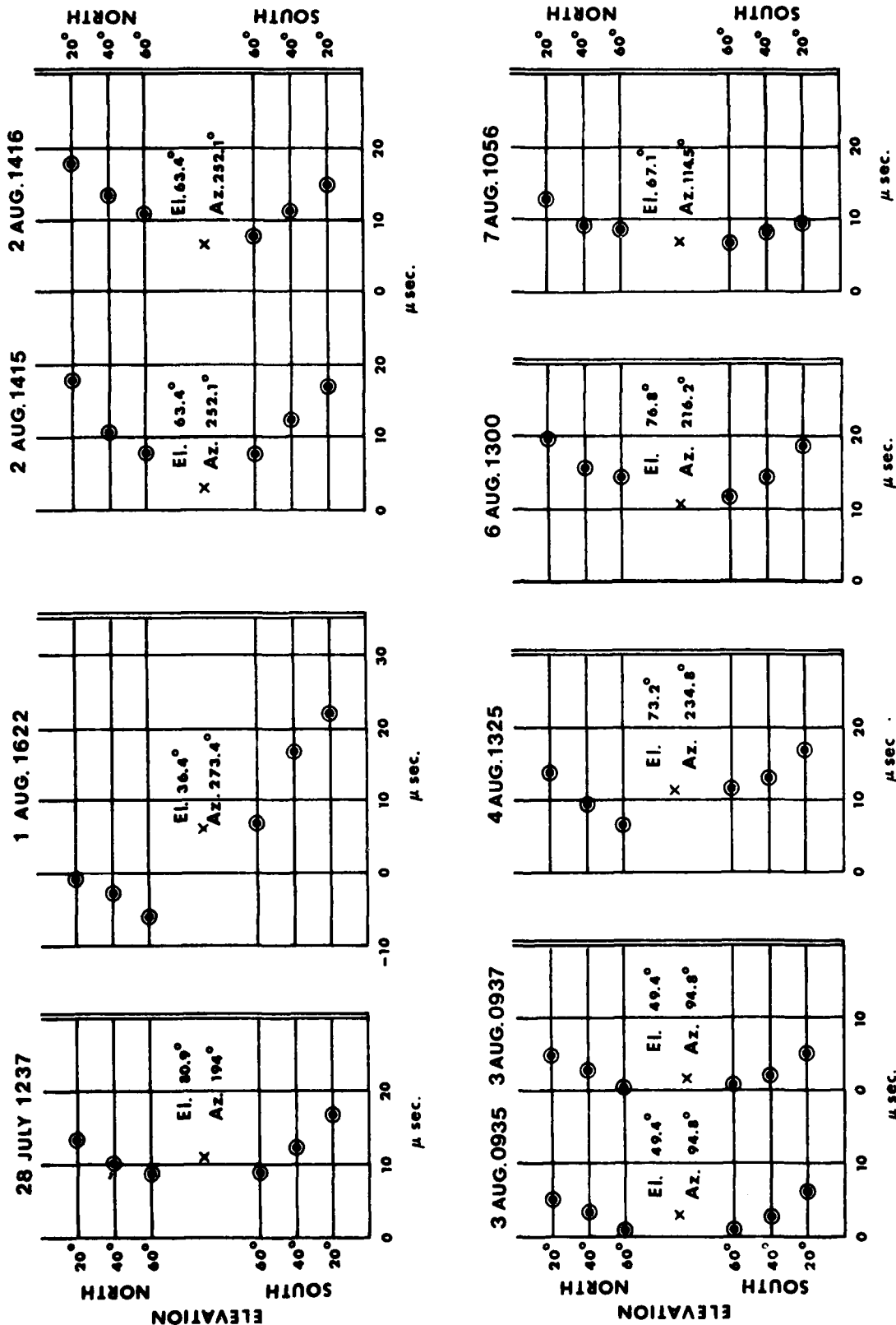


Fig. 7.1 TIME DELAYS (x) DELAY TIMES IN DIRECTION OF SUN. CIRCLES (o) OTHER DIRECTIONS AS SHOWN ON ORDINATE.

#### 7.4 CENTROID OF RADIANCE

Section 5.7 developed the working equations necessary to derive the centroid of radiance one would observe from a position in space if the cloud conditions which prevailed were illuminated by an isotropic source at the location of the camera. These equations lead to the  $x$  and  $y$  coordinates in the image plane in pixels (Equation 5.16) or the  $X$  and  $Y$  coordinates on the top of the overcast in kilometers (Equation 5.22). Table 7.2 presents the results of the computation for six cases.

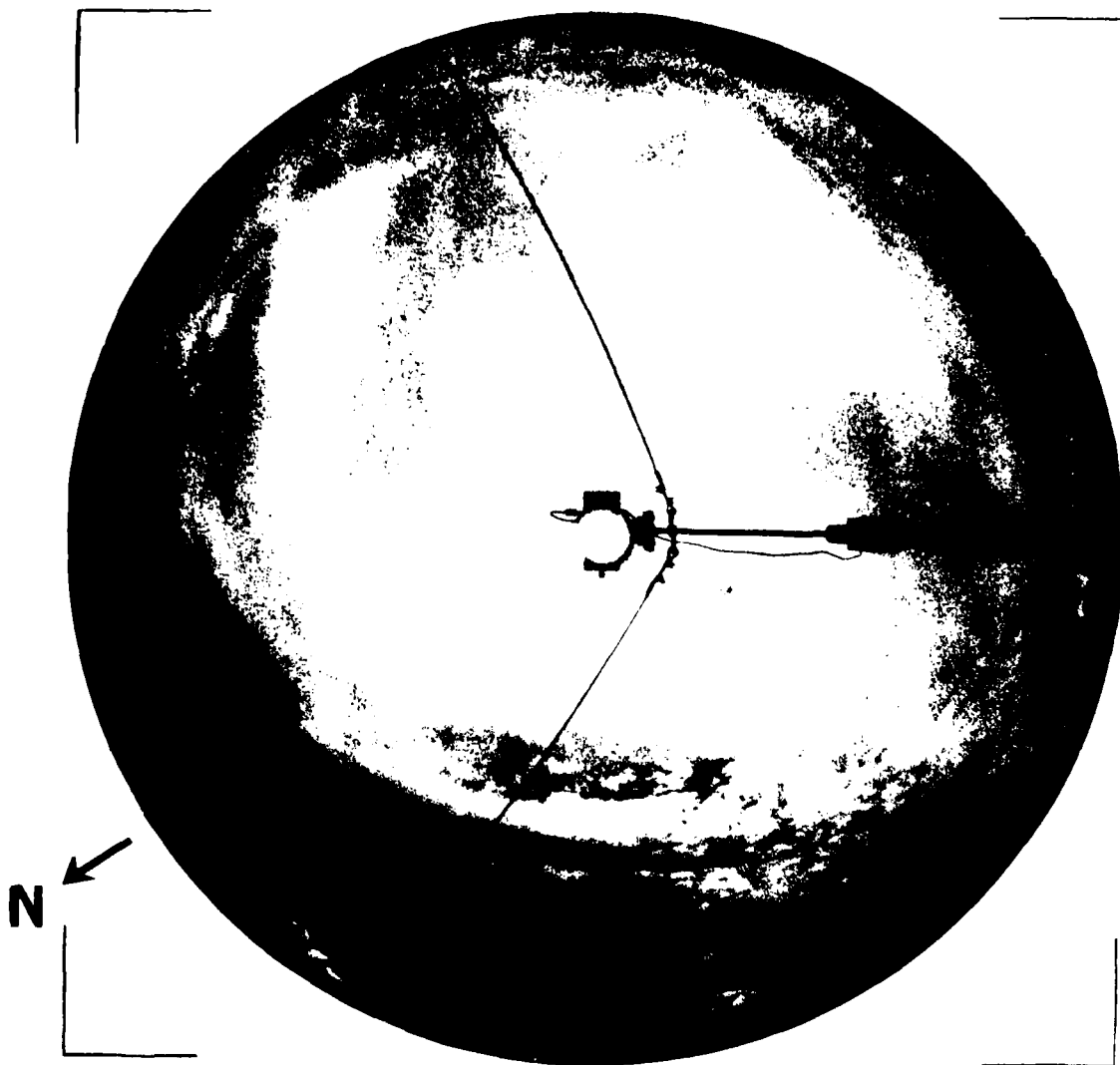
Table 7.2 includes the page number of a photograph which illustrates the cloud conditions which prevailed for each of these results. The coordinates apply to these photographs with upper right quadrant the  $+x$  and  $+y$  (or the  $+X$  and  $+Y$ ) quadrant and the remaining quadrants assigned in the normal way. It is possible to plot the image plane coordinates on the reference photographs knowing the diameter of the photographs to be 401 pixels. If this is done, great caution should be used in drawing conclusions from the results. The photographs illustrate the cloud conditions that prevailed but, in no way, represent the conditions of cloud illumination that were assumed for the centroid calculations. The photographs were taken with the clouds uniformly illuminated by the sun. The centroid coordinates apply to an isotropic radiation source located at ground level underneath the clouds. For a perfectly uniform overcast this mode of illumination would result in the centroid of radiance appearing directly over the isotropic source. It is not surprising all of the centroid locations given in Table 7.2 fall reasonably close to the zenith.

Table 7.2. Coordinates of Radiance Centroid

DATE	TIME	Image Plane		Top of Overcast		Ref. Photo
		x (pixels)	y (pixels)	X (km)	Y (km)	Page
8/1/77	1622	+8.8	-41.0	+0.86	-1.71	109
8/1/77	1623	+10.3	-59.7	+1.20	-2.89	109
8/2/77	1415	+13.8	+0.6	+0.76	+0.01	117
8/2/77	1416	+16.6	+2.3	+1.15	-0.01	125
8/3/77	0935	-7.5	+20.9	-0.11	+0.36	133
8/3/77	0937	-5.7	+18.7	-0.15	+0.38	141

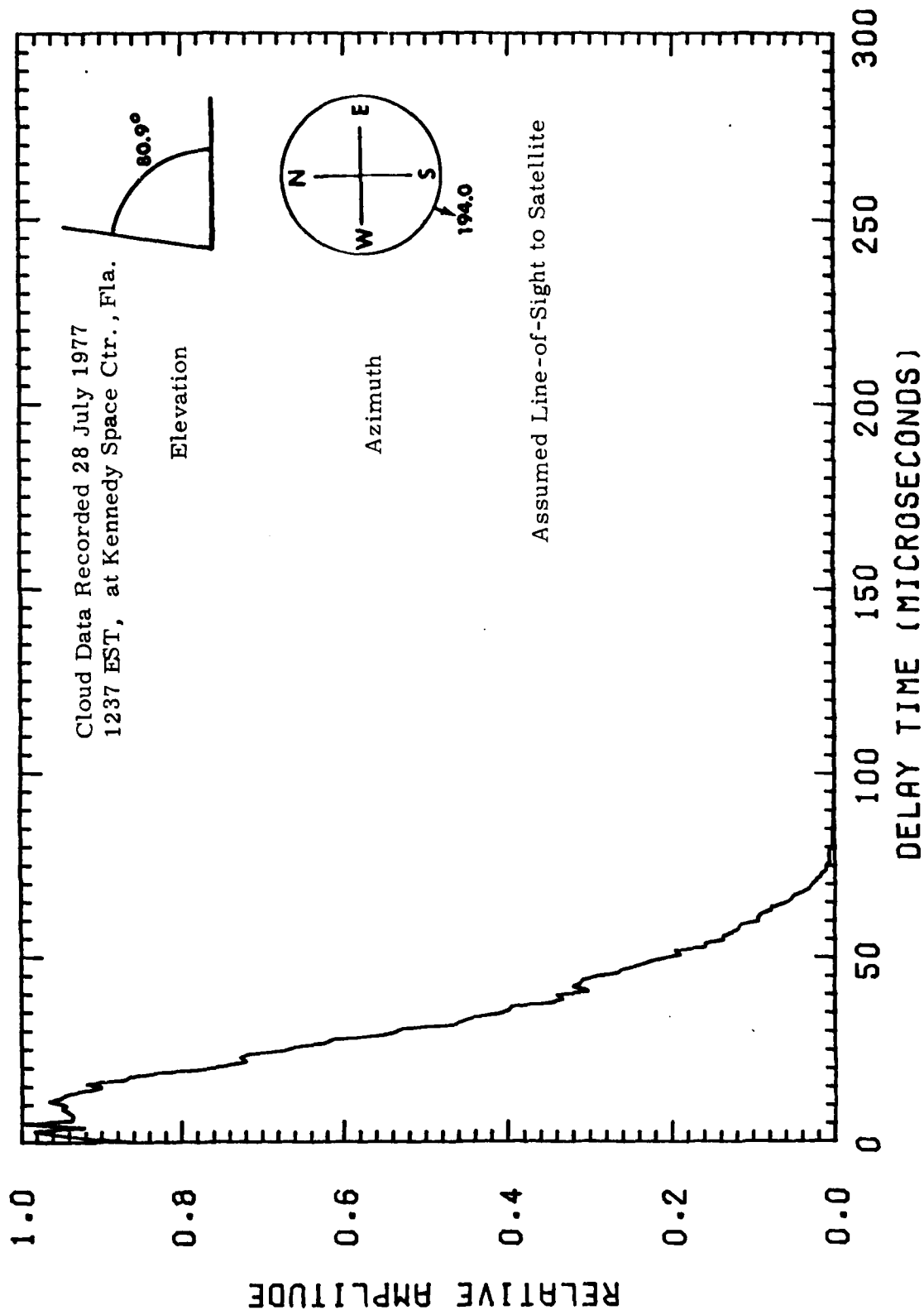
## 7.5 EFFECT OF EARTH ALBEDO

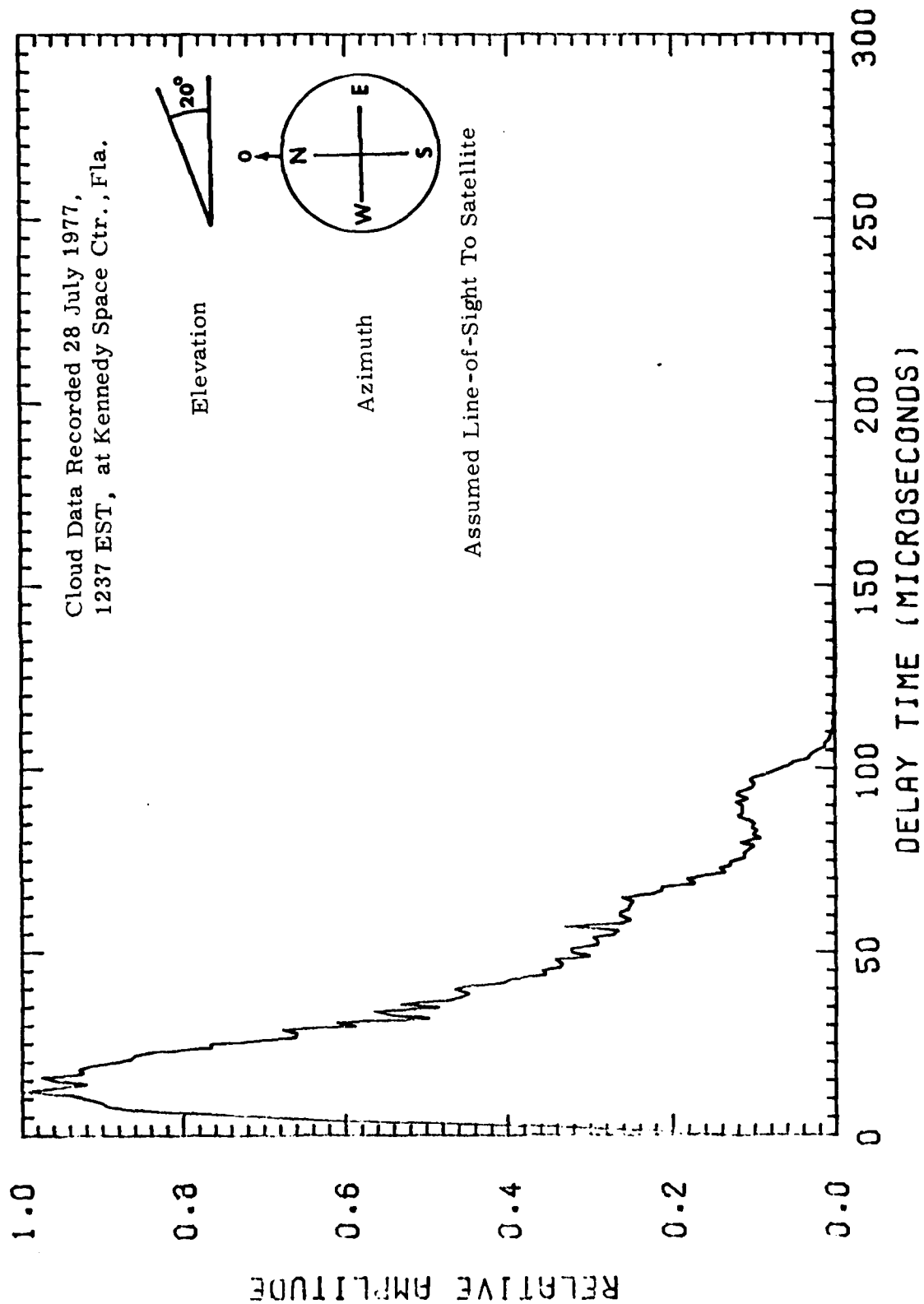
It was pointed out in Section 5.8 that the work presented in this report assumed an isotropic source radiating into the upper hemisphere. Equation 5.23 developed in that section was evaluated for a single case to estimate the magnitude of the error introduced by this assumption. The data from 8/2/77 at 1414 EST was used for this calculation using the worst-case ground reflectivity of unity. The results indicate a potential error of 20 percent in the coupling coefficient. For more realistic values of ground reflectivity the potential error was considered negligible in comparison with other error sources.

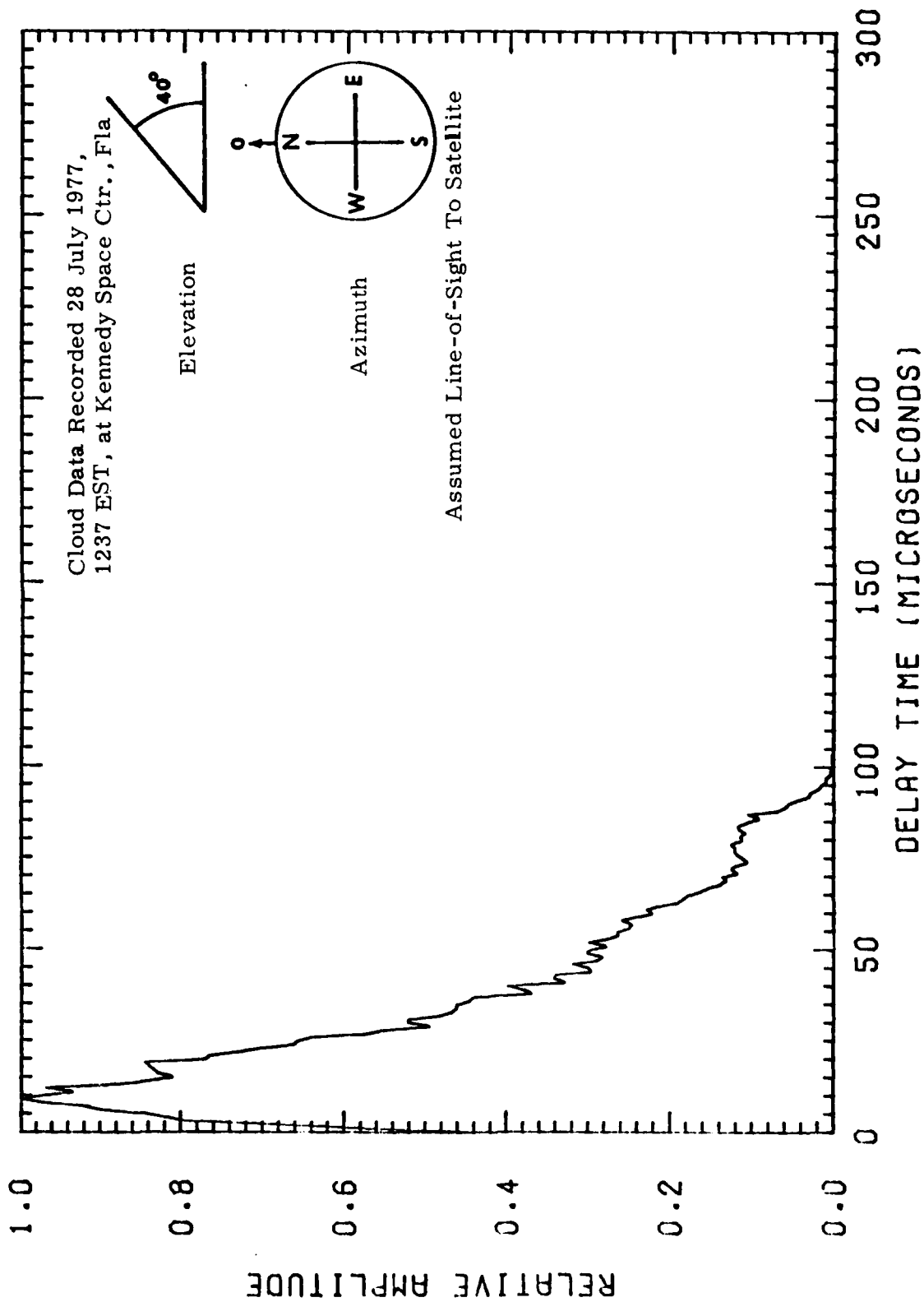


Date 28 July 1977

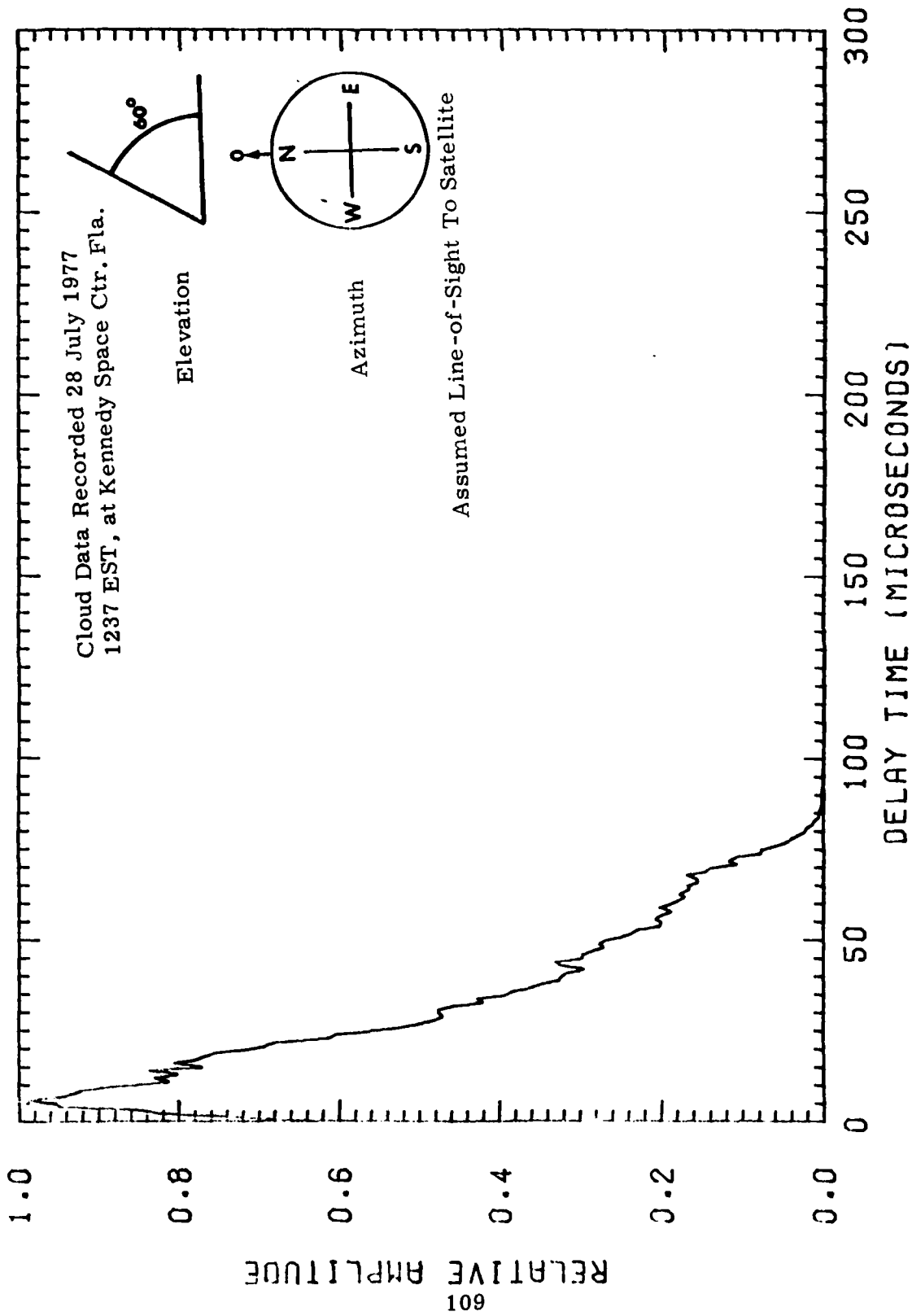
Time 1237 EST

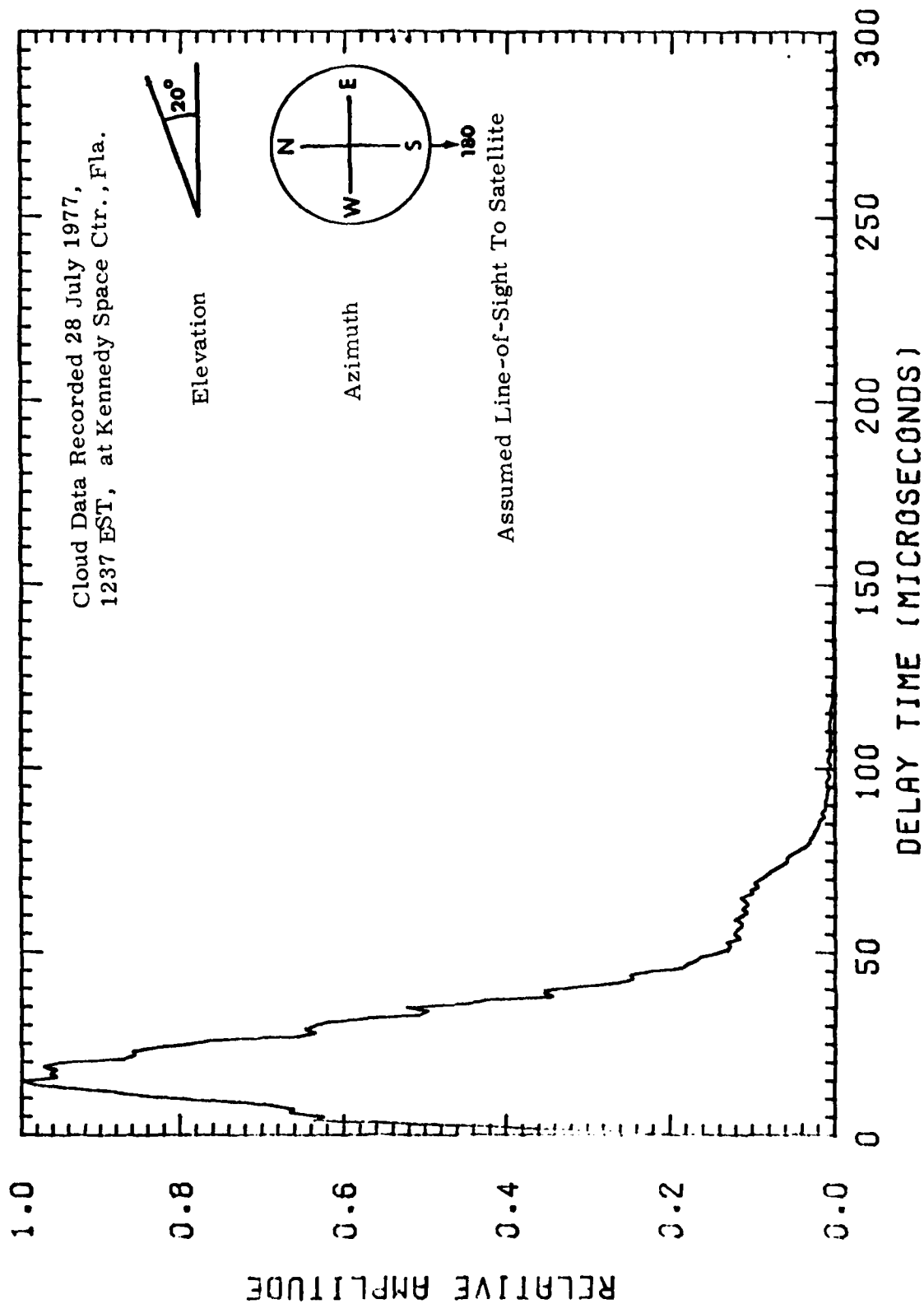


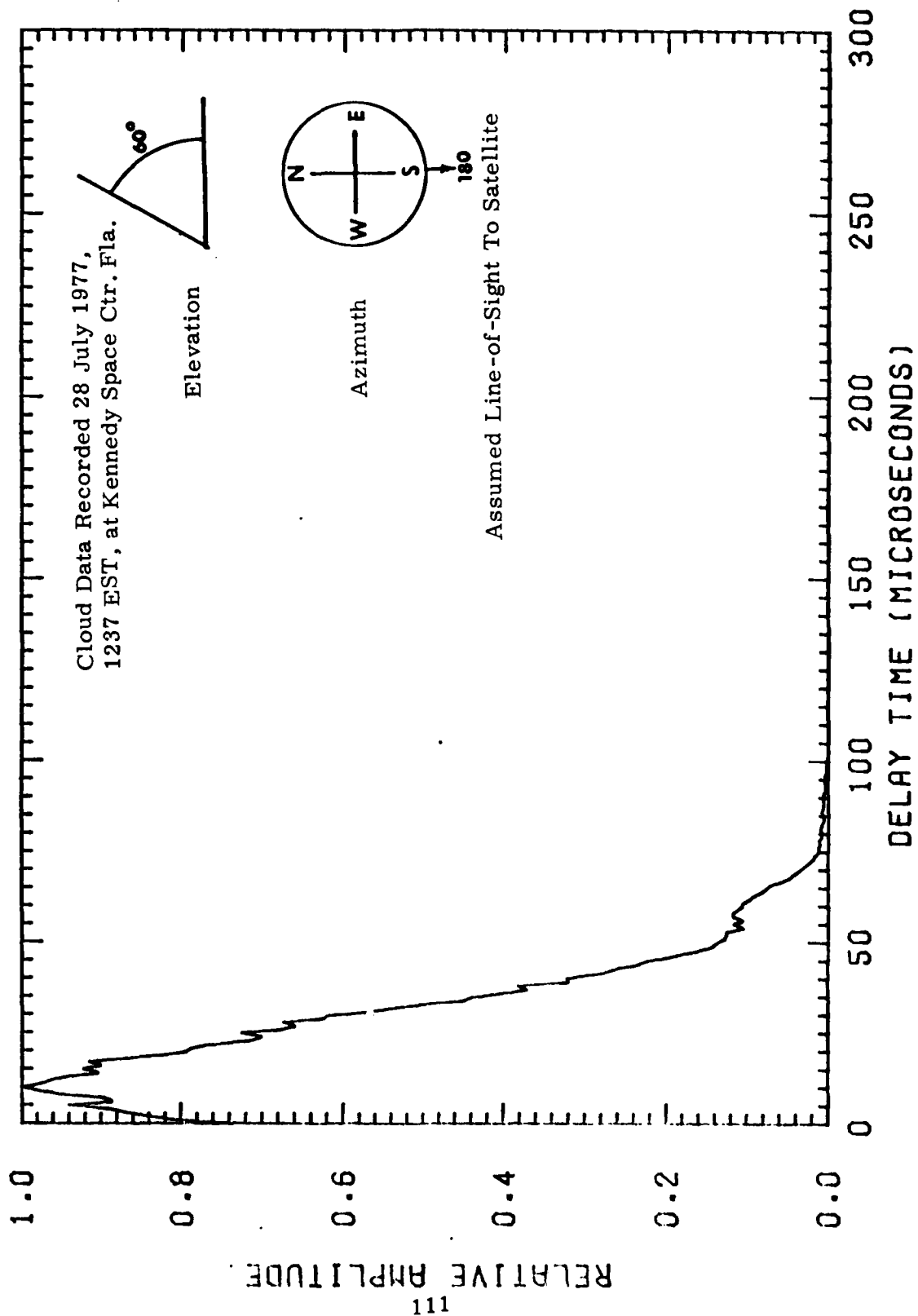


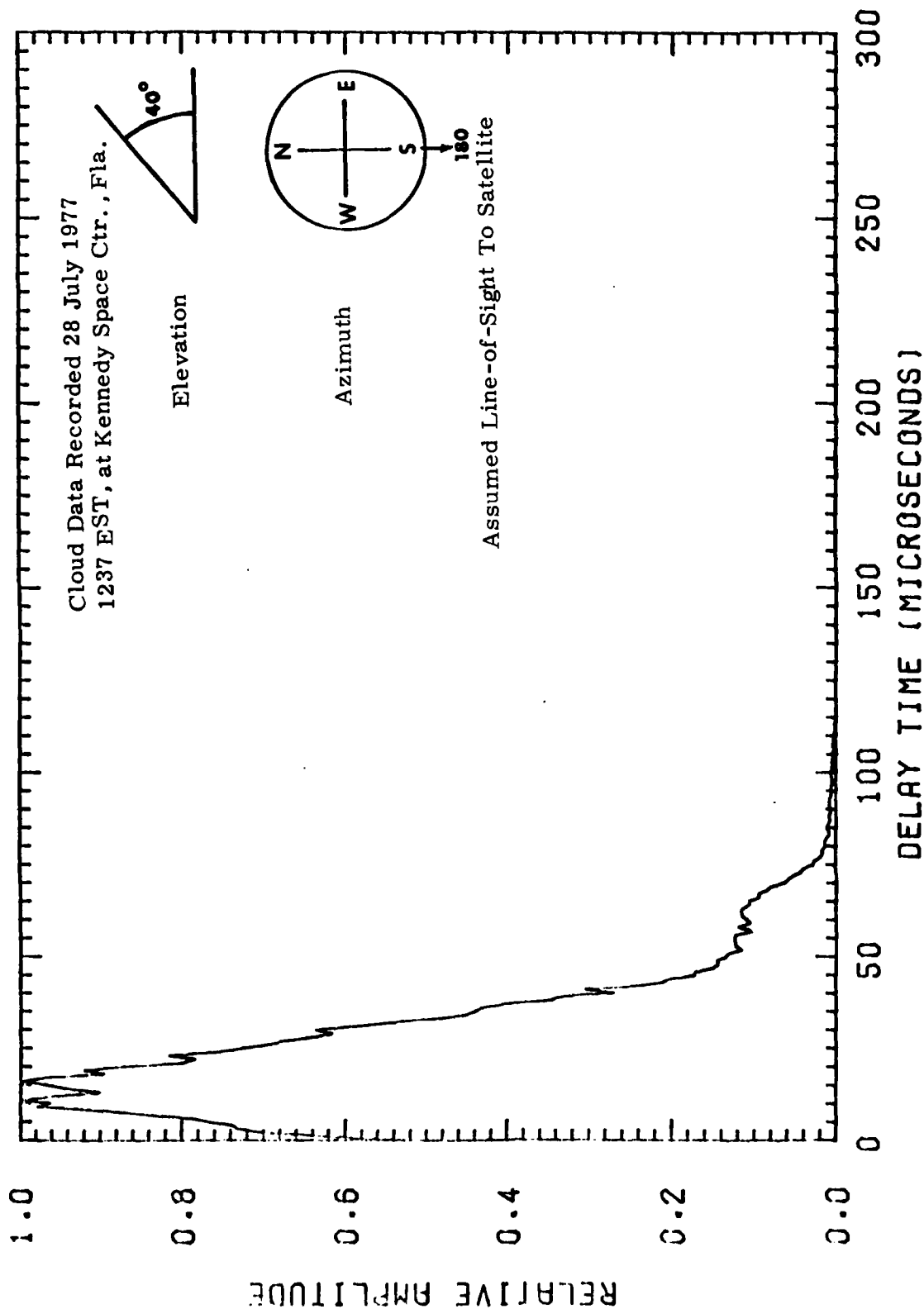


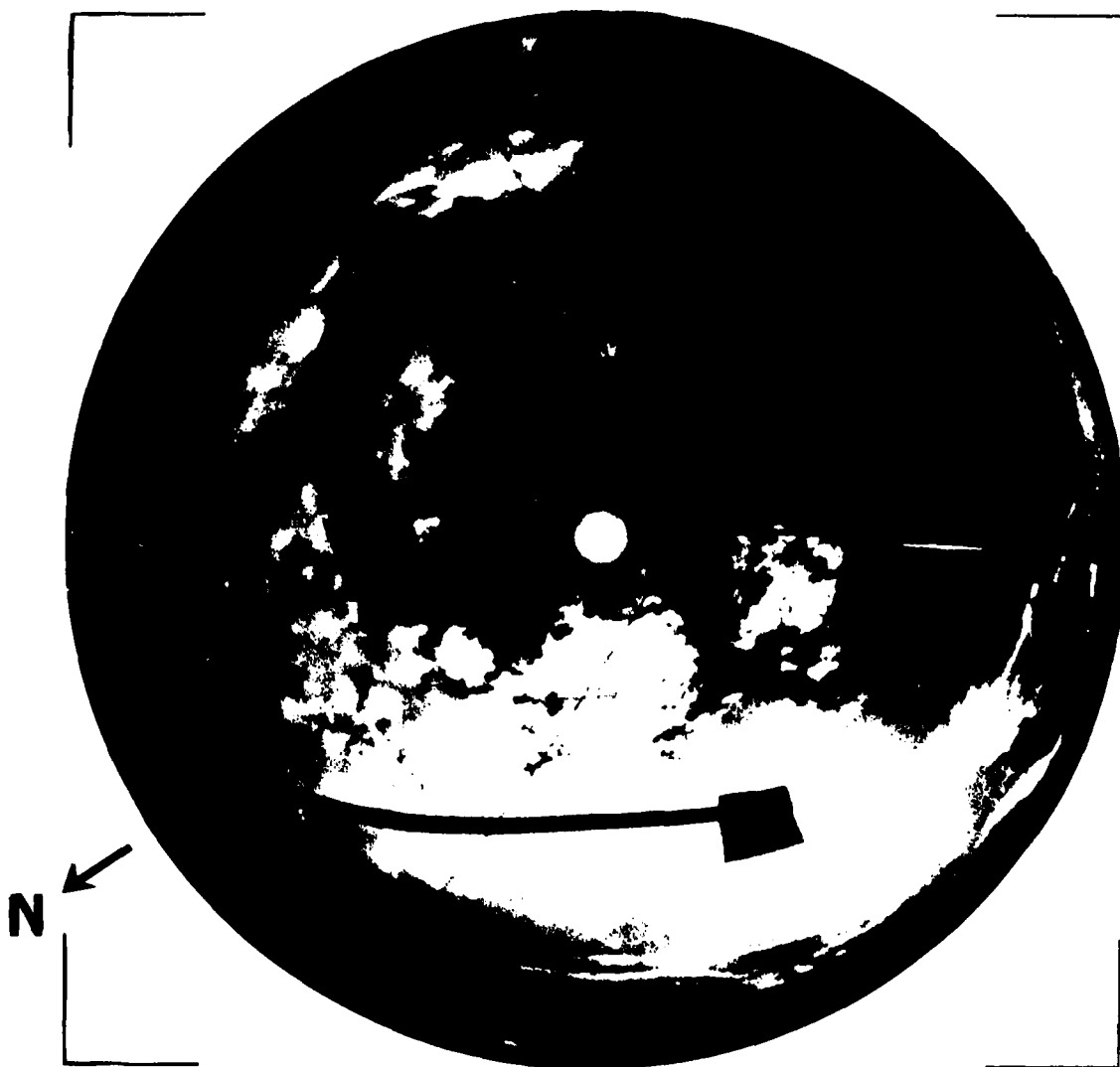






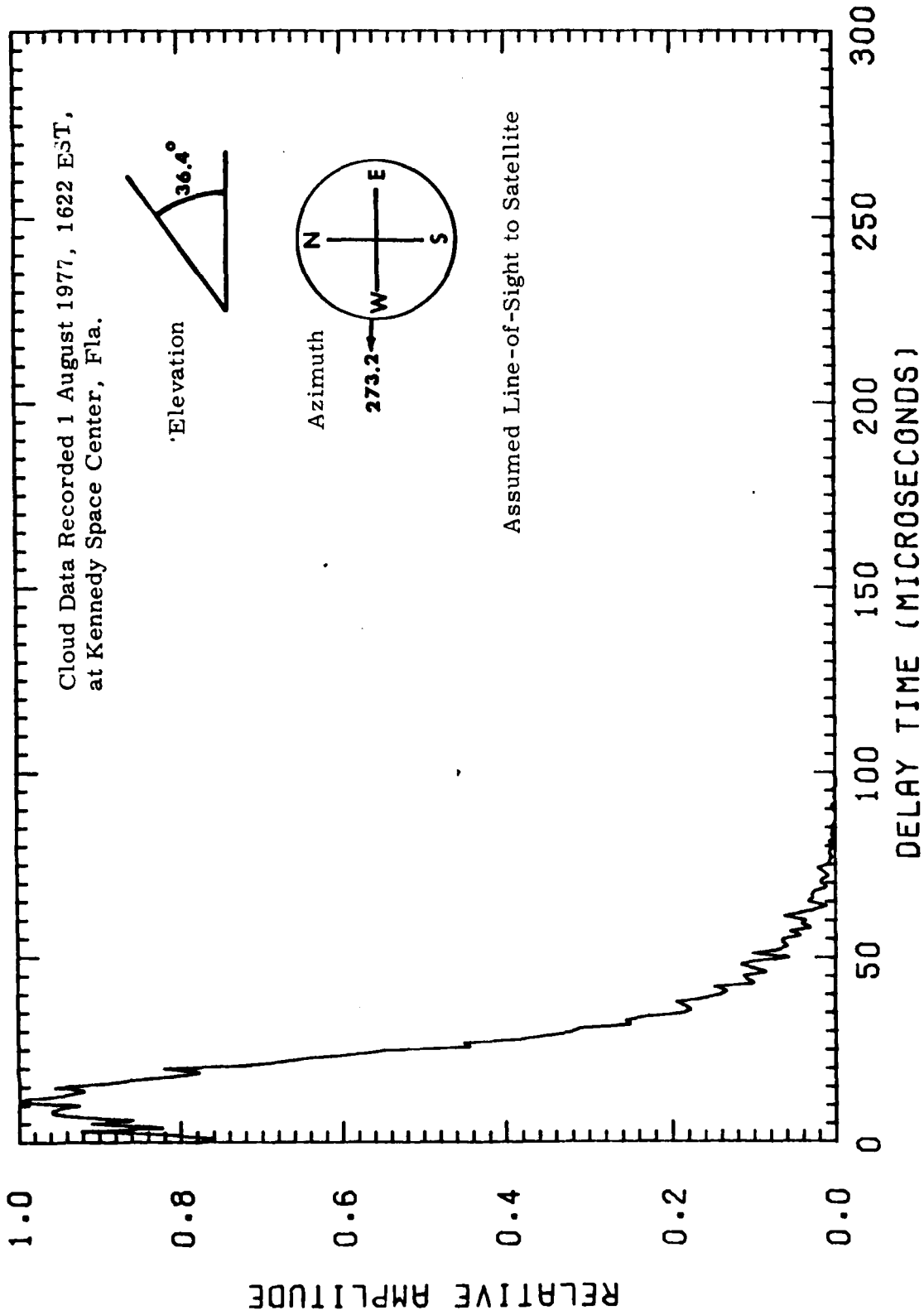


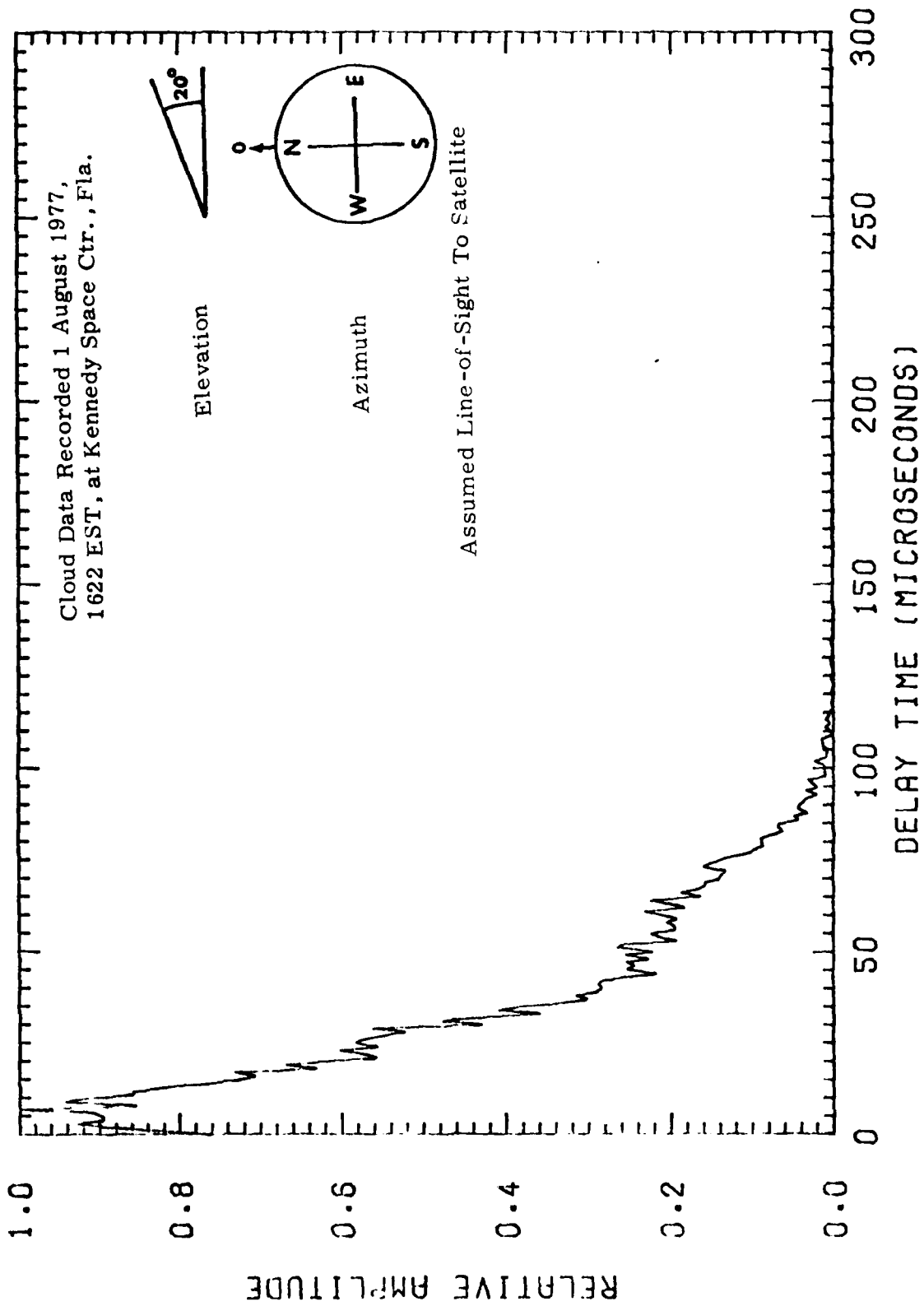


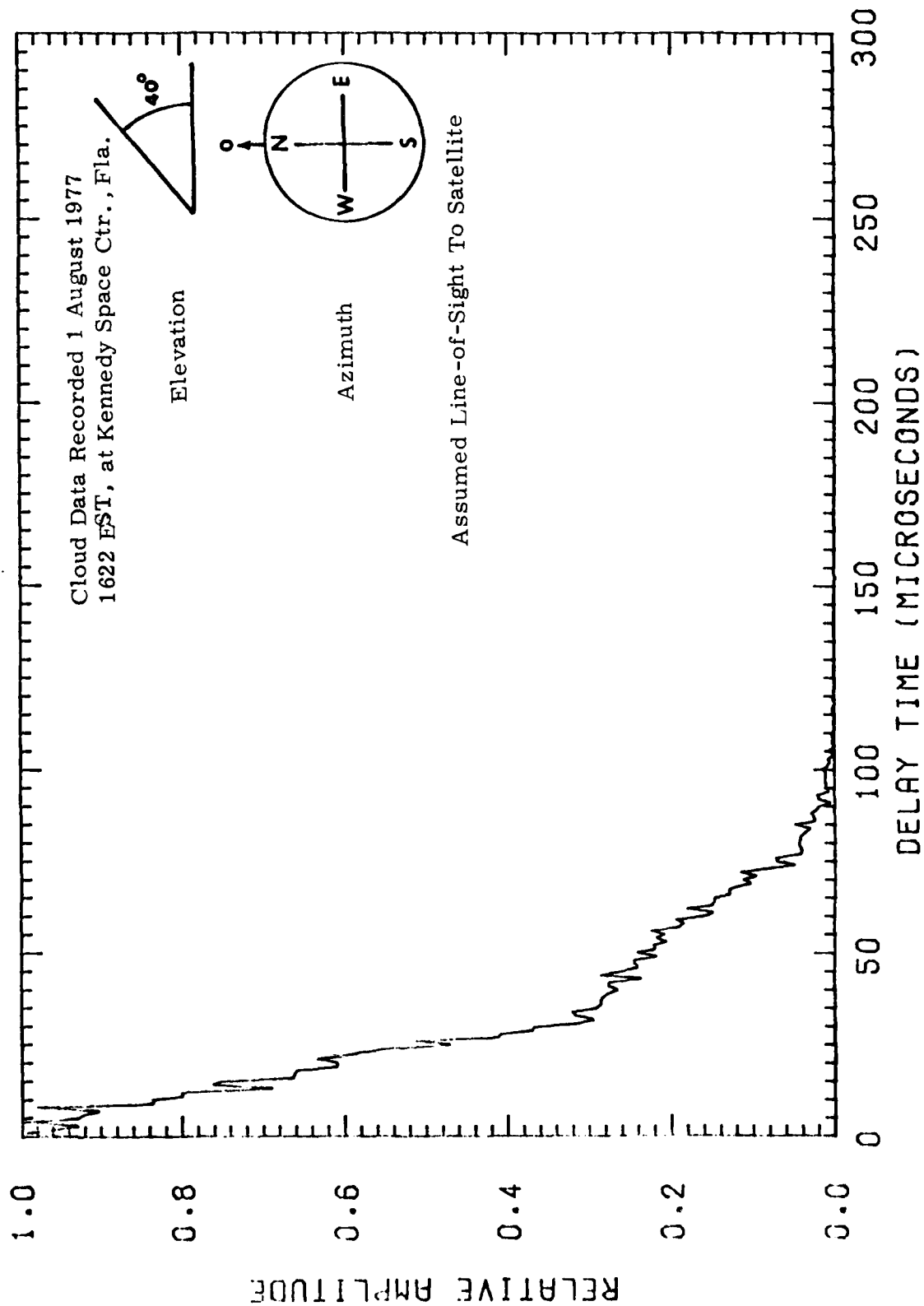


Date 1 August 1977

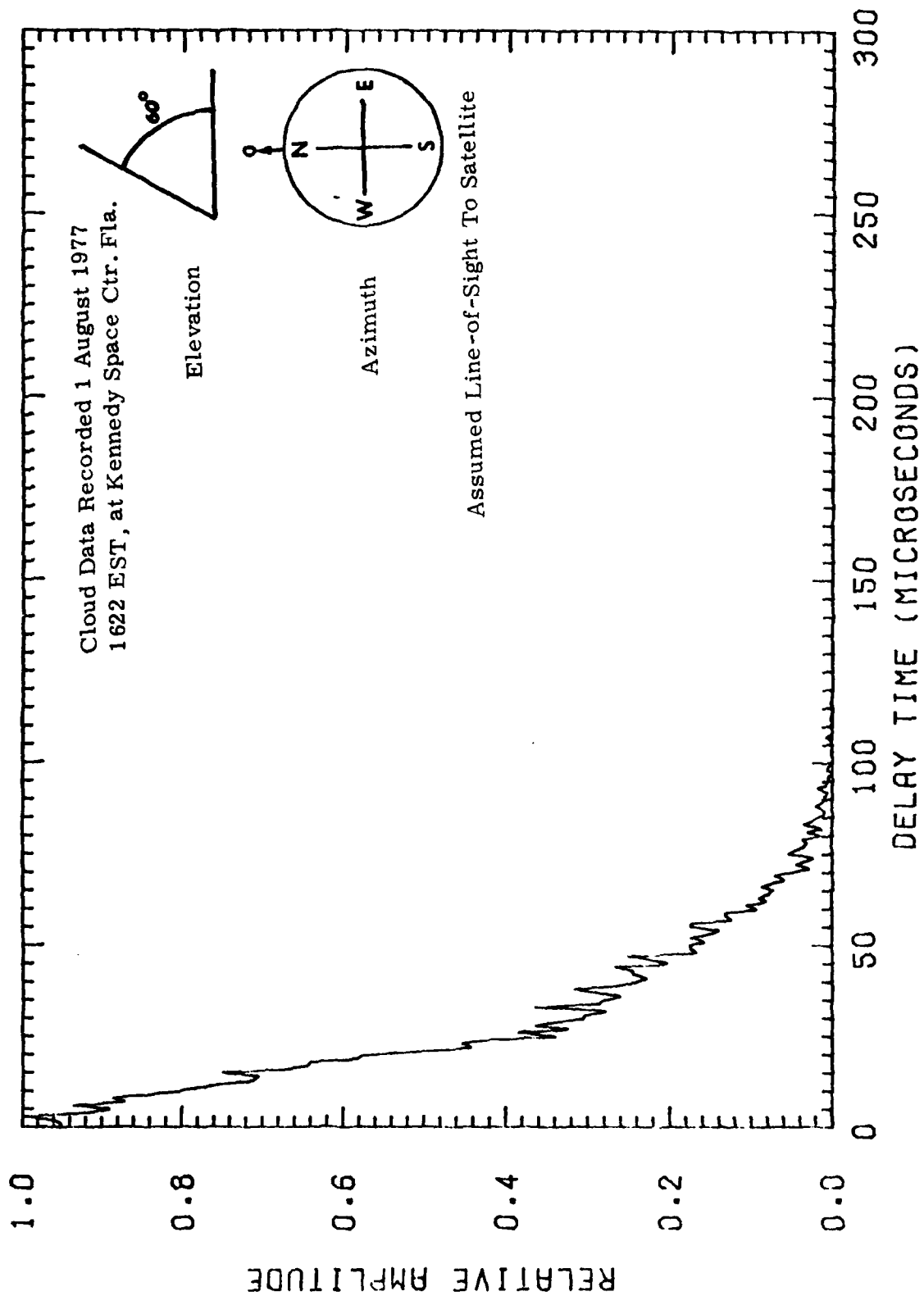
Time 1622 EST

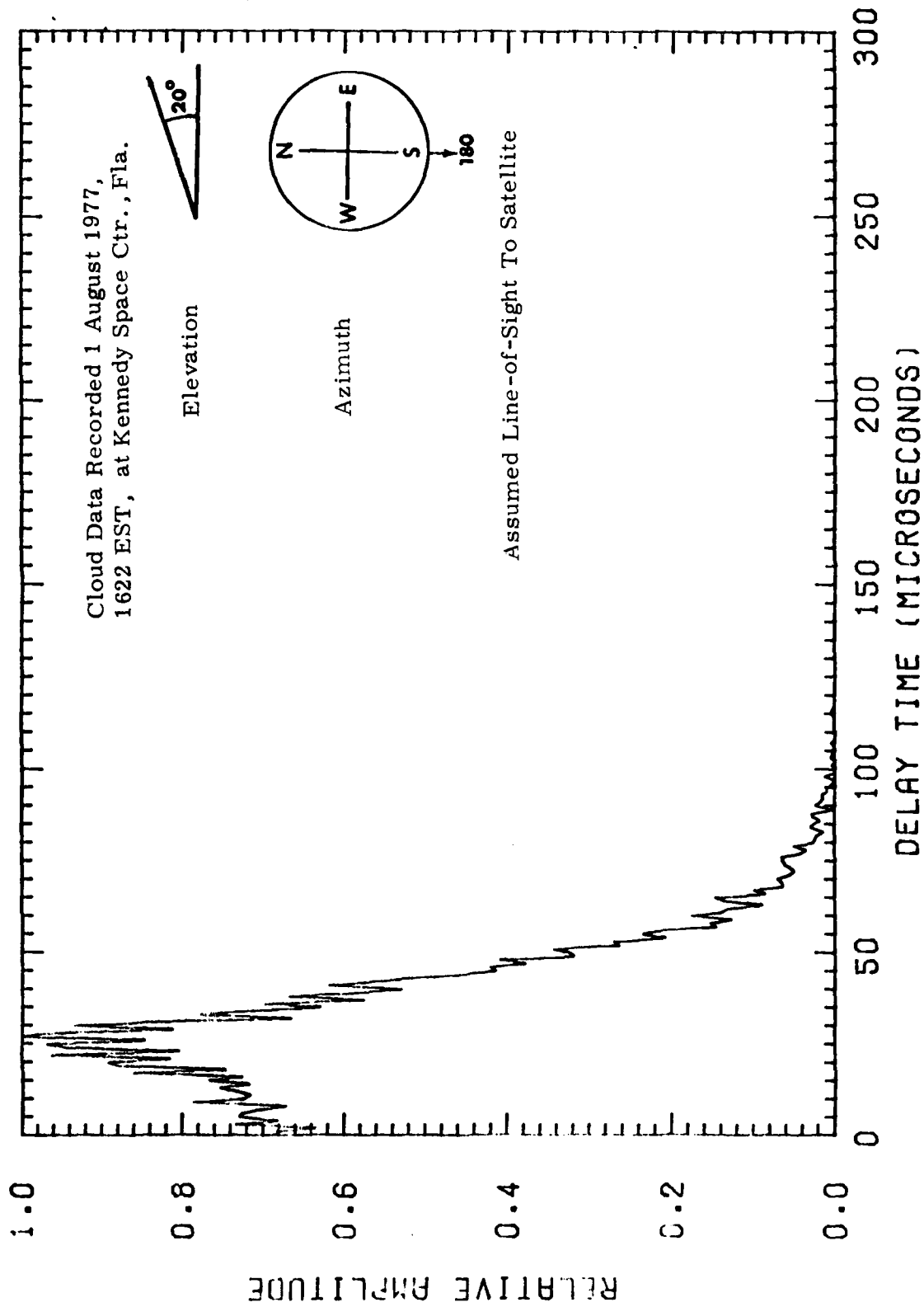


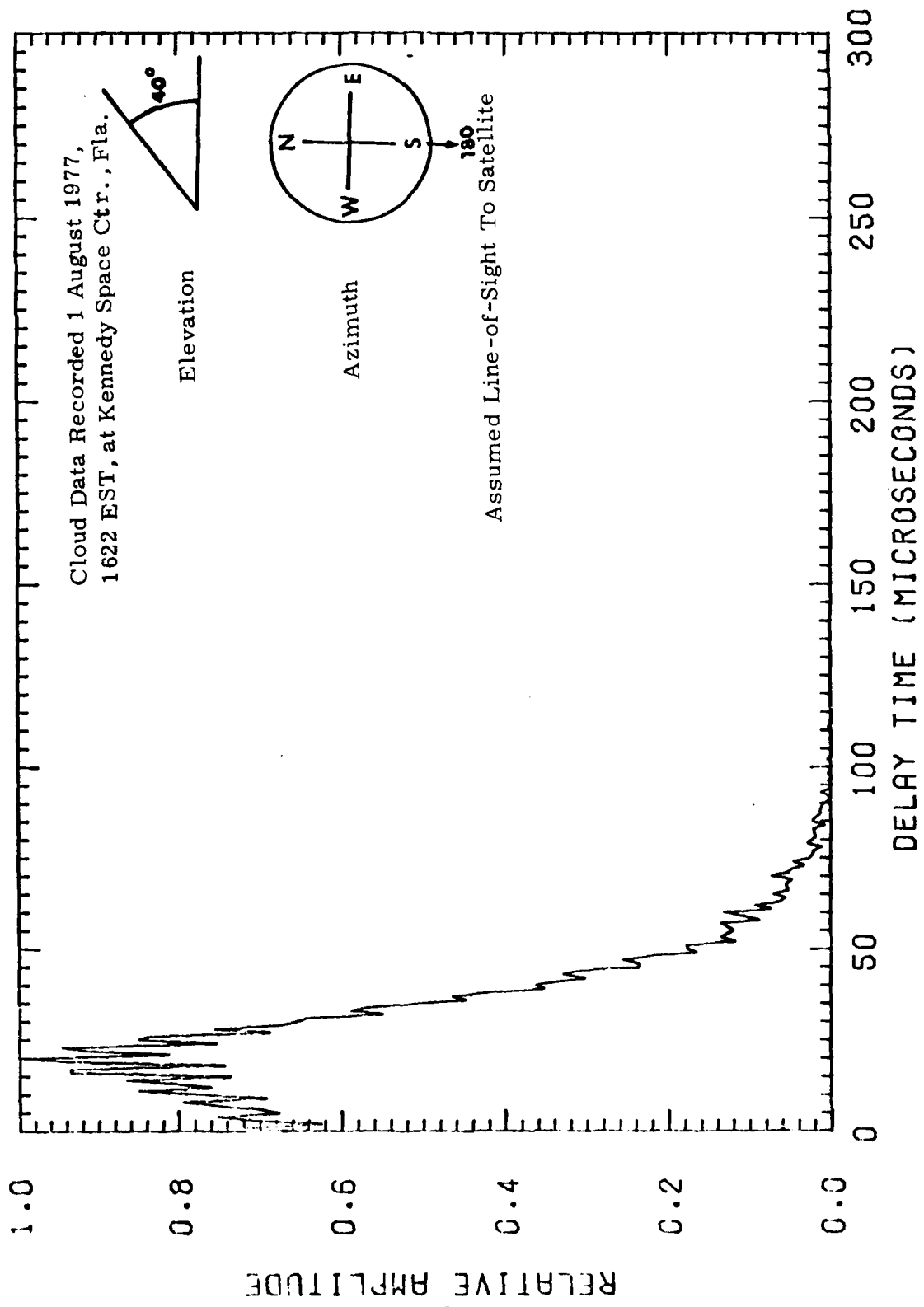


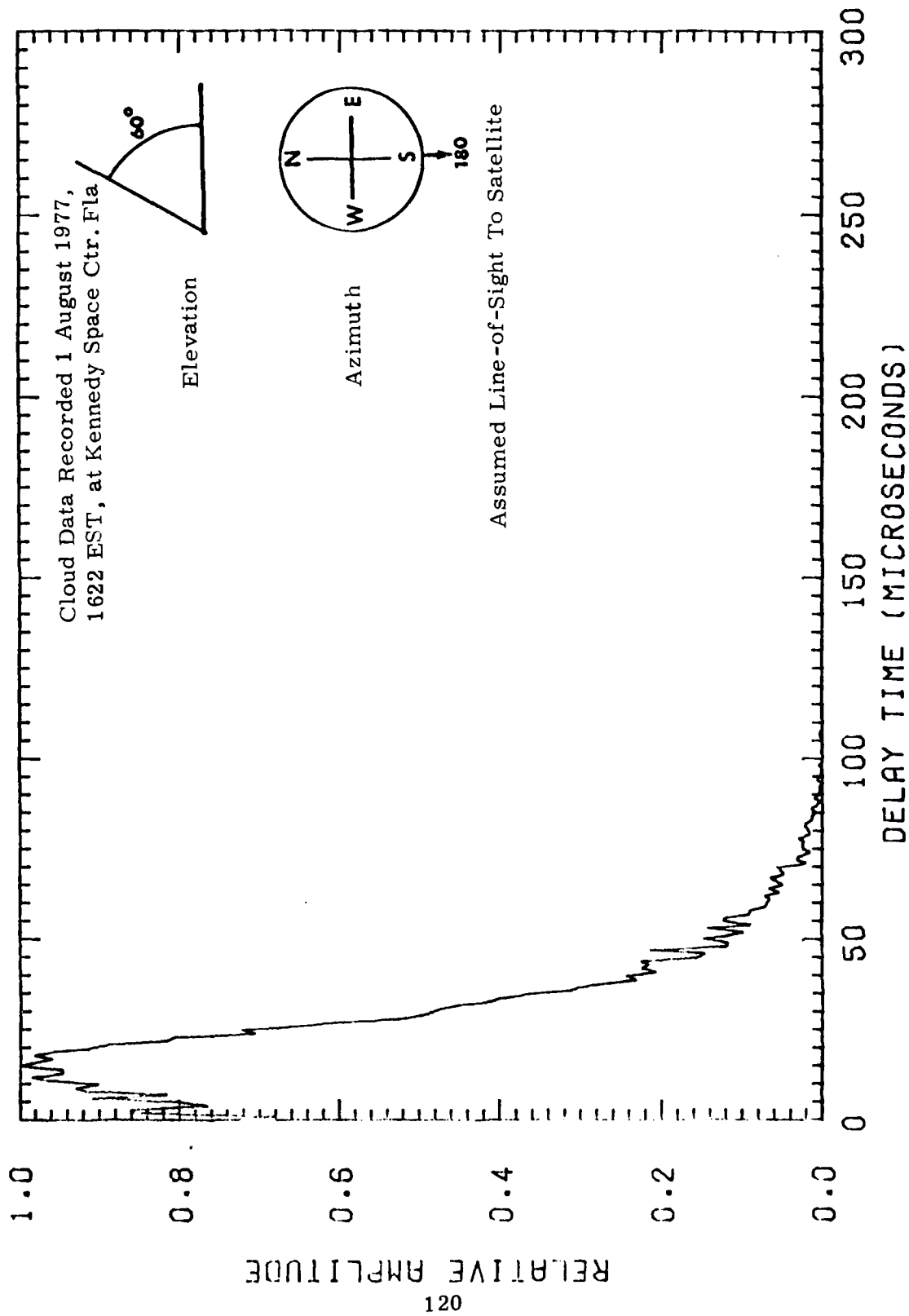


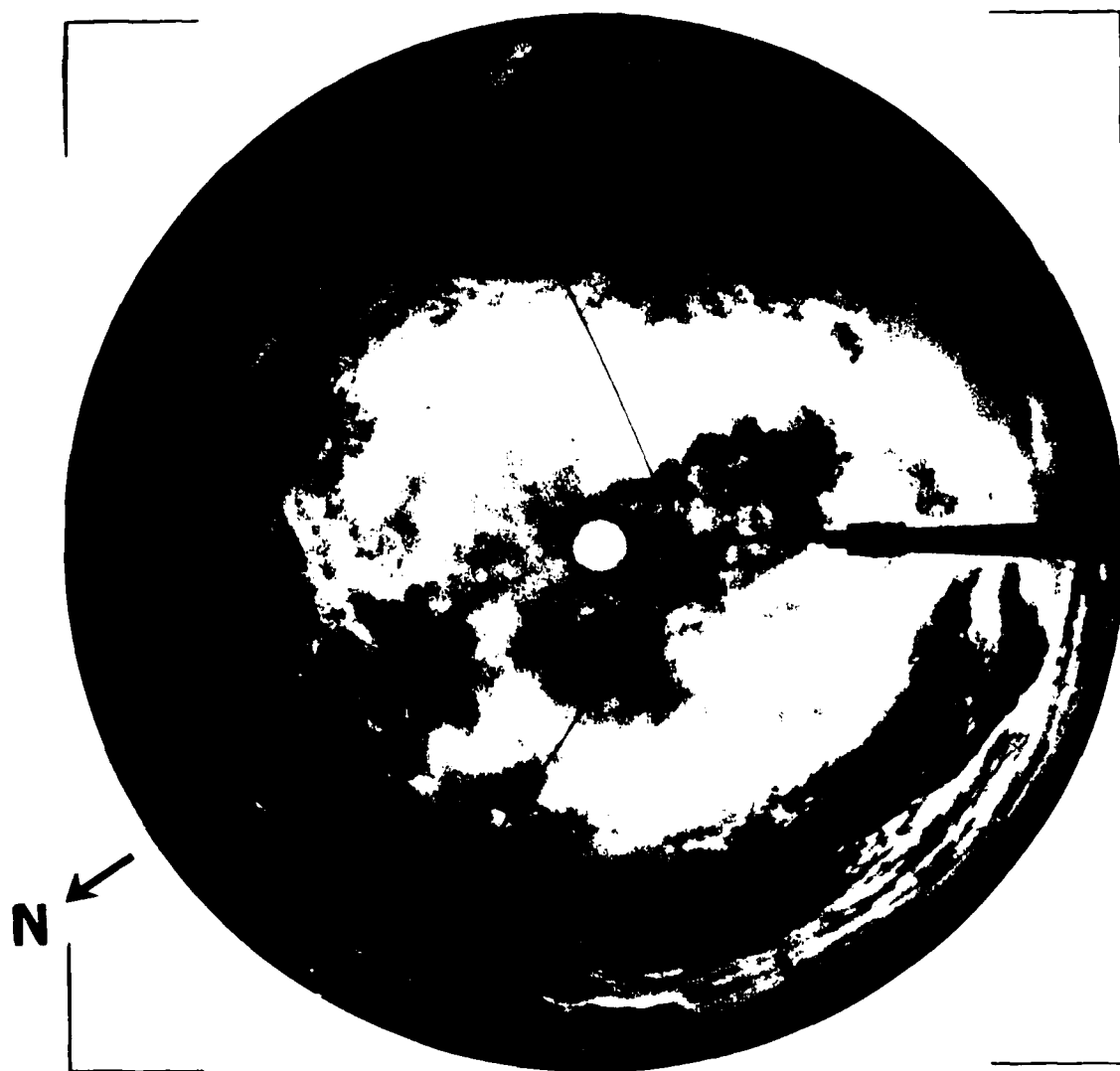




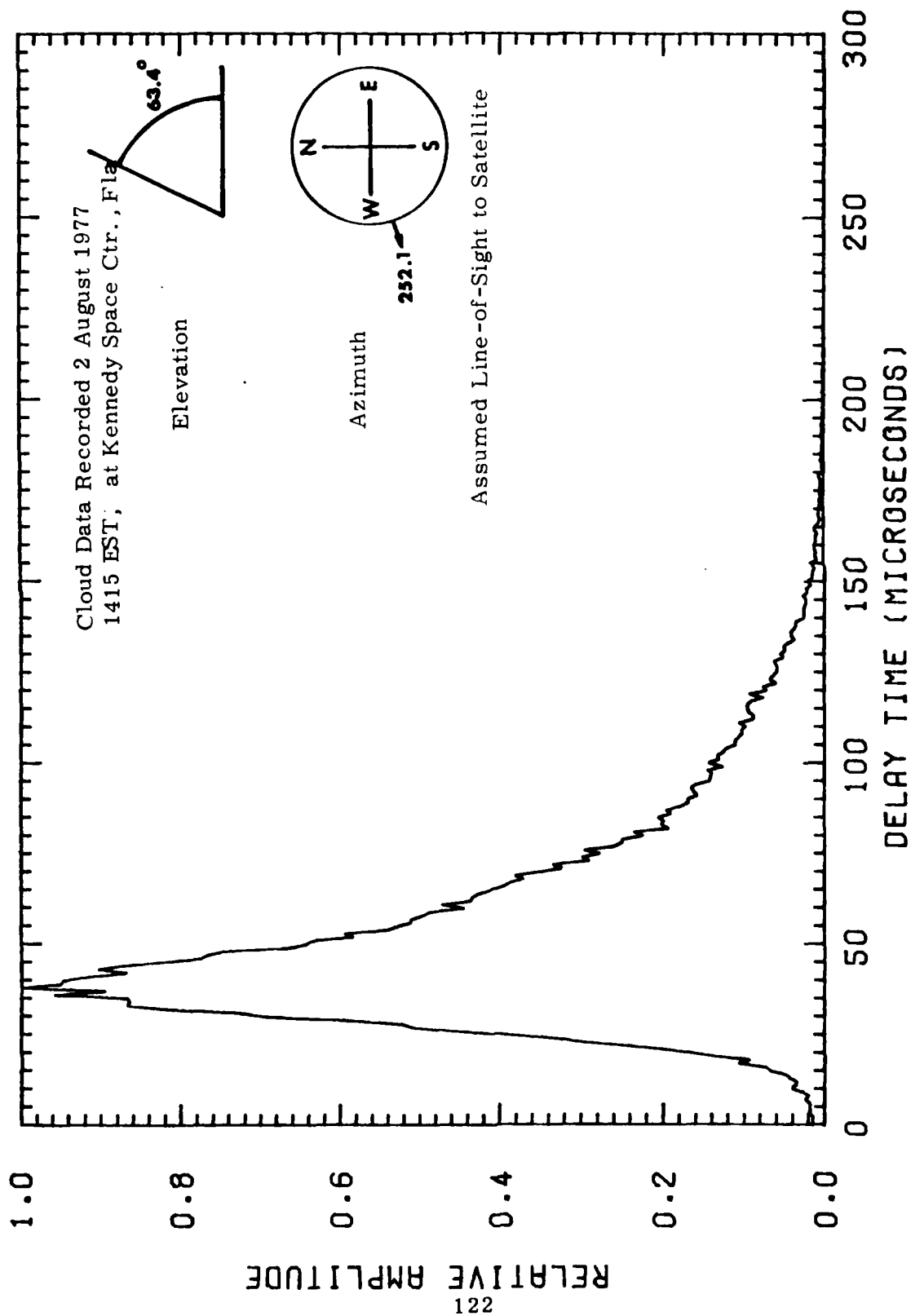


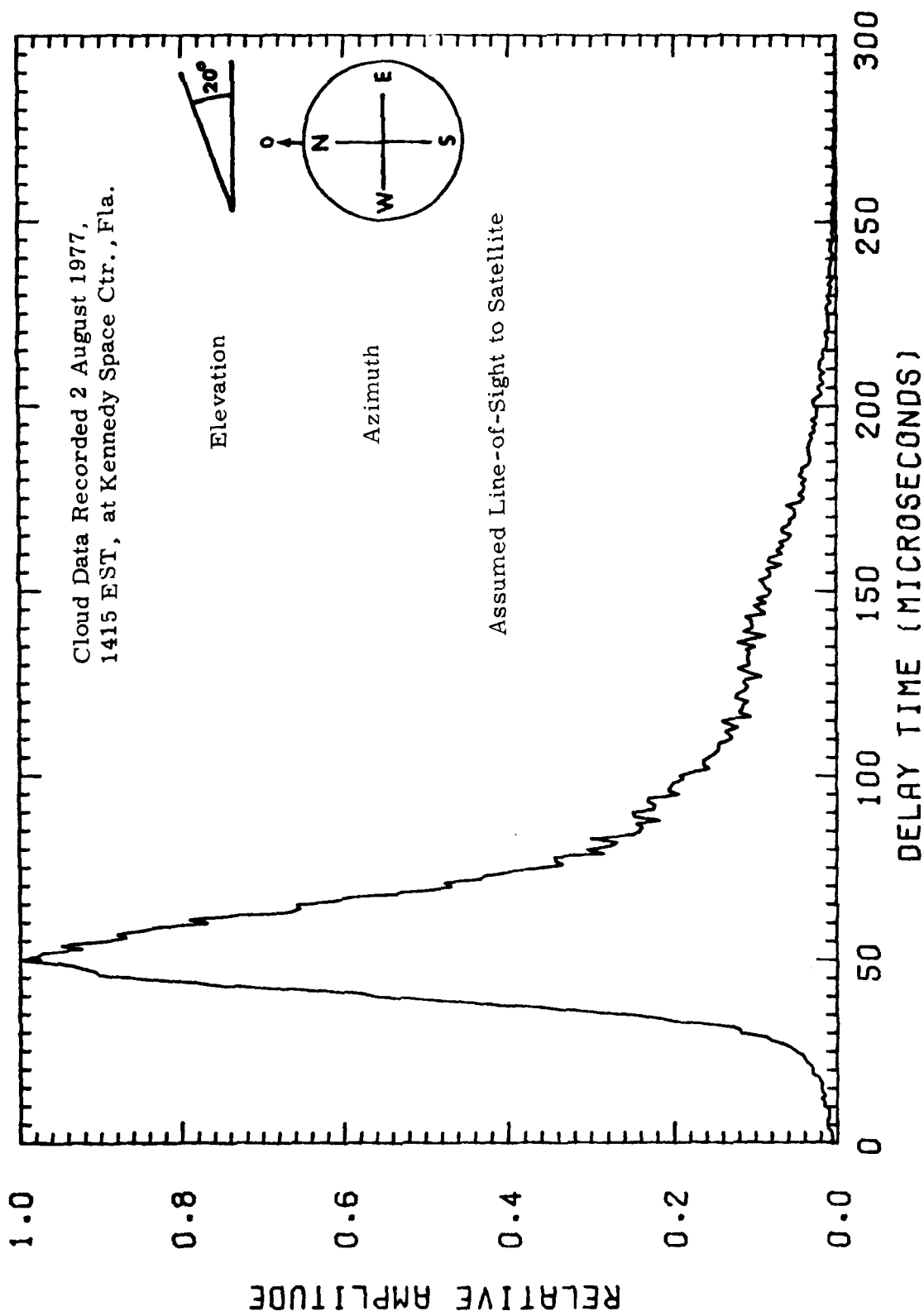


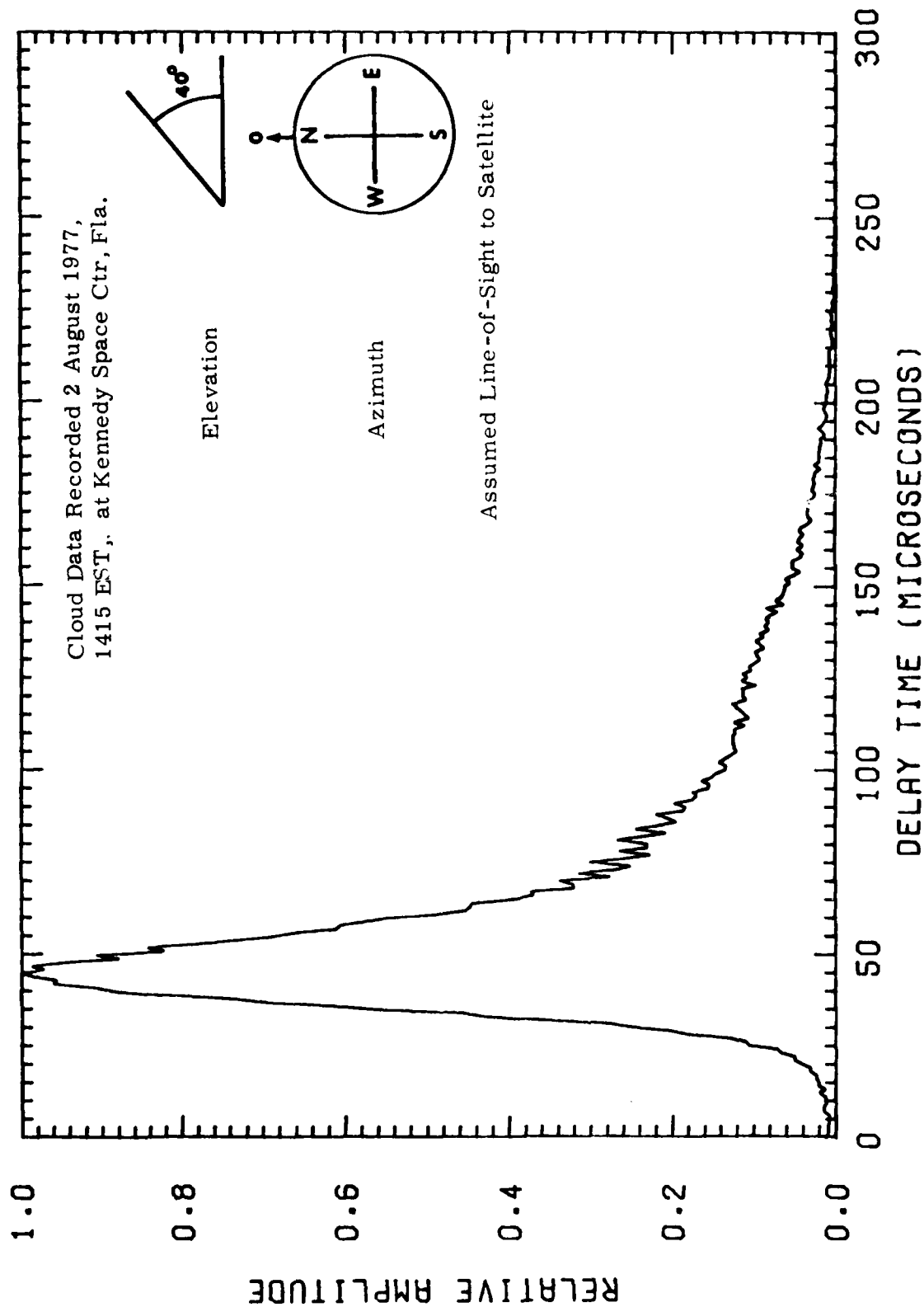




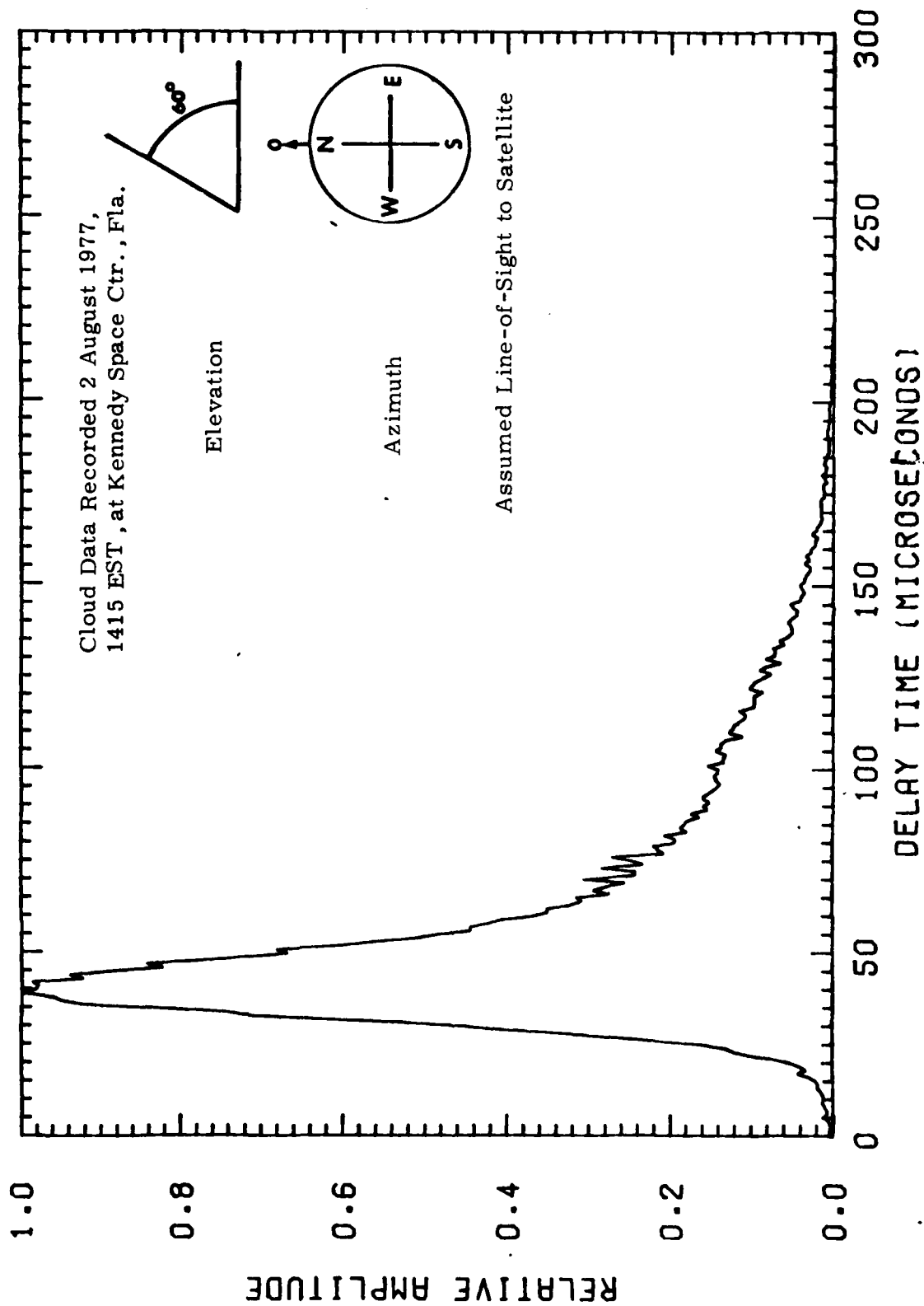
Date 2 August 1977  
Time 1415 EST

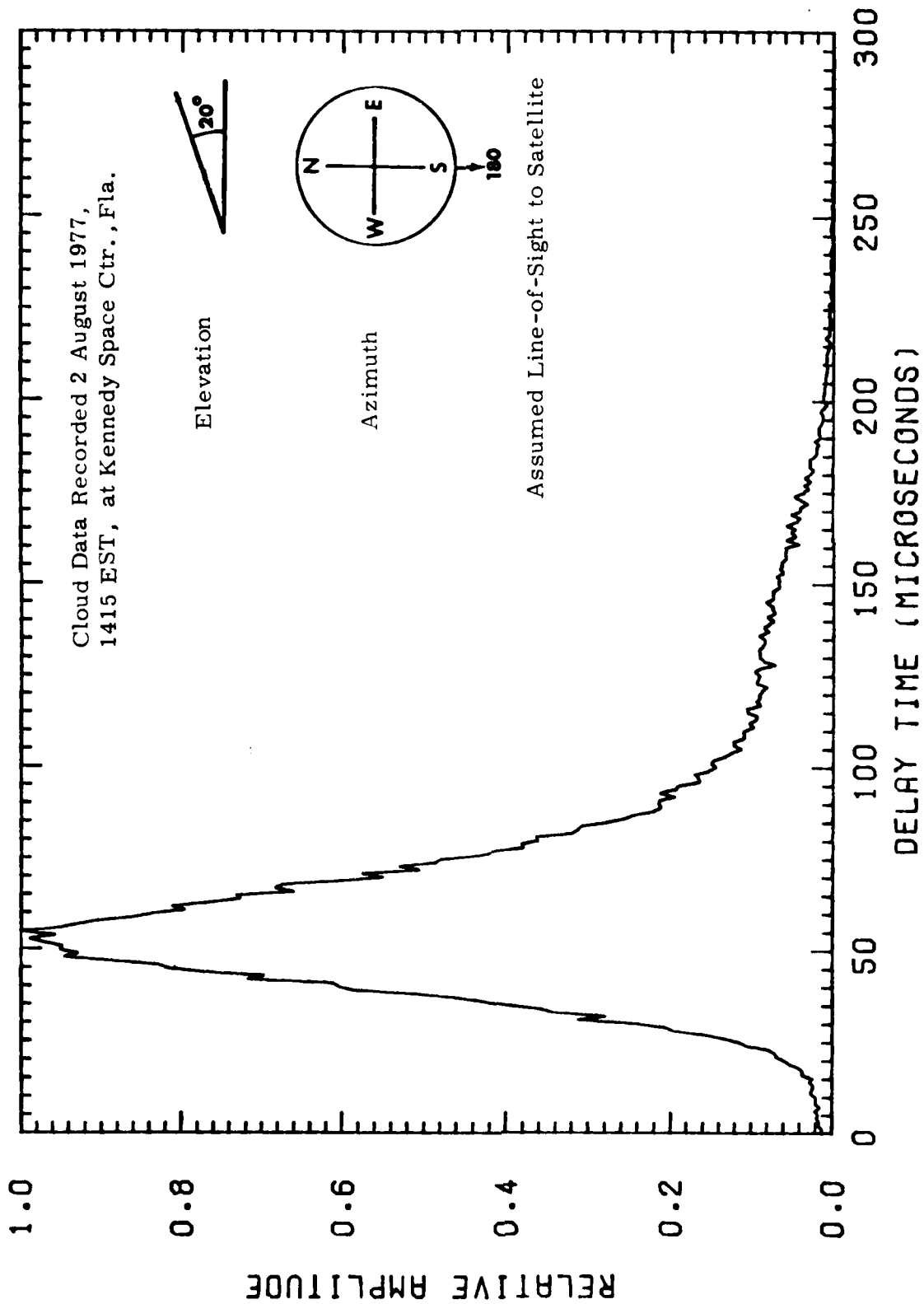


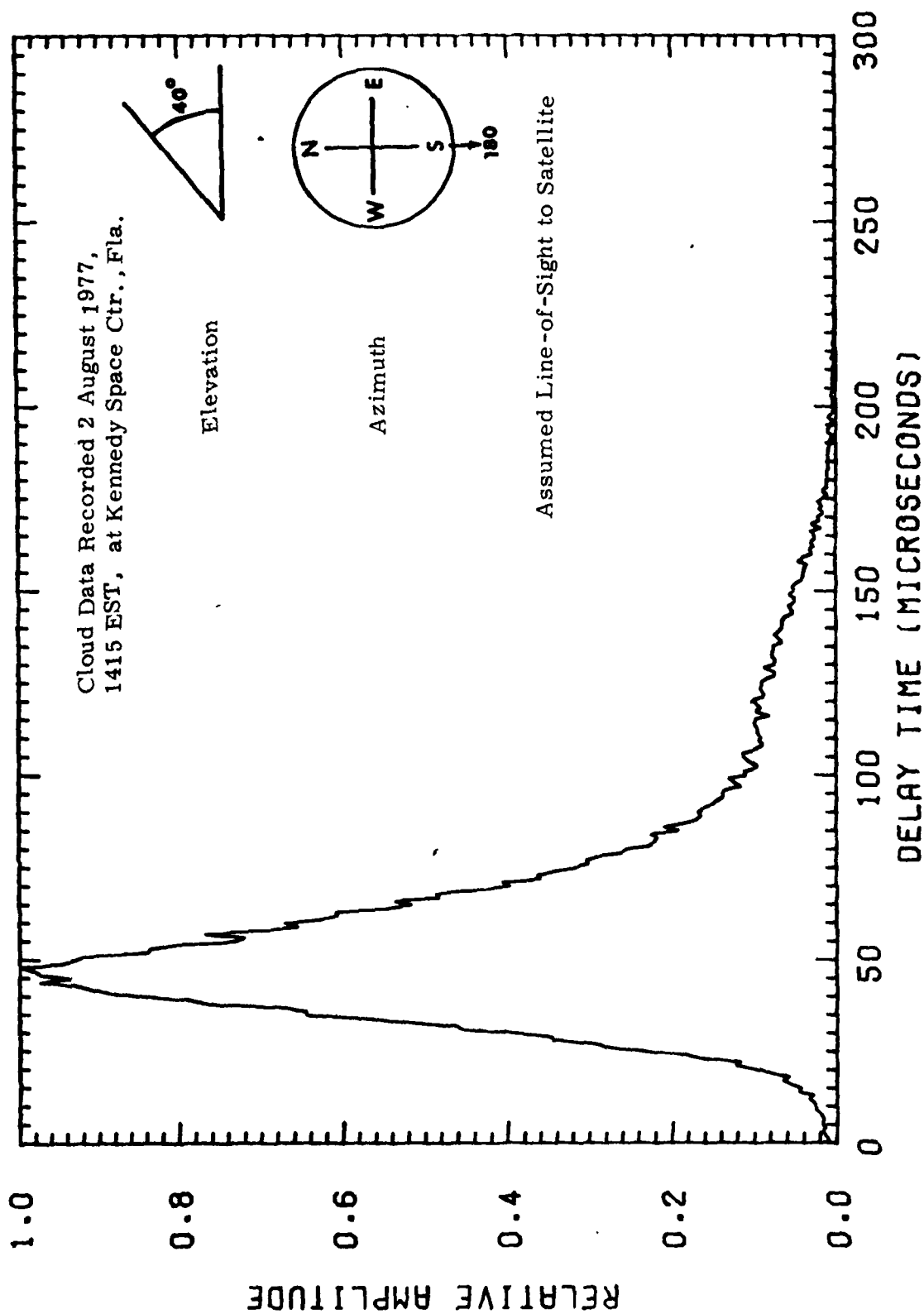


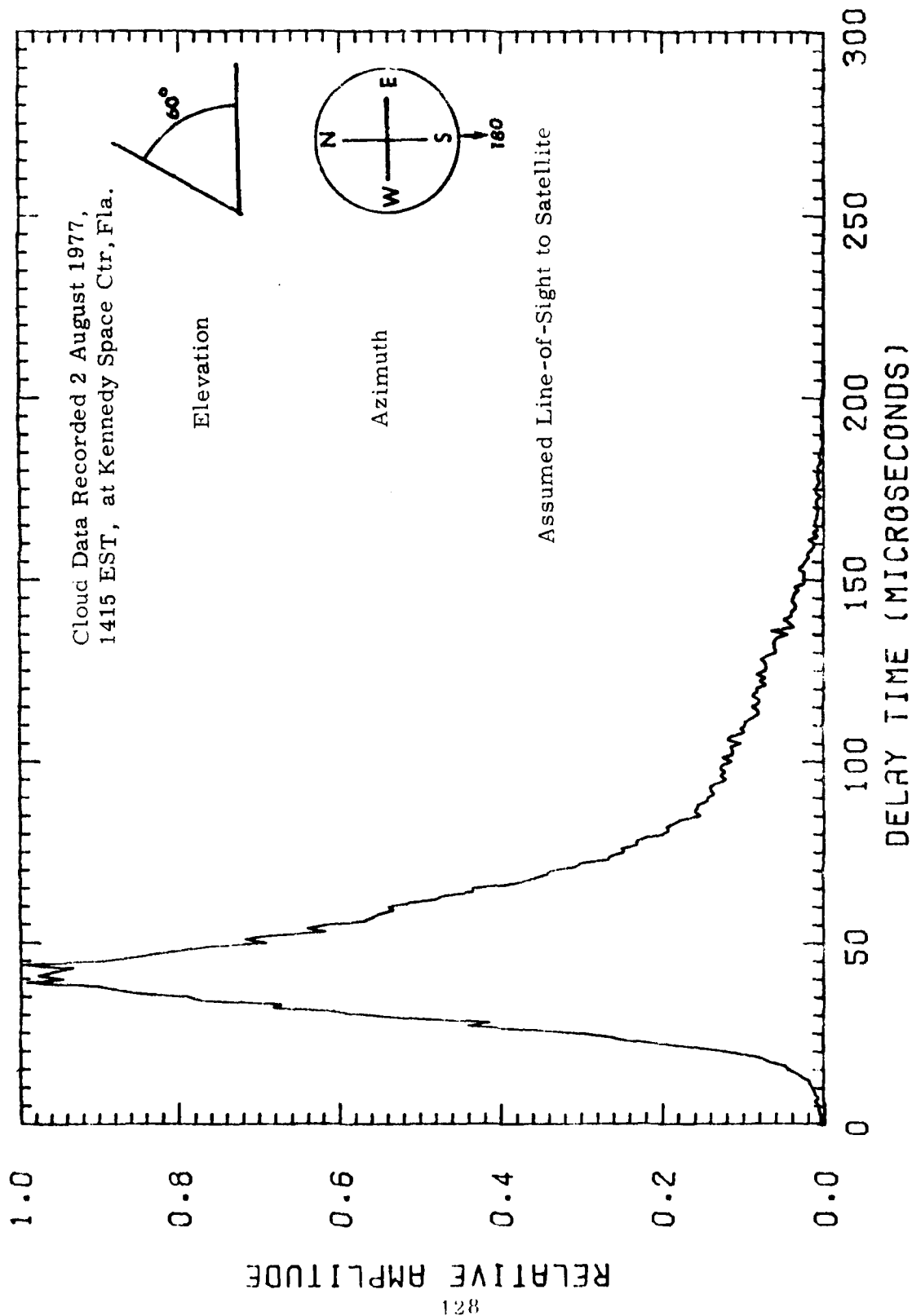


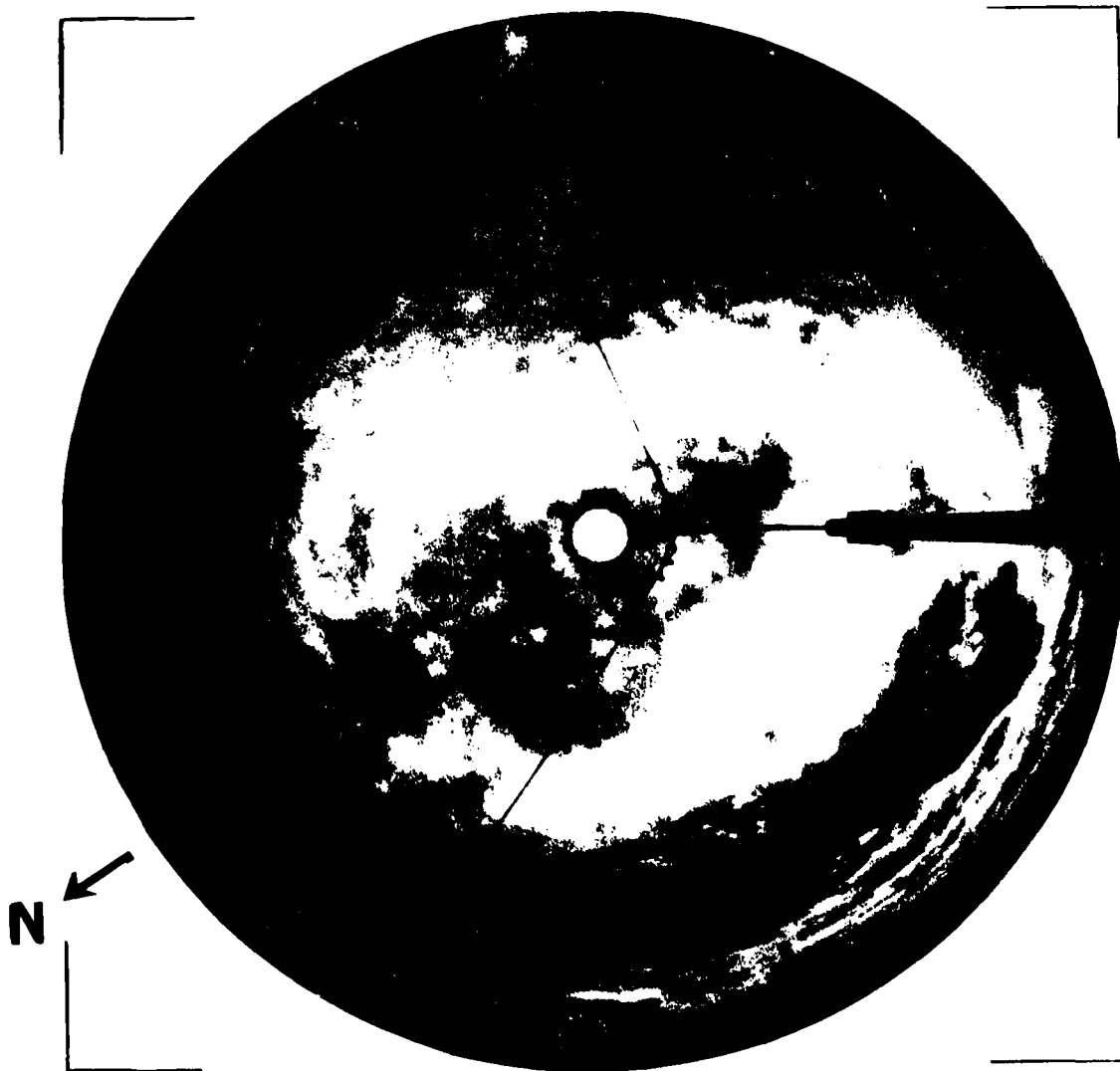






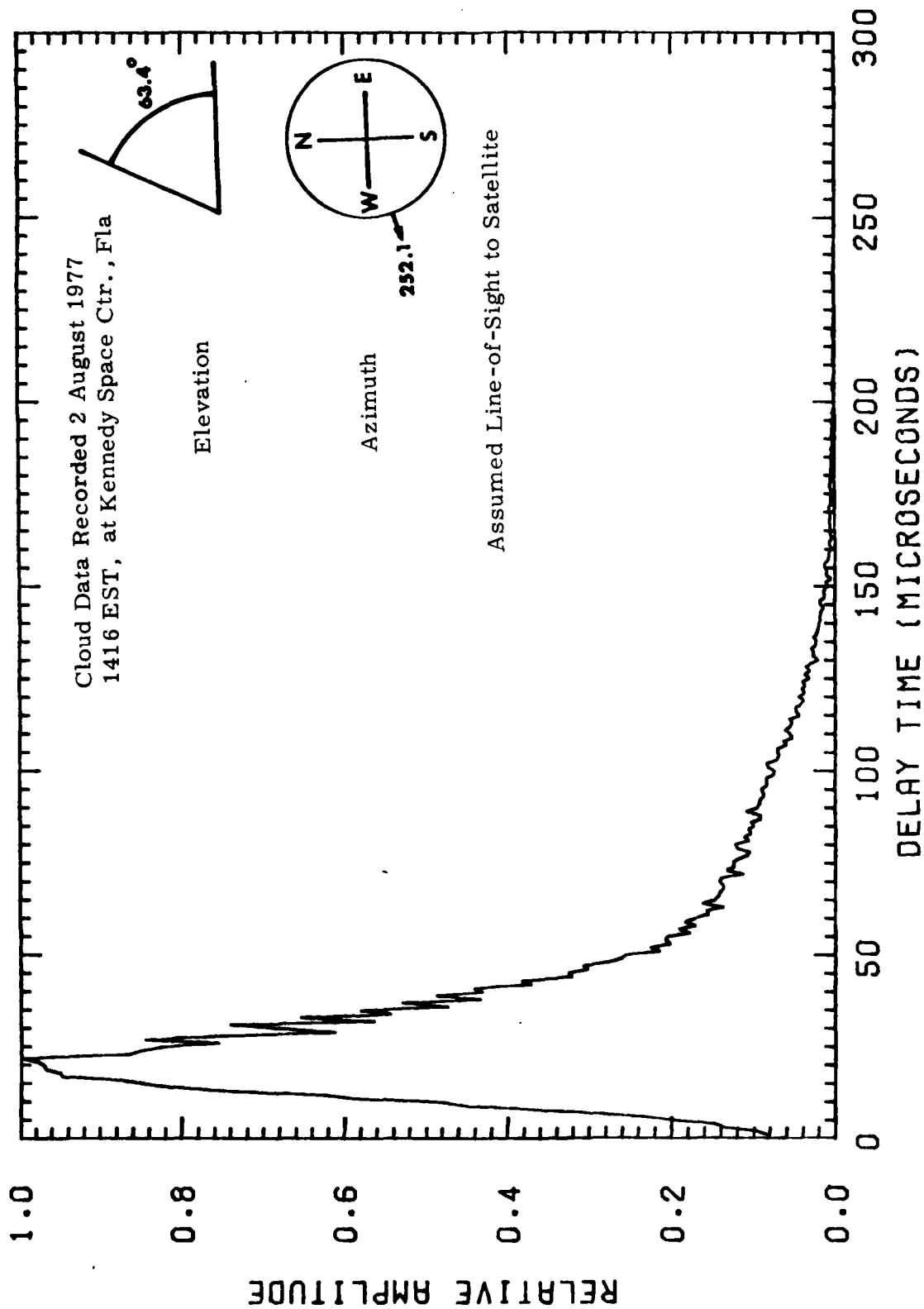


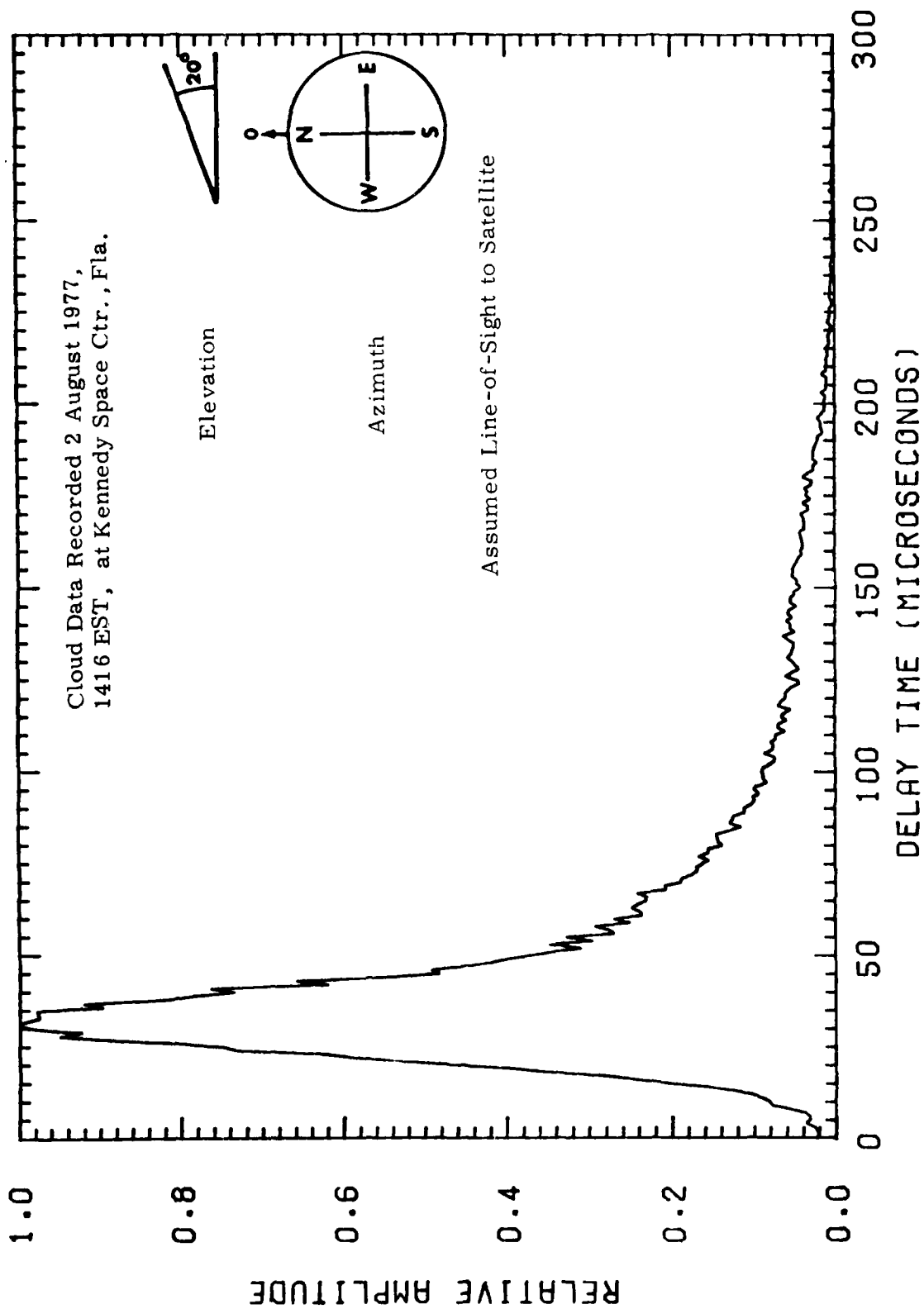


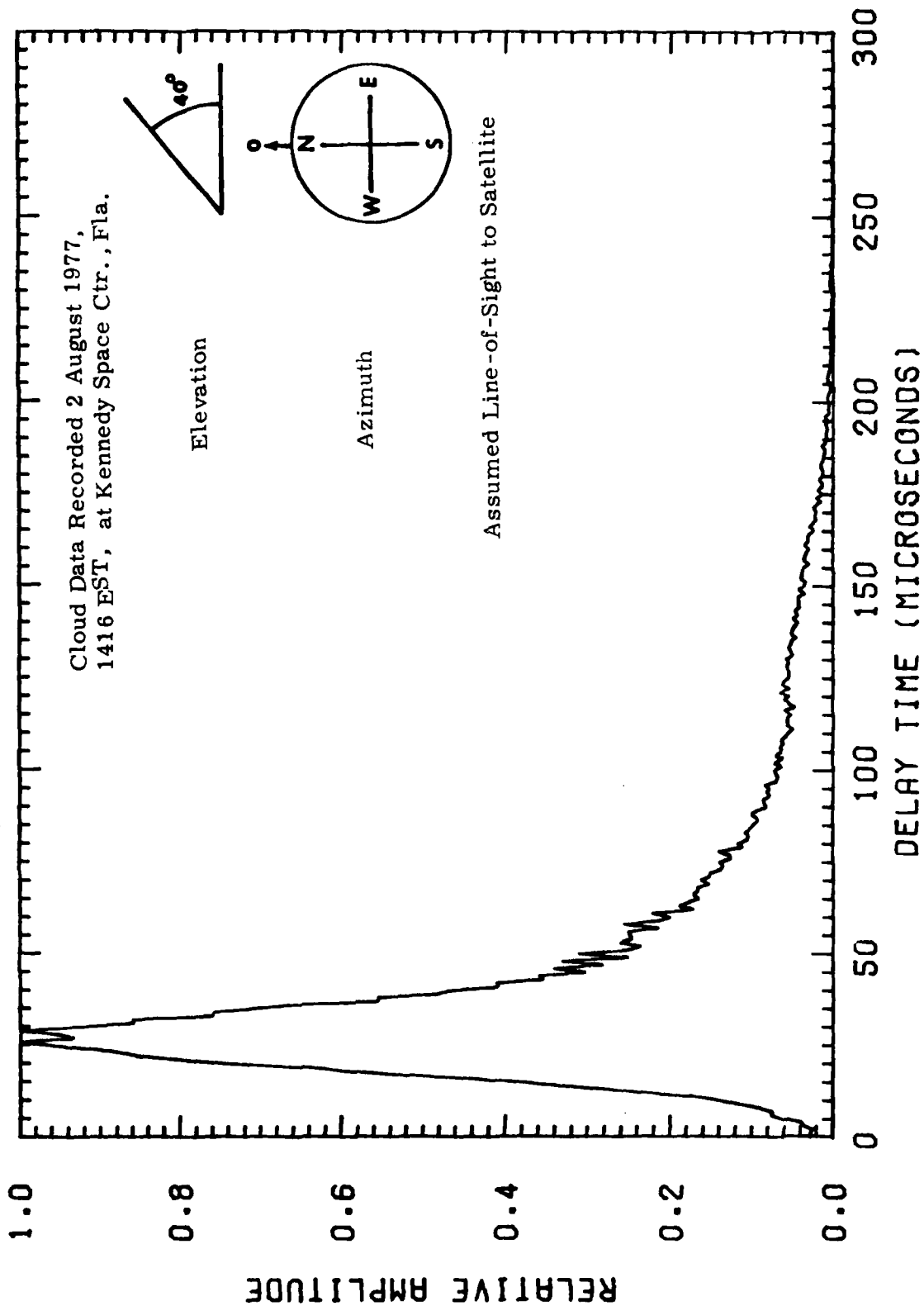


Date 2 August 1977

Time 1416 EST







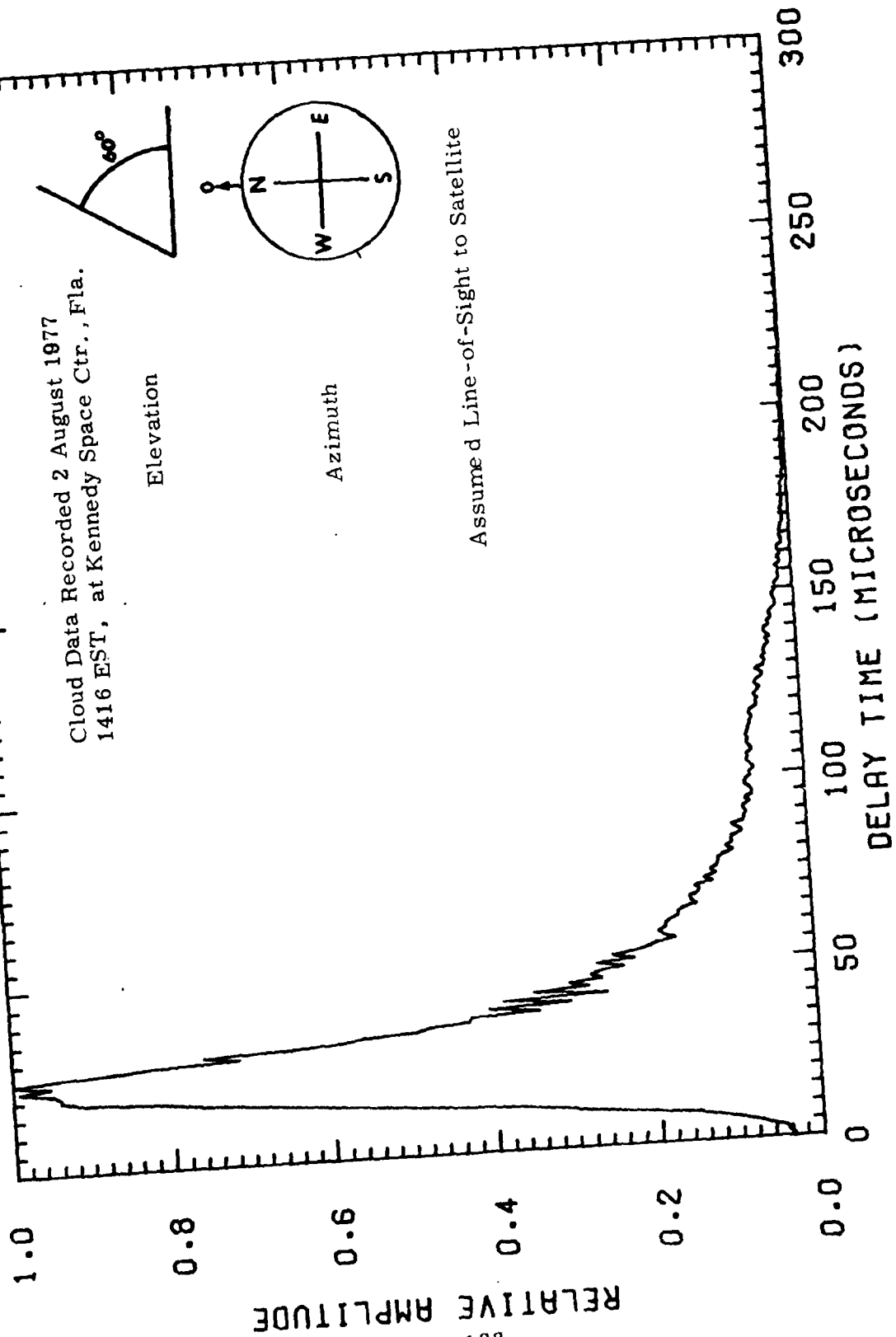
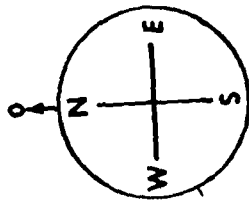
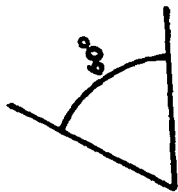


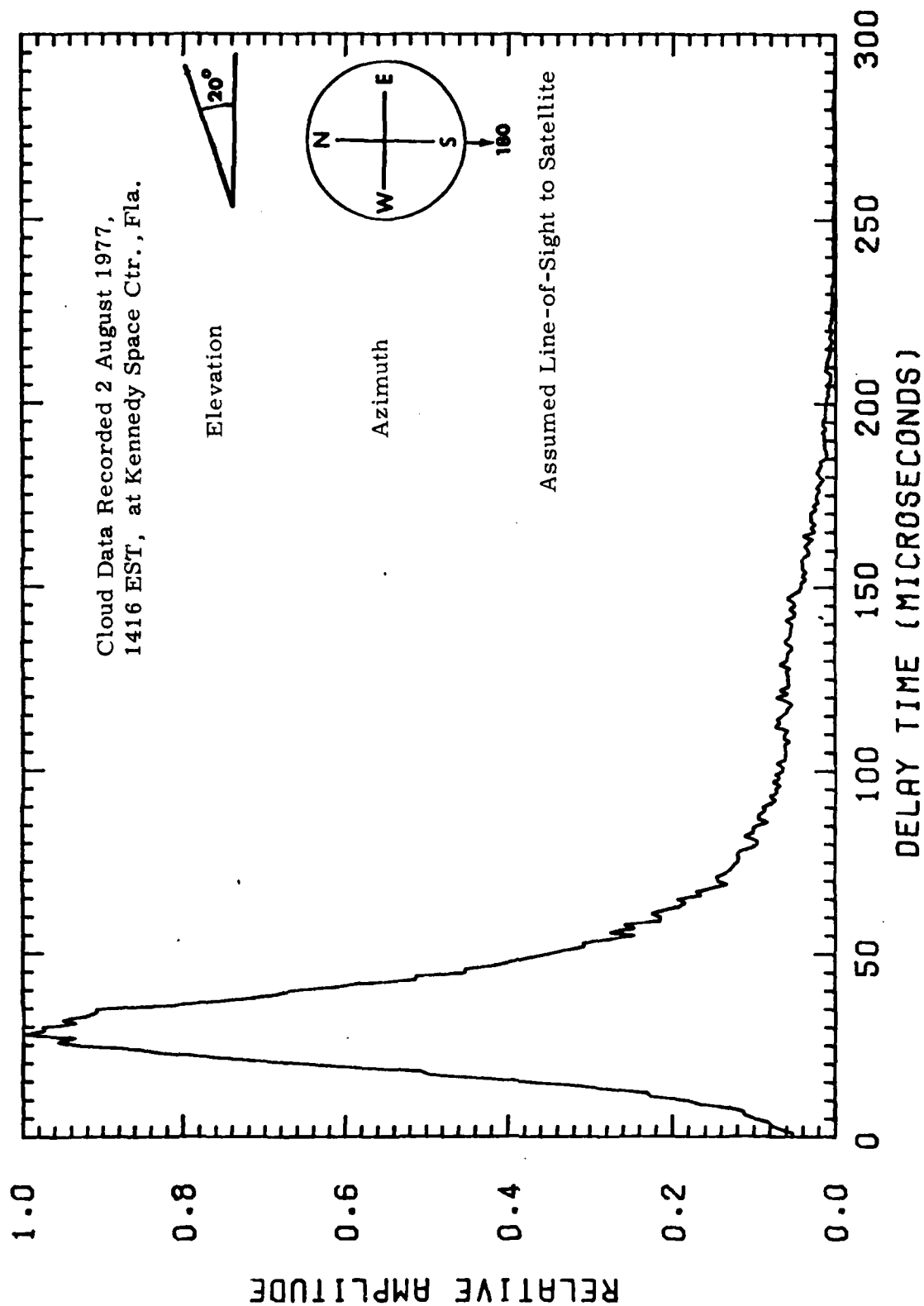
Cloud Data Recorded 2 August 1977  
1416 EST, at Kennedy Space Ctr., Fla.

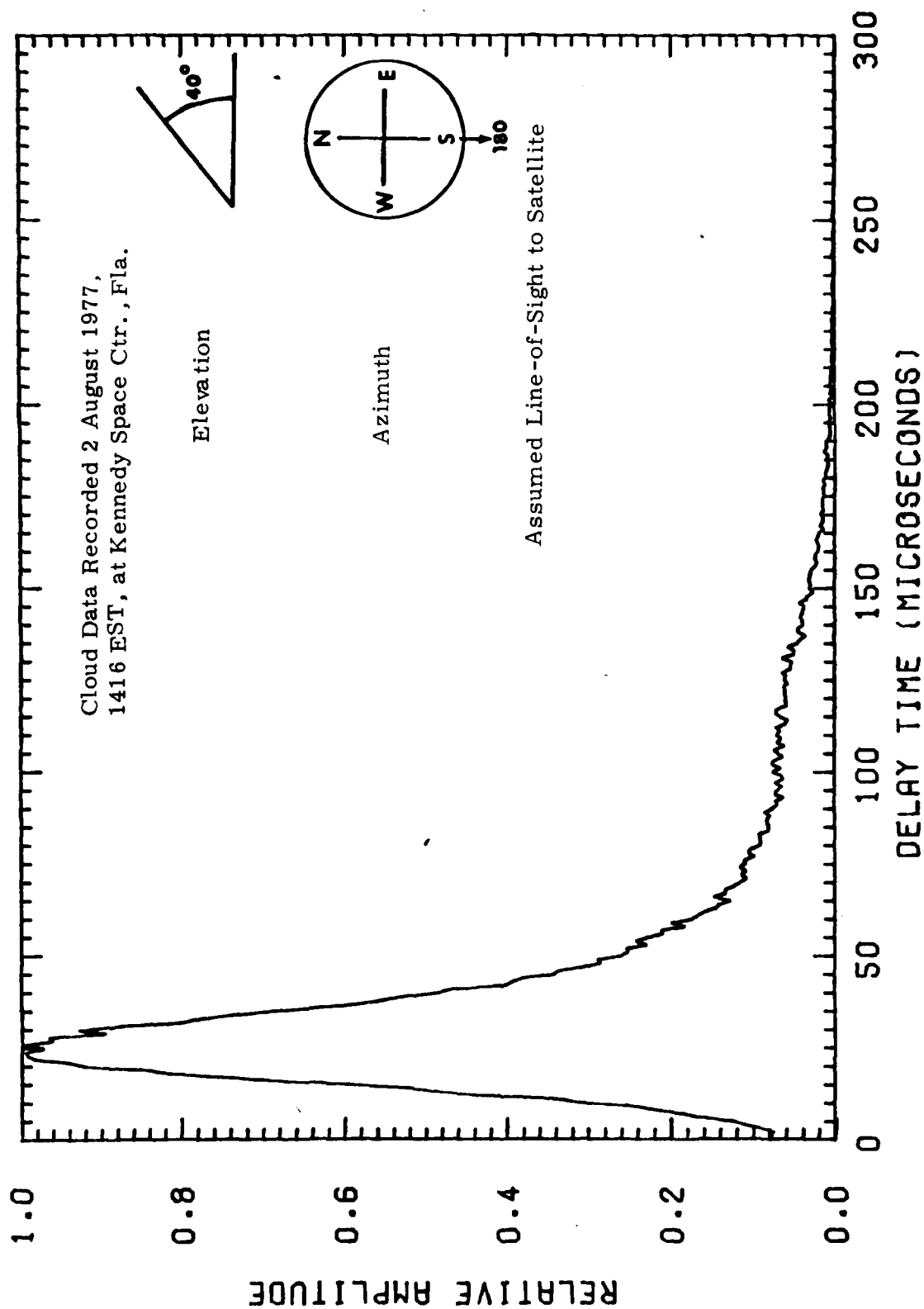
Elevation

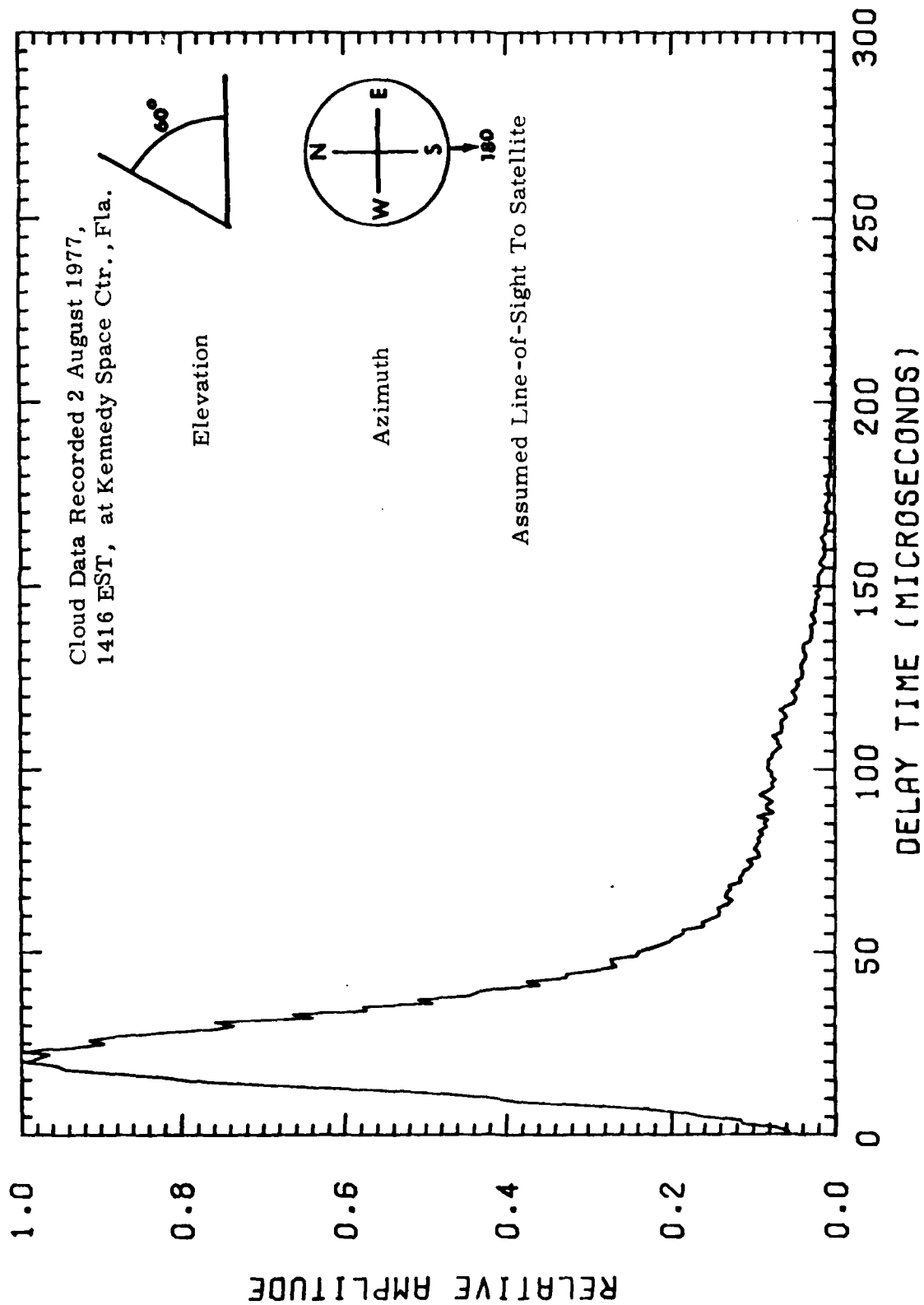
Azimuth

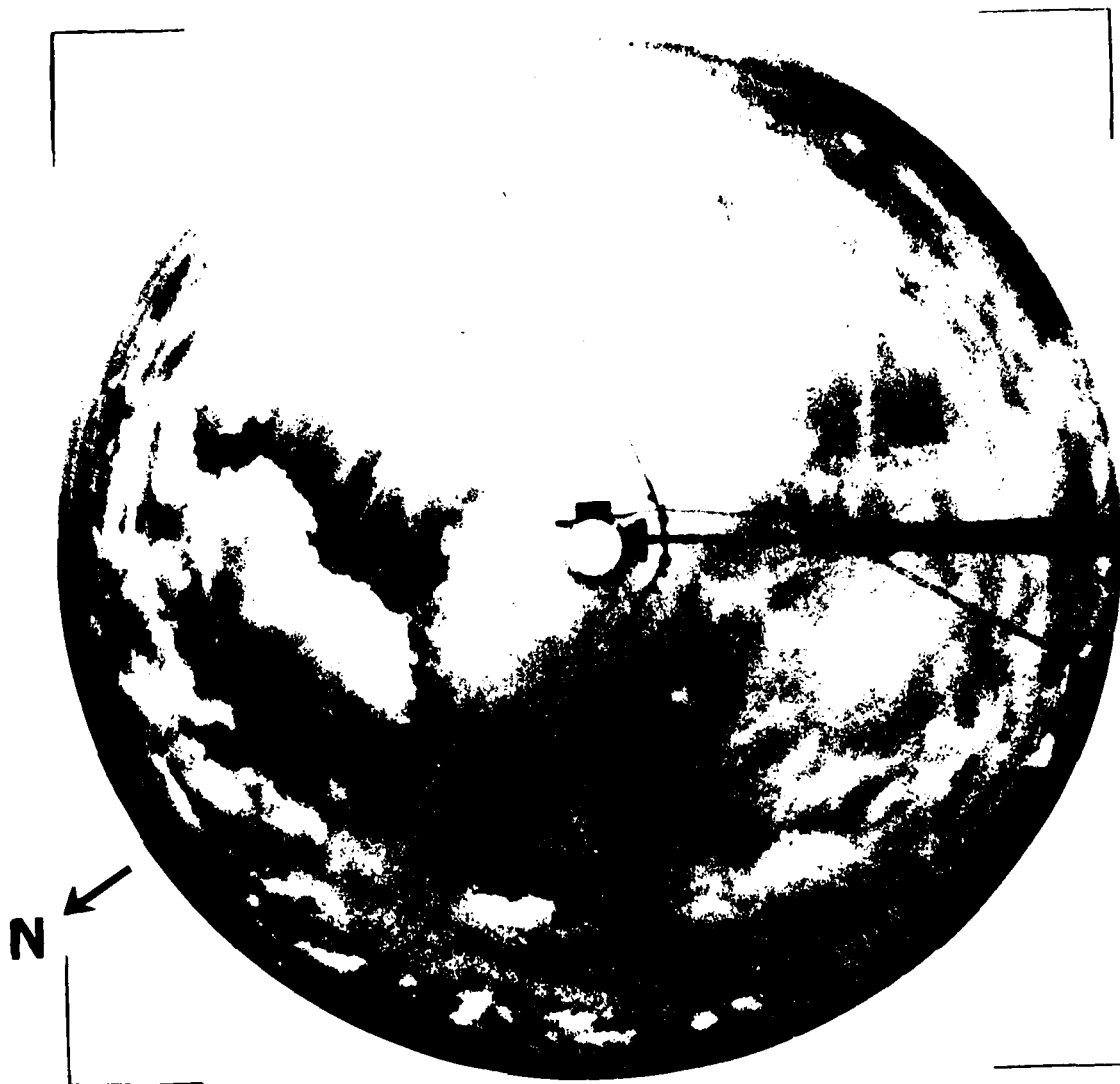
Assumed Line-of-Sight to Satellite



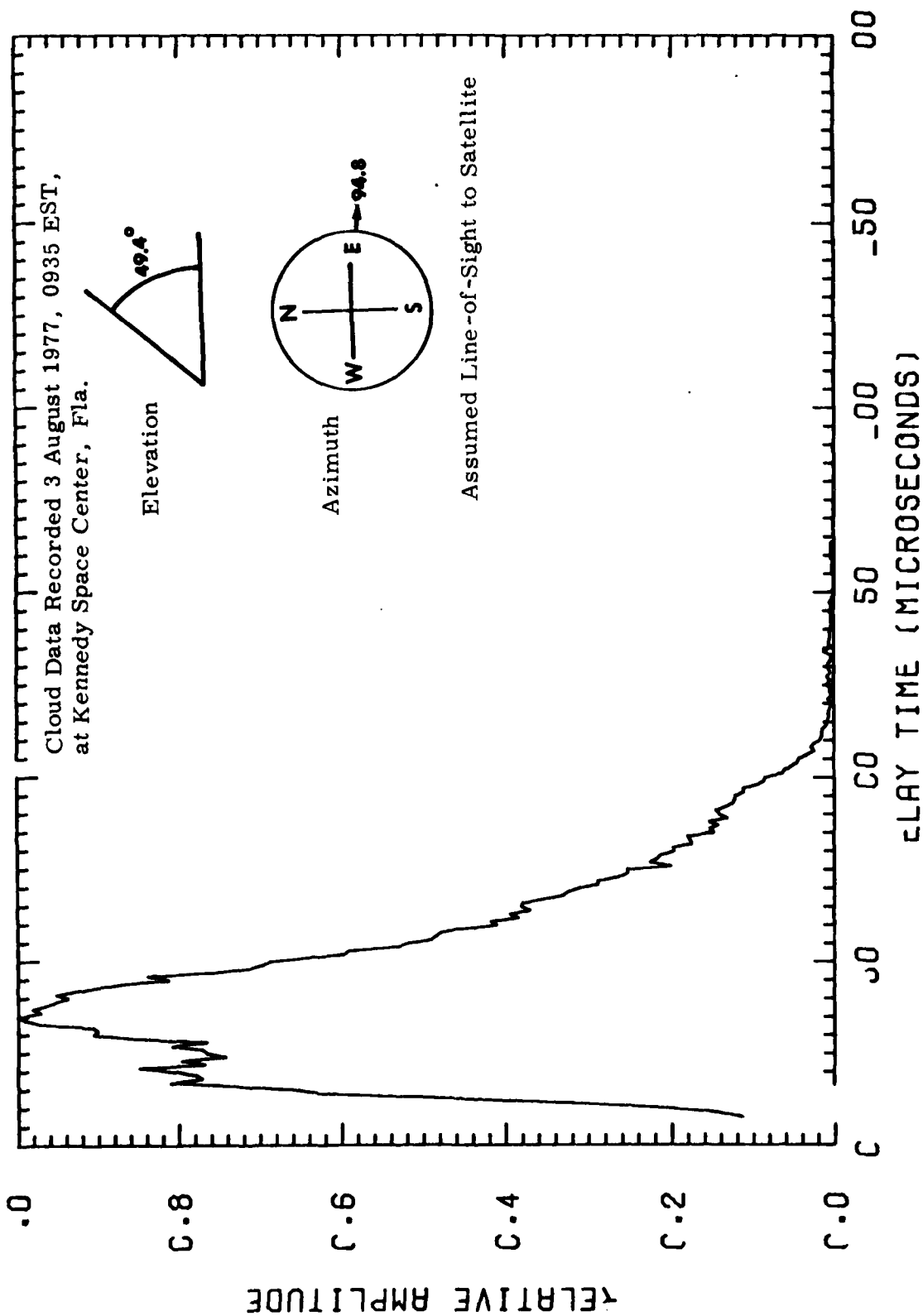


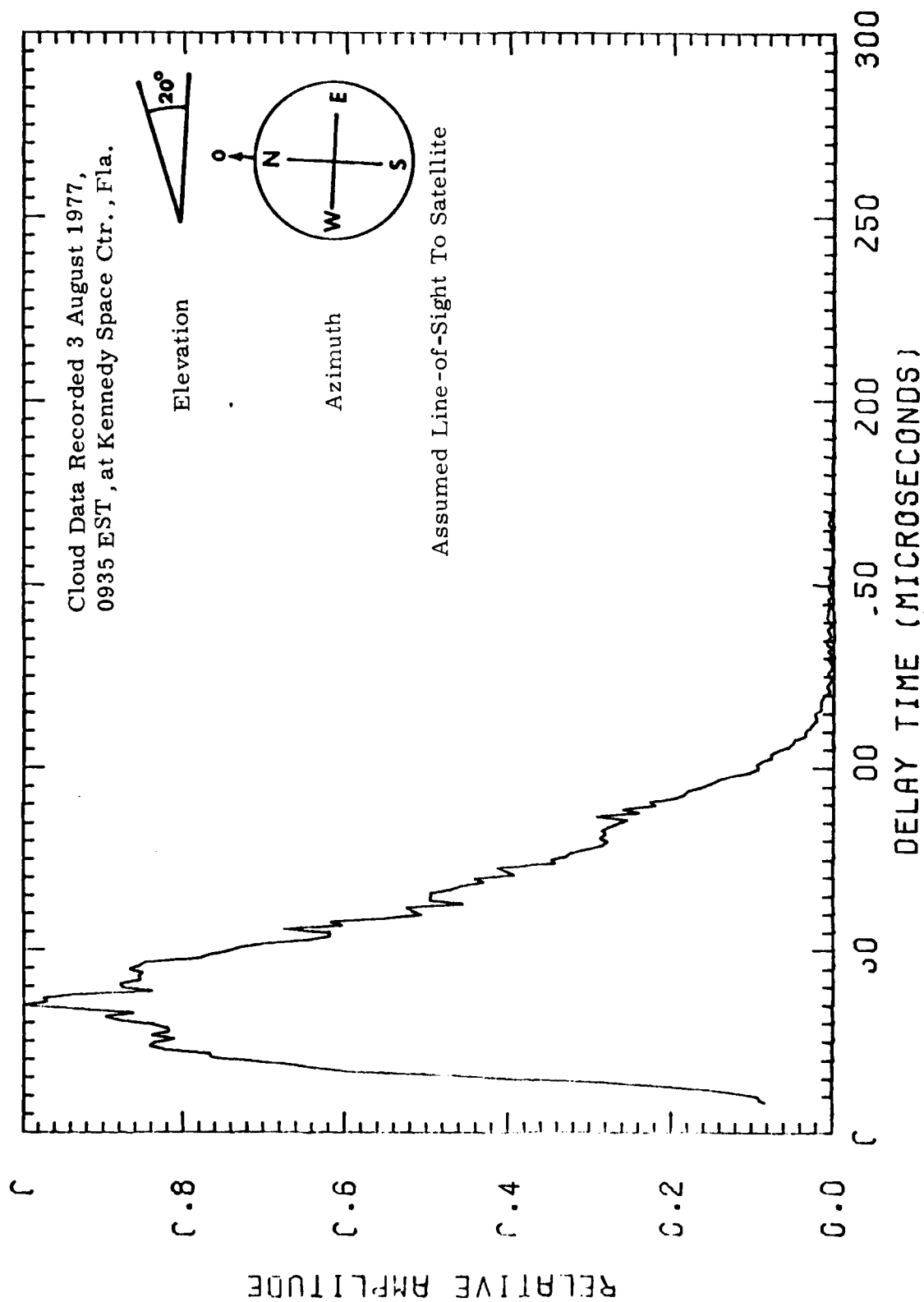


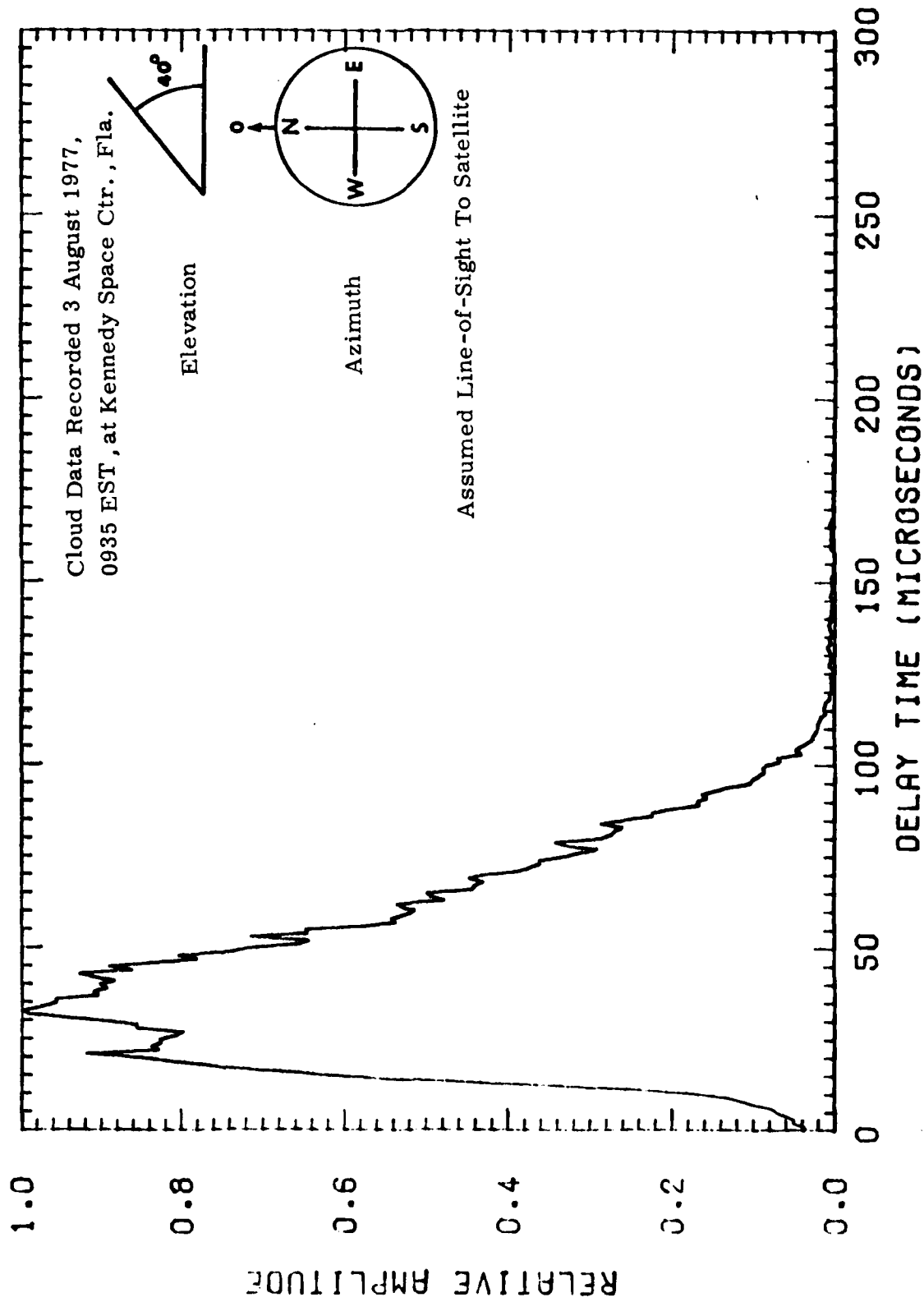




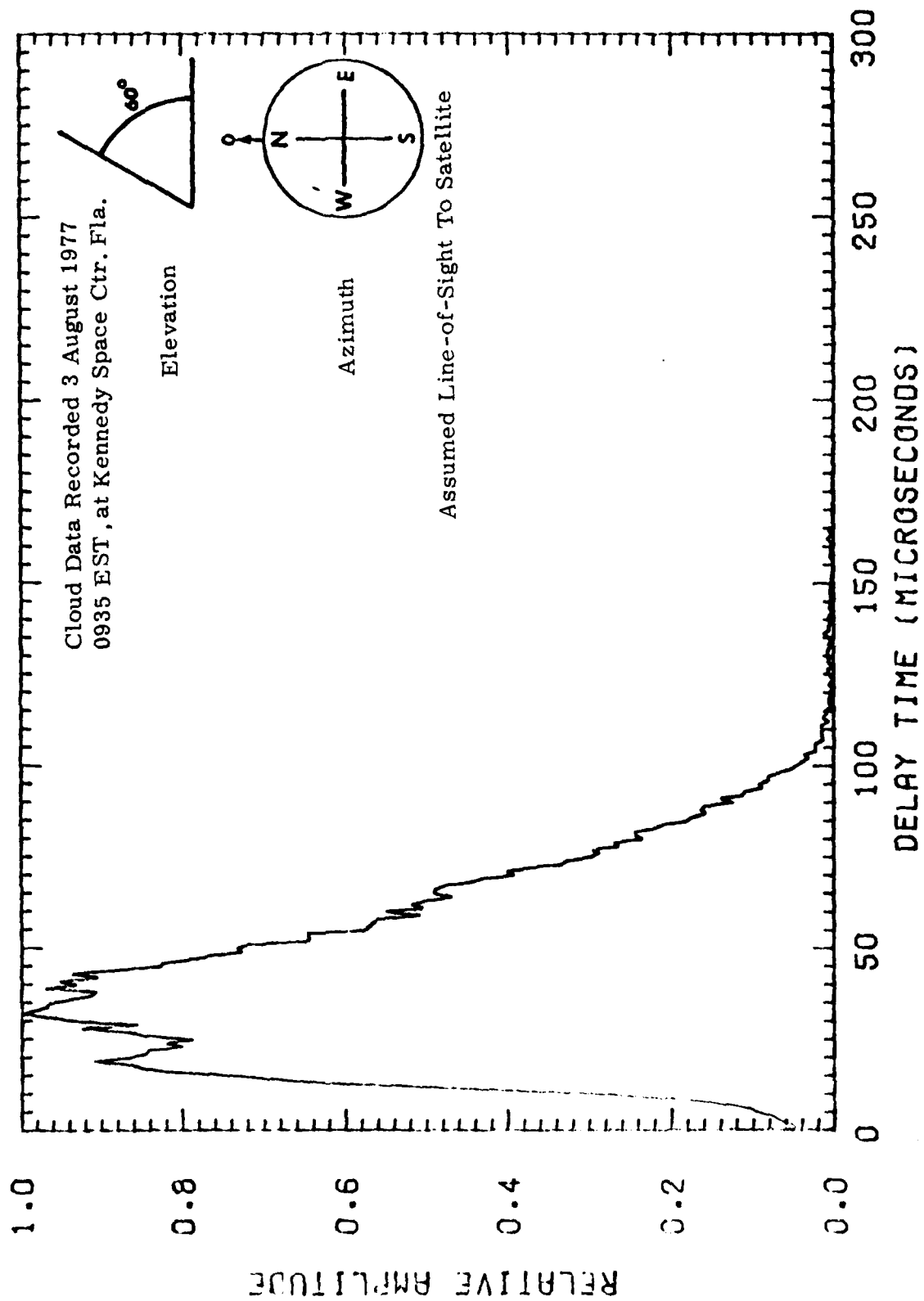
Date 3 August 1977  
Time 0935 EST

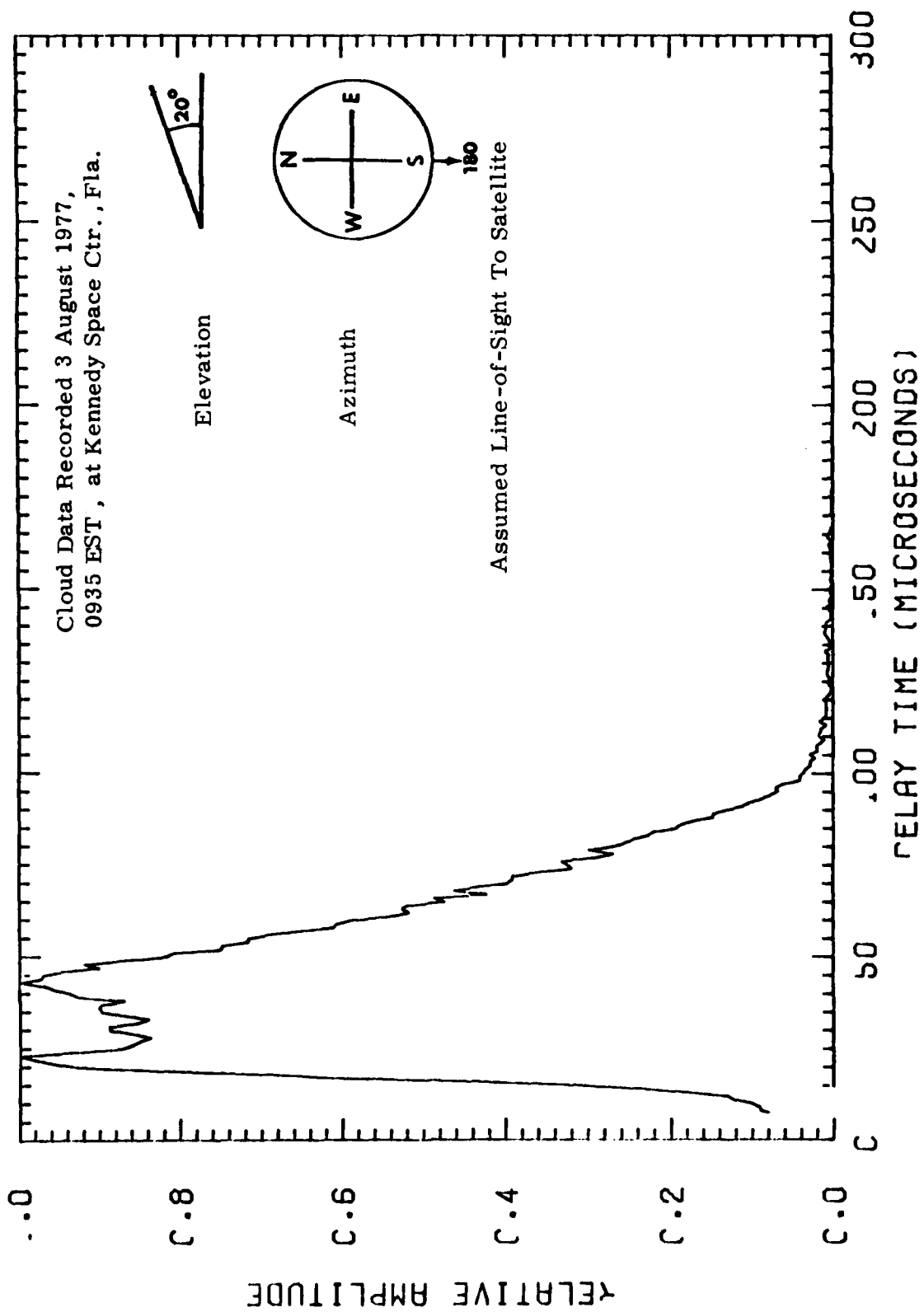


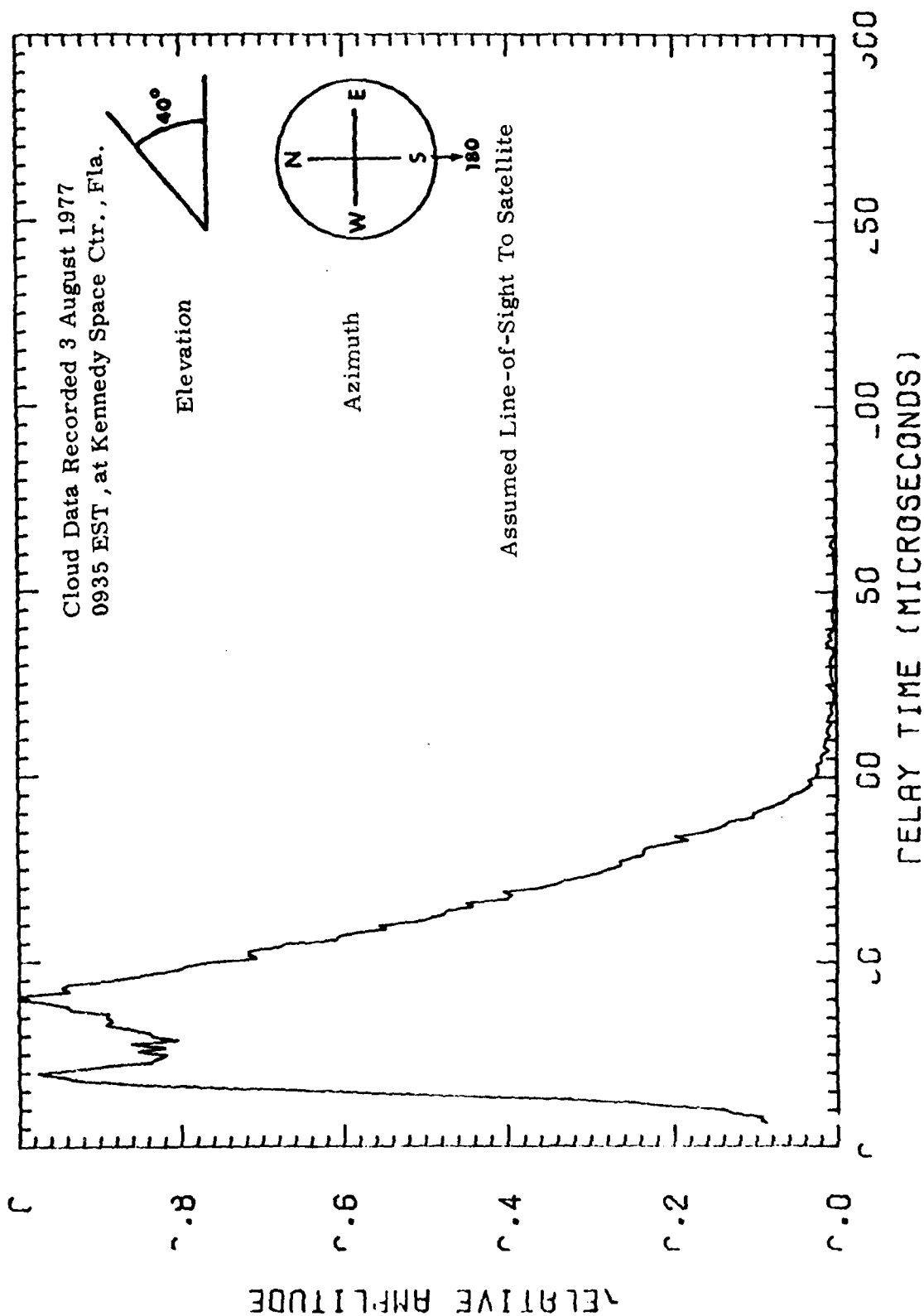


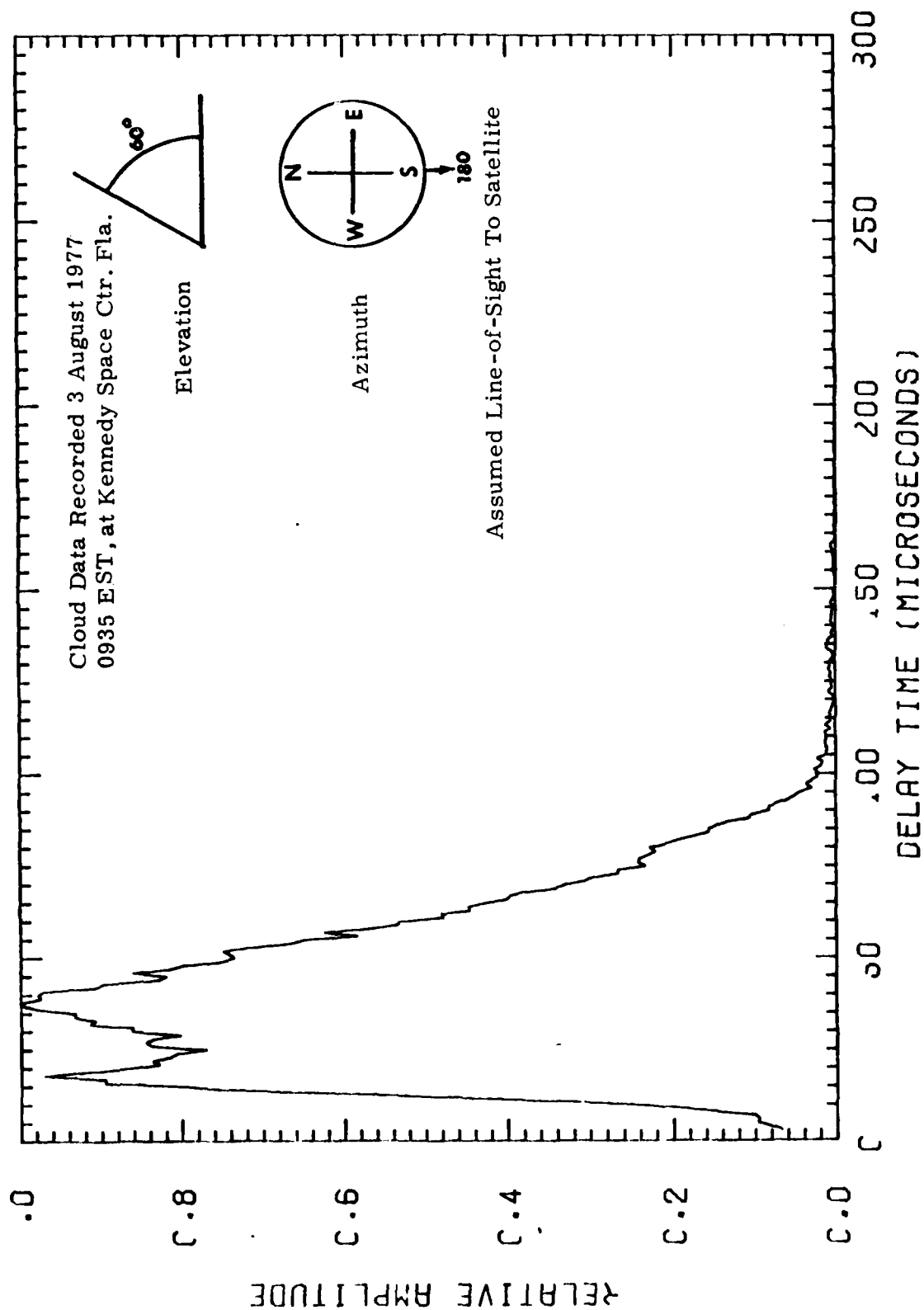


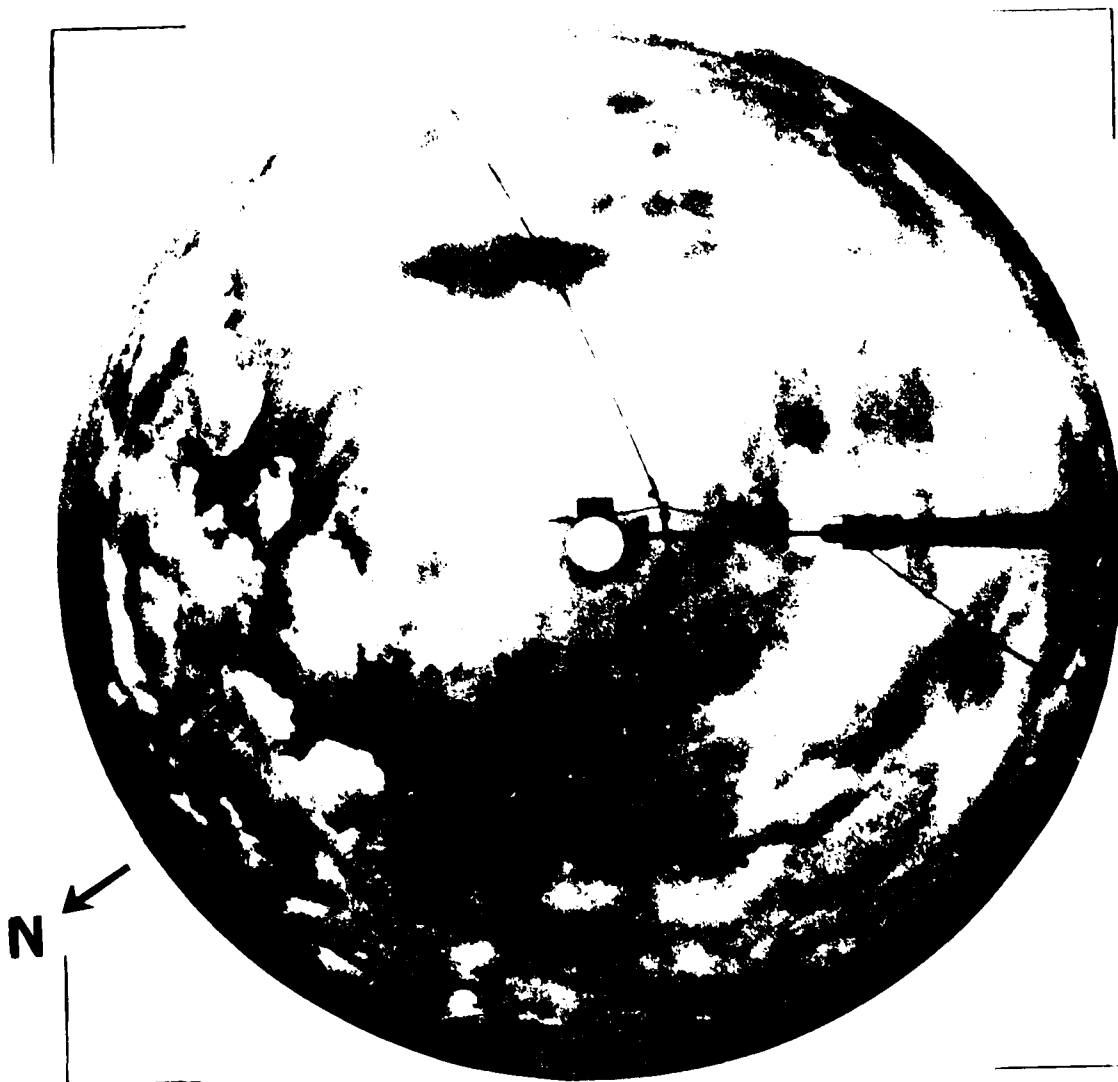






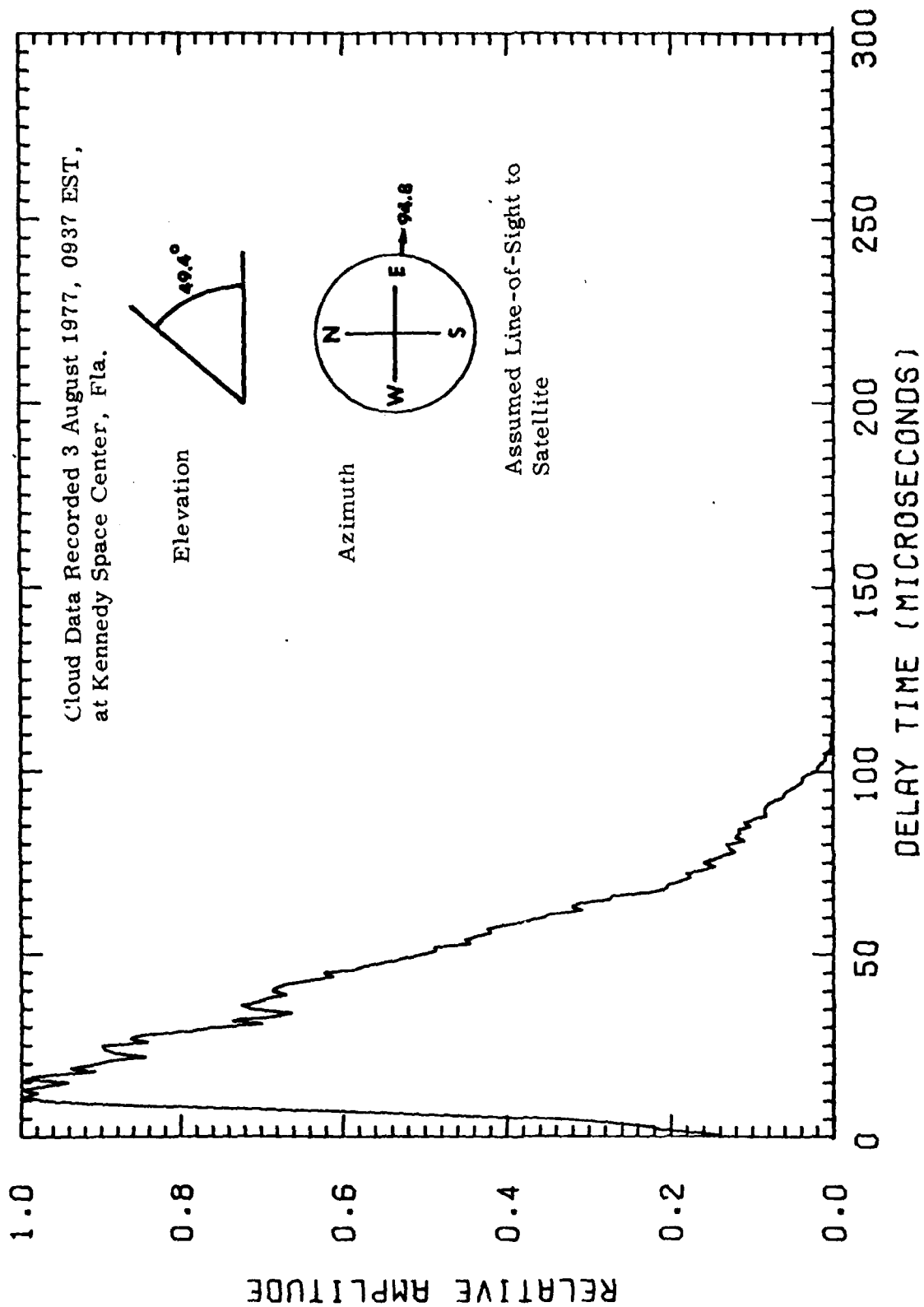


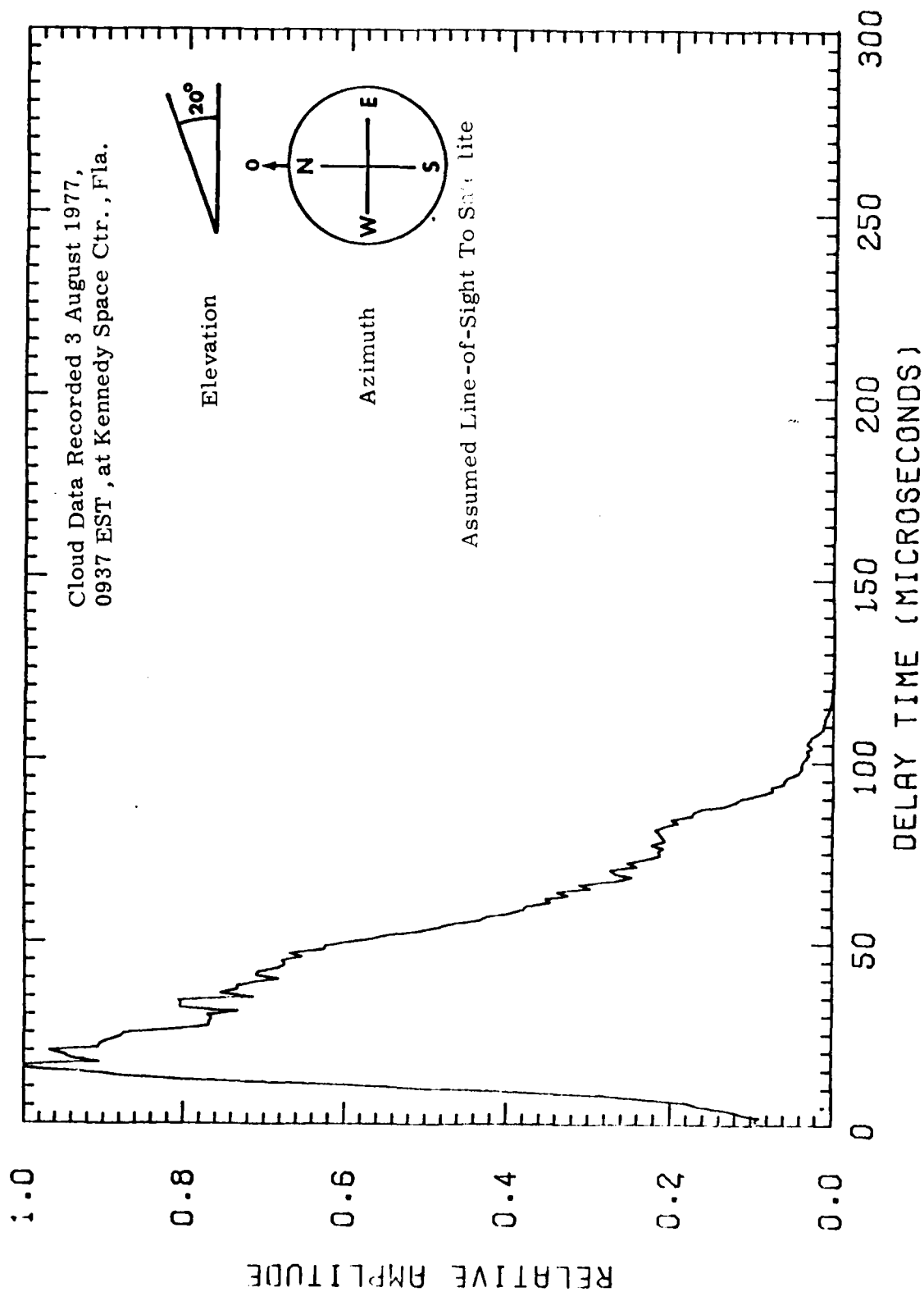


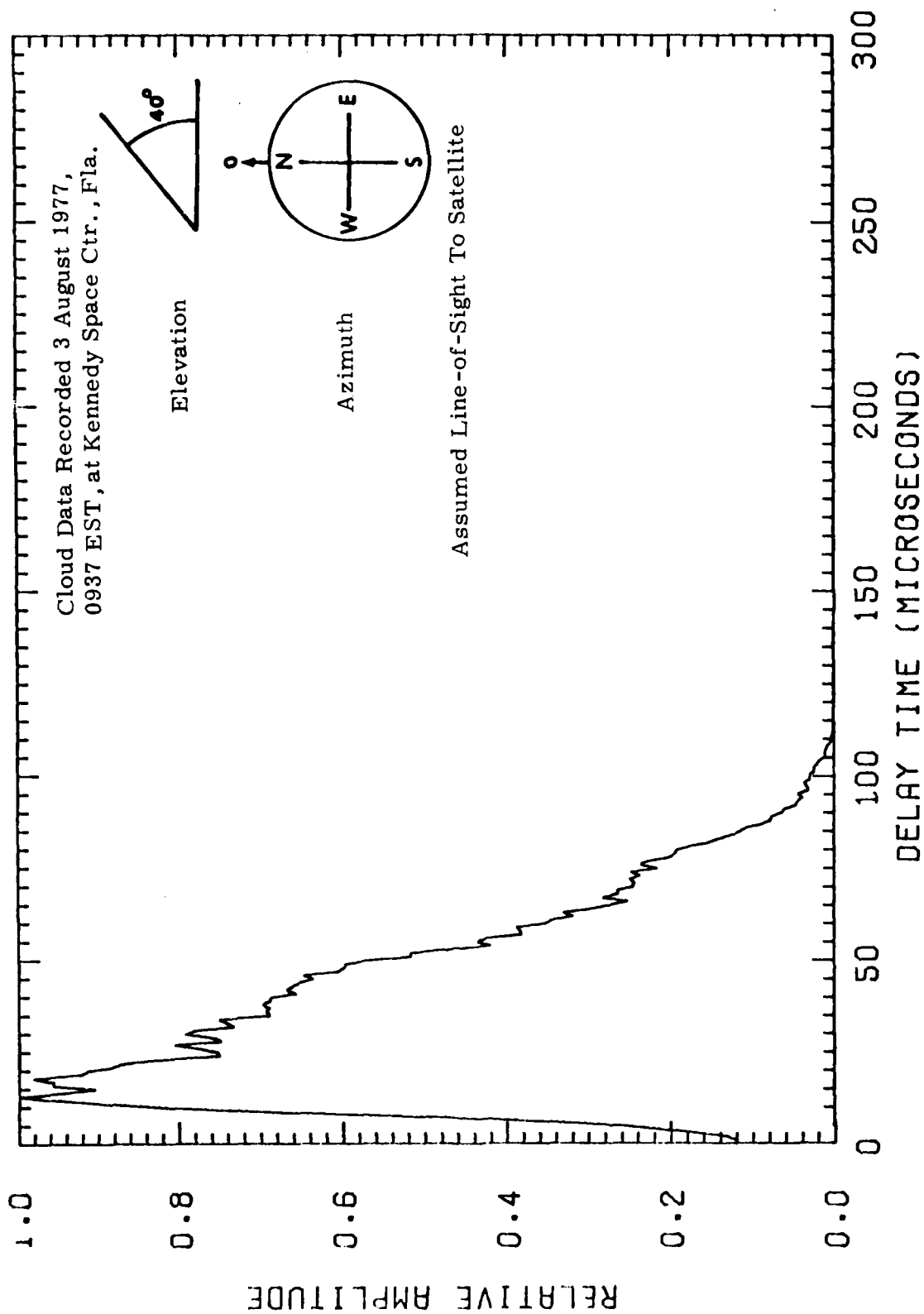


Date 3 August 1967

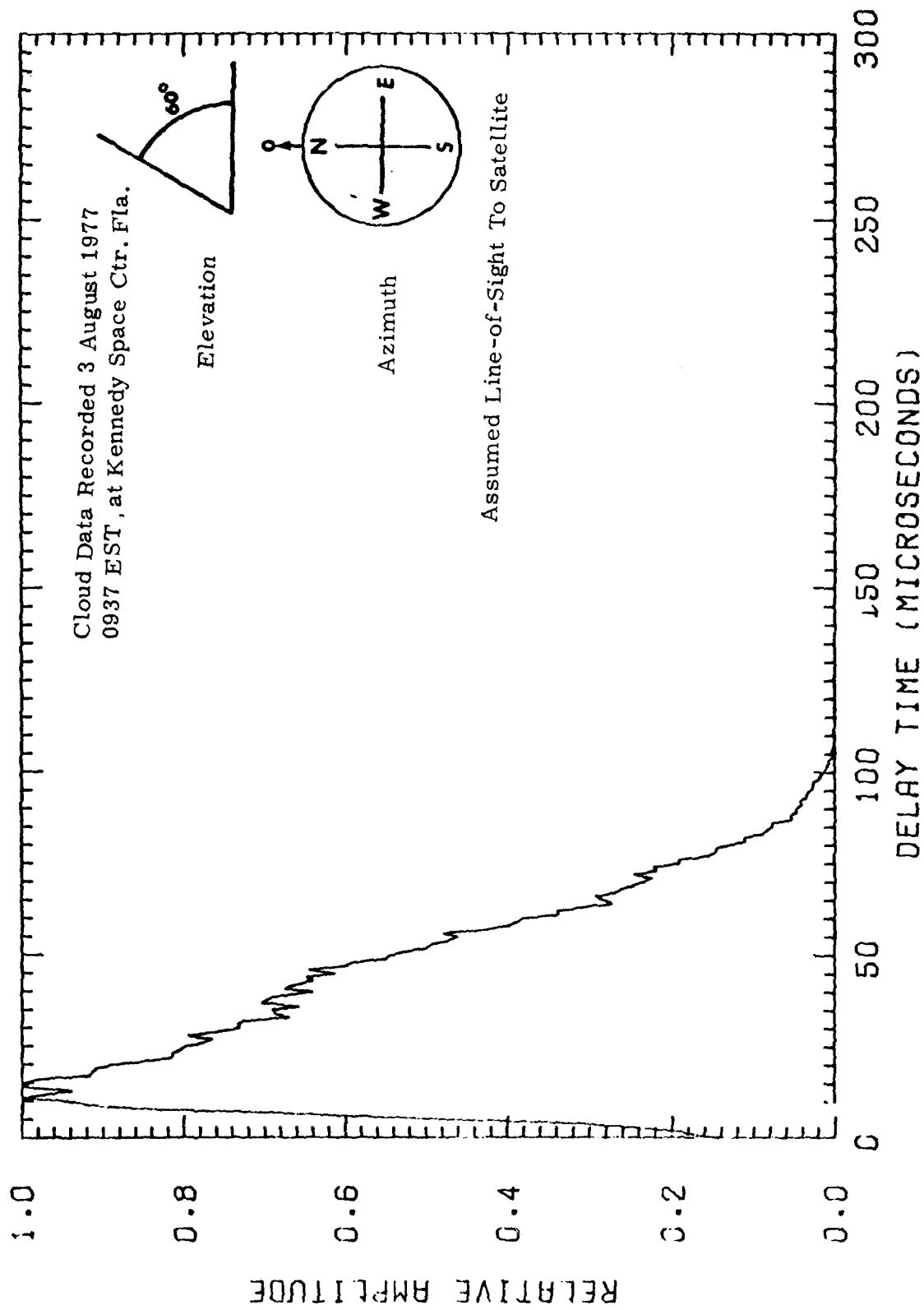
Time 9:37 EST

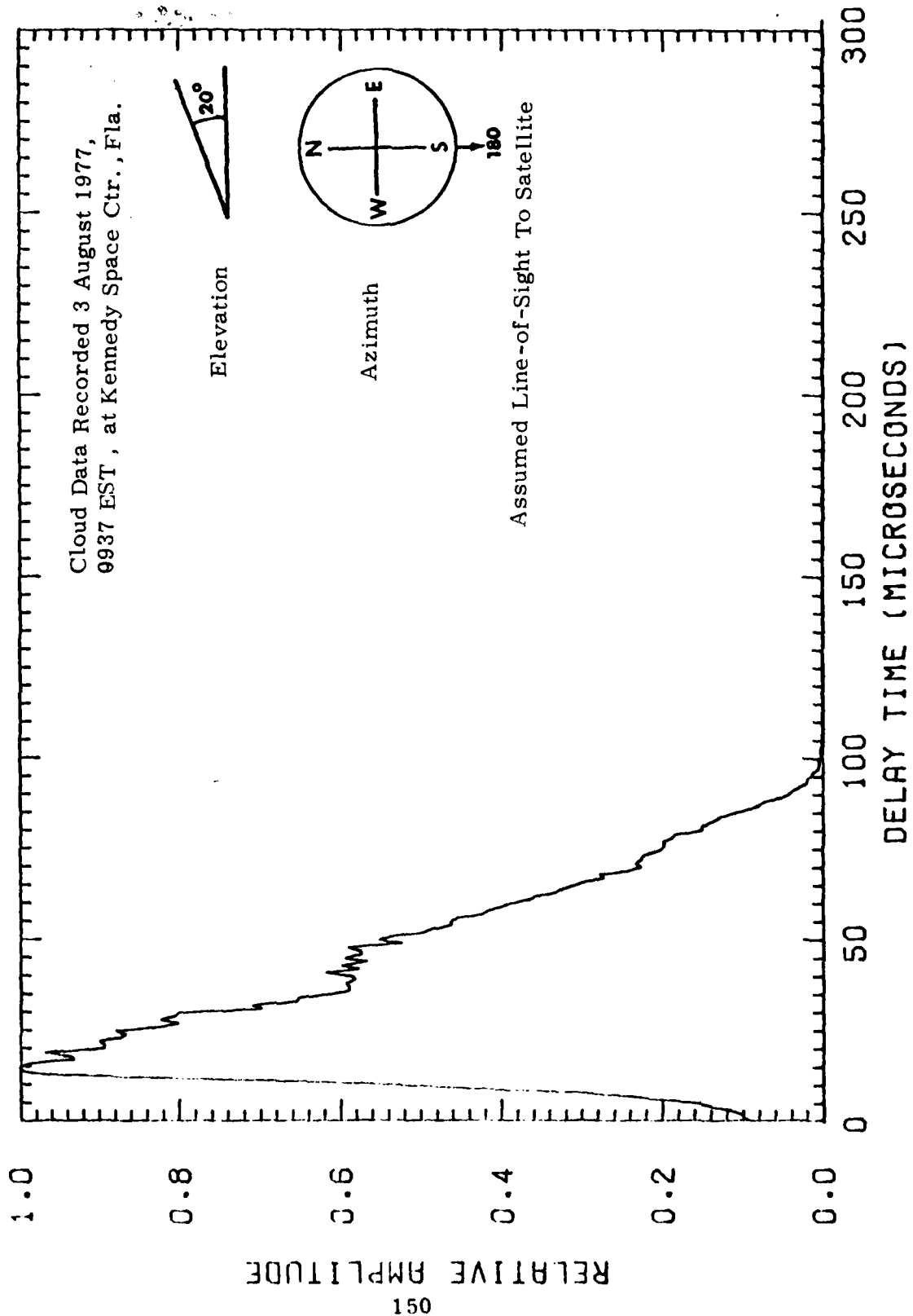


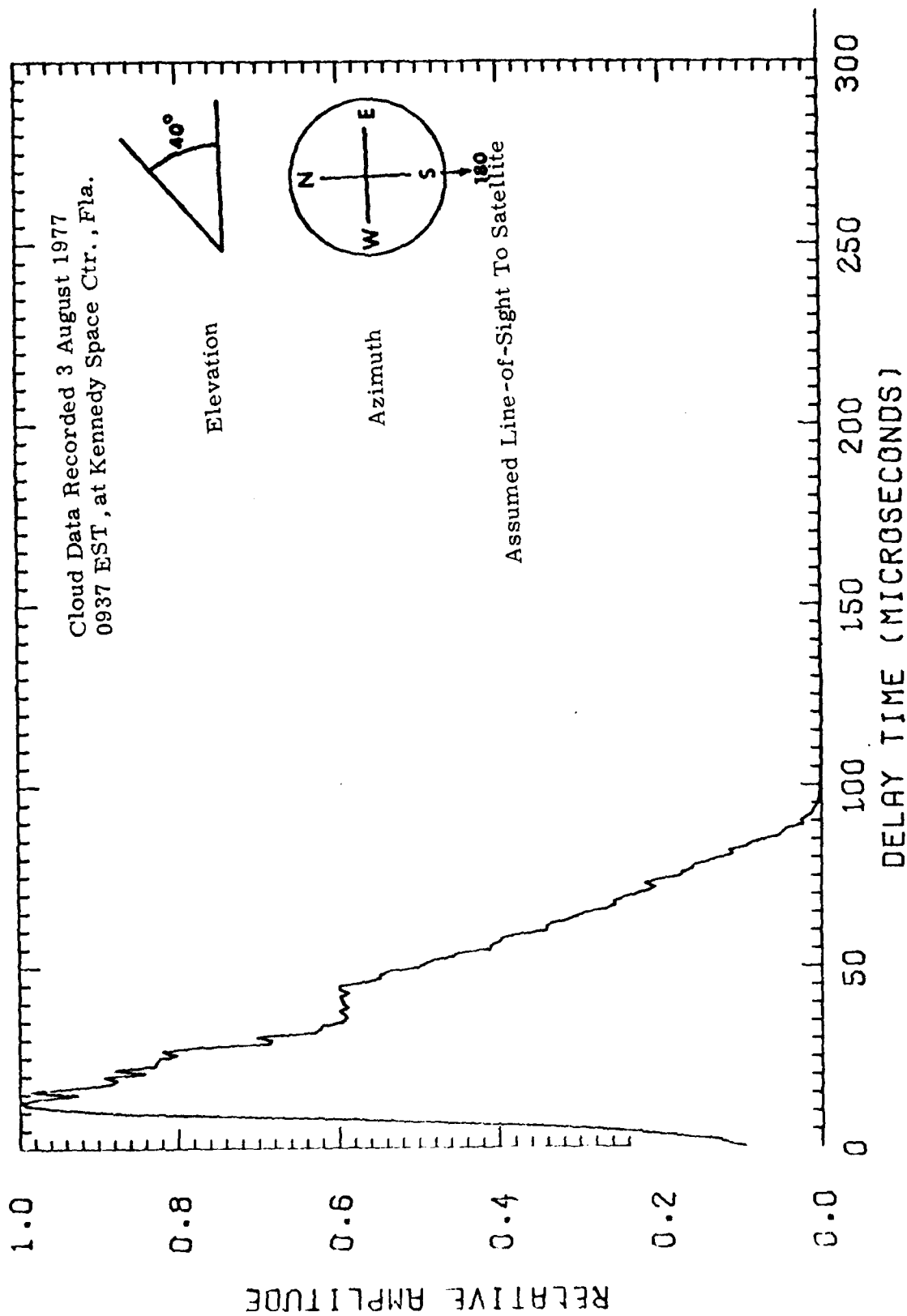


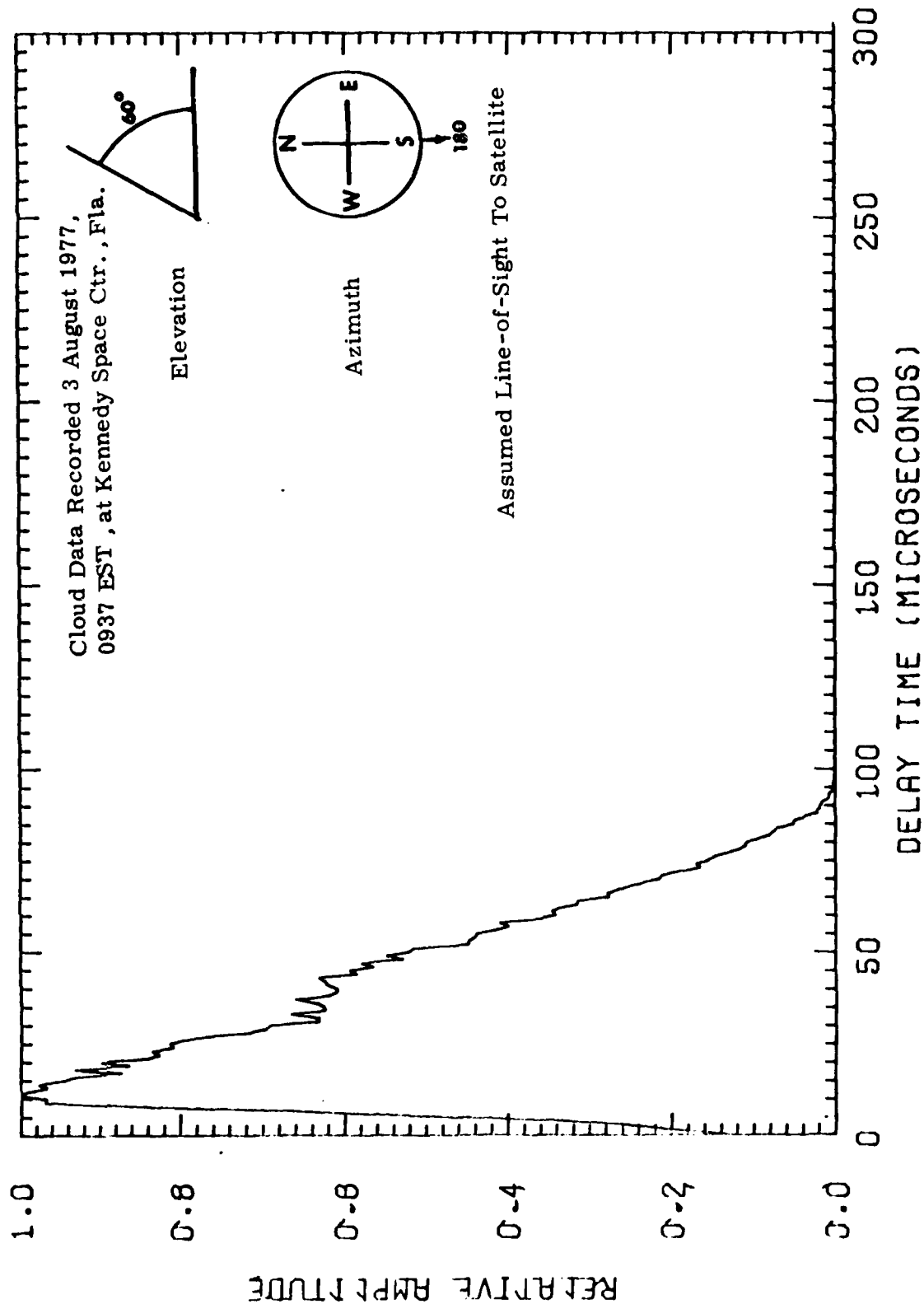


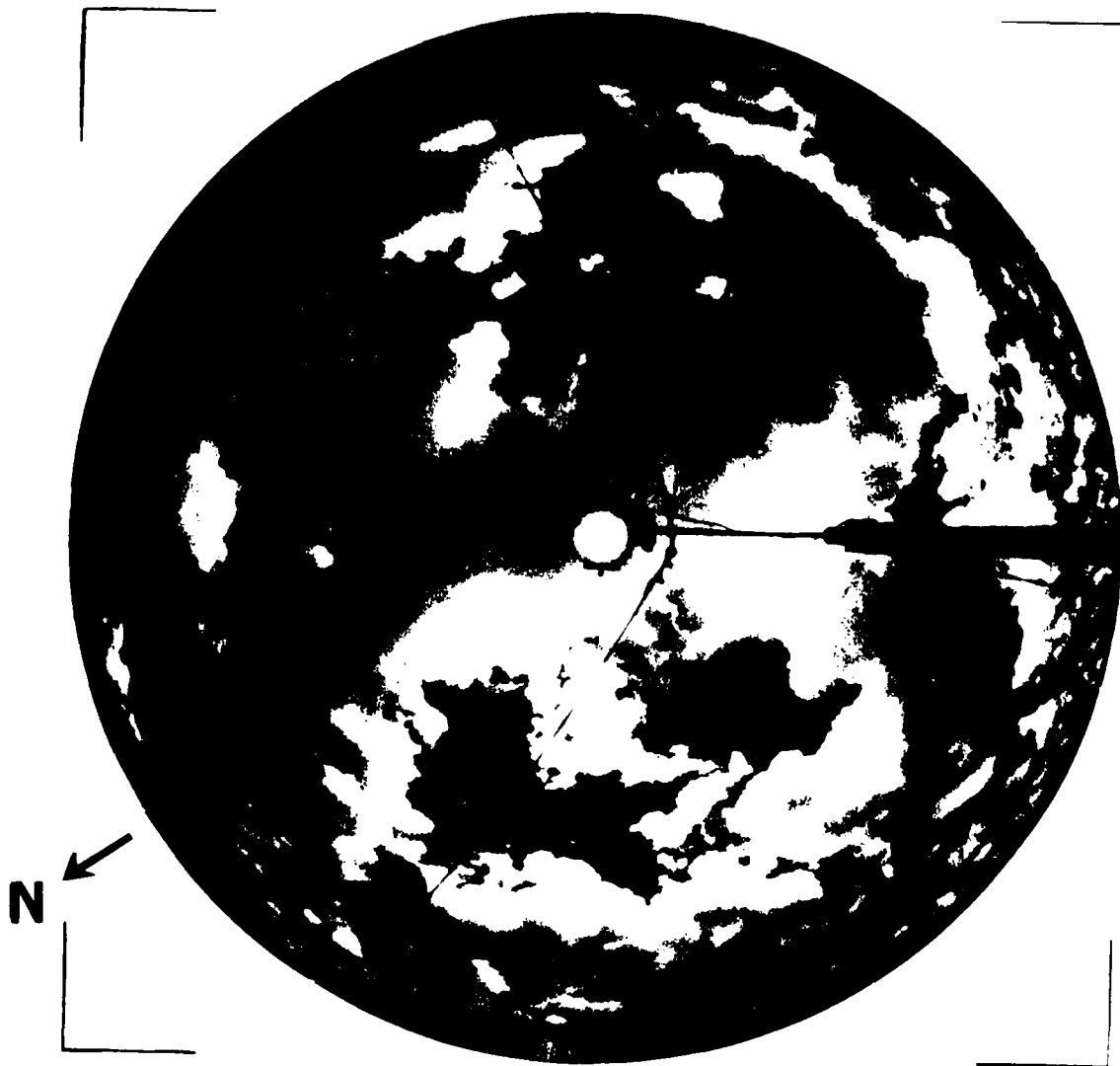




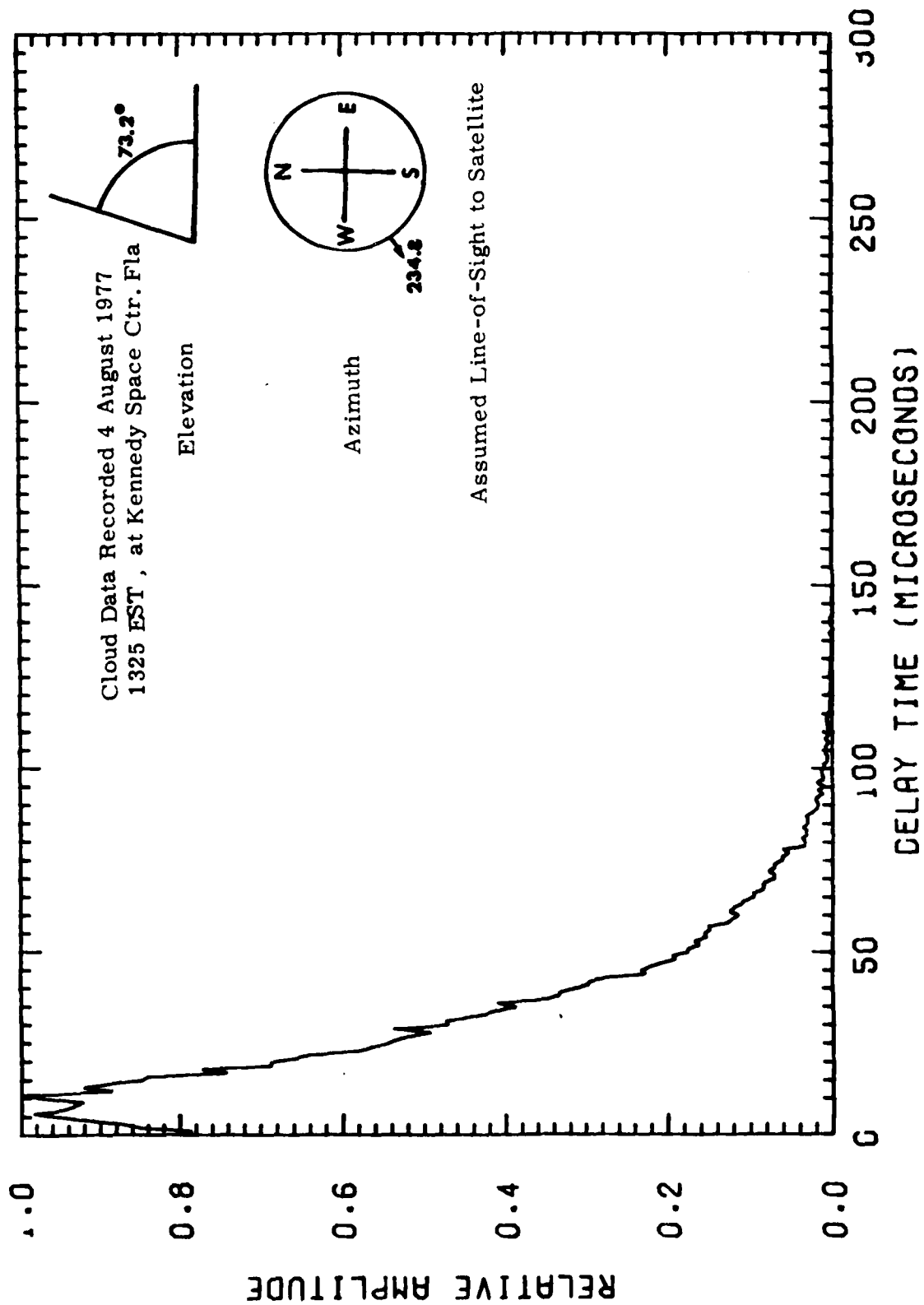


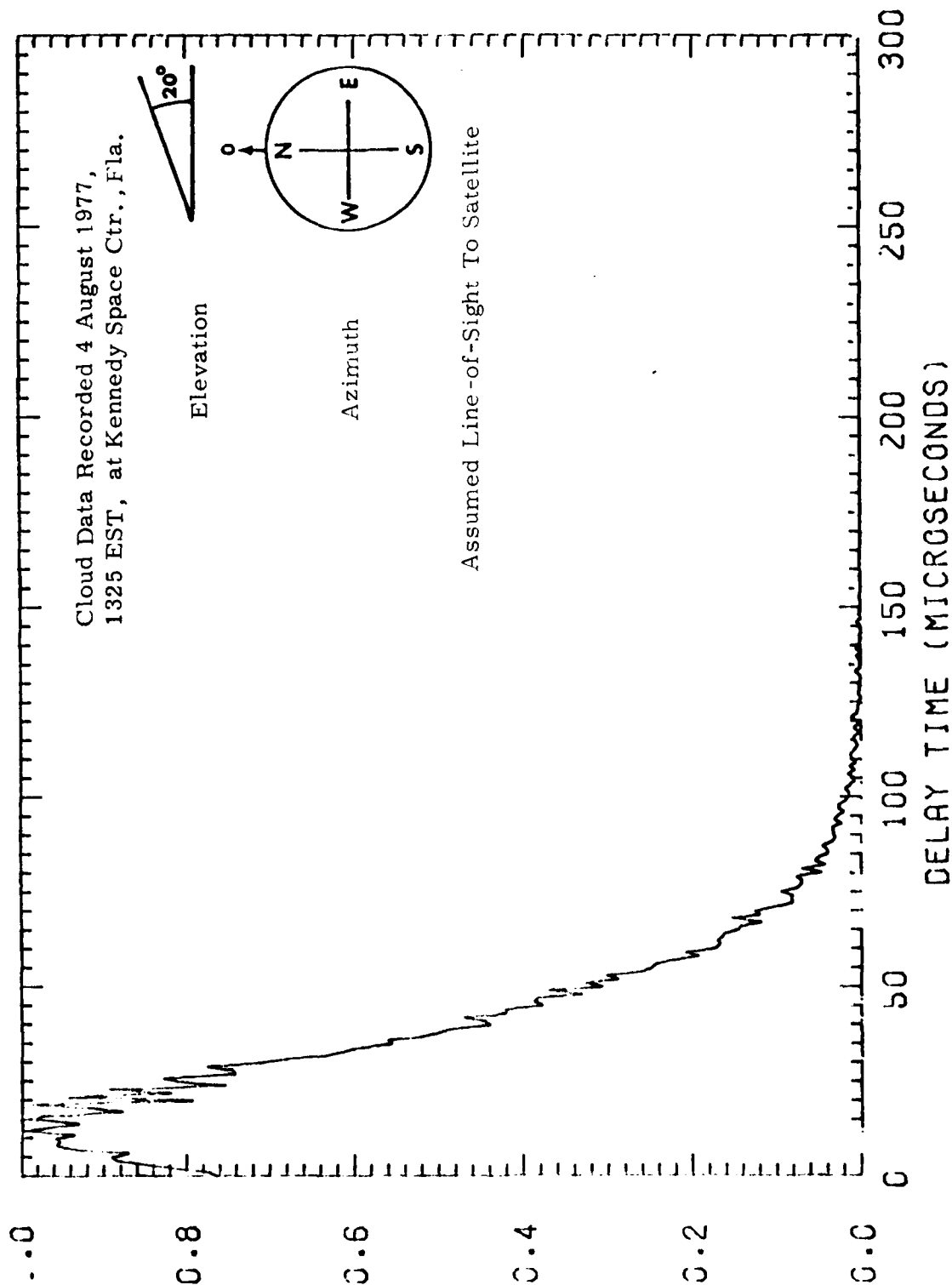


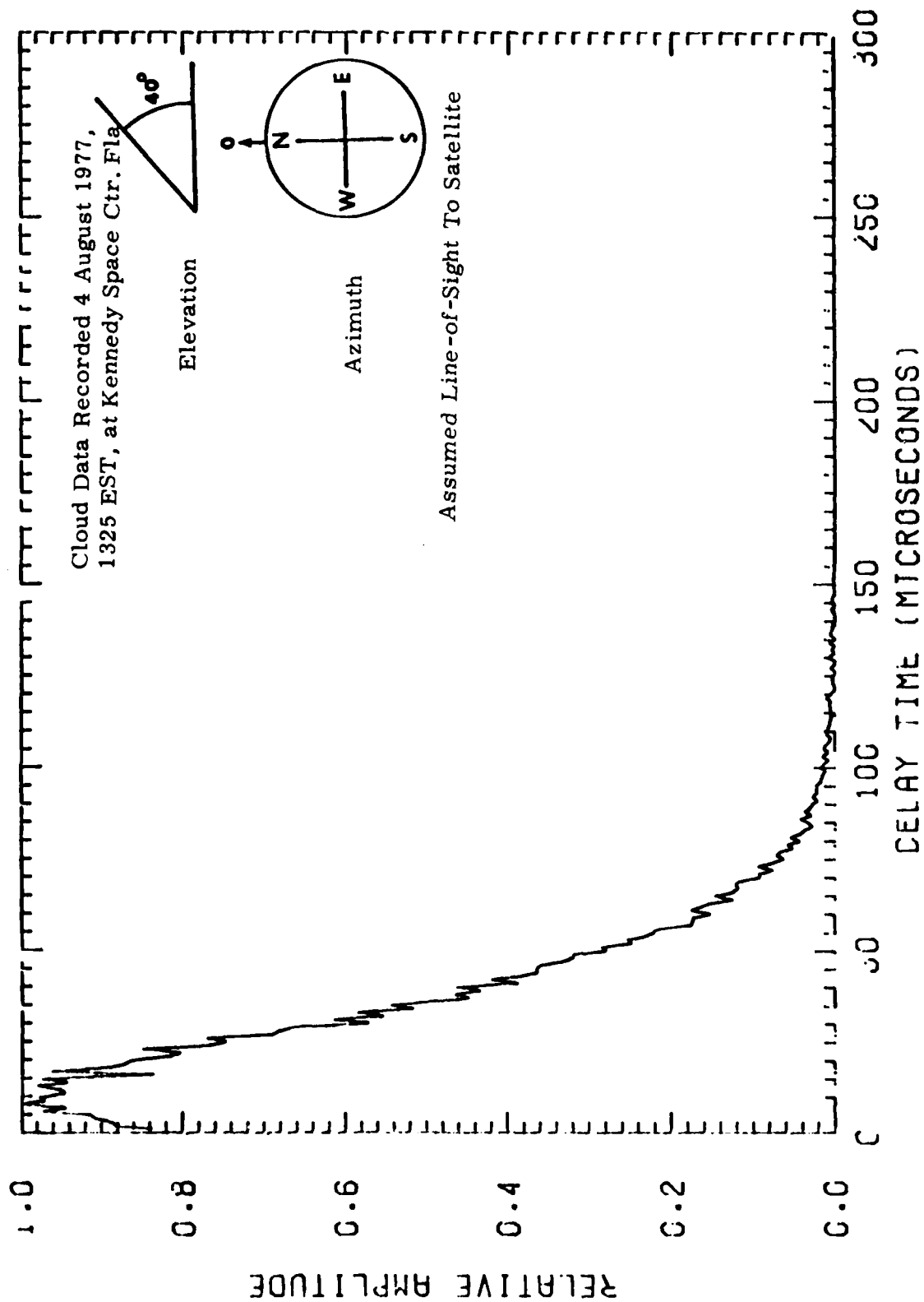




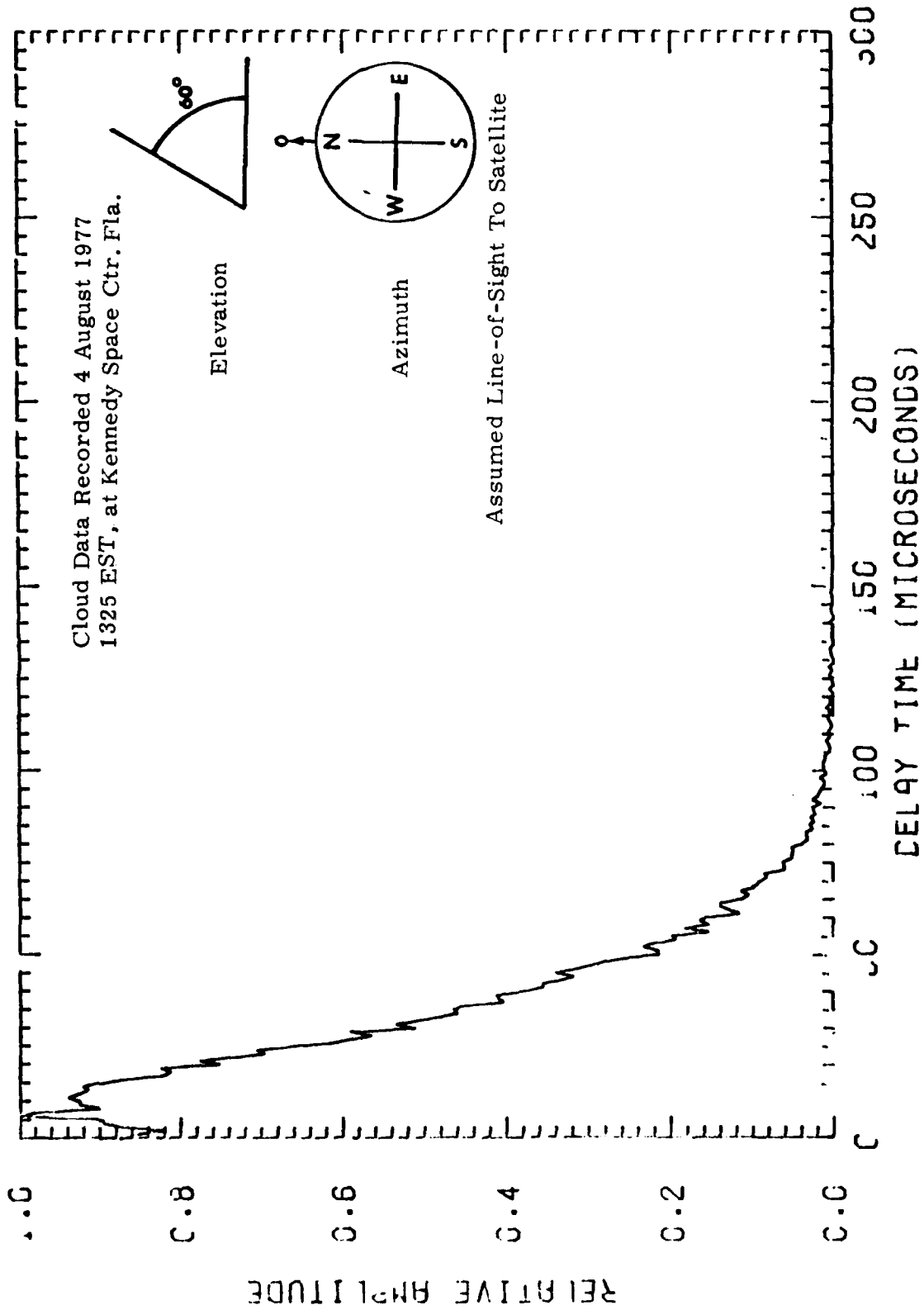
Date 4 August 1977  
Time 1325 EST

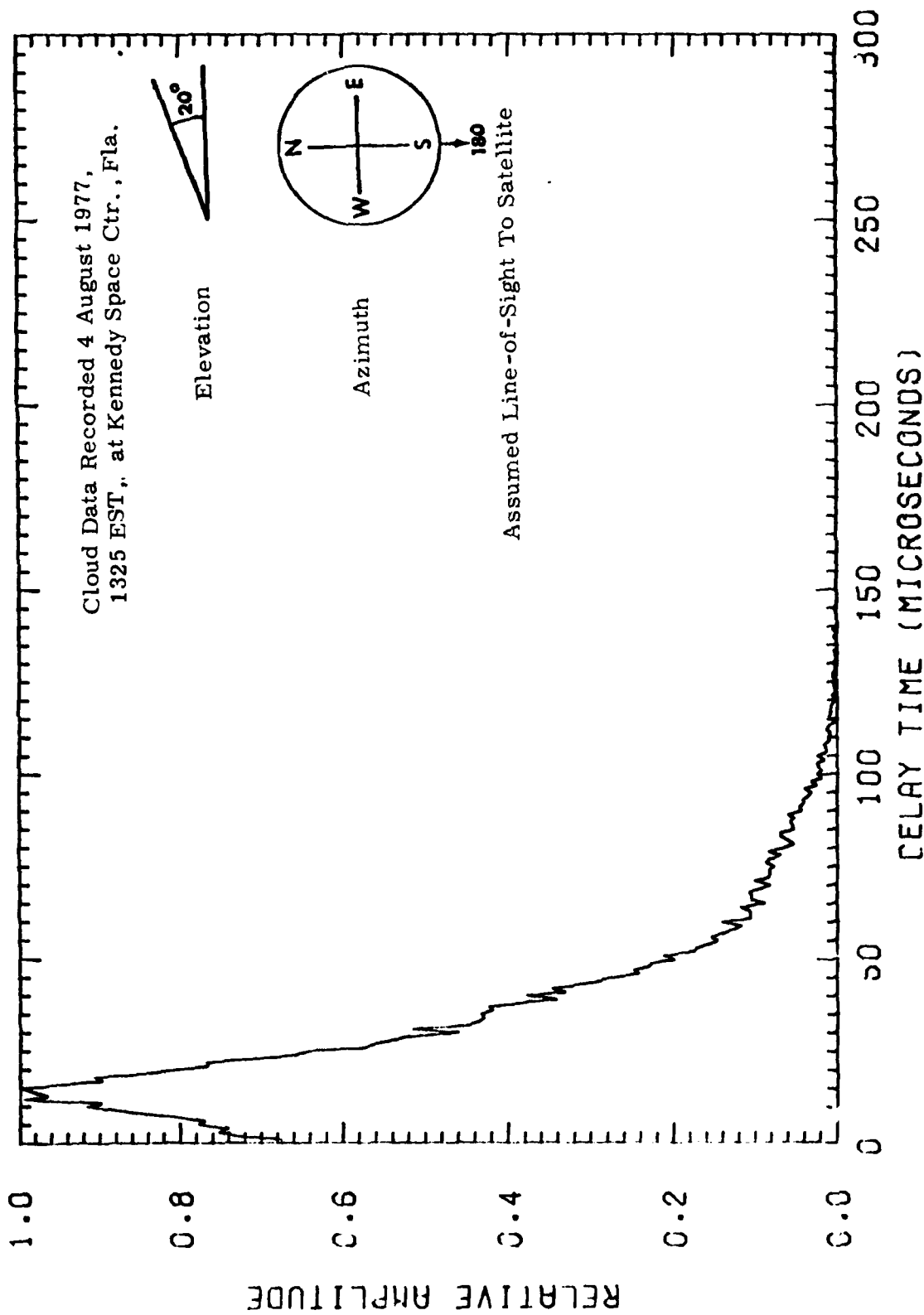


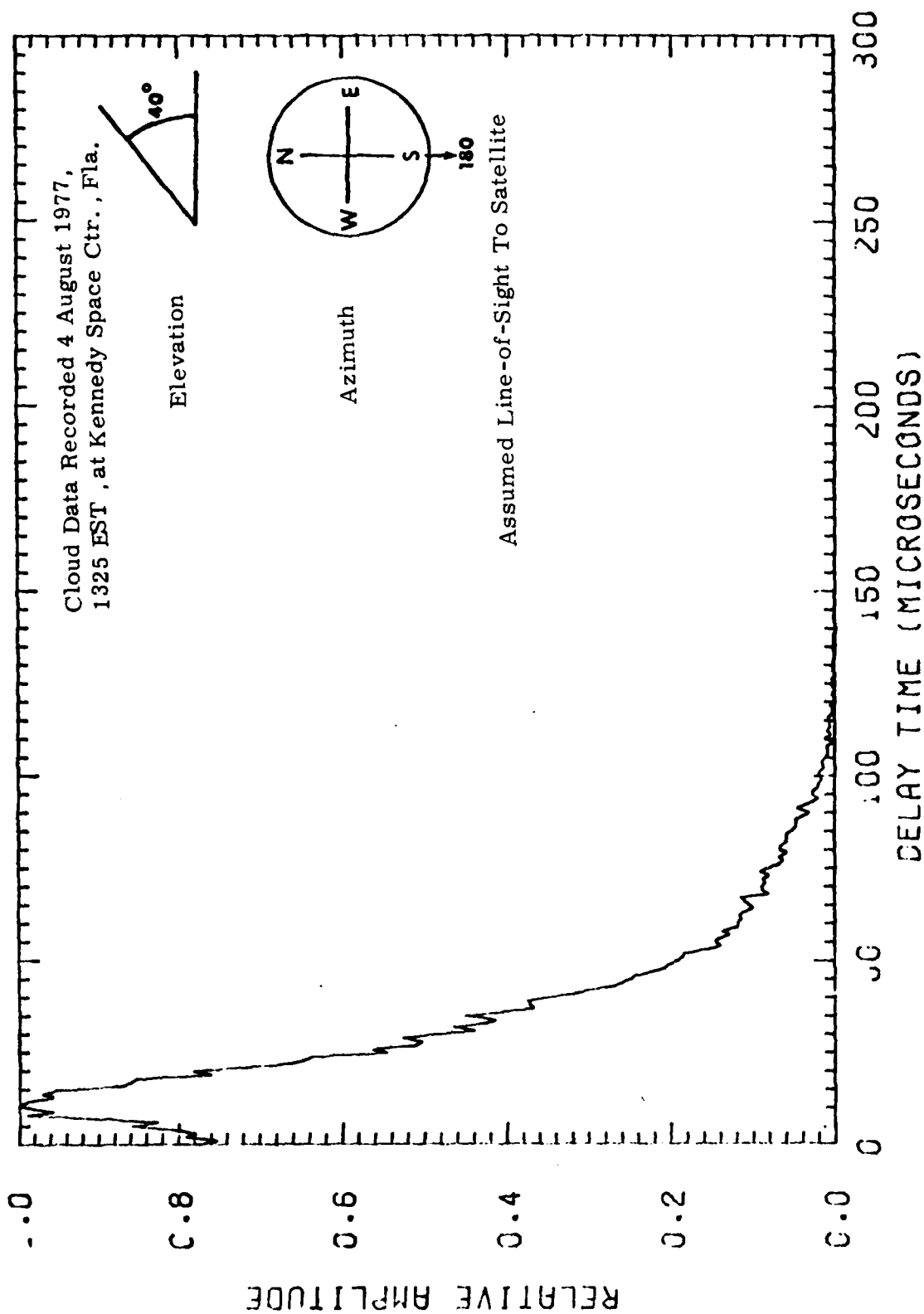


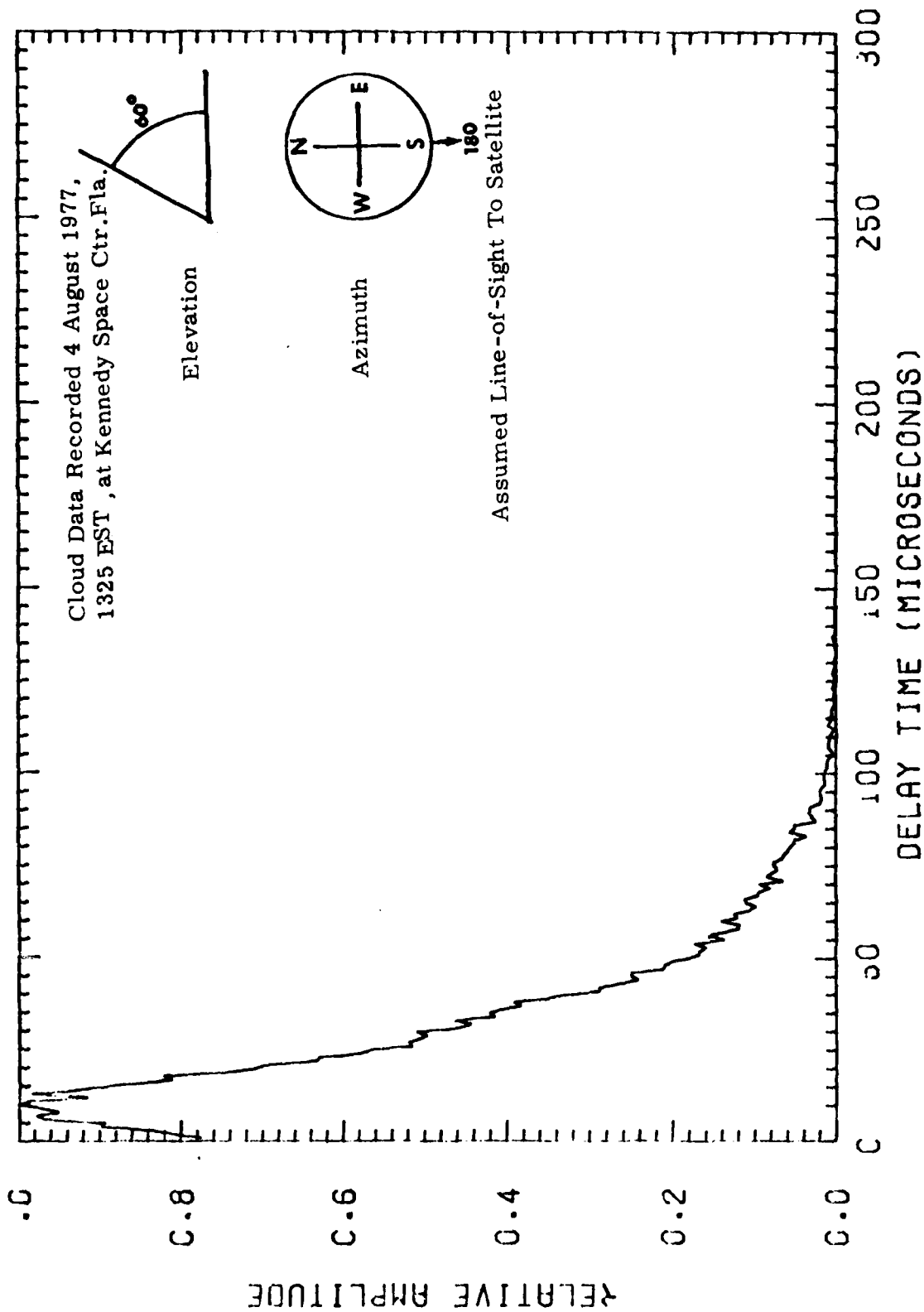


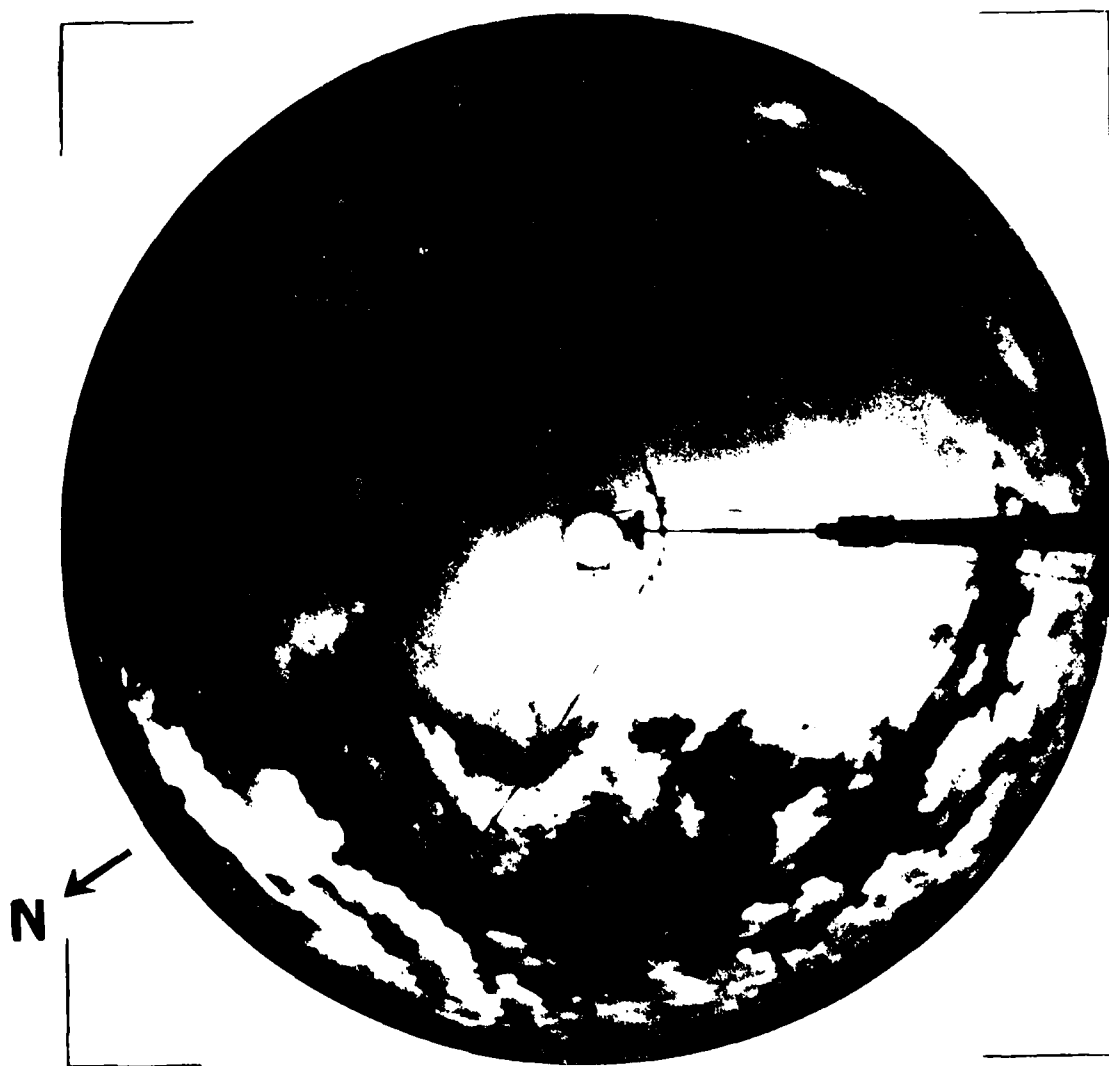






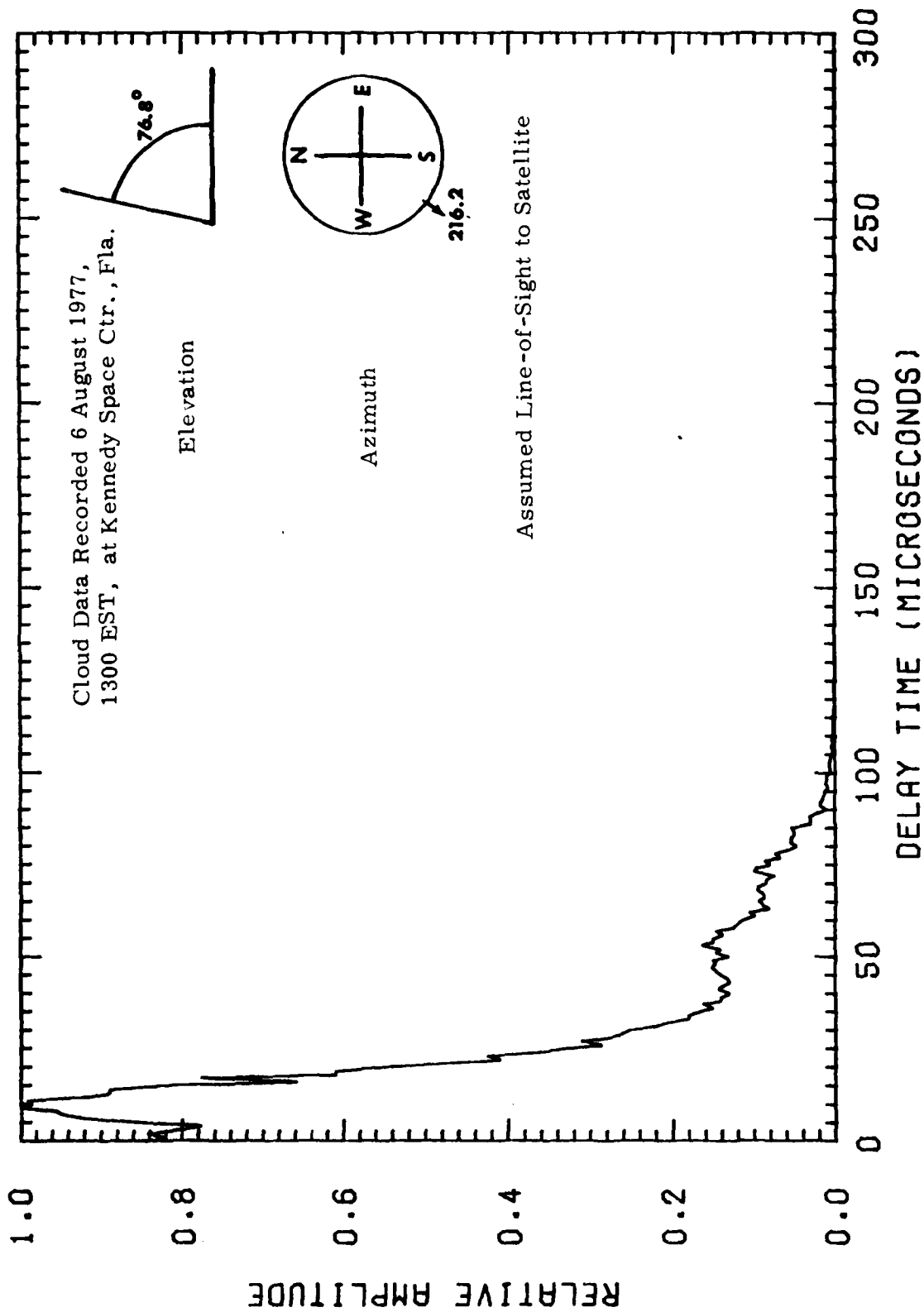


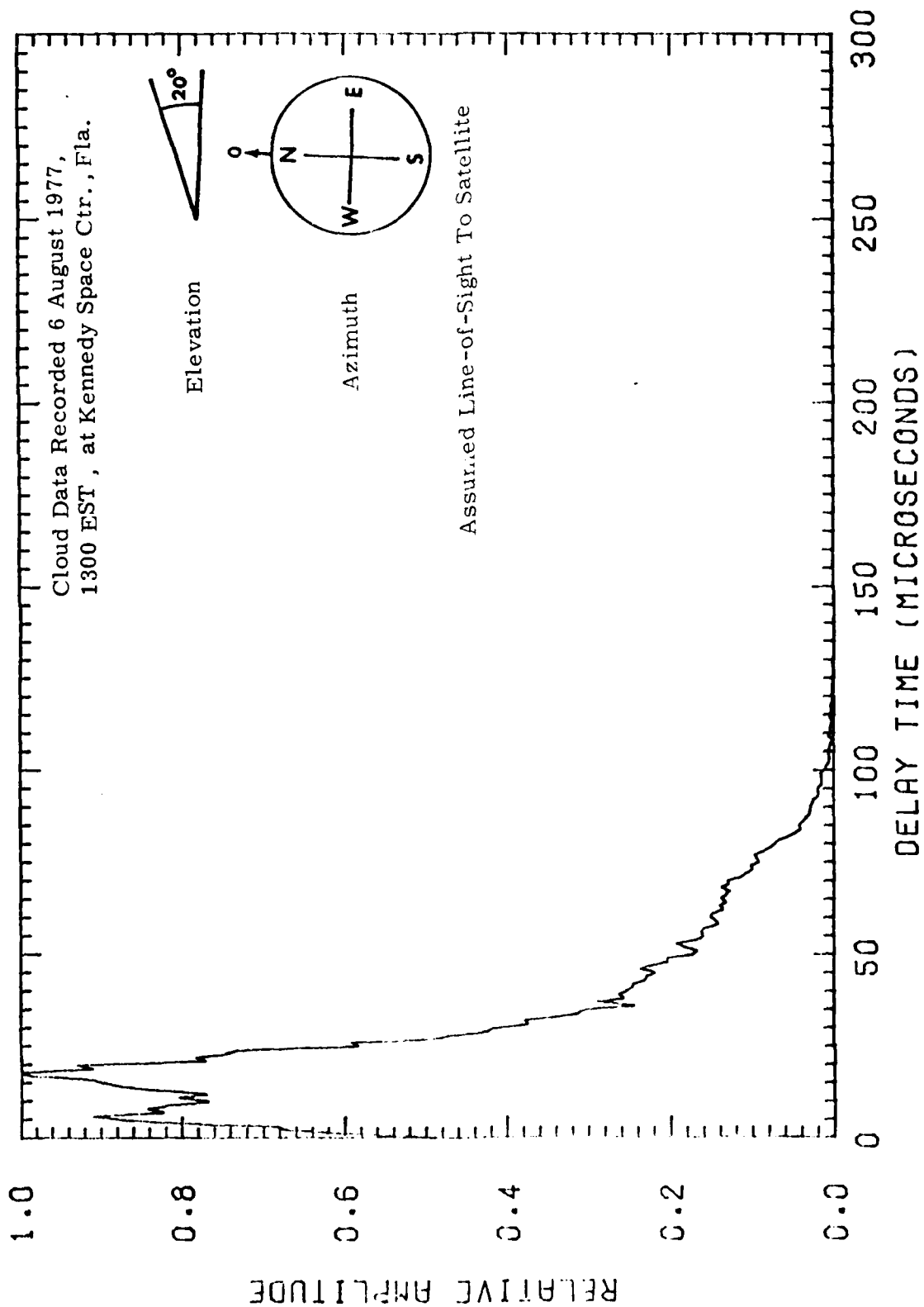


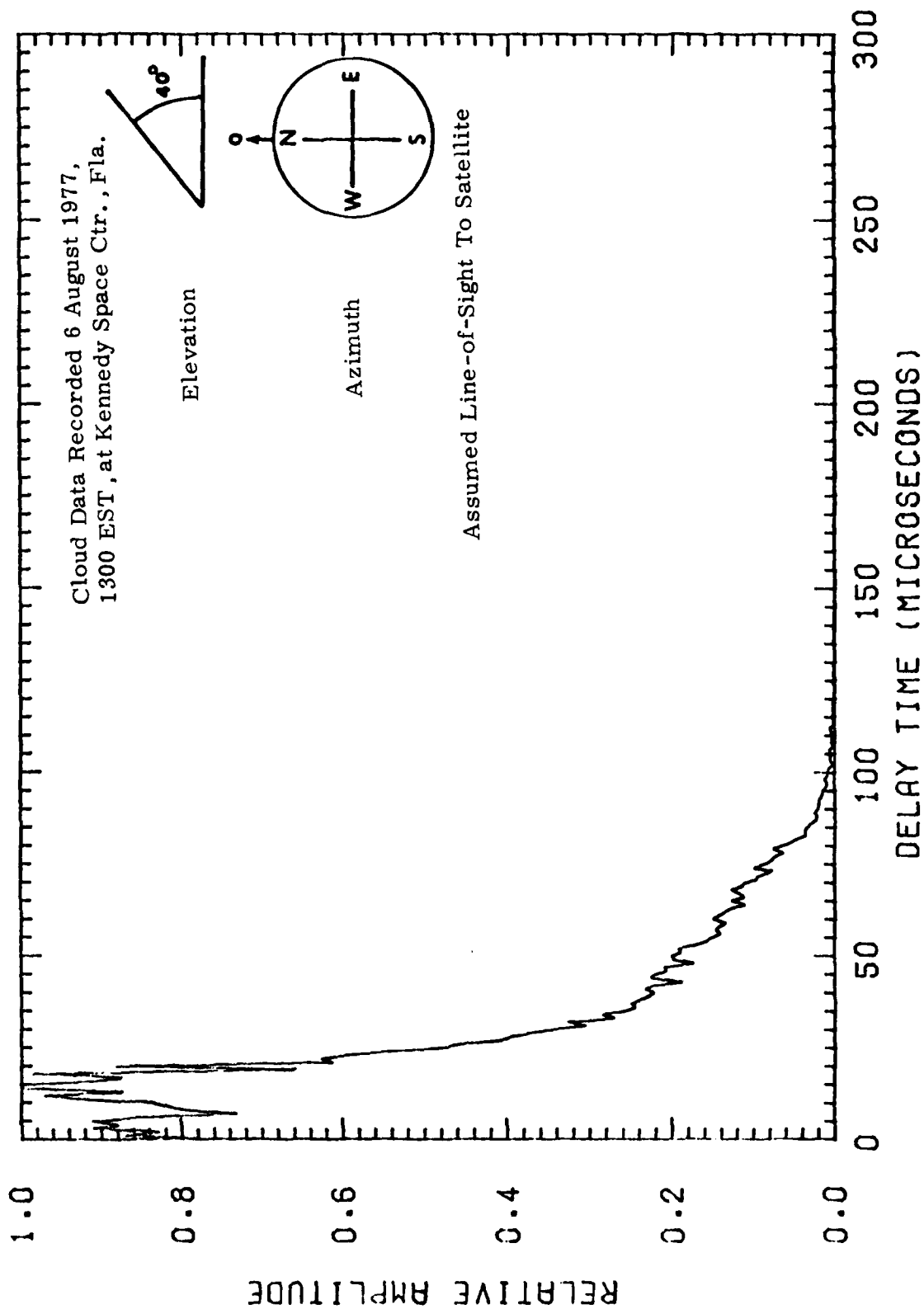


Date 6 August 1977

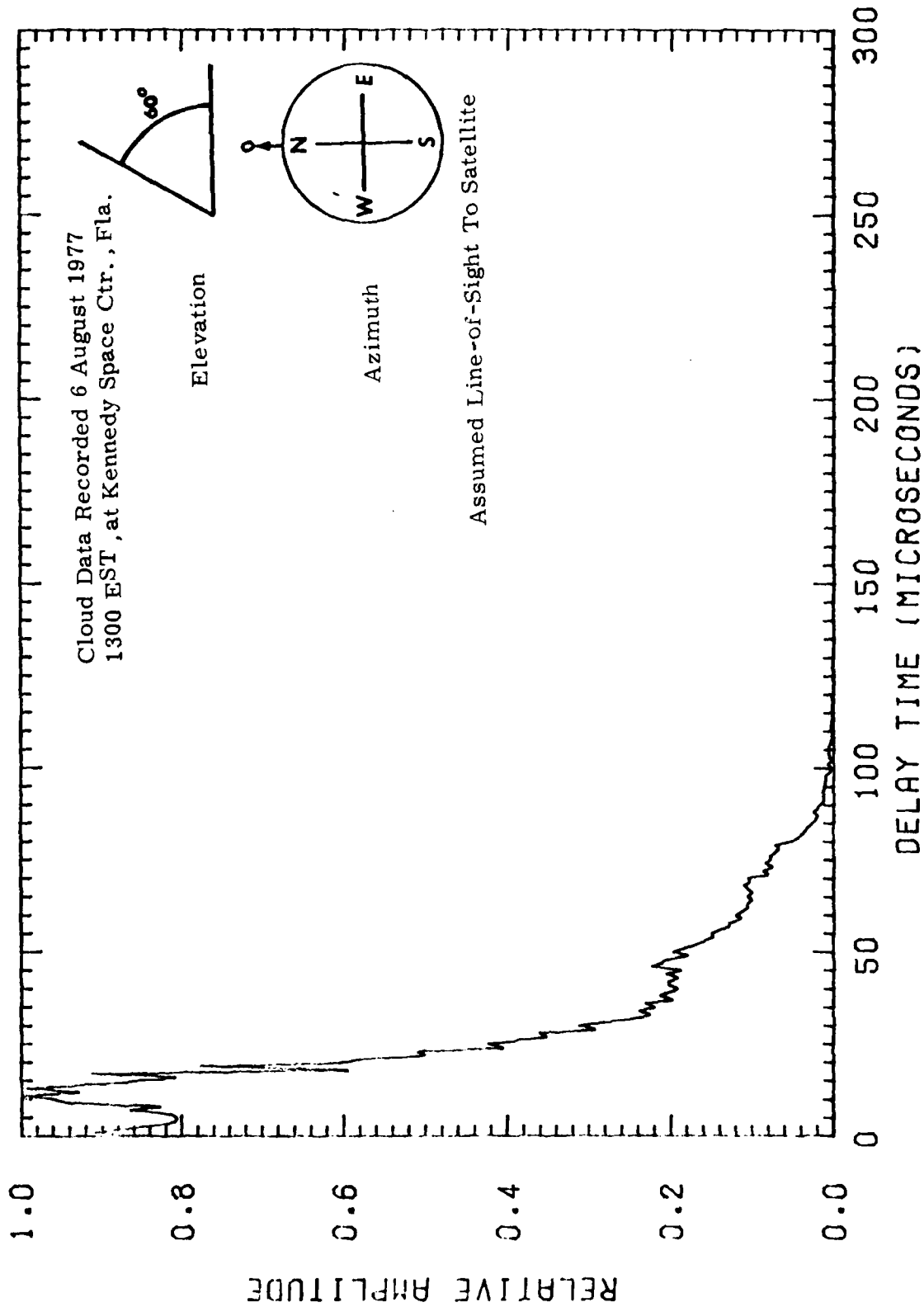
Time 1300 EST

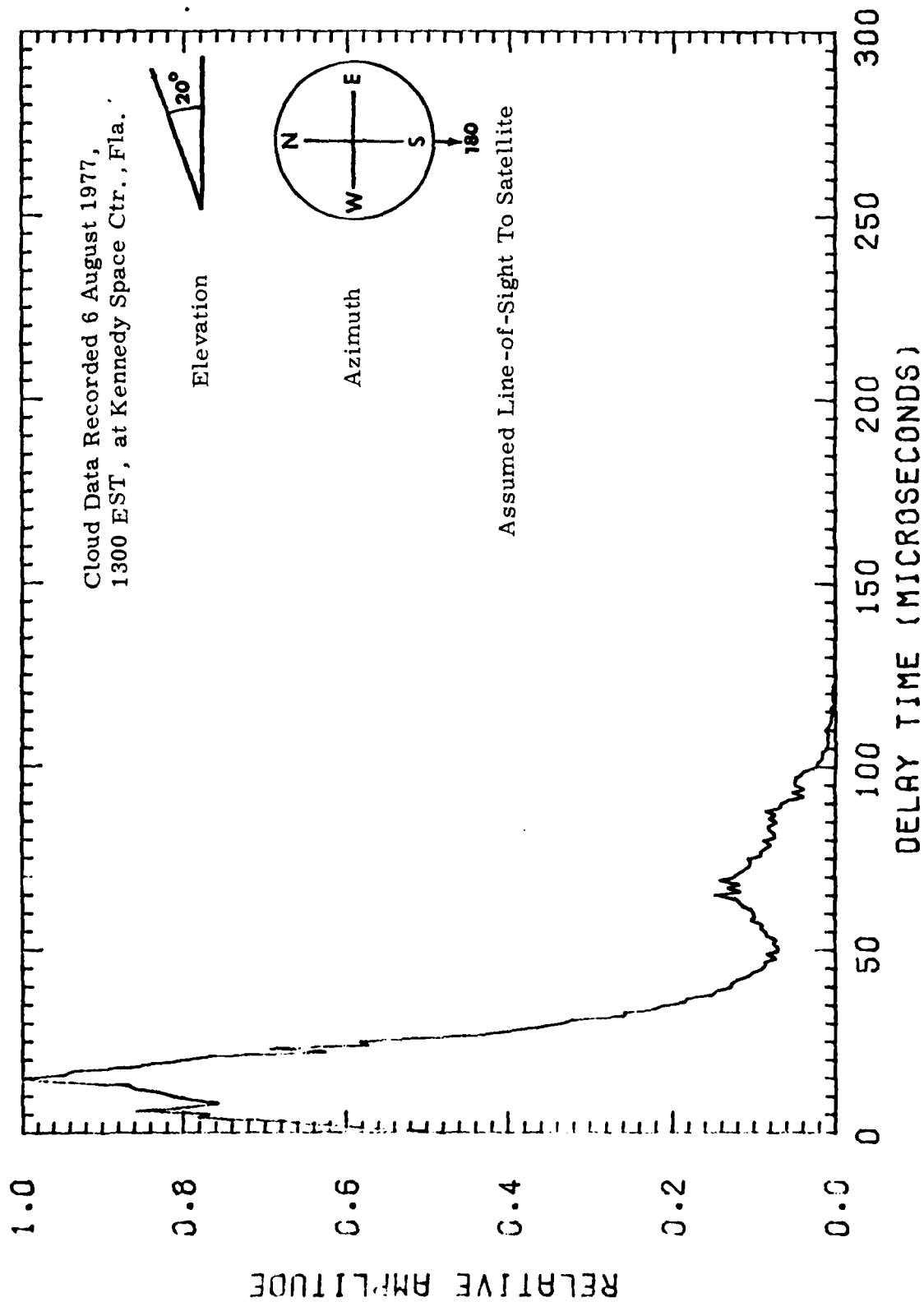


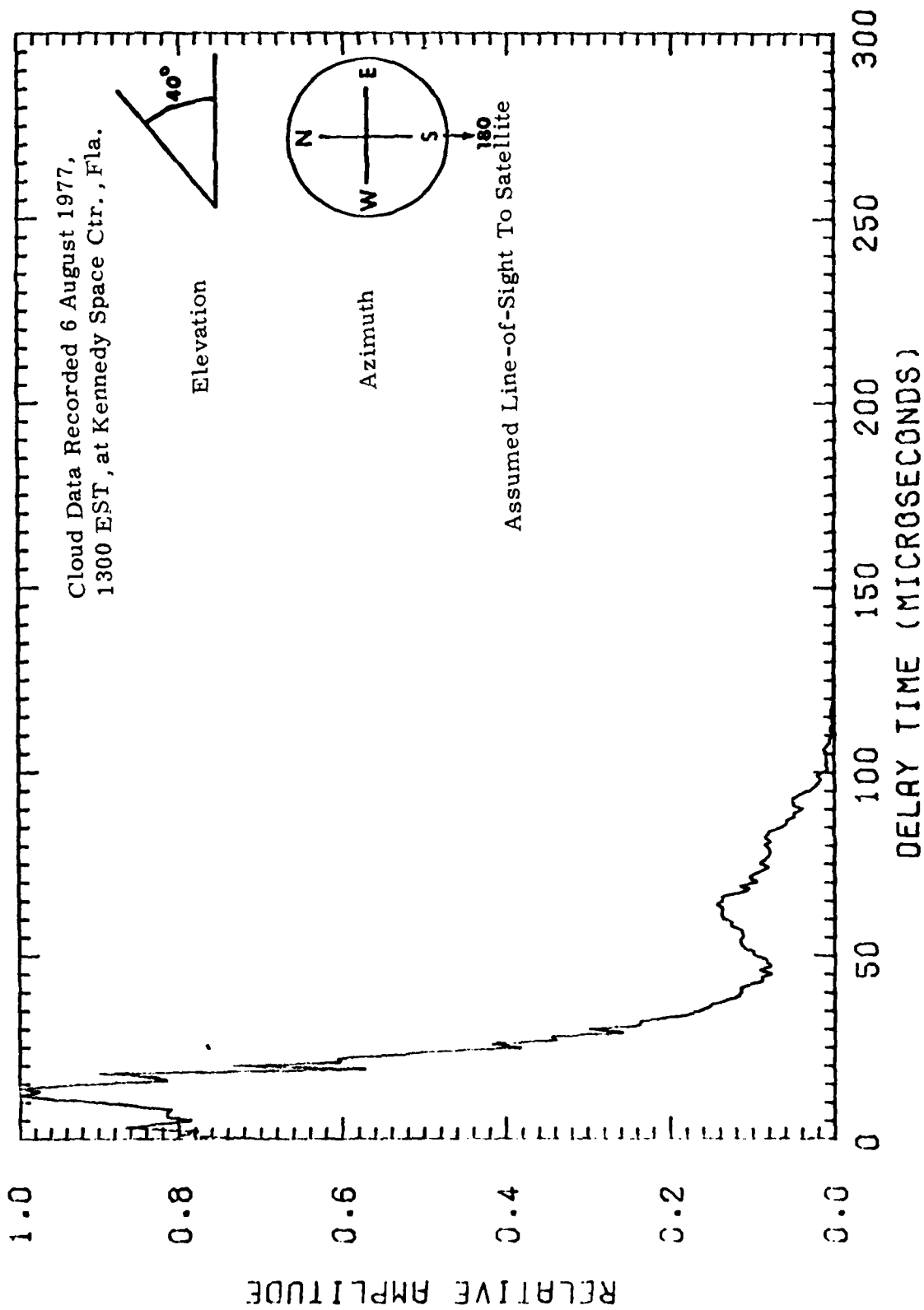


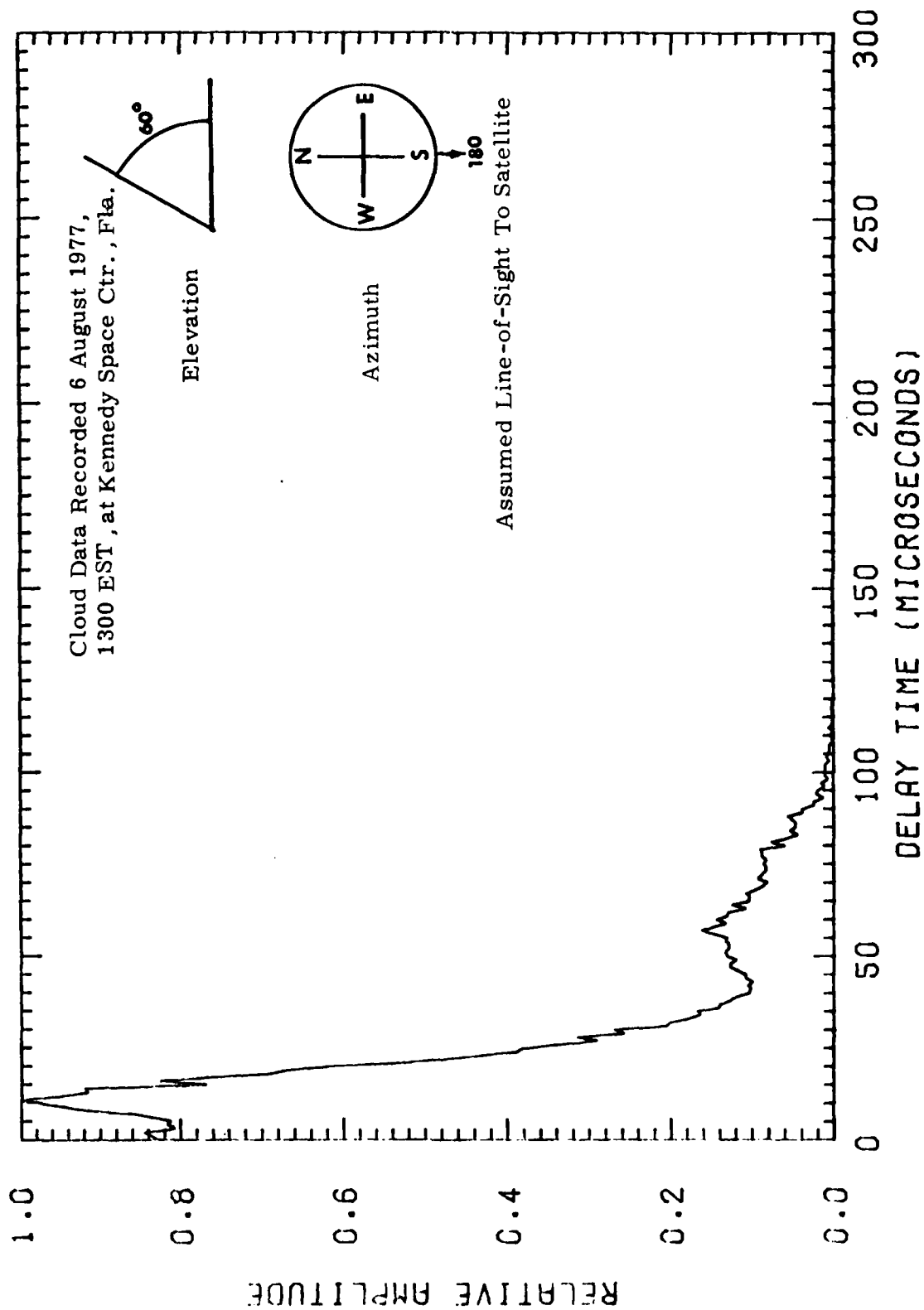








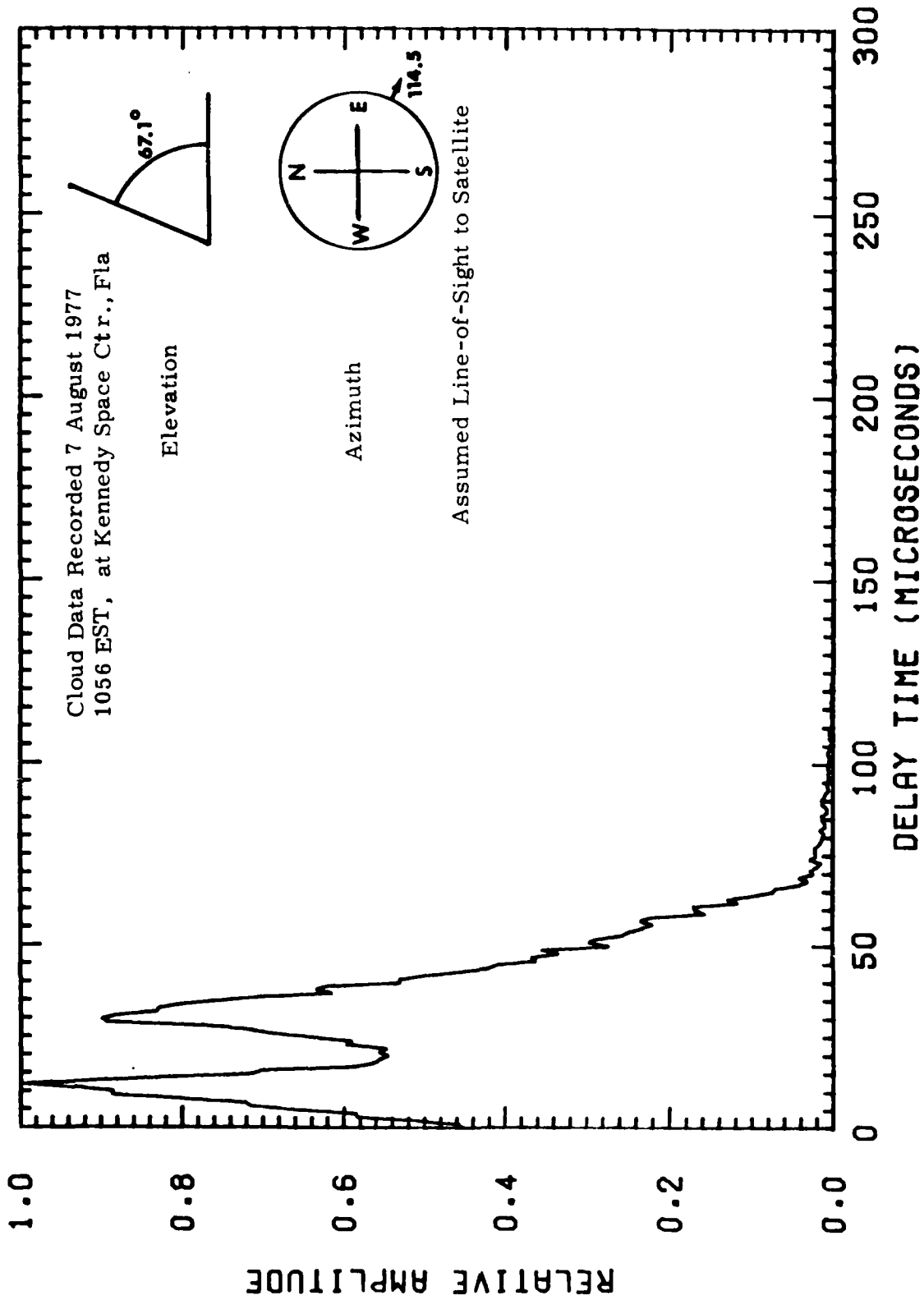


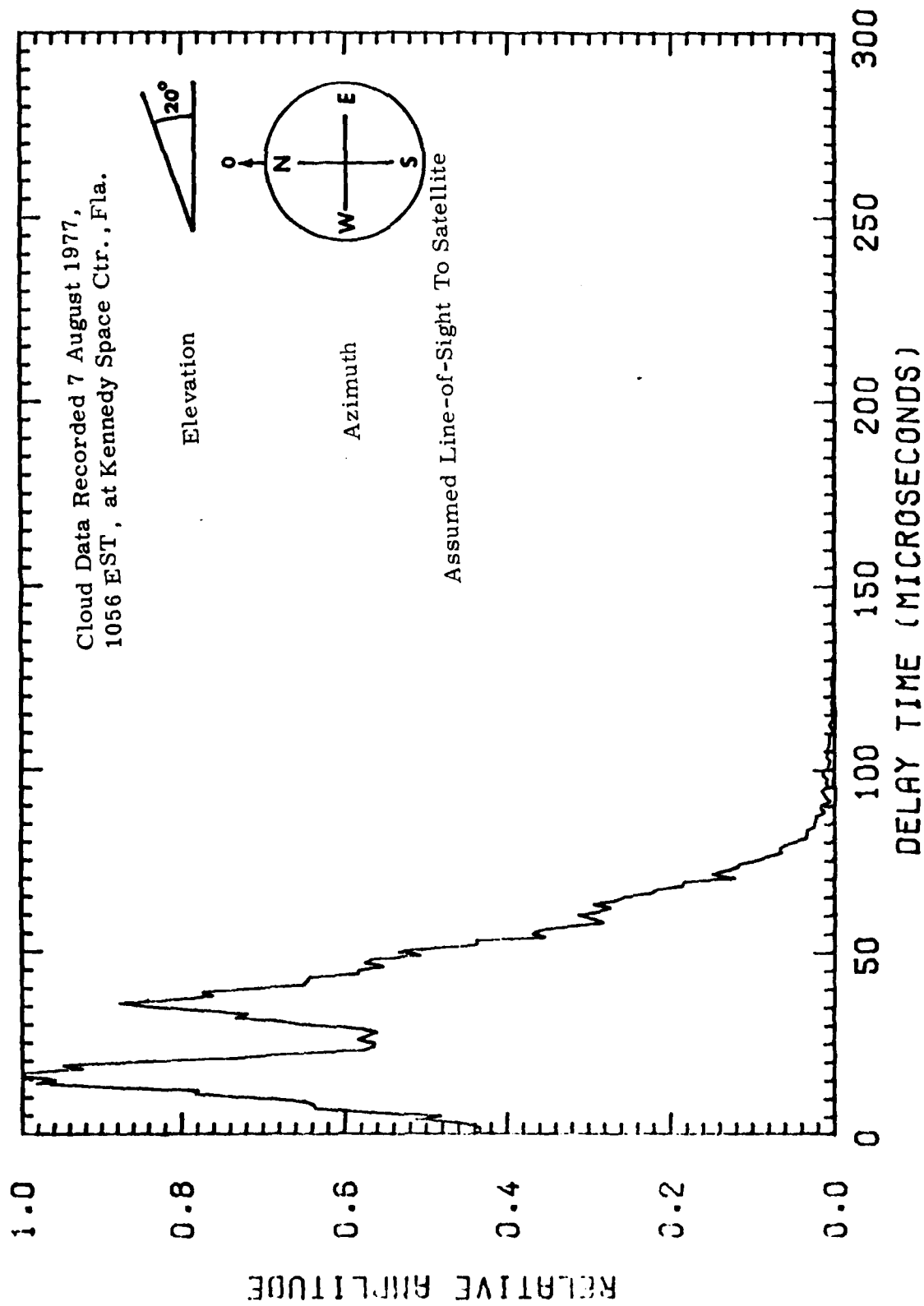


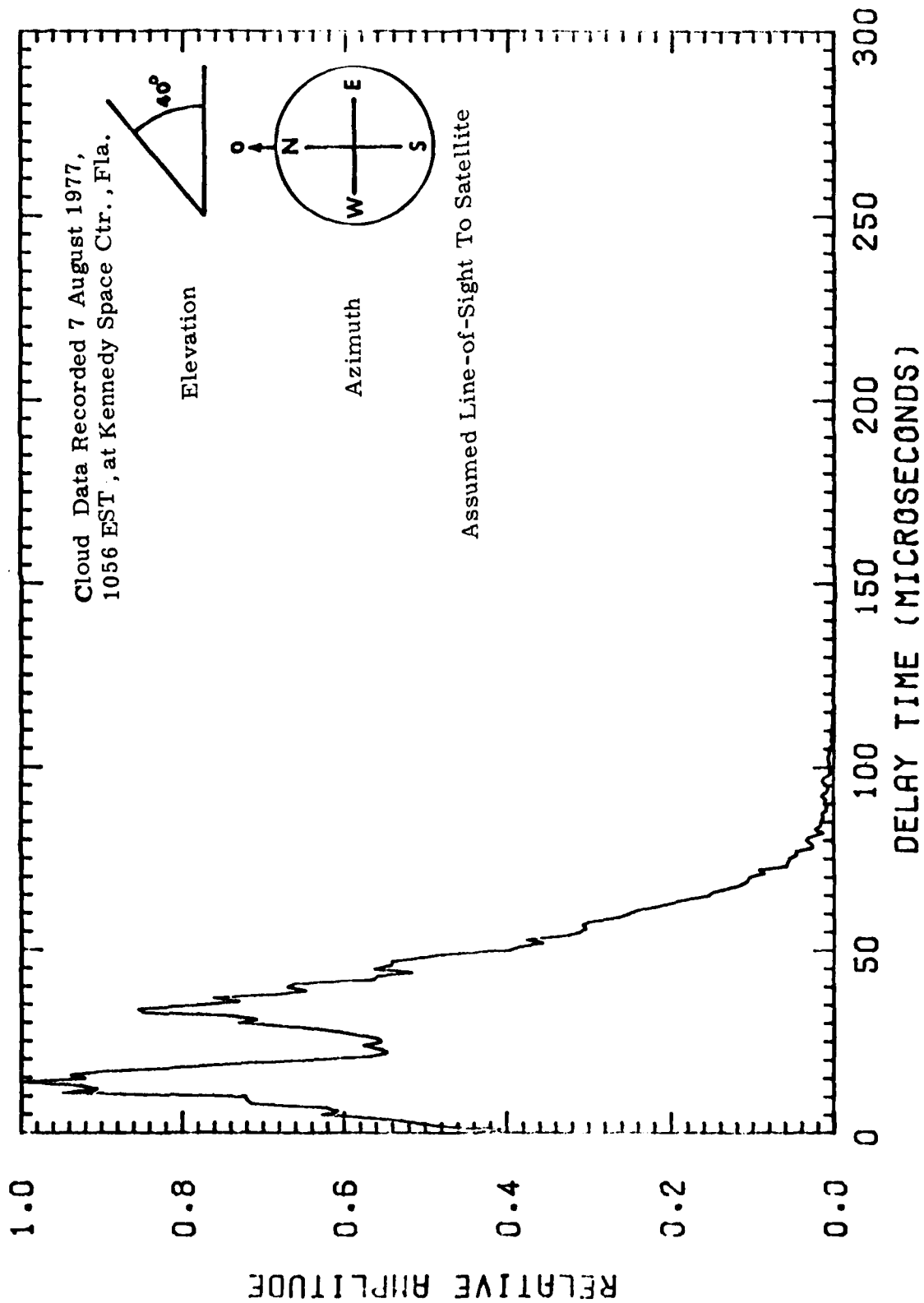


Date: 10/10/70

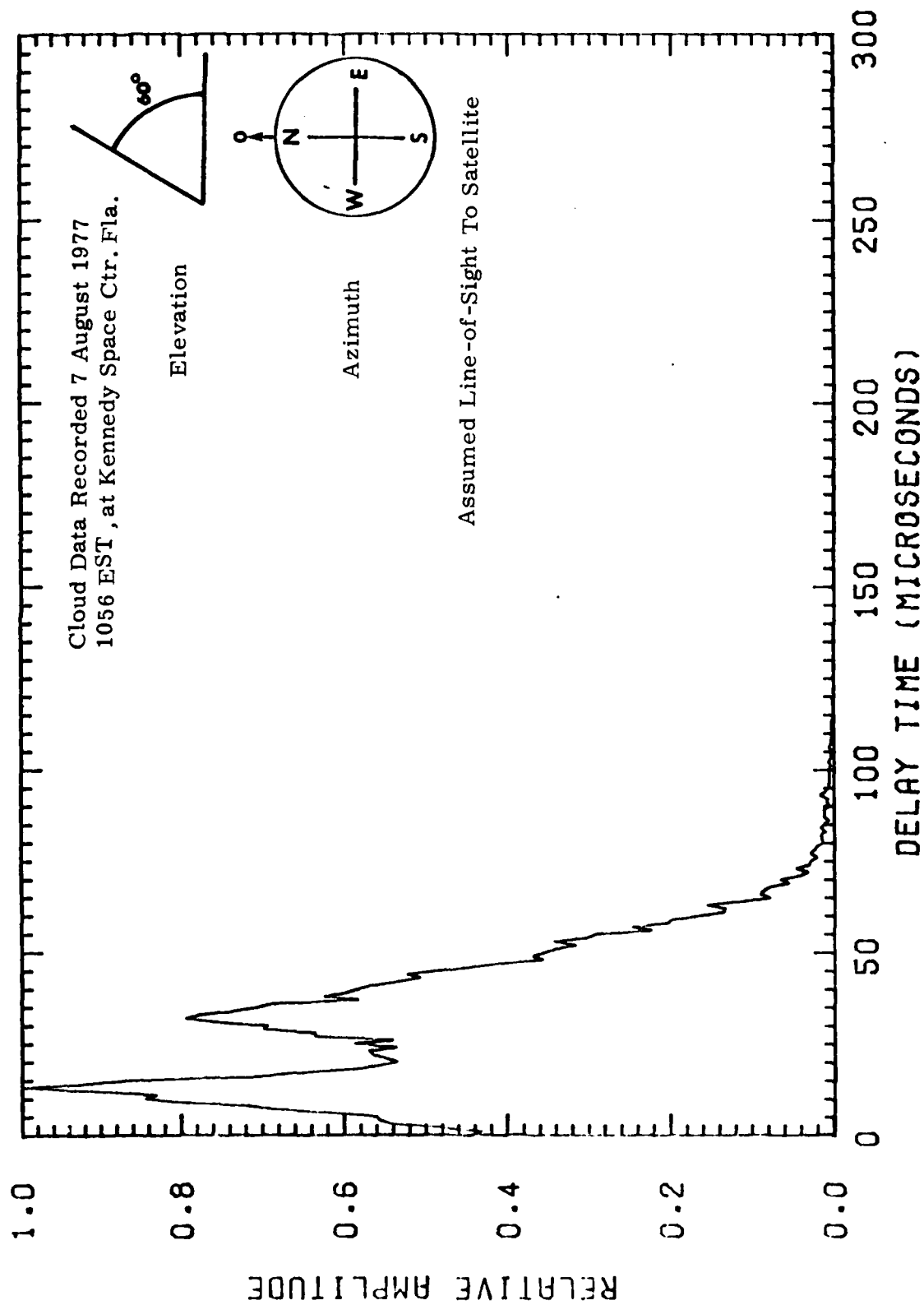
Time: 04:00

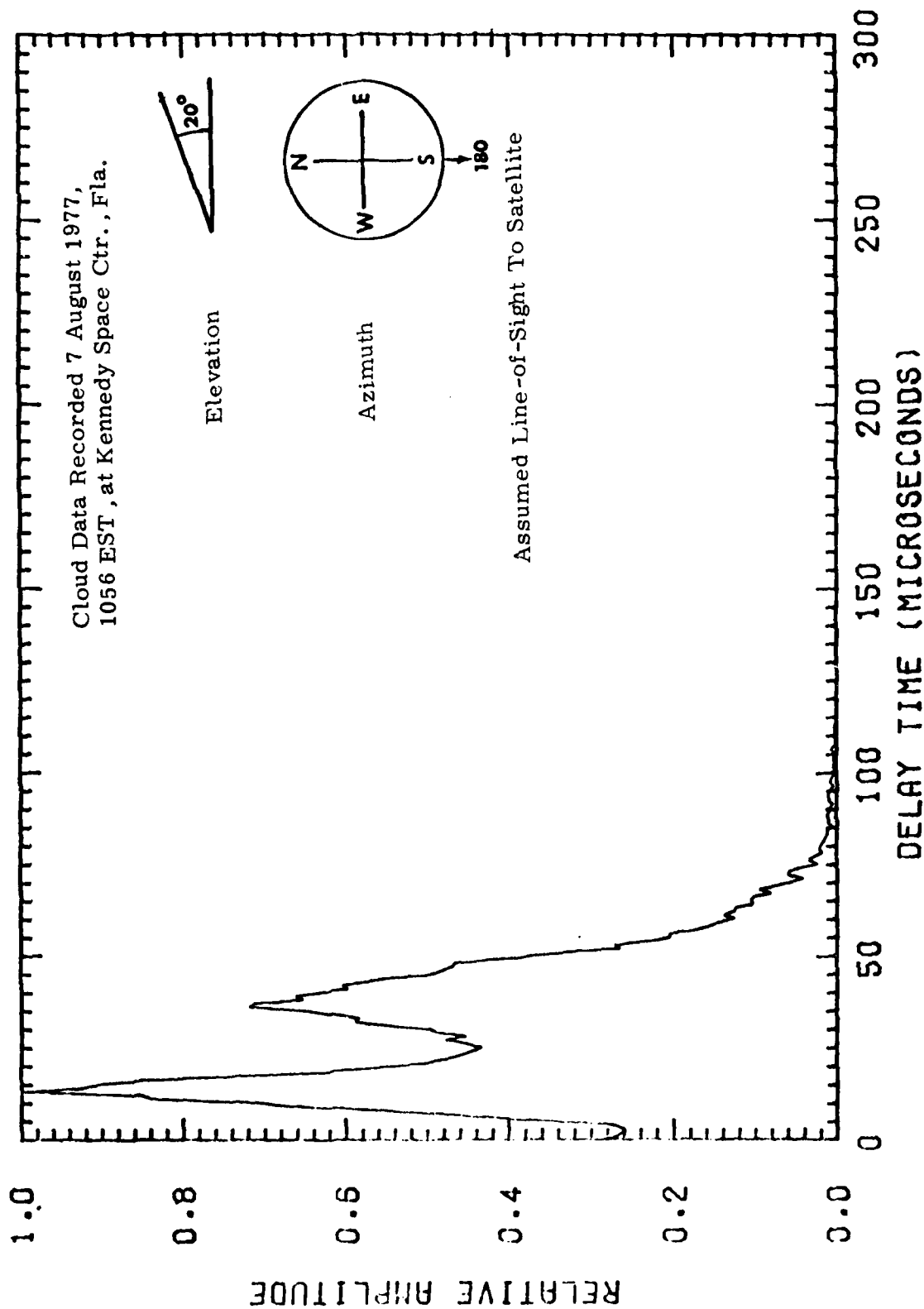


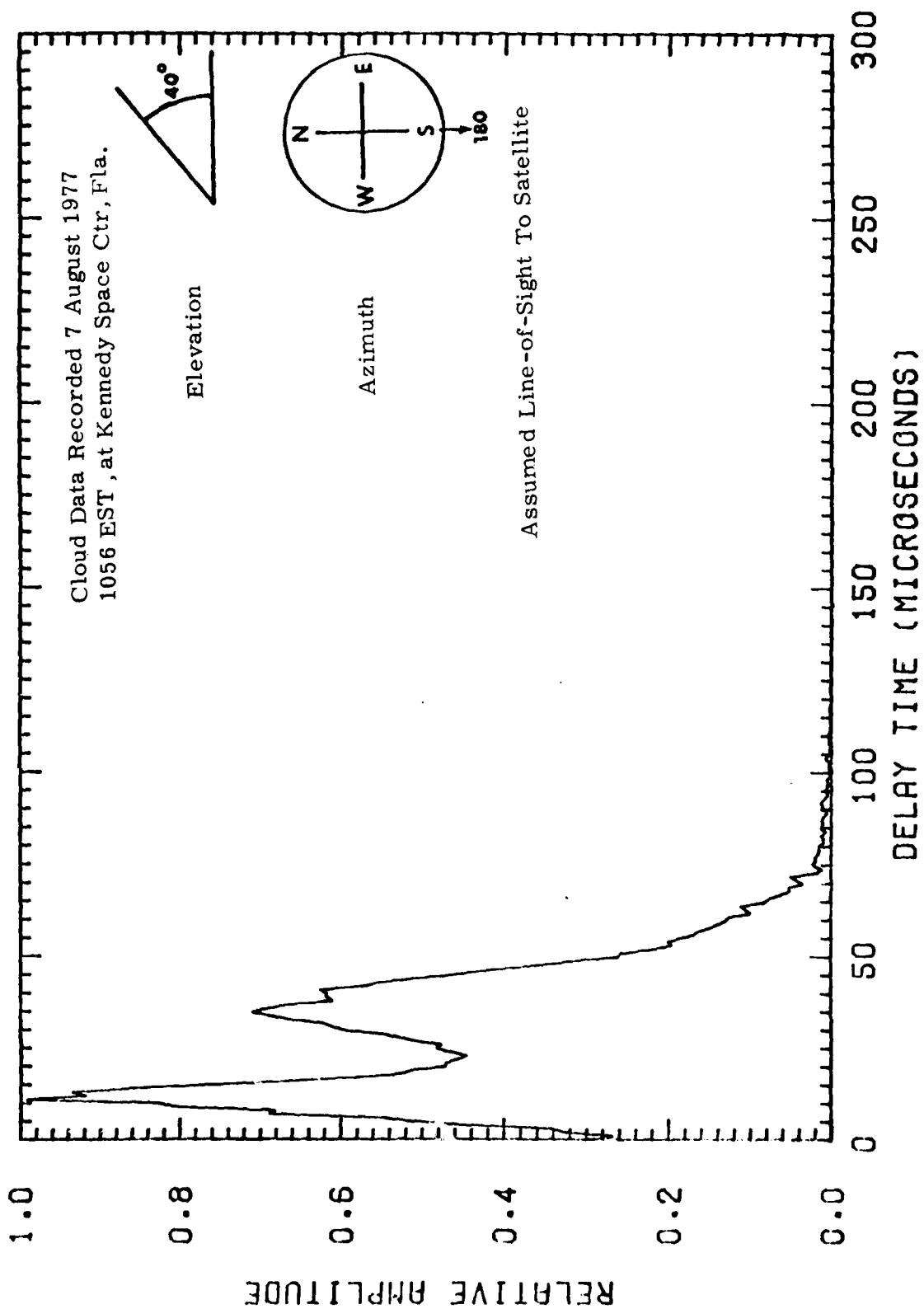


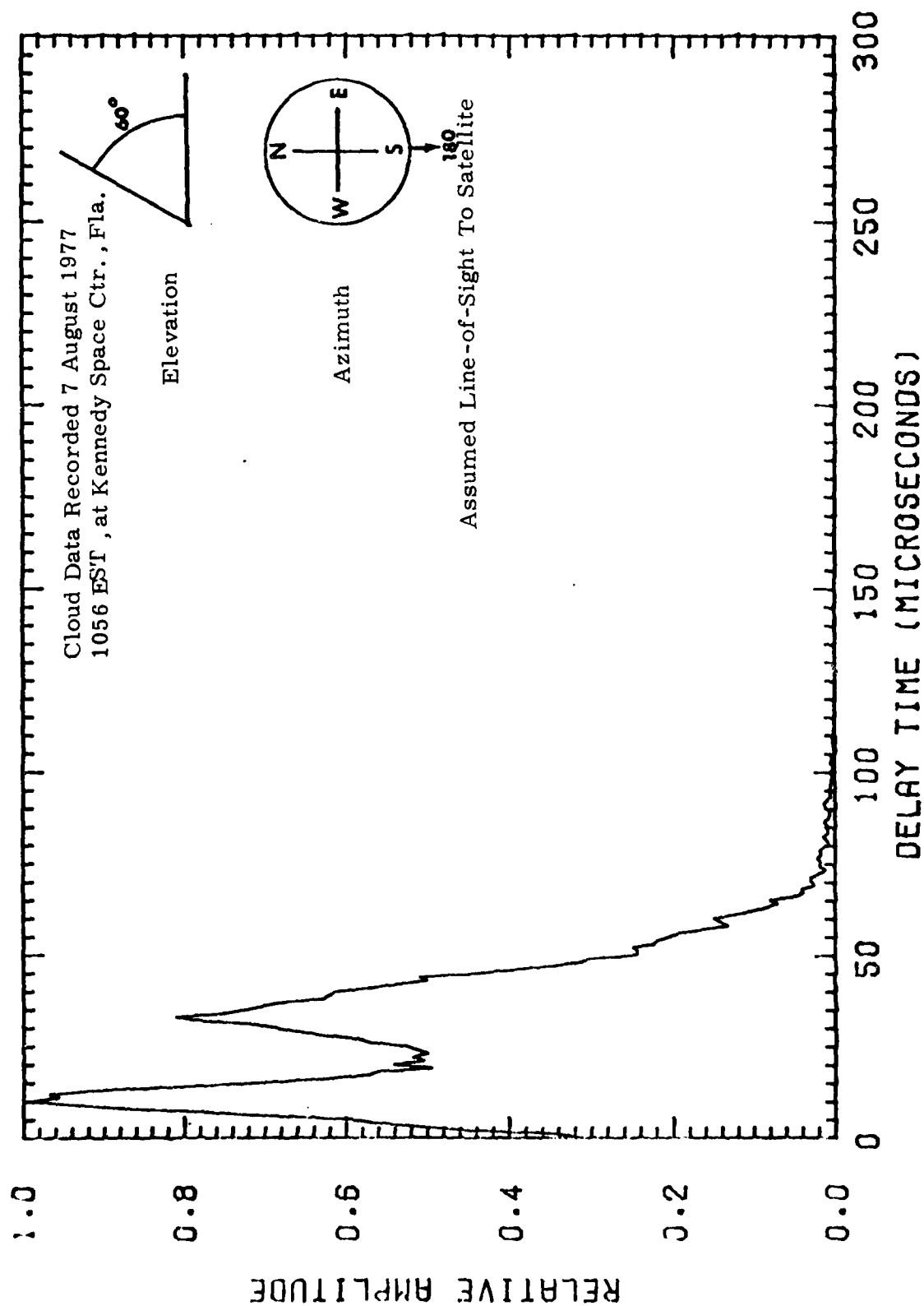












## 8. CONCLUSIONS

The system of data acquisition and reduction developed for this project has produced reasonable results. In two test situations data runs were made a minute or two apart and were reduced independently. For each situation the associated two data runs resulted in almost identical results. The data reduction process was almost done in a hands-off manner however erratic behavior of the shutter on the camera used to make the on-band/off-band pictures resulted in calculated oxygen path length errors of as much as  $\pm 10$  km. Such errors were consistent for all values derived for a particular data run. A method for estimating the magnitude of the resulting error was made based on the assumption of a reasonable shape for the data-predicted light pulse curves. This hands-on step is part of the data interpretation process that was used in this report. It is not basic to the technique developed for this problem but it is used because of equipment failure.

This is a passive technique in which steady state observations are used to calculate what would happen as a function of time to a light pulse. The reciprocity theorem was invoked so that observations of downward flowing sunlight could be used to predict the behavior of upward flowing light from a source near the earth's surface. Since a pulsed source is of interest a time dependent reciprocity relationship has been enunciated and has been used in this work. The validity of the time dependent relationship has not been demonstrated. It is accepted for this work because it "seems reasonable" and is required to get the job done.

A single number has been chosen to represent the effects of clouds on the transfer of a pulse of radiation from a source near the ground to a satellite. The number is the time in microseconds necessary for the delayed pulse to build up to some selected fraction of its maximum value. Values for the fraction of maximum used here are 0.8 and 0.6. The times

so determined are taken to be representative of the cloud induced errors in the geodetic timing. For the 63 calculations made in this report the average of the times of delay of the 0.8 (or 0.6) of maximum point is about 15  $\mu$ sec. There are seven delay values for each of the nine data runs. The maximum spread of the delay values has been determined for each data run. The average of these nine spread values is 10  $\mu$ sec. Figure 7.1 gives a detailed presentation of this information.

In Figure 7.1 the plots for 1 August shows two points with negative delay. This is unreasonable and could be corrected by a new choice of the zero correction. When the probable corrected zero times of Table 7.1 were established it was decided that there would be no second guessing. The 1 August plots result from this effort to stay honest.

An expected correlation between the half width of the time delay curve and the coupling coefficient was not demonstrated. This is shown in Table 8.1. The coupling coefficient, CC, is the ratio of the radiation from the whole sky incident on an isotropic detector to the radiation that would have been incident from the sun outside the atmosphere.

The radiance of the base of overcasts or clouds is dependent in part on the reflectivity of the ground. This effect has not been included in the data reduction. It can be of considerable importance especially when there is foliage on the ground. This is due to the rapid increase in reflectivity of foliage with wavelength increase between 0.7  $\mu$  and 0.8  $\mu$ . Future observations should include careful study of ground reflectivity. An ideal location for measurements involving  $O_2$  absorption at 0.76  $\mu$  would be at sea.

The most uncertain measured input to the data reduction was the height of the base of the overcast or cloud layer. For data reduction at any particular time a single value of base height was used for all clouds

Table 8.1 Comparison of the coupling coefficient with characteristics of relative amplitude vs delay curves.

DATE	TIME	TIME OF MAX	WIDTH AT 1/2 MAX	CC
7/28	1237	6 $\mu$ sec	30	0.99
8/1	1622	10	25	0.57
8/2	1415	38	32	0.22
8/2	1416	20	27	0.22
8/3	0935	20 35	43	1.02
8/3	0937	12	43	0.98
8/4	1325	8	30	0.58
8/6	1300	10	20	0.70
8/7	1056	10 30	42	0.64

and overcast present. This value was the average of several stereo determinations.

Thickness of cloud or overcast was calculated using Equation 5.6 for the data taken on 2 August at 1415 and 1416. Equation 5.6 assumes that only the cloud base is viewed and it is horizontal. In addition it is assumed that the cloud is thick enough to be described by diffusion theory. As a result of this sunlit and thin portions of the overcast had extraordinary thicknesses assigned to them. A major effort was invested in attempts to improve the calculation of cloud thickness but in the end it was decided to assign cloud thickness from any reasonable input available (cloud type etc.). Tests showed that the relative amplitude vs delay time curves are reasonably insensitive to the assigned cloud thickness.

The time delay curves are generated from radiance values appropriate to the clouds and overcast. The blue sky is neglected intentionally. A more mature data analysis technique should include contributions from the clear sky.

The principles of the technique would not be modified if the data were taken properly by some electro-optical system. If this were done there could be great saving in data manipulation before data reduction and an almost real time system might be possible.



## REFERENCES

1. Helmholtz, H., "Theorie der Wärme,
2. Minnaert, M., "The Reciprocity Principle in Lunar Photometry", *Astrophys. J.*, 93, 403-410 (1941).
3. Fritz, S., "Scattering of Solar Energy by Clouds of Large Drops, *Journal of Meteorology* 11, 291-300, August 1954.
4. Weisskopf, V. F., "The Science and Engineering of Nuclear Power", Clark Goodman, Ed., (Addison-Wesley, Cambridge, 1947), pp87-97.
5. Bucher, E. A., *Applied Optics* 12, 2391 (1973).
6. Schuster, A., "Radiation Through a Foggy Atmosphere", *Ap. J.* 21, 1-22, 1905.
7. Dietzius, R., "Die Absorption des Lichtes in Truben Medien, insbesondere Nebel and Wolken", *Beitr. z. Phys. d.f. Atm.* 11 69-74, 1923.
8. Mecke, R., "Über Zerstreuung und Beugung des Lichtes durch Nebel und Wolken", *Ann d. Phys.* 65, 257-273, 1921.
9. Stewart, H., "The Diffusion of Light Through an Overcast", University of Rochester Report to ARPA under Contract No. AF49(638)-1072, May 1961.
10. Basilio, M., Fox, D., and Stewart, H., "Final Report on the Distortion of Pulsed Light Signals by Scattering in and Between Clouds", Contract AF(29-1)-1183, Subcontract(113-2) July, 1961.
11. DeGroot, J., and Stewart, H., "Cloud Effects on the Signature of X-Ray Induced Fluorescent Light from a Nuclear Burst in Space", EHPA C73-64(U) 3 No. 56361, Aug. 14, 1964, Report under Contract AF33(657)-13599, AFTAC No. VT/5061/ASD(59).
12. DeGroot, J., Frank, R., Stewart, H., "Effects of Clouds on X-Ray Induced Fluorescent Light from A Nuclear Burst in Space", EHPA C73-65(U) 11 No. 56551, Jan. 29, 1965, Report under Contract AF33(657)-13599, AFTAC No. VT/5061/ASD(59).
13. van de Hulst, H. C., *Bull. Astron. Inst. Neth.* 20, 77 (1968).
14. Danielson, R. E., Moore, D. R., and van de Hulst, H. C., *J. Atmos Sci.* 26, 1078-1087 (1968).

#### REFERENCES (cont.)

15. McClatchey, R.A., et al, "Optical Properties of the Atmosphere (Third Edition)", AFCRL-72-0497, August 1972, pp 29-31.
16. Kingslake, R., Editor, "Applied Optics and Optical Engineering", Academic Press, p. 139, 1965.
17. Curcio, J.A., and Krestrick, G.L., "An Atlas of the Absorption of the Atmosphere from 5400 to 8520 A", NRL Report 4601, Aug. 1955.

## APPENDIX A

### EXPERIMENTAL EQUIPMENT

The experimental phase of this project spanned a six week period during July and August of 1977. The equipment was designed and constructed at HSS Inc in Bedford, MA. and transported to Kennedy Space Center, FL. for installation. The site provided was a NASA photographic station not currently in use. The coordinates of this station have been given in Section 5 of this report. This site provided a concrete pad of sufficient size flanked on three sides by a paved area. Most important this site provided an almost clear line-of-sight in all directions down to a zenith angle of  $85^\circ$ . There were a small number of local structures that did block an insignificant portion of the total field-of-view above the  $85^\circ$  horizon. This site was the primary site and was designated as the A site. Approximately 1 km from the A site a secondary site, B, was located for stereo picture purposes. The B site was visible from the A site and the connecting line was used as a reference line for orienting the camera formats. The A site and B site were connected by field telephone. The instrument complement at each site was:

#### A Site

- Red/blue all sky camera
- On/off band all sky camera
- Flight Research stereo camera
- Automax stereo camera
- All-sky radiometer
- Teleradiometer
- Sun photometer
- Camera controller

### B Site

Flight Research stereo camera

Automax stereo camera

Camera controller

Figure A1 is a general view of the A site. The two pipe stands in the foreground support the primary data Nikon cameras and their reflecting spheric mirrors, the camera on a side arm above and the mirror on a side arm below. Just in back of these cameras are the A site stereo cameras, a Flight Research Multidata 4C camera with 60 ° field-of-view lens on the left and an Automax camera with Fairchild All-sky lens on the right. Both cameras are mounted in watertight enclosures and adjusted to bring the optic axis of the lens vertical. The 60 ° field-of-view of the Flight Research camera was accommodated by a flat window in the top of the camera enclosure. The all-sky lens of the Automax required a hyper-hemispheric dome to accommodate the full field-of-view. The all-sky radiometer appears immediately behind the right pipe stand. The tele-radiometer is located in a tripod at the right of the picture.

Figure A2 shows the two stereo cameras located at the B site. The cables lead to the camera controller located in a watertight box off to the side. The square box sitting near the base of the Automax camera enclosure is simply an aluminum foil covered cardboard box placed over the top of the camera enclosures when pictures are not being taken to reflect sunlight and keep the enclosure as cool as possible for film protection.

Figure A3 is a detailed view of the reflecting spheric mirror used with on-off band primary camera. The red/blue primary camera had an identical mirror. The mirror mount provides for translation in two directions, rotation about the pipe stand, and accurate leveling. These motions permit the accurate location of the center of the small white button on the top of the mirror, the zenith button, directly under the optic



Figure A1. General view of equipment installation at A site.

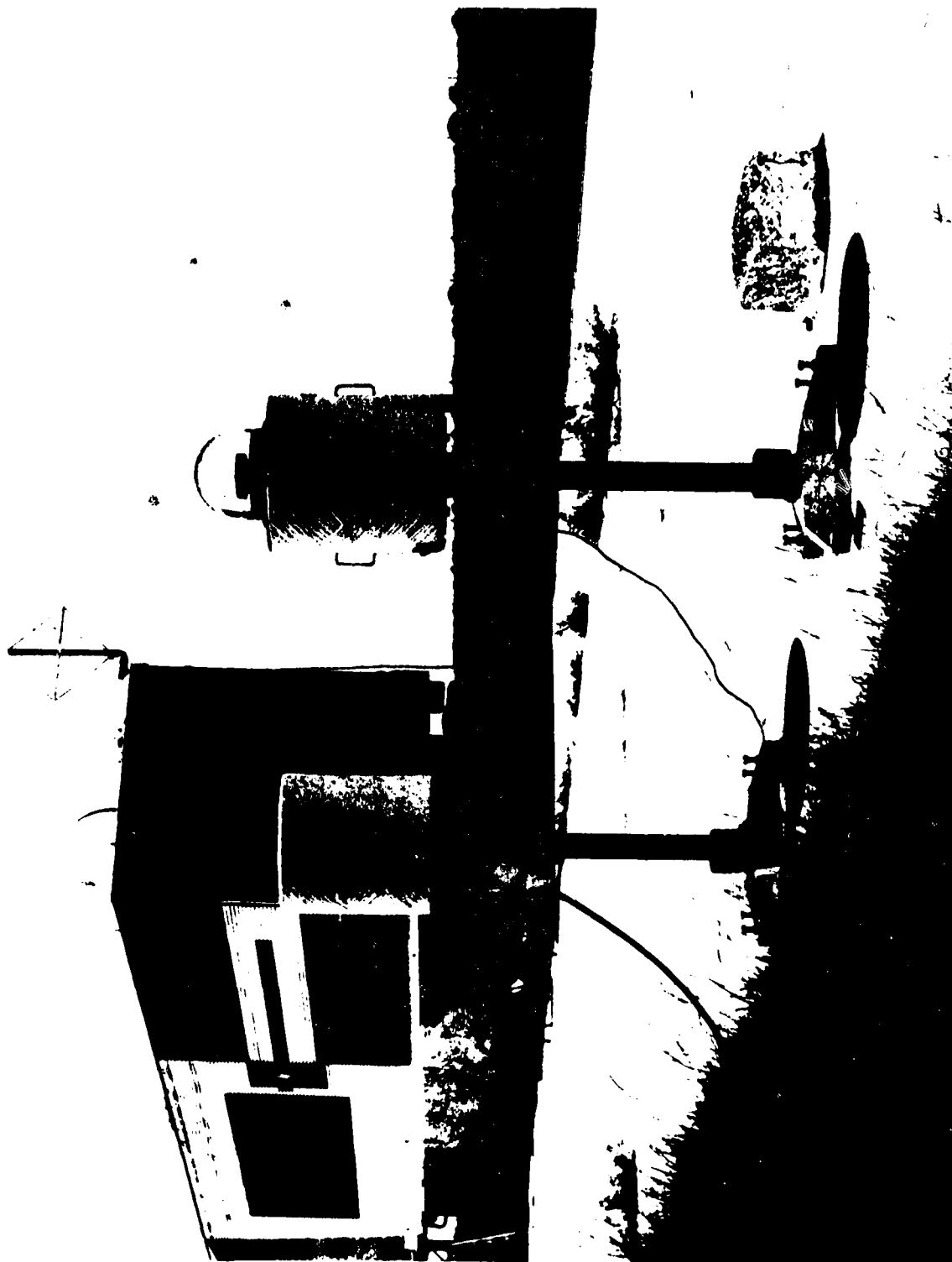


Figure A2. General view of equipment installation at B site (foreground).



Figure A7. Detail view of spherical mirror and support structure.

axis of the camera located on the side arm above. The camera itself was mounted in a manner which permitted the optic axis of the lens to be rotated to the vertical.

Once the camera support stand was set up and lagged to the concrete pad the primary camera alignment procedure was as follows. First the camera/mirror separation was adjusted to the desired distance. Then the camera axis was made vertical using a sensitive level (0.17 degrees tilt per 0.1 inch of bubble movement) mounted on the camera. The mirror position was then adjusted until the zenith button appeared centered on the crosshairs of the camera view finder. When in position a series of test exposures were made and processed. The test exposures from both the on/off band and the red/blue cameras were measured to determine the image distance for the two fiducial marks appearing on the mirror support plate (see Figure A3). (During manufacture the distance between the fiducial marks on each mirror support plate were made equal.) The measured distance between marks for each camera was converted to the magnification for that camera and the two compared. The camera/mirror distance for one camera was then changed and the alignment repeated until the camera magnifications agreed within a resolution element on the film.

Figure A4 shows a detailed view of the all sky radiometer. The reflecting spheric mirror can be seen in the center of dome. A collar surrounds the mirror as a field-of-view limiter. The reflected energy enters the optical system located in the tube directly above the mirror and falls on a silicon detector. The detector output signal is carried by cable to the electronics located in the housing below the dome. This housing has a removable, watertight transparent plate (removed in Figure A4) which allows the complete unit to operate unattended. In this mode the output signal is recorded on a strip chart recorder. The arm which appears





Figure 1. A large metal drum or barrel, possibly a fuel tank, lying on its side.

AD-A087 242

H S S INC BEDFORD MASS

F/G B/5

TIME DELAY OF TERRESTIAL LIGHT PULSES PROPAGATING THROUGH CLOUD--ETC(U)

JUL 80 H S STEWART, L B WOOLLAVER

F08606-77-C-0024

UNCLASSIFIED

HSS-B-058

AFTAC-TR-80-23

NL

3 OF 3

AD-A087 242



END

DATE

FILED

9-80

DTIC

in the photograph is used to block the direct rays from the sun under some conditions of measurement.

Figure A5 shows the teleradiometer. This instrument is very similar to the all sky radiometer except that it has very limited field of view. The radiometer housing was designed to accept any of the filters used in the primary data cameras, red, blue, on band, or off band. The output signal is read on the all sky radiometer electronics. The tripod mount for the teleradiometer also supported a boresighted elbow telescope for identifying the point being viewed by the teleradiometer.

The sun photometer (not shown) is a hand-held instrument designed by Fred Volz. The instrument measures the irradiance of the sun in a narrow field-of-view. Once calibrated the reading obtained can be related to the transmission of the atmosphere in the spectral band being observed from observer to outside the atmosphere. Each instrument provides several wavelength bands of measurement.

The experimental data recording procedure was as follows using a three-man crew, two at A site and one at B site. When a cloud structure of interest appeared, the B site operator was notified by telephone to turn on the camera control units, make the stereo camera identification exposures, and stand by for a count. The same procedure was carried out at the A site. The identification exposures were made on both stereo cameras and served to identify the next group of stereo pictures as to site, time, date, camera, and film number. When both sites were ready a verbal count was started over the phone to synchronize the stereo pairs. At the A site the two operators immediately made the four primary data exposures. B site was then again called, the count repeated and more stereo pairs exposed. The four primary data exposures were then repeated followed by a final group of synchronized stereo pairs. This sequence completed a data recording set. The operation of the all sky

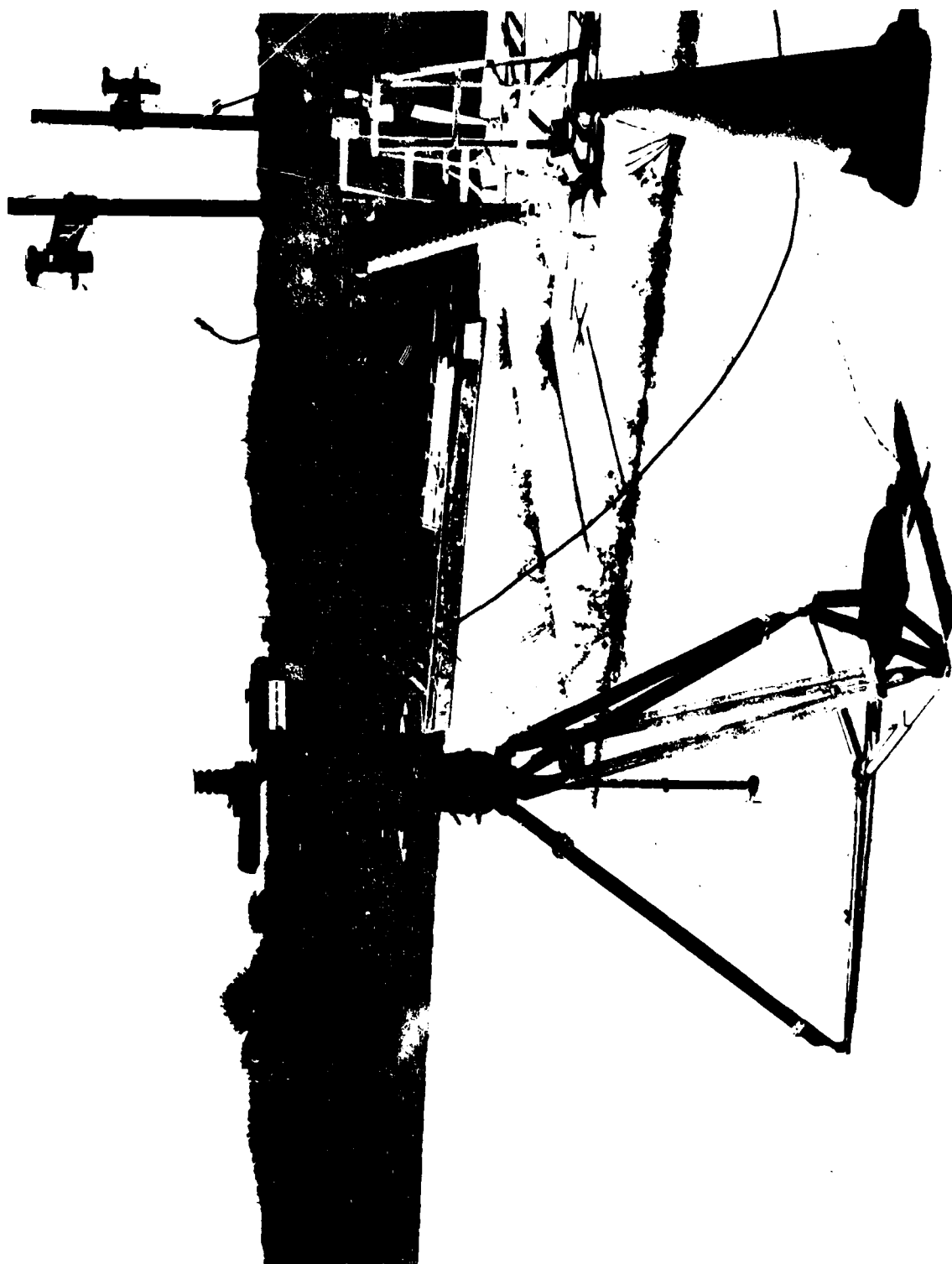


Figure A5. View of Toleradiometer and Support.

radiometer, teleradiometer, and sun photometer were not included in a primary data set run. These instruments were operated in a support mode to collect calibration and additional data.

DISTRIBUTION LIST

<u>DEFENSE DEPARTMENT</u>	<u>No. Copies</u>
DARPA (DEO) 1400 Wilson Boulevard Arlington, VA 22209 Attn: Cmdr. Tom Wiener	1
Deputy Under Secretary of Defense for Research and Engineering (Director, Communication Systems) The Pentagon Washington, D. C. 20301 Attn: G. Salton	1
DTIC-TC Cameron Station Alexandria, VA 22314	2
<u>NAVY</u>	
Commanding Officer Naval Research Laboratory Washington, D. C. 20375 Code 5540 (Dr. P. Ulrich) Code 5540 (Dr. W. Watt) Code 5540 (Dr. R. Burnham) Code 7005 (Dr. J. Schwartz) Code 5503 (EOPTPO, Dr. J. McCallum)	5
Commander Naval Air System Command Washington, D. C. 20361 NAIR-360A (F. J. Leuking)	1
NAVELEX Washington, D. C. 20360 Attn: M. L. Parker (Code 3102) Attn: Dr. R. LeFande (PME117-20)	2
Office of Naval Research Boston Branch Bldg. 114 Section D 666 Summer Street Boston, MA 01730 Attn: Dr. Matthew White	1

DISTRIBUTION LIST (Cont.)

	<u>No. Copies</u>
<u>NAVY (Cont.)</u>	
NOSC 271 Catalina Boulevard San Diego, CA 94152 Attn: Dr. L. Stotts Attn: Dr. G. Mooradian Code 8114 Attn: Dr. M. Geller Code 8114	3
<u>AIR FORCE</u>	
HQ, USAF/INYS (Lt. Col. Peterson) Washington, D.C. 20330	1
AFTAC/TFE Patrick AFB, FL 32925 Attn: Maj. J. VanWorkum	5
Wright-Patterson AFB Electro-Optics Division Dayton, OH 45433	1
HQ SD/YGJE P.O. Box 92960 Worldway Postal Center Los Angeles, CA 90009 Attn: Lt. Col. C. Radoy Attn: Lt. Col. A. H. Hayden Attn: Maj. L. L. Swartzkopf	3
JSTPS/JPST Offutt AFB, Nebraska 68113 Attn: Maj. R. E. Wiley	1
AFGL Hanscom AFB, MA 01731 Attn: Dr. A. T. Stair (OPA) Attn: Dr. R. Fenn (OPA)	2
U.S. Air Force Academy Dept. of Physics Colorado Springs, CO 80840 Attn: Capt. Bobby N. Turman	1

DISTRIBUTION LIST (Cont.)

	<u>No. Copies</u>
<u>DEPT. OF COMMERCE</u>	
NOAA/OAS3 NESS Washington, D. C. 20233 Attn: Dr. Harold Yates	1
NOAA (WPL/ERL) R45X9 Boulder, CO 80303 Attn: Dr. Freeman Hall	1
<u>INSTITUTE/FOUNDATIONS</u>	
Institute for Defense Analysis Science and Technology Division 400 Army-Navy Drive Arlington, VA 22202 Attn: Dr. V. J. Corcoran	1
National Science Foundation Engineering Division 1800 G Street, NW Washington, D. C. 20550 Attn: Dr. Elias Schutzman	1
<u>UNIVERSITIES/LABORATORIES</u>	
Lawrence Livermore Laboratory P. O. Box 808-L-372 Livermore, CA 94550 Attn: Dr. Lowell Wood Attn: Dr. J. Marling	2
Oregon Graduate Center for Study and Research 19600 NW Walker Road Beaverton, OR 97005 Attn: J. Richard Kerr Attn: R. A. Elliot	2



DISTRIBUTION LIST (Cont.)

	<u>No. Copies</u>
<u>UNIVERSITIES/ LABORATORIES (Cont.)</u>	
The Johns Hopkins University Applied Physics Laboratory John Hopkins Road Laurel, MD 20810 Attn: Dr. Milton Linevsky	1
Massachusetts Institute for Technology Lincoln Laboratories P.O. Box 73 Lexington, MA 02173 Attn: Richard Osgood	1
University of California, San Diego Visibility Laboratory P.O. Box 6049 San Diego, CA 92106 Attn: R. W. Austin	1
Los Alamos Scientific Lab. (LASL) P.O. Box 1663 Los Alamos, NM 87544 Attn: Doyle Evans, P4, M436 Attn: Paul Glore Attn: Harold Argo Attn: Henry Horak Attn: Guy Barasch	5
Sandia Laboratories P.O. Box 5800 Albuquerque, NM 87115 Attn: H. M. Dumas (Div. 1240) Attn: Tim Taylor (Div. 1242) Attn: Dave Henry (Div. 1241) Attn: S.K. Fletcher (Div. 1241) Attn: B. A. Wickesberg (Div. 1242) Attn: G. H. Mauth (Div. 1243) Attn: C. F. Jacobs (Div. 1243) Attn: R. E. Spalding (Div. 1244) Attn: G. J. Dodrill (Div. 1244) Attn: A. D. Thornbrough (Div. 1245)	10

DISTRIBUTION LIST (Cont.)

	<u>No. Copies</u>
<u>COMPANIES</u>	
Avco Everett Research Laboratory 2385 Revere Beach Pwy Everett, MA 02149 Attn: Dr. J. Daugherty Attn: Dr. J. Jacobs Attn: Dr. D. Trainor Attn: Dr. I. Itzkan Attn: H. A. Hyman	5
Booz-Allen Hamilton 4330 East West Highway Bethesda, MD 20014 Attn: A. E. Durling	1
Charles Stark Draper Laboratory, Inc 555 Technology Square Cambridge, MA 02139 Attn: Dr. F. Scammel Attn: G. A. Ouellete	2
Hughes Research Laboratory 3011 Malibu Cayon Road Malibu, CA 90265 Attn: Dr. R. Abrams	1
Hughes Aircraft Co. Centinela & Teale Culver City, CA 90230 Attn: Dr. N. R. Hauser	1
Hughes Aircraft Co. El Segundo Site P.O. Box 92919 Los Angeles, CA 90009 Attn: T. S. Hartwick	1
ITEK Corporation 10 Maguire Road Lexington, MA 02173 Attn: Dr. J. Hardy Attn: A. J. MacGovern	2

DISTRIBUTION LIST (Cont.)

	<u>No. Copies</u>
<u>COMPANIES (Cont.)</u>	
Rockwell International Corp. Rocketdyne Division 6633 Canoga Avenue Canoga Park, CA 91304 Attn: W. Mower	1
SRI International 333 Ravenswood Avenue Menlo Park, CA 94025 Attn: Dr. J. D. Malick Attn: Dr. J. Naar Attn: Dr. N. A. Walker Attn: Dr. R. Honey Attn: Dr. D. Heustis	5
W. J. Schaefer Associates 10 Lakeside Office Park Wakefield, MA 01880 Attn: Dr. F. W. French	1
United Technology Research Center 400 Main Street East Hartford, CT 06108 Attn: Dr. W. Nighan Attn: Dr. R. Brown	2
GTE Sylvania Box 188 Mountain View, CA 94042 Attn: Bob Hostetter	1
Radiation Research Assoc., Inc. (RRA) 3550 Hulen Street Fort Worth, TX 76107 Attn: Dave Collins Attn: Mike Wells	2
Science Applications, Inc 5 Palo Alto Square, Suite 200 Palo Alto, CA 94304 Attn: Richard Hillendahl Attn: Doug Moffat	2
Ford Aerospace & Comm. Corp. 3939 Fabian Way Palo Alto, CA 94303 Attn: John Blake, MS U-60	5

DISTRIBUTION LIST (Cont.)

	<u>No. Copies</u>
<u>COMPANIES (Cont.)</u>	
Lockheed Palo Alto Research Laboratories 3251 Hanover Street Palo Alto, CA 94304 Attn: Dr. A. Title Attn: Dr. L. R. Lunsford Attn: Dr. Louise Decker	3
La Jolla Research Corp. P.O. Box 1207 La Jolla, CA 92038 Attn: Dr. W. P. Rudolph	1
McDonnell-Douglas Astronautics Box 516 St. Louis, MO 63133 Attn: Dr. J. Kackson Attn: Dr. J. D. Kelley Attn: Dr. Monte Ross Attn: C. Ciany	4
Maxwell Labs., Inc. 9244 Balboa Avenue San Diego, CA 92123 Attn: Dr. J. Tilson	1
Mathematical Science Northwest P.O. Box 1187 Bellevue, WA 98009 Attn: Dr. R. Center Attn: Dr. C. Fisher	2
Northrop Research and Technology 1 Research Park Palos Verdes Peninsula, CA 90274 Attn: Dr. M. Bhaumik	1
Pacific Sierra Research 1456 Cloverfield Boulevard Santa Monica, CA 90404 Attn: Dr. R. Lutomirski Attn: Dr. A. P. Ciervo Attn: Dr. E. C. Fields	3

DISTRIBUTION LIST (Cont.)

<u>COMPANIES (Cont.)</u>	<u>No. Copies</u>
Aerospace Corp. P.O. Box 92957 Los Angeles, CA 9009 Attn: Charles Praut	1
HSS Inc 2 Alfred Circle Bedford, MA 01730	10